

Tensile response of Strain-Hardening Ultra High Performance Fiber Reinforced Concretes under low loading rates and low temperatures

Thèse N° 7336

Présentée le 26 juillet 2019

à la Faculté de l'environnement naturel, architectural et construit
Laboratoire de maintenance, construction et sécurité des ouvrages
Programme doctoral en génie civil et environnement

pour l'obtention du grade de Docteur ès Sciences

par

Mohamed Abdul HAFIZ

Acceptée sur proposition du jury

Dr P. Lestuzzi, président du jury
Dr. E. Denarié, directeur de thèse
Prof. R. Gettu, rapporteur
Prof. L. Sorelli, rapporteur
Prof. K. Scrivener, rapporteuse

2019

*To my beloved parents,
Amina Kutty and Abdul Nazer*

“Dreams are not what you see in sleep, dreams are those which do not let you sleep”

- Dr. A. P. J. Abdul Kalam

-Former President of India

- 15 October 1931 – 27 July 2015

Foreword

Research and development work at MCS/EPFL since 1999 with SH-UHPFRC have demonstrated that these materials are ideally suited for applications in composite SH-UHPFRC-RC structures. With the appropriate combination with reinforcement bars, they provide a very efficient (often the only possible) technique to reinforce existing structures without increasing deadweight. After numerous successful cast-in-place applications of these materials in Switzerland and abroad since 2004, this intervention technique has entered a new industrial scale with the reinforcement of the Chillon viaducts in Switzerland in 2014/2015. Some research topics related to this technique remained however unexplored, among which the tensile response of SH-UHPFRC under very low loading rates.

The development of autogenous shrinkage and eigenstresses under restraint in cementitious materials, as it is the case for SH-UHPFRC cast-in-place over existing reinforced concrete substrates, exhibits a complex behavior related to the effects of temperature on the various acting phenomena (driving forces of autogenous shrinkage, hydration of clinker, reaction of supplementary cementitious materials, evolution of stiffness and ageing viscoelastic response, restraint). The associated loading rates, in terms of imposed shrinkage deformations, are very low, typically 10^{-9} 1/s, a thousand times lower than those for quasi-static loading. The tensile response of SH-UHPFRC (elastic limit, strength and deformability) governs the ability of these materials to withstand the effects of eigenstresses without cracking, to ensure their effectiveness for the rehabilitation of structures. This response under loading rates in the range of those active under restrained shrinkage, under different curing temperatures, has never been studied, particularly for Strain-Hardening UHPFRC with the massive replacement of clinker by mineral additions.

In this context, Mohamed Hafiz works shed new light on the tensile response of UHPFRC with results under very low loading rates never studied so far. They open the way to new generations of more sustainable low clinker SH-UHPFRC as well as confirm the applicability of SH-UHPFRC cast-in-place under winter climatic conditions.

Mohamed Hafiz demonstrated throughout his thesis his ability to conduct research in multidisciplinary domains with a creative and critical vision. He successfully found his way in the labyrinths of a very challenging topic. In the name of the whole team of MCS, I thank him for his constant and deep dedication to his research topic as well as for his professional skills, openness of mind, enthusiasm and scientific curiosity.

Lausanne, July 2019

Dr. Emmanuel Denarié

Acknowledgements

Even before embarking on this roller coaster ride for achieving a doctorate, I knew it was going to be difficult. But then nothing worthwhile will come easy. This doctoral thesis is the outcome of four years of intense, but delightful work through which I have achieved immense professional and personal development in different aspects of my life. It taught me to be professional, systematic, methodological and efficient, but more importantly, to be calm and patient. The four years of research would have been really difficult if not for the immeasurable support and encouragement of many outstanding and kind hearted people, whom I have come across over the years.

First of all, I would like to express my immense and sincere gratitude to my thesis director, Dr. Emmanuel Denarié, without whom this thesis would not have been a reality. You truly are one of the most patient and kind hearted human being that I have ever seen. You are a very good scientist, an extremely good teacher, but most importantly, an outstanding guide. The way you guided me whenever I had reached a dead end, will always be appreciated. It was your tireless support over the past four years that helped me pass through some of my most difficult periods of life. Thank you very much from the bottom of my heart for all the help that you have given me. I will try my best to impart the knowledge and wisdom that you have provided me, to all the others that I will come across in the future.

I would also like to thank Prof. Eugen Brühwiler for granting me the precious opportunity to work in MCS lab and for the trust that was placed in me. You are the epitome of self-confidence and forward thinking. There is always an air of positivity around you, which is also imparted to the others around you. I have always admired the way you start a conversation and the way you accommodate the people around into it. Thank you very much for your valuable advices over the innumerable coffee breaks that we had together. Thank you once again for allowing me to be a part of MCS.

The life in MCS would not have been enjoyable if not for the endless support and friendship of my colleagues in MCS. I will never forget the company of my office mate and dear friend, Amir over the past four years. I could not have asked for a better roommate than you. You are easily among the most efficient people that I have seen in my life. Thank you for your help with my experimental tests, for your assistance in writing the articles and most importantly for boosting me up whenever I was feeling low. I hope our paths will cross again in the near future. I would also like to extend my extreme gratitude to the SENIORS of MCS when I had arrived; Malena, Basil and Christophe, without whom I would have had a hard time settling in EPFL after my arrival. Special thanks to Christophe for being my Ski teacher and for pushing me to do things that I was lazy about. I would also like to express my immense gratitude to my other colleagues; Gianni, for being one of the nicest guys and for arranging the countless number of hot pot dinners, Bartek and Philippe, for your countless humorous conversations and Imane, for the innumerable help that you have given me over many things and for being my French speaker over the years. Special thanks to Dr. Hamid Sadouki for his help in assisting me with the simulations using DIANA and for his personal

advices. Settling in EPFL would not have been smooth, if not for the immense help given by Ms. Florence Grandjean. Thank you for helping me with all the administrative works and for making my life in EPFL easy and smooth.

A huge part of the experimental tests during my thesis was done in the GIS lab of EPFL, which is comprised of some of the best (if not THE best) technicians among all the universities in the world. I would not have been able to complete my thesis if not for the strong support and hard work of the technicians. I would specially like to acknowledge the help given by Serge Despont and for his immense contribution in my experimental tests. I have always felt that you deserve much more than a PhD degree for your incredible ideas and way of thinking. Your high quality, meticulous and precise work regarding the preparation of my specimens and test setup will always be remembered. Equal credits should also be given to Gilles Guignet for his kind support over the past years, and for single handedly developing many devices and test setups that I have used during my thesis. All these would not have been possible if not for the proper coordination of Sylvain Demierre, who is by far the jolliest person I have ever seen. There was not even a single time that I didn't have a smile on my face while talking to you. I would also like to express my thankfulness to Gérald, Frédérique, François and Armin for their contributions, conversations as well as for their smiles. Thank you all for creating such a pleasant atmosphere in the laboratory.

The different experiments done during the thesis would not have been complete without the help from people and laboratories outside of MCS and GIS. The help given by Hadi Kazemi, who was also a previous member of MCS, is very much appreciated. His timely advices and tips on carrying out the experiments were truly helpful. I would also like to acknowledge the assistance of Lionel Sofia and Jean Dias Rego in the preparation of most of my experimental specimens and that of Yosra Briki in helping me conduct the Isothermal Calorimetry tests in LMC, EPFL. I am also really thankful to Prof. Jørgen Skibsted of Aarhus University for his help in conducting the ^{29}Si MAS NMR tests and for the deconvolutions of the resulting spectra.

I would like to extend my gratitude to the members of the jury for my oral exam, Dr. Pierino Lestuzzi, Prof. Karen Scrivener, Prof. Ravindra Gettu and Prof. Luca Sorelli. Thank you very much for your valuable suggestions for bringing out the best in my doctoral thesis. Special thanks to Prof. Luca Sorelli for his valuable support and advices during his period of stay in EPFL and for being a very good friend over the time.

Life in Switzerland would not have been enjoyable without the presence of my “mallu” friends in Switzerland; Riyaz, Aswin, Arif, Aslam, Deepu, Fahadkka and family. The countless trips that we have had throughout Europe and the special memories that we had over the years will always be there in my mind. Special mention to my flat mate Riyaz, for being the most supportive person throughout my entire stay here in Switzerland. Thank you very much for your understanding, for the food you cooked for me and for the countless drives that you did for us. Thank you Aswin for being around me throughout my stay in EPFL. Thank you Arif and Aslam for creating that Malappuram vibe and making me feel at home. Without you people, life in Switzerland would have been impossible.

Special mention also goes to my other companions in EPFL with whom I had countless number of trips including Anwar, Ranit, Vidit, Sai and Vyajyanti. I can also not forget my badminton companions; Sai, Kunal, Akshay, Satheesh, Anudeep, Aravind, Mukul, Aashish, Adhi, Thomas and Pascal, without whom life would have been too monotonous and boring.

And last of all, but not the least, my family. Thanks to my grandmother, my biggest loss during these four years. I will never forget your final smile and the way you asked me to come back as a proud doctor. Thanks to my brothers, sister, brother-in-law, niece and nephew, my uncles and my aunts for your unconditional love and support. Thanks to my lovely wife for all the sacrifices that you made over the last few years. Moreover, to my little princess, my lovely daughter, for waiting for me to come home back to you to spend the rest of my life with you.

And finally, my parents. Uppa (Dad) and Umma (Mom), I simply love you for all what you have done for me. Both of you have spent your entire lives to take care of me, my brothers and my sister, during which you had sacrificed your own dreams and desires. You have been so special in my life that even writing this brings tears into my eyes. You have been my home, my shelter, my food, my legs, my wings and my soul. Thank you both for your eternal support and immeasurable love. I will make sure that I will take care of you for the rest of your lives. This thesis is for you, a very small token of my appreciation. Thank you very much.

Lausanne, July 2019

Mohamed Abdul Hafiz

Summary

Strain-Hardening Ultra High Performance Fiber Reinforced Concretes (SH-UHPFRC) are cementitious materials with exceptional mechanical properties and outstanding durability making them ideal materials for rehabilitation, for the improvement of load carrying capacity and protective functions of existing structures. However, cast in-situ UHPFRC undergoes restrained autogenous deformations leading to the development of tensile eigenstresses with very low strain rates. Even though, in majority of the cases, the strain-hardening capability and tensile viscoelastic potential of the material help in mitigating these eigenstresses, in specific cases, a combination of detrimental fiber orientation and adverse climatic conditions (especially low temperature winter casting) may lead to the exhaustion of the strain-hardening potential. This results in the development of localized macrocracks, making the objective of using SH-UHPFRC as a onetime intervention strategy in rehabilitation application obsolete.

The main objective of this thesis was to investigate the influence of very low strain rates and moderate to low temperatures on the tensile response of two types of SH-UHPFRC mixes; Mix I with pure type I cement, silica fume and steel fibers and Mix II with 50% replacement of cement with limestone filler and a similar fibrous mix. The influence of temperature on hydration kinetics and development of elastic modulus was studied at a material level, which was then used to explain the trends found for the tensile response at a structural level.

An extensive experimental campaign was carried out to investigate the tensile response of the mixes. At the material level, Isothermal Calorimetry, ^{29}Si MAS NMR and Vibration Resonance Frequency tests were carried out to study the development of degree of hydration and reaction of cement and silica fume as well as the development of elastic modulus at different temperatures (5 °C, 10 °C and 20 °C). At a structural level, the Temperature Stress Testing Machine (TSTM) was used to determine the autogenous deformations and associated eigenstresses, while an electromechanical test setup was used to investigate the influence of very low strain rates (1×10^{-5} 1/s – 5×10^{-9} 1/s) on the tensile resistance parameters like elastic limit, elastic modulus, tensile strength and strain at tensile strength, at different temperatures (5 °C, 10 °C and 20 °C). Furthermore, a viscoelastic-viscohardening model was developed to predict the tensile response of both SH-UHPFRC mixes at low and high stress levels.

The results indicated that the elastic limit decreased considerably with a decrease in the strain rate, with a reduction of more than 20% at a strain rate of 5×10^{-9} 1/s when compared to that at a quasi-static strain rate. The full restraint tests in the TSTM at different temperatures revealed that, except for Mix I cured at 20 °C, the eigenstresses in none of the other tests reached the respective elastic limit, after one month, even under low temperatures. Moreover, because of its higher relaxation potential, the rate of development of eigenstresses in Mix II was considerably lower than that of Mix I. However, the eigenstresses in Mix II reached close to the strain-hardening domain after three months.

The results also revealed that the resistance parameters like elastic limit and tensile strength were dependent on the kinetics of hydration of the mixes, with Mix II exhibiting a slightly slower development of hydration when compared to Mix I. The ^{29}Si MAS NMR tests showed that the pozzolanic reaction develop at different rates in two stages, which leads to different rates of development of autogenous shrinkage and eigenstresses.

The developed viscoelastic-viscohardening model was able to predict the tensile responses of the mixes at different loading conditions. The model was used to discuss the interaction of ageing, hydration, early age volume changes, viscoelastic phenomena and damage and their influence on the overall tensile behavior of UHPFRC. It showed that under very low strain rates, the UHPFRC might exhibit an apparent strain softening response, which was attributed to the combined effect of hardening and a more dominant non-linear viscous relaxation.

Keywords: SH-UHPFRC, tensile response, low strain rates, low temperatures, autogenous shrinkage, eigenstresses, relaxation, early age, low clinker, limestone filler, degree of hydration, maturity, silica fume, TSTM, isothermal calorimetry, ^{29}Si MAS NMR, acoustic emission, viscoelastic-viscohardening model.

Résumé

Les bétons armés fibrés à ultra hautes performance avec un comportement écouissant (SH-BFUHP) sont des matériaux cimentaires qui présentent des propriétés mécaniques exceptionnelles et une durabilité remarquable, faisant d'eux des matériaux idéaux pour la réhabilitation, l'amélioration de la capacité de charge et pour la protection des structures existantes. Cependant, couler le BFUHP in-situ peut engendrer des déformations autogènes restreintes, qui conduisent au développement de contraintes résiduelles de traction avec des taux de déformations faibles. Même si dans la majorité des cas, la capacité du durcissement en déformation de ces matériaux et leur potentiel viscoélastique en traction aide à atténuer ces contraintes propres. Dans des cas spécifiques, une combinaison d'une orientation de fibre préjudiciable et des conditions climatiques défavorables (en particulier, les coulées en hiver à basse température) peut entraîner l'épuisement du potentiel de l'écrouissage. Cela se traduit par le développement de macro-fissures localisées qui rend l'utilisation des SH-BFUHP dans les interventions de réhabilitation obsolète.

L'objectif principal de cette thèse était d'étudier l'influence des taux de déformation très faibles et des basses températures sur la réponse en traction des deux types de mélanges SH-BFUHP; Mélange I avec le ciment pur de type I, les fumées de silice et les fibres d'acier et le Mélange II en remplaçant 50% de ciment avec le filler calcaire et un mélange fibreux similaire. L'influence de la température sur la cinétique d'hydratation et le développement du module d'élasticité a été étudiée à un niveau matériel, qui a été ensuite utilisé pour expliquer les tendances trouvées pour la réponse en traction à un niveau structurel.

Une vaste campagne expérimentale a été menée pour étudier la réponse en traction des mélanges. Au niveau matériel, la calorimétrie isothermique, RMN MAS du ^{29}Si et les essais de fréquence de résonance vibratoire ont été réalisés pour suivre le développement du degré d'hydratation et la réaction du ciment et des fumées de silice, ainsi que le développement du module d'élasticité à différentes températures (5 °C, 10 °C et 20 °C). Au niveau structurel, la machine d'essai (TSTM) a été utilisée pour déterminer les déformations autogènes et les contraintes résiduelles associées, tandis qu'une configuration d'essai électromécanique a été utilisée pour étudier l'influence des taux de déformation très faibles (1×10^{-5} 1/s – 5×10^{-9} 1/s) sur les paramètres de résistance à la traction tels que la limite élastique, le module d'élasticité, la résistance à la traction et la déformation à la résistance à la traction, à différentes températures (5 °C, 10 °C et 20 °C). En outre, un modèle viscoélastique-viscoécrouissant a été développé pour prédire la réponse en traction des mélanges SH-BFUHP à des niveaux de contraintes faibles et élevés.

Les résultats indiquent que la limite élastique a considérablement diminué avec une diminution de la vitesse de déformation, et une réduction de plus de 20 % à un taux de déformation de 5×10^{-9} 1/s comparé à un taux de déformation quasi-statique. Les essais TSTM encastés à différentes températures ont révélé, à l'exception du mélange I traité à 20 °C, que les contraintes résiduelles ont atteint la limite d'élasticité après un mois, même sous de basses températures. En outre, les contraintes résiduelles en mélange II à n'importe quel

âge ont été considérablement inférieures à celles du mélange I, en raison du potentiel de relaxation élevé. Les résultats ont révélé que les paramètres de résistance comme la limite d'élasticité et la résistance à la traction dépendaient de la cinétique d'hydratation des mélanges, avec le mélange II présentant un développement d'hydratation un peu plus lent comparé au mélange I. Les essais du RMN MAS du ^{29}Si ont montré que la réaction pouzzolanique se développe à des rythmes différents en deux étapes, ce qui conduit à des taux différents de développement du retrait autogène et des contraintes résiduelles.

Le modèle viscoélastique-viscoécrouissant peut prédire les réponses de résistance à la traction des mélanges à des conditions de chargement différent. Le modèle a été utilisé pour discuter l'interaction du vieillissement, l'hydratation, les changements de volume à jeune âge, les phénomènes et endommagements visco-élastiques et leur influence sur le comportement global en traction du BFUHP. Il a été montré que pour des taux de déformation très bas, le BFUHP peut présenter une réponse d'adoucissement apparent de déformation, qui a été attribuée à l'effet combiné de l'écrouissage et d'une relaxation visqueuse non linéaire plus dominante.

Mots-clés : SH- BFUHP, réponse en traction, taux de déformation faible, basse température, retrait autogène, contrainte résiduelle, relaxation, jeune âge, faible clinker, filler calcaire, degré d'hydratation, maturité, fumée de silice, TSTM, calorimétrie isotherme, ^{29}Si RMN, émission acoustique, modèle viscoélastique-viscoécrouissant.

Table of Contents

Foreword	v
Acknowledgements	vii
Summary	xi
Résumé.....	xiii
Table of Contents.....	xv
List of figures	xxi
List of tables	xxvii
Glossary	xxix
Abbreviations	xxix
List of Symbols	xxx

Chapter 1 - Introduction..... 1

1 Context	3
2 Motivation and scope	4
2.1 Restrained shrinkage and eigenstresses	4
2.2 Influence factors.....	8
2.3 Tensile response (resistance envelope) of SH-UHPFRC.....	9
2.4 Sustainability.....	11
3 Objectives.....	12
4 Organization of the thesis	13
References.....	14

Chapter 2 - Tensile response of low clinker UHPFRC subjected to fully restrained shrinkage..... 19

Abstract	19
1 Introduction	21
2 Experimental.....	23
2.1 Materials and preparation	23
2.2 Vibration Resonance Frequency Test (VRFT)	27
2.3 Isothermal calorimetry tests	28
2.4 Temperature Stress Testing Machine (TSTM)	28
2.5 Loading programs for the TSTM tests.....	29

3	Results and discussion	31
3.1	Development of dynamic elastic modulus.....	31
3.2	Heat of hydration	33
3.3	Temperature evolution in the TSTM.....	34
3.4	Development of autogenous deformations	36
3.5	Development of eigenstresses	40
4	Conclusions.....	44
	Acknowledgements.....	44
	References	45

Chapter 3 - Tensile response of UHPFRC under very low strain rates and low temperatures..... 53

	Abstract	53
1	Introduction.....	55
2	Experimental	59
2.1	Material.....	59
2.2	Uniaxial tensile test	60
2.3	Specimen shape and preparation	61
2.4	Test setup and loading	62
2.5	Acoustic emission tests.....	63
3	Results and Discussions	63
3.1	Overview of the tests	63
3.2	Effect of very low strain rates.....	66
3.2.1	Elastic limit	66
3.2.2	Elastic limit detection using Acoustic Emission measurements	67
3.2.3	Elastic modulus	70
3.2.4	Tensile strength	71
3.2.5	Strain at tensile strength	73
3.2.6	Hardening modulus	74
3.3	Effect of moderate to low temperatures	76
3.3.1	Age vs Maturity.....	76
3.3.2	Elastic limit	77
3.3.3	Elastic modulus	78
3.3.4	Tensile strength	78
3.3.5	Strain at tensile strength	79

3.4	Effect of mix type	80
3.4.1	Elastic limit and tensile strength.....	80
3.4.2	Elastic modulus.....	81
3.4.3	Strain at ultimate strength.....	82
4	Analytical models	82
4.1	Overview.....	82
4.2	Effect of strain rate on f_{Ute}	83
4.3	Effect of strain rate on ε_{Utu}	85
5	Conclusions	86
	Acknowledgements	87
	References.....	87

Chapter 4 - Modelling of the tensile behavior of SH-UHPFRC at low and high stress levels, under very low loading rates97

	Abstract	97
1	Introduction	99
2	Viscoelastic – viscohardening model	101
2.1	Overview.....	101
2.2	Incremental constitutive relationship.....	104
2.2.1	Below the elastic limit	105
2.2.2	Above the elastic limit.....	105
2.3	Summary	106
3	Materials	106
4	Calibration of the model.....	107
4.1	Overview.....	107
4.2	Calibration of $E_{tot,M1}$ – Vibration resonance frequency tests (VRFT)	108
4.3	Calibration of M1 parameters, E_k and τ_k – Full restraint tests in TSTM	109
4.4	Calibration of $E_{L,M2}$ and the influence of strain rates– uniaxial tensile tests	110
4.5	Calibration of M2 parameters, E_l and τ_l – Non-linear relaxation tests in the hardening domain.....	113
4.6	Combination of M1 and M2 applied to TSTM results	114
5	Applications and discussions	115
5.1	Effect of degree of restraint on the development of eigenstresses.....	115
5.1.1	Modelling of tests with partial restraint.....	115
5.1.2	Parametric study – effect of degree of restraint.....	116

5.2	Relaxation behavior before the elastic limit	117
5.2.1	Comparison with literature	117
5.2.2	Parametric study	118
5.3	Relaxations in the linear and non-linear domain	119
5.4	Tensile creep	120
5.5	Incremental relaxation tests and loading history effect	121
5.6	Effect of early age hydration on the tensile response	122
5.7	Parametric study on the effect of very low strain rates on the tensile response.	123
6	Conclusions	127
	Acknowledgements.....	128
	References	128
	Appendix A	133
	Appendix B	137

Chapter 5 - Influence of low curing temperatures on the tensile response of low clinker Strain-Hardening UHPFRC under full restraint..... 141

	Abstract	141
1	Introduction.....	143
2	Experimental.....	145
2.1	Materials	145
2.2	Isothermal calorimetry tests.....	148
2.3	Degree of hydration from ²⁹ Si MAS NMR	148
2.4	Dynamic and static modulus of elasticity	149
2.5	Uniaxial tensile tests.....	149
2.6	Development of Autogenous deformations	150
2.7	Development of eigenstresses under full restraint.....	150
3	Results and discussions.....	151
3.1	Isothermal calorimetry.....	151
3.1.1	Heat of hydration.....	151
3.1.2	Maturity and activation energy	153
3.1.3	Double Danish model.....	154
3.1.4	Degree of hydration.....	156
3.2	Degree of hydration from ²⁹ Si MAS NMR	158
3.3	Development of elastic modulus	162
3.4	Tensile resistance from uniaxial tensile tests	165

3.5	Development of autogenous deformations	166
3.6	Development of eigenstresses	171
4	Material level vs Structural level	175
4.1	Overview	175
4.2	Zone I	176
4.3	Zone II	177
4.4	Zone III	178
5	Conclusions	178
	Acknowledgements	179
	References	179
	Appendix A	188
	Appendix B	190

Chapter 6 - Conclusions and Outlook 193

1	Overview	195
2	Synthesis of main findings	195
2.1	Influence of very low strain rates on the tensile response of SH-UHPFRC	195
2.1.1	Tensile response under monotonic strain rates	195
2.1.2	Tensile response under restrained shrinkage deformations	196
2.2	Influence of moderate to low curing temperatures on the kinetics of hydration and tensile response of SH-UHPFRC	196
2.2.1	Kinetics of hydration	197
2.2.2	Tensile response	197
2.3	Development of a viscoelastic-viscohardening model to predict the tensile response of SH-UHPFRC in the elastic and hardening domain.	198
2.4	Influence of partial replacement of cement clinker with limestone filler.	199
2.5	Overall conclusion	199
3	Perspectives and future works	201
3.1	Mix development	201
3.2	Material level investigation	202
3.3	Structural level investigation	202
3.4	Modeling	204
	References	205

Curriculum Vitae..... 209

List of figures

Chapter 1 - Introduction

Figure 1: a) the roof of the Montpellier TGV station in France. The 5000m ² roofing system consisted of 115 post tensioned modular elements called “palmes”, each with dimensions 24 m x 2.4 m x 3 m, b) mold for the casting of a single palm element, photos E. Denarié.....	5
Figure 2: Application of UHPFRC to the rehabilitation of Log Čezsoški bridge – Soča river – Slovenia - July 2009, a) cross section of the bridge with concept of rehabilitation, b) lateral sides of curbs. photo E. Denarié.....	6
Figure 3: Application of UHPFRC. a) Chillon Viaduct, Switzerland– 2 x 1200 m ³ – 2014/2015 (reinforcement of bridge decks), b) reinforcement Turret Le Cabon, Brittany, France, 2013, photos E. Denarié.....	6
Figure 4: Application of UHPFRC for the strengthening of the underpass in “Creux de Genthod” in Geneva, Switzerland in 2010, photo E. Denarié.	7
Figure 5: Evolutionary mechanisms affecting the tensile response of SH-UHPFRC	8
Figure 6: Schematic tensile response of SH-UHPFRC, a) elasto-hardening response, b) softening response including the effect of unloading at tensile strength.....	10

Chapter 2 (Paper I) - Tensile response of low clinker UHPFRC subjected to fully restrained shrinkage

Figure 1: Particle size distribution of the mixes along with that of the individual components.	24
Figure 2: Schematic representation of the TSTM setup.....	29
Figure 3: Development of dynamic elastic moduli of Mix I and II obtained from the VRF tests. The static modulus of elasticity of both the mixes are also shown at 7, 14 and 28 days.....	31
Figure 4: Effect of silica fume content and the water/cement ratio on the relative humidity within various cement paste and mortar specimens	32
Figure 5: Heat flow per unit volume of Mix Im and Mix IIm, from isothermal calorimetry tests at 20 °C.....	33
Figure 6: a) Cumulative heat per unit volume of Mix Im and Mix IIm, from isothermal calorimetry tests at 20 °C, b) Overall degree of hydration of Mix Im and Mix IIm at 20 °C	34
Figure 7: Evolution of temperature in the restrained test specimens in the TSTM setup (focusing near the peak of the temperature curves)	35
Figure 8: Evolution of free autogenous deformations (increasing deformation represents shrinkage) in the FS setup of the TSTM; a) overall trend, b) early age.....	36
Figure 9: Evolution of autogenous deformations zeroed at the end of the swelling phase	37

Figure 10: The different phases in the evolution of the autogenous deformations of Mix I and II, in the FS setup of the TSTM	37
Figure 11: Average shrinkage curves of Mix I and Mix II from the FS setup of the TSTM	38
Figure 12: Comparison of the evolution of the autogenous shrinkage in Mix I and II with the corresponding development of elastic modulus	39
Figure 13: Comparison of LVDTs A and B in the; a) Mix I-20C-FR1 full restraint test, b) Mix I-20C-PR1 partial restraint test	40
Figure 14: Comparison of the development of eigenstresses in the full restraint tests in the present study and tests using the incremental procedure of [2,3]; a) time scale as measured, b) time scale adjusted.....	41
Figure 15: Development of eigenstresses in the full and partial restraint tests in the RS setup of the TSTM; a) overall trend, b) early age behavior	42
Figure 16: Average normalized specific creep of Mix I and II under tension, loaded at an age of 14 days.....	42

Chapter 3 (Paper II) - Tensile response of UHPFRC under very low strain rates and low temperatures.

Figure 1: Schematic tensile response of SH-UHPFRC, a) elasto-hardening response, b) softening response including the effect of unloading at tensile strength.....	56
Figure 2: Evolutionary mechanisms affecting the tensile response of UHPFRC.....	56
Figure 3: Geometry of the dumbbell specimens, along with the positions of the LVDTs and the Acoustic Emission sensors S1, S2, S3 and S4 (all measurements are in mm).	62
Figure 4: a) Electromechanical KAPPA 250 DS test setup from ZWICK/ROELL with the dumbbell specimen for uniaxial tensile test, b) grips for fixed boundary conditions.....	63
Figure 5: Stress displacement curves for; a) M1-20C at 1×10^{-5} 1/s, b) M1-20C at 1×10^{-7} 1/s, c) M1-20C at 1×10^{-8} 1/s, d) M1-5C at 1×10^{-5} 1/s, e) M1-5C at 1×10^{-7} 1/s, f) M1-5C at 5×10^{-9} 1/s, g) M2-20C at 1×10^{-5} 1/s, h) M2-20C at 1×10^{-7} 1/s, i) M2-20C at 1×10^{-8} 1/s (dashed lines) and M2-20C at 5×10^{-9} 1/s (solid lines), j) M2-10C at 1×10^{-5} 1/s, k) M2-10C at 1×10^{-7} 1/s, l) M2-10C at 5×10^{-9} 1/s, m) M2-5C at 1×10^{-5} 1/s, n) M2-5C at 1×10^{-7} 1/s and o) M2-5C at 5×10^{-9} 1/s.....	65
Figure 6: graphical representation of the procedure for determining the elastic limit using the inverse analysis method (specimen MixI-SR12-S1, strain rate 1×10^{-5} 1/s at 20 °C)	66
Figure 7: Effect of strain rate on the elastic limit of Mix I and II	67
Figure 8: Determination of the elastic limit using the 10% secant modulus drop method, along with the development of cumulative Acoustic Emission events at 20 °C, for a) specimen Mix I-20C-SR13-S1, strain rate of 1×10^{-5} s ⁻¹ , and b) specimen Mix I-20C-SR13-S2, strain rate of 1×10^{-5} s ⁻¹	68
Figure 9: Development of Acoustic Emission events at various stress levels during a uniaxial tensile test in a dumbbell specimen Mix I-20C-SR15-S1 at a strain rate of 1×10^{-5} 1/s at 20 °C.....	69

Figure 10: Effect of strain rate on the elastic modulus in tension, of Mix I and II.	70
Figure 11: DIF for elastic modulus in tension, of Mix I and II at very low loading rates.....	71
Figure 12: Effect of strain rate on the tensile strength of Mix I and II.....	72
Figure 13: Effect of strain rate on the strain at tensile strength of Mix I and II.....	74
Figure 14: Trilinear tensile response from the average values of E_{mod} , f_{Ute} , f_{Utu} and ϵ_{Utu} for; a) M1-20C, b) M1-5C, c) M2-20C, d) M-10C and e) M2-5C.	75
Figure 15: Effect of strain rate on the hardening modulus of Mix I and II, loaded at an age of 14 days.	76
Figure 16: Effect of temperature on the elastic limit for different mix type and loading rates [X-axis - "Mix type-strain rate (1/s)"].....	77
Figure 17: Effect of temperature on the elastic modulus for different mix type and loading rates [X-axis - "Mix type-strain rate (1/s)"]	78
Figure 18: Effect of temperature on the tensile strength for different mix type and loading rates [X-axis - "Mix type-strain rate (1/s)"]	79
Figure 19: Effect of temperature on the strain at tensile strength for different mix type and loading rates [X-axis - "Mix type-strain rate (1/s)"]	79
Figure 20: Effect of mix type on the elastic limit for different strain rates and curing temperatures [X-axis - "temperature-strain rate (1/s)"]	80
Figure 21: Effect of mix type on the tensile strength for different strain rates and curing temperatures [X-axis - "temperature-strain rate (1/s)"]	80
Figure 22: Effect of mix type on the elastic modulus for different strain rates and curing temperatures [X-axis - "temperature-strain rate (1/s)"]	81
Figure 23: Effect of mix type on the strain at tensile strength for different strain rates and curing temperatures [X-axis - "temperature-strain rate (1/s)"].....	82
Figure 24: DIF for elastic limit of Mix I and II at very low loading rates, along with the predictions of analytical models (M&R - Malvar and Ross)	84
Figure 25: DIF for strain at tensile strength of Mix I and II at very low loading rates, along with the predictions of analytical models.....	85

Chapter 4 (Paper III) - Modelling of the tensile behavior of SH-UHPFRC at low and high stress levels, under very low loading rates

Figure 1: Mechanisms affecting the overall tensile response of UHPFRC.....	99
Figure 2: Schematic representation of the Viscoelastic-Viscohardening model with M1 acting below the elastic limit and M2 acting above the elastic limit.	103
Figure 3: Development of elastic modulus for Mix I and II at 20 °C from the VRF tests	108

Figure 4: Evolution of autogenous deformations (zeroed at the end of swelling) in the FS setup of TSTM at 20 °C for a) Mix I, b) Mix II.	109
Figure 5: Model prediction of the development of eigenstresses in Mix I under full restraint conditions below the elastic limit, along with the experimental full restraint tests for Mix I at 20 °C; a) overall trend, b) early age behavior.....	110
Figure 6: Model prediction of the development of eigenstresses in Mix II under full restraint conditions below the elastic limit, along with the experimental full restraint tests for Mix II at 20 °C; a) overall trend, b) early age behavior.....	110
Figure 7: Prediction of the tensile response under different strain rates for; a,b,c) Mix I and d,e,f) Mix II.....	112
Figure 8: Experimental test and prediction of relaxation response of Mix I in the non-linear domain, loaded at an age of 14 days to a strain level of 0.8%.....	113
Figure 9: Prediction of the eigenstresses development under full restraint for Mix I at 20 °C, above and below the elastic limit using M1 and M2 of the VE-VH model.....	114
Figure 10: Model prediction of the development of eigenstresses under partial restraint conditions, along with the experimental partial restraint tests for Mix I at 20 °C.....	116
Figure 11: Prediction of the development of eigenstresses under different restraint conditions for; a) Mix I, b) Mix II. The resistance curves of f_{Ute} and f_{Utu} are also shown.....	116
Figure 12: Experimental results of linear relaxation response of CM22_TKK, for a loading age of 3 days to a stress level of 30% of the tensile strength, along with the prediction of the VE-VH model.....	117
Figure 13: Comparison of the linear relaxation response of Mix I and II at a loading age of; a) 24 hours, b) 48 hours, c) 168 hours and d) 672 hours.....	118
Figure 14: Prediction and comparison of the linear relaxation response at different ages of loading for; a) Mix I, b) Mix II (t_0 represents the loading age).....	119
Figure 15: Comparison of the relative relaxations in the linear and non-linear domains of the tensile response.....	119
Figure 16: Transformed relaxation curves from tensile creep tests (stress level of 5.4 MPa) using the Bazant algorithm, along with the predictions of the model for; a) Mix I, b) Mix II.	120
Figure 17: Loading pattern in the incremental relaxation tests.	121
Figure 18: Experimental relaxation response at each step of loading in the incremental relaxation test along with the predictions of the VE-VH model; a) shows the first three steps of loading, b) shows the final four steps of loading.....	121
Figure 19: Predictions of the tensile response of Mix I, under different strain rates, loaded at an age 1 hour after the setting time.....	123
Figure 20: Eigenstresses vs shrinkage strain curves for the full restraint tests of Mix I.	123
Figure 21: Predictions of the tensile response of a) Mix I, b) Mix II, under different strain rates, loaded at an age of 14 days.	125

Figure B.1: Schematic representation of the Viscoelastic-Viscohardening model with the restraint spring with stiffness E_0 acting in series with M1 or M2.	137
---	-----

Chapter 5 (Paper IV) - Influence of low curing temperatures on the tensile response of low clinker Strain-Hardening UHPFRC under full restraint

Figure 1: (a) Average cumulative heat per unit volume and (b) average heat flow per unit volume of Mix I _m and II _m from isothermal calorimetry tests at different temperatures.	152
Figure 2: Average cumulative heat per unit volume of Mix I _m in the (a) age domain (b) maturity domain and for Mix II _m in the (c) age domain and (d) maturity domain.	154
Figure 3: (a) Representative cumulative heat per unit volume of Mix I _m , (b) Double Danish model prediction of Mix I _m , (c) representative cumulative heat per unit volume of Mix II _m , and (d) Double Danish model prediction of Mix II _m	156
Figure 4: Development of overall degree of hydration of Mix I _m and Mix II _m at different temperatures, calculated using equation (5), from the cumulative heat of hydration curves from isothermal calorimetry tests in the (a) age domain and (b) maturity domain.	157
Figure 5: ²⁹ Si MAS NMR spectra of the hydrated samples of Mix I _m cured at a temperature of 20 °C.	158
Figure 6: Development of the degree of cement hydration (α_{cem}) at different temperatures in the age domain for (a) Mix I _m and (b) Mix II _m	159
Figure 7: Development of degree of silica fume reaction (α_{SF}) at different temperatures in the age domain for (a) Mix I _m and (b) Mix II _m	160
Figure 8: Development of α_{cem} in the maturity domain for, a) Mix I _m , b) Mix II _m ; development of α_{SF} in Development of α_{cem} in the maturity domain for (a) Mix I _m and (b) Mix II _m . Development of α_{SF} in the maturity domain for (c) Mix I _m and (d) Mix II _m . Variation in the α_{SF}/α_{cem} ratio in the maturity domain for (e) Mix I _m and (f) Mix II _m	161
Figure 9: Development of dynamic and static elastic moduli at different temperatures in the age domain for (a) Mix I and (b) Mix II.	163
Figure 10: Comparison of the development of average dynamic elastic modulus of Mix I and II at different curing temperatures in the age domain.	163
Figure 11: Development of dynamic elastic moduli at different temperatures in the maturity domain for (a) Mix I and (b) Mix II.	164
Figure 12: Development of dynamic and static elastic moduli at different temperatures in the degree of hydration domain for (a) Mix I and (b) Mix II.	165
Figure 13: Development of autogenous deformations as measured (with an initial swelling phase) in the FS setup of TSTM for Mix I and II at different quasi-isothermal temperatures in the age domain; (a) overall behavior and (b) early-age behavior.	167

Figure 14: Development of autogenous deformations zeroed after the swelling for Mix I and II at different quasi-isothermal temperatures in the age domain; (a) overall behavior and (b) early-age behavior.....	167
Figure 15: Comparison of the average autogenous deformations zeroed after swelling at different quasi-isothermal temperatures for Mix I and II in the age domain.	168
Figure 16: Comparison of the average autogenous deformations zeroed after swelling at different quasi-isothermal temperatures for Mix I and II in the maturity domain.	168
Figure 17: Comparison of the average autogenous deformations zeroed after swelling at different quasi-isothermal temperatures for Mix I and II in the DOH domain.	169
Figure 18: Comparison of the average autogenous deformations zeroed after swelling at different quasi-isothermal temperatures for Mix I and II in the DOR domain.	170
Figure 19: Development of eigenstresses under full restraint for Mix I and II under different quasi-isothermal temperatures in the age domain; (a) overall behavior and (b) early-age behavior.	171
Figure 20: Comparison of the average eigenstresses development at different quasi-isothermal temperatures for Mix I and II in the age domain.	172
Figure 21: Comparison of the eigenstresses developed under full restraint with the resistance curves of elastic limit and tensile strength for (a) Mix I and (b) Mix II.	173
Figure 22: Comparison of the average eigenstresses development at different quasi-isothermal temperatures for Mix I and II in the maturity domain.....	174
Figure 23: Comparison of the average eigenstresses development at different quasi-isothermal temperatures for Mix I and II in the DOR domain.	175
Figure 24: Comparison of the trends observed at the material level and the structural level. Material level: (a) development of degree of reaction from the isothermal calorimetry tests, (b) development of elastic modulus from VRF tests, (c) development of α_{cem} from ^{29}Si MAS NMR, and (d) development of α_{SF} from ^{29}Si MAS NMR. Structural level: (e) development of eigenstresses under full restraint in the TSTM and (f) development of autogenous deformations zeroed after swelling in the TSTM (All the tests were carried out at a curing temperature of 20 °C).....	176

List of tables

Chapter 2 (Paper I) - Tensile response of low clinker UHPFRC subjected to fully restrained shrinkage

Table 1: Compositions of Mix I and II.....	25
Table 2: Chemical compositions of cement and SF _{SEPR}	26
Table 3: Properties of Mix I and II in the fresh state (average value from 4 tests).....	26
Table 4: Properties of Mix I and II in the hardened state.....	27
Table 5: Total potential heat release of Mix I and II at full hydration, Ht _{100%}	34
Table 6: Trends of temperature evolution in the TSTM experiments.....	35
Table 7: Summary of fracture tests done in the TSTM.....	43

Chapter 3 (Paper II) - Tensile response of UHPFRC under very low strain rates and low temperatures.

Table 1: Compositions of Mix I and II.....	60
Table 2: Properties of Mix I and II in the fresh state (average value from 4 tests).....	60
Table 3: Overview of the uniaxial tensile tests.....	64
Table 4: Maturity at the time of testing under different temperatures.....	76
Table 5: Parameters of the analytical models for the prediction of effect of strain rate on the DIF for f_{Ute}	84
Table 6: Parameters of the analytical models for the prediction of effect of strain rate on the DIF for ϵ_{Utu}	85

Chapter 4 (Paper III) - Modelling of the tensile behavior of SH-UHPFRC at low and high stress levels, under very low loading rates.

Table 1: Compositions of Mix I and II.....	106
Table 2: Properties of Mix I and II in the fresh state (average value from 4 tests).....	107
Table 3: The list of parameters of the VE-VH model and the tests used for their calibration.....	107
Table 4: Tensile mechanical properties of Mix I and II under different strain rates.....	111
Table 5: General equations for the elastic limit and strain at tensile strength for Mix I and II.....	111

Table 6: Table showing the time needed to reach a strain level of 2‰ under various strain rates	124
Table A.1: Parameters of first set of Maxwell chains for Mix I.....	133
Table A.2: Parameters of second set of Maxwell chains for Mix I.....	134
Table A.3: Parameters of first set of Maxwell chains for Mix II.....	135
Table A.4: Parameters of second set of Maxwell chains for Mix II.....	136

Chapter 5 (Paper IV) - Influence of low curing temperatures on the tensile response of low clinker Strain-Hardening UHPFRC under full restraint.

Table 1: Compositions of Mixes I and II.....	146
Table 2: Type of mixes used for different tests.....	147
Table 3: Properties of Mix I and II in the hardened state, cured at 20 °C.....	147
Table 4: Properties of Mix I and II in the fresh state (average value from 4 tests).....	148
Table 5: Summary of uniaxial tensile tests to determine the resistance parameters like f_{Ute} and f_{Utu}	150
Table 6: Summary of tests carried out in the TSTM.....	151
Table 7: Parameters of the double Danish model for Mix I and II.....	155
Table 8: Total potential heat release of Mix I _m and Mix II _m at full hydration, $H_{T100\%}$	157
Table 9: Summary of uniaxial tensile tests.....	166
Table A.1: Data from the deconvolutions of the ^{29}Si MAS NMR spectra of Mix Im at different ages of hydration and cured at different temperatures.....	188
Table A.2: Data from the deconvolutions of the ^{29}Si MAS NMR spectra of Mix IIm at different ages of hydration and cured at different temperatures.....	189

Glossary

Abbreviations

^1H -NMR – Proton Nuclear Magnetic Resonance

^{29}Si MAS NMR – Silicon Solid State Magic Angle Spinning Nuclear Magnetic Resonance

AE – Acoustic Emission

BET – Brunauer, Emmett, Teller

C_2S – Dicalcium Silicate

C_3S – Tricalcium Silicate

$\text{Ca}(\text{OH})_2$ – Calcium Hydroxide

CO_2 - Carbon dioxide

CSH – Calcium Silicate Hydrate

DIF – Dynamic Increase Factor

DOH – Degree of hydration

DOR – Degree of Reaction

FA – Fly Ash

FFT – Fast Fourier Transform

FS – Free Setup (of TSTM)

GBFS - Granulated Blast Furnace Slag

GGBFS – Ground Granulated Blast Furnace Slag

HPC – High Performance Concrete

HPFRCC – High Performance Fiber Reinforced Cement Composite

HSHDC – High Strength High Ductility Concrete

LVDT – Linear Variable Differential Transformer

NMR - Nuclear Magnetic Resonance

OPC – Ordinary Portland Cement

PSD – Particle Size Distribution

RH – Relative Humidity

RPC – Reactive Powder Concrete

RS – Restrained Setup (of TSTM)

SCM – Supplementary Cementitious Material

SEM – Scanning Electron Microscope

SF – Silica Fume

SH-UHPFRC – Strain-Hardening Ultra High Performance Fiber Reinforced Concrete

SP – Superplasticizer

TEM – Transmission Electron Microscope

TSTM – Temperature Stress Testing Machine

UHPC – Ultra High Performance Concrete (UHPFRC matrix)

UHPFRC – Ultra High Performance Fiber Reinforced Concrete

VE-VH – Viscoelastic - Viscohardening

VRFT – Vibration Resonance Frequency Test

List of Symbols

f_{Ute} – elastic limit (of UHPFRC)

ϵ_{Ute} – strain at elastic limit (of UHPFRC)

E_{mod} – Elastic modulus (in tension or compression)

f_{Utu} – tensile strength (of UHPFRC)

ϵ_{Utu} – strain at tensile strength (of UHPFRC)

E_{har} – hardening modulus

ϵ_{free}^{free} – free autogenous deformations in the free setup (FS) of TSTM

ϵ_{res}^{free} – free autogenous deformations in the restrained setup (RS) of TSTM

ϵ_{res}^{res} – restrained autogenous deformations in the restrained setup (RS) of TSTM

E_a – Apparent Activation Energy

R – Universal Gas constant

$\alpha(t)$ – overall degree of hydration at an age t

α_{cem} – Degree of hydration of cement

α_{SF} – Percentage of SF reacted for pozzolanic reaction

$M(t)$ – Maturity at time t

T_{ref} - reference temperature

$T(t)$ – temperature at time t

$H_T(t)$ – cumulative heat of hydration at time t

$H_{T\infty}$ - asymptotic value of cumulative heat of hydration

$H_{T100\%}$ - theoretical cumulative heat release for full hydration

V_f – volume fraction of fibers

l_f – length of fiber

d_f – diameter of fiber

λ - factor that accounts for the average pullout length, fiber orientation effects and group reduction effects

ΔT_{tot} - total rise in temperature in TSTM

t_{peak} - time to peak of the temperature curve

t_{as} - time to the end of apparent swelling of autogenous deformations (apparent setting time)

ΔT_{as} - rise in temperature up to the end of apparent setting time

σ_{as} - eigenstress value at the apparent setting time

$\dot{\epsilon}_s$ - quasi-static strain rate in tension

$\dot{\epsilon}$ - applied strain rate in tension

E_k - stiffness of the spring element in Maxwell unit k in M1

E_l - stiffness of the spring element in Maxwell unit l in M

τ_k - retardation time of the dashpot element in Maxwell unit k in M1

τ_l - retardation time of the dashpot element in Maxwell unit l in M2

$\epsilon_{VE(M1)}$ - viscoelastic strain in M1

$\epsilon_{VH(M2)}$ - viscohardening strain in M2

$\sigma_{VE(M1)}$ - stress in M1

$\sigma_{VH(M2)}$ - stress in M2

σ_k^{i+1} - stress in Maxwell unit k at the end of the time interval Δt

σ_k^i - stress in Maxwell unit k at the beginning of the time interval Δt

E_k^{i+1} - stiffness of the spring element in Maxwell unit k at the end of the time interval Δt

E_k^i - stiffness of the spring element in Maxwell unit k at the beginning of the time interval

Δt

$\Delta \epsilon^i$ - strain increment in time Δt

Δt - duration of the time interval

E_0 – stiffness of the restraint spring

Chapter – 1

Introduction

1 Context

The built environment with structures like buildings, bridges, roads, tunnels, retaining walls etc., brings significant value to the economic and social lives of human beings. Because of the high initial cost of the built environment, it would be ideal to have structures that allow unrestricted utilization with very long service life, to meet the ever-growing demands of the population and traffic. Moreover, structures also have historical and cultural values and represent the identity of the place and period in which they were built. However, the durability of these structures is very much affected by the detrimental environmental conditions and surroundings. Among all the different exposure cases, those where a direct contact with liquid water containing aggressive chemical substances is involved, are the most severe for reinforced concrete structures. As such, these structures need to be monitored for their performance and if needed interventions of conservation should be carried out.

The conservation projects may be either rehabilitation or reinforcement of existing structures. Rehabilitation refers to the re-establishment of the previous structural performance and protective properties, whereas reinforcement refers to the enhancement of the previous structural response in terms of its strength and deformability and durability properties. Improvement of the existing structures is essential to meet the growing needs of traffic, and needs to be carried out without replacing the structures with minimum interruptions and disturbances. Cementitious materials with outstanding mechanical and protective properties are therefore needed to carry out a one-time intervention strategy for conservation rather than having multiple interventions during the lifetime of the structure [1].

Strain-Hardening Ultra High Performance Fiber Reinforced Concretes (SH-UHPFRC) fulfill all the criteria needed for a material to be used for rehabilitation and improvement of structures. The ultra-compact cementitious matrix with low water/binder ratio along with a suitable fibrous mix, leads to exceptional mechanical properties like high compressive strength (150-200 MPa), high tensile strength (12-20 MPa) and significant strain-hardening (1-5 %) along with outstanding protective properties such as very low air permeability ($k_t = 0.003 \times 10^{-16}$ to $0.010 \times 10^{-16} \text{ m}^2$) and very low water capillary absorption (around $40 \text{ g/m}^2 \cdot \text{h}^{0.5}$) [2,3].

In recent years, many cast onsite applications of SH-UHPFRC have been carried out for rehabilitation or reinforcement of structures [1,4]. From the point of view of an economic and social well-being, the reinforcement of Chillon Viaduct in Switzerland [5,6] is the biggest application of cast-on site SH-UHPFRC in the world with 53000 m^2 45 mm thick R-UHPFRC cast, whereas from the point of view of preservation of the historical and cultural aspects, the strengthening of Guillermaux bridge in Payern, Switzerland [7] serves a good example.

2 Motivation and scope

2.1 Restrained shrinkage and eigenstresses

SH-UHPFRC materials are ideally suited for the reinforcement of existing concrete structures without increasing the deadweight. For a maximum utilization of their stress and strain capacity, the stress level in the material at service state, should be close to or even within the strain-hardening domain. In rehabilitation applications, a new layer of SH-UHPFRC reinforcing and/or protective layer is applied on the existing structure for the improvement of the load carrying capacity and protective functions. The new layer of SH-UHPFRC is subjected to early age volume deformations such as autogenous shrinkage, thermal deformations and drying shrinkage in certain situations. These deformations that take place at very low strain rates (1×10^{-8} 1/s to 1×10^{-11} 1/s) are restrained to different extents, depending on the relative stiffness of the new layer and the existing substrate and depending on the boundary conditions of the support, lead to the development of tensile eigenstresses in the material. [8,9] showed that the degree of restraint can be even more than 90% depending on the stiffness of the existing structure and boundary conditions. The developed eigenstresses will lead to premature cracking of the material if it crosses the elastic limit and tensile strength of the material [10], as is often seen in the case of normal strength concrete overlays. However, except in very special cases of unfavorable fiber orientations, the strain-hardening capability of SH-UHPFRC provides a deformation potential that is larger than their free shrinkage, thereby removing the possibility of localized macro cracks in the new layer. The significant viscous potential of SH-UHPFRC also helps in relaxing the eigenstresses due to restrained shrinkage, to maintain the protective functions of the layer.

The resistance and deformability offered by UHPFRC depends largely on the orientation of the fibers in practical applications [3]. Strain-Hardening UHPFRC with a constant tensile response under any situation of application, is an idealistic vision. A more realistic goal is to have "robust" mixes that exhibit a tensile hardening response in a wide range of applications, such as that classified in the French standard as "strongly hardening – T3" after material tests characterizations [11]. However, even the best mix in the lab, if improperly placed, with an inappropriate workability, or in confined conditions with too narrow rebar spacing or clearance with formwork surfaces can lose its strain-hardening character and lead to premature cracking, compromising the expected protective properties that motivate its use. The tensile response of UHPFRC might also be insufficient in certain prefabrication applications with complex shapes, where the molds are not enough deformable. This can lead to the formation of microcracks in sharp corners due to stress concentration. Moreover, in certain situations, the aesthetic and architectural considerations may limit the volume of fibers used in the UHPFRC mixes, thereby increasing the chances of microcracking in the structures. Both these situations of complex non-deformable molds and architectural limitations for fiber volume (due to the required use of expensive stainless steel fibers) were encountered during the construction of the roof of the TGV station in Montpellier, France, as shown in figure 1.

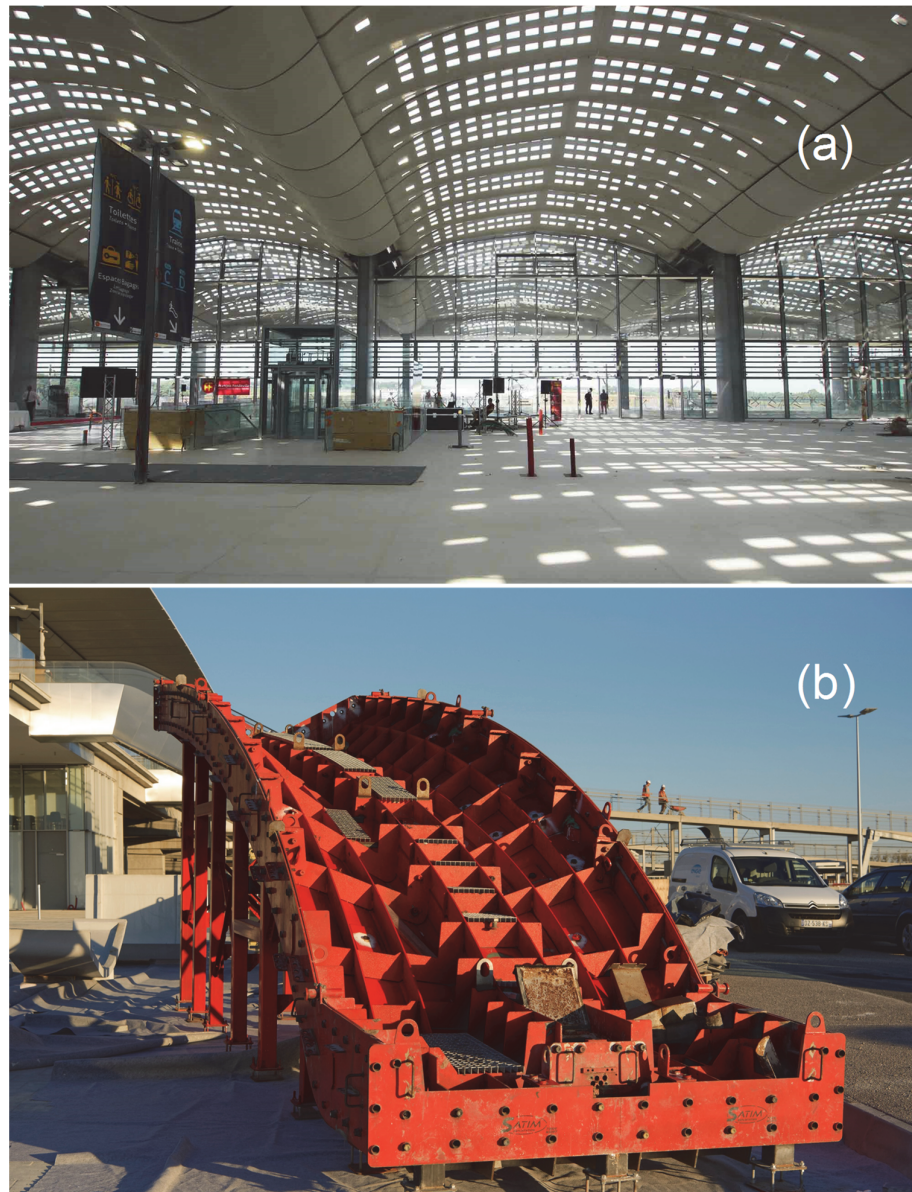


Figure 1: a) the roof of the Montpellier TGV station in France. The 5000m² roofing system consisted of 115 post tensioned modular elements called “palms”, each with dimensions 24 m x 2.4 m x 3 m, b) mold for the casting of a single palm element, photos E. Denarié.

Figures 2 and 3 illustrate various cases of restraint in cast-on site applications of rehabilitation or reinforcement with UHPFRC, all in spring or summer conditions (temperatures between 20 to 35 °C) [4]. For the Log Čezsoški bridge rehabilitation, the massive cross section of the box-girder induced a very high restraint, even for the UHPFRC overly cast on the deck. Despite this, no cracks were observed on all UHPFRC surfaces 2 years after casting. This application was the first use of a SH-UHPFRC mix developed with Slovenian components, with 50 % replacement of clinker by limestone filler. The application on the Chillon viaducts in 2014/2015 was focused on the reinforcement of the deck slabs.

It was the first of its kind at an industrial scale with 2 times 1200 m³ cast in place with a special machine. The reinforcement of Turret Le Cabon in Brittany in 2013 is an extreme case of restraint comparable to a ring test with a massive core. A 60 mm UHPFRC shell was cast-in place around the existing structure, fully covering it. To face the extreme restraint and potential ongoing swelling reactions (AAR) in the existing masonry core, a special UHPFRC mix was developed with strain-hardening and shrinkage reducing admixtures.

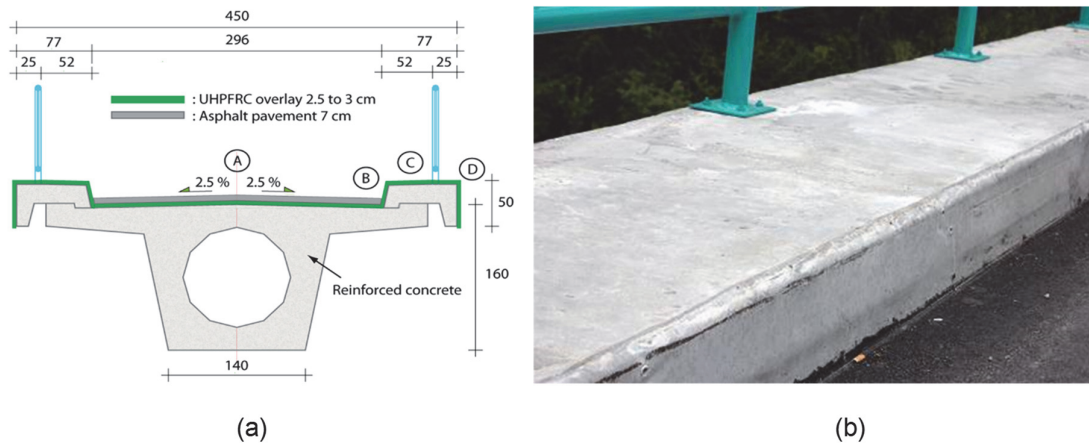


Figure 2: Application of UHPFRC to the rehabilitation of Log Čezsoški bridge – Soča river – Slovenia - July 2009, a) cross section of the bridge with concept of rehabilitation, b) lateral sides of curbs. photo E. Denarié.



Figure 3: Application of UHPFRC. a) Chillon Viaduct, Switzerland– 2 x 1200 m³ – 2014/2015 (reinforcement of bridge decks), b) reinforcement Turret Le Cabon, Brittany, France, 2013, photos E. Denarié.

Furthermore, along with the detrimental fiber orientation, harsh microclimatic state of the substrate and adverse climatological conditions (temperature and relative humidity) of the site, may also lead to the exhaustion of the strain-hardening capacity of the SH-UHPFRC by the eigenstresses, leading to the formation of localized macrocracks. This is more probable under low temperature curing conditions, which is representative of on-site casting conditions in winter. There was an evidence of localized macro cracking in a SH-UHPFRC layer, applied on the upstream outer face of the curb of a bridge over the river “La Morge” in Wallis, Switzerland, two weeks after the application of the same. The SH-UHPFRC layer was applied during late autumn in 2004, under low temperature conditions (0 °C to 5 °C). However, similar localized macrocracking was not found in other parts of the bridge (deck and prefabricated curb, cast by mild temperatures), and the protective performances of all parts of the bridge rehabilitated with UHPFRC were excellent with extremely low profiles of chloride penetration after 10 years.

No cracks were also observed in the case of another SH-UHPFRC application under low temperatures (0 °C to 5 °C) for the underpass “Creux de Genthod” in Geneva, Switzerland in the fall of 2010 [1] (figure 4). The geometrical conditions were more favorable in “Creux de Genthod” with casting only on the bridge deck, which may have led to better fiber orientations compared to the vertical casting in “La Morge” upstream curb rehabilitation. Furthermore, a UHPFRC mix very different from that used for the bridge over la Morge (CEM I + Silica Fume binder), was used for the first time in Switzerland for the Creux de Genthod application, with 50 % mass replacement of clinker by limestone filler.



Figure 4: Application of UHPFRC for the strengthening of the underpass in “Creux de Genthod” in Geneva, Switzerland in 2010, photo E. Denarié.

These two applications highlighted the lack of knowledge of the influence of very low strain rates and low temperatures on the tensile response or the resistance of SH-UHPFRC including the strength and deformability, for mixes with different matrices. Apart from the explanations of difference in the fiber orientation, the reason for the development of macrocracks in one case and the absence of the same in the other were unexplained. To the best of author's knowledge, the lowest tensile strain rate that was applied to study the tensile response of UHPFRC materials is 10^{-6} 1/s [12], while the rate of shrinkage strain varies between 1×10^{-8} 1/s - 1×10^{-11} 1/s. Moreover, no study has been reported in literature to investigate the influence of moderate to low temperatures (20 °C - 5 °C) on the tensile response of SH-UHPFRC materials. **As such, fundamental research is needed to understand the tensile response of SH-UHPFRC subjected to very low strain rates and low temperatures.**

2.2 Influence factors

The kinetics of various mechanisms influence the mechanical response of UHPFRC as shown in figure 5.

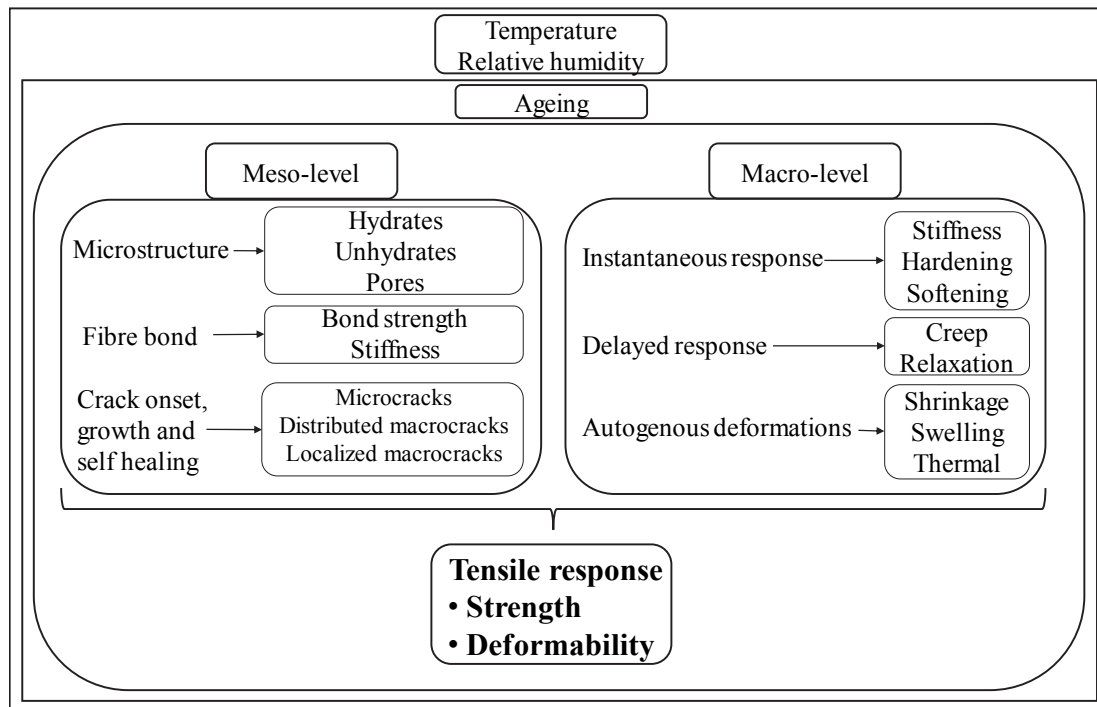


Figure 5: Evolutionary mechanisms affecting the tensile response of SH-UHPFRC.

The phenomenon of ageing affects the responses of the material at the meso and macro levels. At the meso-level, it affects the development of degree of hydration and microstructure of the material, development of interfacial bond strength between the fibers and the matrix and the phenomena of crack onset, growth and self-healing. The trends in the meso-level affect the responses at the macro level, including the early age volume changes like autogenous deformations, drying shrinkage and thermal deformations, stiffness of the material and the viscoelastic phenomena like creep and relaxation. There is a complex interaction of these different phenomena especially under very low strain rates making it challenging to separate the contributions of the individual mechanisms. The phenomenon of ageing is prevalent mainly in the younger material (up to 3-5 days after addition of water), whereas in the long term, the influence of viscoelasticity and damage become dominant. Under very low strain rates, the viscoelasticity and damage, which produce similar effects (increased deformations and loss of stiffness), interact with each other depending on the stress level. On the one hand, for low strain rates, viscoelasticity plays an important role in the development of microcracks and crack propagation, first shown by Rusch [13]; whereas on the other hand, at high stress levels, the presence of microcracks leads to the development of non-linear viscoelasticity [14–16]. Moreover, the external climatological factors like temperature and relative humidity, affect the overall ageing of the material and thereby all the other mechanisms. There is a complex interaction between the effect of temperature on the ageing and creep response of cementitious materials. On the one hand, a higher temperature leads to a higher creep response; whereas on the other hand, a higher curing temperature would lead to a higher apparent age (maturity) of the material and consequently a lower creep response [17].

Moreover, due to the low degree of hydration of conventional UHPFRC mixes (about 30%) with 100% cement clinker, a part of the cement clinker could be advantageously replaced by Supplementary Cementitious Materials (SCM) like Ground Granulated Blast Furnace Slag, Fly ash, Limestone filler etc. The introduction of SCMs will change the kinetics of hydration and development of microstructure and also leads to changes in the mechanical and viscous responses of the material, which in turn affect the overall tensile response of the material.

2.3 Tensile response (resistance envelope) of SH-UHPFRC

The tensile response of SH-UHPFRC is shown schematically in figure 6, which can be divided into three main domains;

1. Elastic domain: the region from the beginning until the elastic limit.
2. Hardening domain: the region from the elastic limit until the tensile strength.
3. Softening domain: the region from the tensile strength until full separation of the specimen.

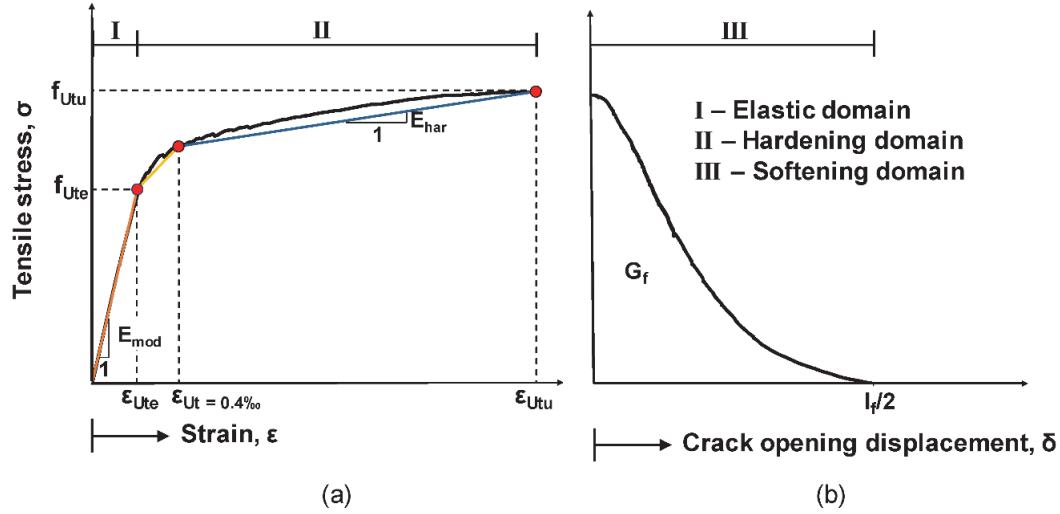


Figure 6: Schematic tensile response of SH-UHPFRC, a) elasto-hardening response, b) softening response including the effect of unloading at tensile strength.

The focus of the present study will be on the elastic and hardening domains and the effect of very low strain rates and moderate to low temperatures on the mechanical properties in these domains will be investigated. In the elastic region, the elastic limit (f_{Ute}) and the elastic modulus in tension (E_{mod}) will be studied whereas in the hardening domain, the tensile strength (f_{Utu}), the strain at tensile strength (ϵ_{Utu}) and the hardening modulus (E_{har}) will be looked into. The f_{Ute} is the stress level until which the tensile stresses are proportional to the strains, with the corresponding strain given by ϵ_{Ute} . The slope of the stress strain curve in the elastic domain is given by the elastic modulus E_{mod} . The f_{Utu} and ϵ_{Utu} correspond to the coordinates of the peak stress in the tensile response. In this thesis, E_{har} is defined as the slope of the line joining the stress-strain coordinate corresponding to a strain level of 0.4‰ and that corresponding to the peak stress, as shown in figure 6.

In the elastic domain, f_{Ute} roughly corresponds to the tensile strength of the matrix, although some authors have demonstrated that f_{Ute} is dependent on the fiber geometry and volume fraction [18,19]. Studies have shown that the incorporation of microfibers along with macrofibers, just like in the present study, might lead to an increase in the apparent elastic limit [20,21]. This was attributed to the improved bridging of the microcracks by the microfibers. A few number of microcracks develop even before the apparent elastic limit (as evidenced by Acoustic emission tests in the present study), and as such, a better bridging of these initial microcracks by the micro fibers might therefore increase the elastic limit of the material.

The hardening domain is mainly governed by the response of the discontinuous macro fibers. According to [22], the tensile strength is given by the equation (1), where λ is a factor, which accounts for the average pullout length, fiber orientation effects and group reduction effects, τ is the bond strength of the fiber matrix interface, V_f is the fiber volume fraction and l_f/d_f is the aspect ratio of the fibers.

$$f_{utu} = \lambda \tau V_f \left(\frac{l_f}{d_f} \right) \quad (1)$$

In equation (1), the only factor that is sensitive to the influence of strain rates and temperature is the bond strength τ . As such, the overall tensile response of SH-UHPFRC mixes will depend on the influence on the strain rate and temperature on the bond strength between the fibers and the UHPC matrix. Moreover, unlike mixes with only one type of macrofibers, it was shown in [20,21] that in hybrid mixes containing microfibers and macrofibers, the microfibers were able to reinforce the matrix more to strengthen its hold on the macrofibers, thereby increasing the stresses in the macrofibers and improving their efficiency [23].

To summarize, to fully understand the tensile response of SH-UHPFRC under low curing temperatures, it is necessary to investigate the influence of low temperatures on the development of degree of hydration of the components at the meso-level, and its impact on the driving forces of autogenous shrinkage and eigenstresses and on the resistance parameters like f_{ute} , ϵ_{ute} , E_{mod} , f_{utu} , ϵ_{utu} and E_{har} .

2.4 Sustainability

The environmental impacts of the construction industry are known to be very huge. The cement production sector represents 7% of the total anthropogenic CO₂ emissions and consumes 60% of the extracted raw materials [24] and therefore any reduction in the usage of cement in the new materials will produce huge environmental benefits. The ever-increasing demand on the natural resources has called for the most efficient management of the available resources to reduce the impact on the environment. Furthermore, about 40% of the world population lives in low-income countries, whose built environment need major upgrade for their social well-being. It is thus important that the price of the building material is affordable for these low-income countries. As such, increasing focus is now being given to the use of Supplementary Cementitious Materials (SCM) in UHPFRC mixes in view of sustainability, to reduce the environmental impact and cost of cement production [25]. Since the water/binder ratio is very low in UHPFRC mixes with pure cement (< 0.2), many studies have shown that the degree of hydration of cement in these mixes is as low as 30% after 28 days [17,26]. The unhydrated cement and silica fume simply act as fillers (physical effect), to improve the compactness of the matrix at the micro level and thereby leading to the increase of the mechanical properties at the macro level. As such, the unhydrated cement in these mixes could be advantageously be replaced by supplementary cementitious materials like limestone filler, fly ash or blast furnace slag, without detrimentally compromising the mechanical properties [27,28]. However, the tensile and protective properties of such SCM-UHPFRC mixes have never been investigated before.

At present, only three materials are mainly used as supplementary cementitious materials; Ground Granulated blast furnace slag (GGBFS), Fly ash (FA) and limestone [25]. Due to the increased availability of scrap steel for recycling in the steel industry, the availability of GGBFS, which is a by-product of the iron/steel manufacturing industries, has markedly decreased. Currently more than 90% of the GGBFS is already used as an SCM in cement-based mixes [29]. Fly ash is a by-product of the coal combustion in power plants, which is so far the largest contributor of anthropogenic CO₂ in the atmosphere. The lesser availability of GGBFS and FA in many regions now, has led to an increase in the price of these SCMs and therefore cannot be considered as a long-term solution for sustainability.

However, the third main SCM, which is limestone filler, is still widely available in large quantities in different regions of the world [25]. Even though the acceptable percentage of cement replacement by limestone filler is 35% in the European standards (EN 197-1), [30] showed that 50% cement replacement by limestone filler allows to break the workability barrier and to minimize the cement-superplasticizer incompatibility which is a major problem in low water/binder mixes such as UHPFRC [31]. Moreover, the morphology and size distribution of specific limestone fillers are close to that of the cement making it an excellent candidate to be used as SCM in UHPFRC [30,32]. Another major SCM that is now being increasingly used is calcined clay [33]. However, its potential use in UHPFRC mixes is yet to be explored in more details [34].

As such, fundamental research is needed to develop low clinker SH-UHPFRC mixes, with significant replacement of cement with SCMs, preferably limestone filler. The protective properties of tensile response of these low clinker SH-UHPFRC mixes should be validated and their tensile response under very low strain rates and low temperatures should be investigated in detail.

3 Objectives

The main objective of the thesis is to investigate the influence of very low strain rates and moderate to low temperatures on the tensile response of two types of SH-UHPFRC mixes; Mix I with pure type I cement, silica fume and steel fibers and Mix II with 50% replacement of cement with limestone filler and a similar fibrous mix. The responses at a material level will be used to discuss the trends at structural level. The specific objectives of the thesis are:

1. to review the existing knowledge on the behavior of SH-UHPFRC materials under different strain rates and temperatures, their time dependent behavior and development of hydration.

2. to develop a low clinker SH-UHPFRC with massive replacement of type I cement with limestone fillers, without compromising its mechanical and protective properties.
3. to carry out an experimental campaign with a Temperature Stress Testing Machine (TSTM) to study the influence of moderate to low curing temperatures (5 °C, 10 °C and 20 °C) on the development of autogenous deformations and associated eigenstresses especially under fully restrained conditions, from the time of casting until one month or more.
4. to perform a comprehensive experimental campaign to investigate the influence of very low monotonic strain rates (1×10^{-5} 1/s, 1×10^{-7} 1/s, 1×10^{-8} 1/s and 5×10^{-9} 1/s) and moderate to low temperatures (5 °C, 10 °C and 20 °C) on the tensile resistance parameters like f_{Ute} , ϵ_{Ute} , E_{mod} , f_{Utu} , ϵ_{Utu} and E_{har} .
5. to perform material level experimental investigation using isothermal calorimetry, solid state ^{29}Si MAS NMR and vibration resonance frequency tests to study the development of degree of hydration of the UHPFRC constituents and evolution of elastic modulus under moderate to low curing temperatures (5 °C, 10 °C and 20 °C), from very early age.
6. to develop a viscoelastic-viscohardenening model to predict the tensile response of the investigated SH-UHPFRC mixes under different types of loadings.

4 Organization of the thesis

Besides the introduction chapter, the thesis comprises of four main chapters and a conclusion chapter. For dissemination purposes the four main chapters of this thesis have been written as individual stand-alone texts, that have been submitted in internationally peer reviewed journals. The entire thesis is hence divided into six chapters.

Chapter 1 provides an introduction to the research topic and describes the motivation and scope of the thesis. The primary objectives of the thesis are briefly described.

Chapter 2 (Paper I) investigates the tensile response of two types of SH-UHPFRC mixes subjected to fully restrained shrinkage deformations at a temperature of 20 °C. The development of autogenous deformations at a structural level and degree of hydration and elastic modulus at a material level are also studied for a curing temperature of 20 °C and put into perspective.

Chapter 3 (Paper II) studies the influence of very low monotonic strain rates (1×10^{-5} 1/s, 1×10^{-7} 1/s, 1×10^{-8} 1/s and 5×10^{-9} 1/s) and moderate to low temperatures (5 °C, 10 °C and 20 °C) on the tensile resistance parameters like f_{Ute} , ϵ_{Ute} , E_{mod} , f_{Utu} , ϵ_{Utu} and E_{har} of the two types of SH-UHPFRC mixes.

Chapter 4 (Paper III) develops a viscoelastic-viscohardenening model to predict the tensile response of the two types of SH-UHPFRC mixes. The experimental results in the chapters 2, 3 and 4 are used to develop the model, so that it could predict the tensile response under different loading conditions.

Chapter 5 (Paper IV) investigates the influence of moderate to low temperatures (5 °C, 10 °C and 20 °C) on the hydration kinetics of the two investigated SH-UHPFRC and their binder constituents. The trends at the material level are used to discuss the responses of autogenous deformations and eigenstresses at the structural level.

Chapter 6 summarizes the most important conclusions of the thesis along with an outlook and scope for future research.

References

- [1] E. Denarié, E. Brühwiler, Strain Hardening Ultra-high Performance Fiber Reinforced Concrete: Deformability versus Strength Optimization, *Int. J. Restaur. Build. Monum.* 17 (2011) 397–410.
- [2] K. Wille, S. El-Tawil, A.E. Naaman, Properties of strain hardening ultra high performance fiber reinforced concrete (UHP-FRC) under direct tensile loading, *Cem. Concr. Compos.* 48 (2014) 53–66. doi:<https://doi.org/10.1016/j.cemconcomp.2013.12.015>.
- [3] M. Bastien-Masse, E. Denarié, E. Brühwiler, Effect of fiber orientation on the in-plane tensile response of UHPFRC reinforcement layers, *Cem. Concr. Compos.* 67 (2016) 111–125. doi:[10.1016/j.cemconcomp.2016.01.001](https://doi.org/10.1016/j.cemconcomp.2016.01.001).
- [4] E. Denarié, E. Brühwiler, Cast-on Site UHPFRC for improvement of existing structures – achievements over the last 10 years in practice and research, in: *High Perform. Fiber Reinf. Cem. Compos.* 7, 2015: pp. 473–480.
- [5] E. Brühwiler, M. Bastien Masse, Strengthening the Chillon viaducts deck slabs with reinforced UHPFRC, in: *IABSE Conf. Geneva 2015 “Structural Eng. Provid. Solut. to Glob. Challenges,”* IABSE, 2015: pp. 1171–1178.
- [6] E. Denarié, L. Sofia, E. Brühwiler, Characterization of the tensile response of strain hardening UHPFRC-Chillon Viaducts, in: *Proc. AFGC-ACI-Fib-RILEM Int. Symp. Ultra-High Perform. Fiber-Reinforced Concr. UHPFRC 2017-Pro 106*, RILEM publications SARL, 2017: pp. 242–250.
- [7] E. Brühwiler, P. Schiltz, Le BFUP pour ajouter de la plus-value aux ouvrages en béton armé, *Tracés.* 2 (2018) 6–10.
- [8] E. Denarié, J. Silfwerbrand, H. Beushausen, Structural Behavior, in: *Bond. Cem. Mater. Overlays Repair, Lining or Strength. Slabs or Pavements*, Springer, 2011: pp. 81–106.

- [9] E. Denarié, Deliverable D25b “Guidance for the use of UHPFRC for rehabilitation of concrete highway structures,” 2006.
- [10] L. Sorelli, R. Davila, F. Ulm, V. Perry, P. Seibert, Risk analysis of early-age cracking in UHPC structures, in: Proc. 2nd Int. Symp. UHPC, Kassel, Ger., 2008: pp. 331–338.
- [11] AFNOR. 2016 NF P18-470 - Concrete - Ultra-high performance fiber reinforced concrete - Specifications, performance, production and conformity, Paris, France, 2016.
- [12] K. Fujikake, T. Senga, N. Ueda, T. Ohno, M. Katagiri, Effects of Strain Rate on Tensile Behavior of Reactive Powder Concrete, *J. Adv. Concr. Technol.* 4 (2006) 79–84. doi:10.3151/jact.4.79.
- [13] H. Rüsch, Research toward a general flexural theory for structural concrete, *ACI J.* 57 (1960) 1–28.
- [14] Z.P. Bažant, R. Gettu, Rate Effects and Load relaxation in Static Fracture of Concrete, *ACI Mater. J.* 89 (1992) 456–468.
- [15] E. Denarié, C. Cécot, C. Huet, Characterization of creep and crack growth interactions in the fracture behavior of concrete, *Cem. Concr. Res.* 36 (2006) 571–575. doi:https://doi.org/10.1016/j.cemconres.2005.11.011.
- [16] A. Switek-Rey, E. Denarié, E. Brühwiler, Early age creep and relaxation of UHPFRC under low to high tensile stresses, *Cem. Concr. Res.* 83 (2016) 57–69. doi:10.1016/J.CEMCONRES.2016.01.005.
- [17] M. Kazemi Kamyab, Autogenous Shrinkage and Hydration Kinetics of SH-UHPFRC under Moderate to Low Temperature Curing Conditions, Doctoral thesis No: 5681, Ecole Polytechnique Fédérale de Lausanne, Switzerland, 2013.
- [18] S. Pyo, K. Wille, S. El-Tawil, A.E. Naaman, Strain rate dependent properties of ultra high performance fiber reinforced concrete (UHP-FRC) under tension, *Cem. Concr. Compos.* 56 (2015) 15–24. doi:10.1016/J.CEMCONCOMP.2014.10.002.
- [19] S.-T. Kang, J.-I. Choi, K.-T. Koh, K.S. Lee, B.Y. Lee, Hybrid effects of steel fiber and microfiber on the tensile behavior of ultra-high performance concrete, *Compos. Struct.* 145 (2016) 37–42. doi:10.1016/J.COMPSTRUCT.2016.02.075.
- [20] E. Parant, R. Pierre, F. Le Maou, Durability of a multiscale fiber reinforced cement composite in aggressive environment under service load, *Cem. Concr. Res.* 37 (2007) 1106–1114. doi:https://doi.org/10.1016/j.cemconres.2006.02.021.
- [21] J.S. Lawler, D. Zampini, S.P. Shah, Microfiber and macrofiber hybrid fiber-reinforced concrete, *J. Mater. Civ. Eng.* 17 (2005) 595–604.
- [22] A.E. Naaman, Engineered Steel Fibers with Optimal Properties for Reinforcement of Cement Composites, *J. Adv. Concr. Technol.* 1 (2003) 241–252. doi:10.3151/jact.1.241.

- [23] E. Denarié, E. Brühwiler, Structural rehabilitations with ultra-high performance fibre reinforced concretes (UHPFRC), *Restor. Build. Monum.* 12 (2006) 453–468.
- [24] G. Habert, E. Denarié, A. Šajna, P. Rossi, Lowering the global warming impact of bridge rehabilitations by using Ultra High Performance Fiber Reinforced Concretes, *Cem. Concr. Compos.* 38 (2013) 1–11. doi:<https://doi.org/10.1016/j.cemconcomp.2012.11.008>.
- [25] K.L. Scrivener, V.M. John, E.M. Gartner, Eco-efficient cements: Potential economically viable solutions for a low-CO₂ cement-based materials industry, *Cem. Concr. Res.* 114 (2018) 2–26. doi:<https://doi.org/10.1016/j.cemconres.2018.03.015>.
- [26] A. Kamen, E. Denarié, E. Brühwiler, Thermal effects on physico-mechanical properties of ultra-high-performance fiber-reinforced concrete, *ACI Mater. J.* 104 (2007) 415–423.
- [27] H. Yiğiter, S. Aydın, H. Yazıcı, M.Y. Yardımcı, Mechanical performance of low cement reactive powder concrete (LCRPC), *Compos. Part B Eng.* 43 (2012) 2907–2914. doi:[10.1016/J.COMPOSITESB.2012.07.042](https://doi.org/10.1016/J.COMPOSITESB.2012.07.042).
- [28] W. Huang, H. Kazemi-Kamyab, W. Sun, K. Scrivener, Effect of cement substitution by limestone on the hydration and microstructural development of ultra-high performance concrete (UHPC), *Cem. Concr. Compos.* 77 (2017) 86–101.
- [29] WBCSD Cement Sustainability Initiative, Getting the Numbers Right, Project Emissions Report 2014, 2016. <http://www.gnr-project.org/>.
- [30] E. Denarié, Y. Houst, Cement matrices for high performance fiberreinforced cementitious composites (HPFRCCs), in particular ultra high performance fiber reinforced concretes (UHPFRCs). European patent B-6160-EP [14.07.2009]., 2011.
- [31] R.J. Flatt, Y.F. Houst, A simplified view on chemical effects perturbing the action of superplasticizers, *Cem. Concr. Res.* 31 (2001) 1169–1176. doi:[https://doi.org/10.1016/S0008-8846\(01\)00534-8](https://doi.org/10.1016/S0008-8846(01)00534-8).
- [32] A. Hajiesmaeili, E. Denarié, Next Generation UHPFRC for Sustainable Structural Applications, *Am. Concr. Inst.* 326 (2018) 58.1-58.10.
- [33] K.L. Scrivener, Options for the future of cement, *Indian Concr. J.* 88 (2014) 11–21.
- [34] W. Huang, H. Kazemi-Kamyab, W. Sun, K. Scrivener, Effect of replacement of silica fume with calcined clay on the hydration and microstructural development of eco-UHPFRC, *Mater. Des.* 121 (2017) 36–46. doi:<https://doi.org/10.1016/j.matdes.2017.02.052>.

Chapter – 2

Paper 1

Tensile response of low clinker UHPFRC subjected to fully restrained shrinkage

Reference: M.A. Hafiz¹, A. Hajiesmaeili², E. Denarié³, Tensile response of low clinker UHPFRC subjected to fully restrained shrinkage, *published in Cement and Concrete Research, Volume 124, October 2019.* <https://doi.org/10.1016/j.cemconres.2019.105804>

1 - corresponding author of the paper – conducted all the experiments presented in the paper along with the writing of the full article

2 - helped in developing Mix II

3 – thesis supervisor

Abstract

This paper addresses the tensile response of Strain-Hardening Ultra High Performance Fiber Reinforced Concretes (SH-UHPFRC) subjected to restrained autogenous shrinkage deformations under full and partial restraint conditions, right after casting and until one month. The development of autogenous shrinkage and corresponding eigenstresses under various degrees of restraint were studied for two types of mixes; Mix I with type I cement and silica fume, and Mix II with silica fume and 50% mass replacement of type I cement with limestone filler. The tests under 100% restraint conditions are the first of their kind on SH-UHPFRC and the results show that under these conditions, the material enters into the strain-hardening domain of the tensile response. The development of eigenstresses was much slower in the Mix II when compared to that of Mix I. The development of the dynamic elastic modulus and heat of hydration were also studied and put into perspective.

Keywords: UHPFRC, restrained shrinkage, TSTM, isothermal calorimetry, VRFT, early age, low clinker, limestone filler.

1 Introduction

Ultra High Performance Fiber Reinforced Concretes (UHPFRC) are cementitious materials with very low permeability, outstanding durability and excellent mechanical properties. They have high tensile strength and exhibit significant strain-hardening behavior (1-5%) with a suitable fibrous mix. Because of these outstanding properties, they are very well adapted for the improvement of load carrying capacity and protective functions of existing structures [1].

In composite UHPFRC-concrete structures, a UHPFRC reinforcing and/or protective layer is applied on an existing structure. The UHPFRC layer undergoes intensive early age volume changes due to hydration reactions; thermal effects (more or less pronounced depending on the UHPFRC layer thickness), autogenous shrinkage and to some extent drying shrinkage if the UHPFRC layer remains exposed to the outside. It should also be noted that these deformations, especially the drying shrinkage, not only act in the early age, but can also occur over longer spans of time. These deformations are restrained by the existing structure as well as the reinforcement bars in the UHPFRC layer, if any, which will lead to the development of tensile eigenstresses in the UHPFRC layer [2–4]. The stiffness of the existing structure will affect the degree of restraint imposed by the structure, which in turn affects the value of the eigenstresses developed. Denarié et al. [5] showed that depending on the stiffness of the structure, even more than 90% of the free deformations can be restrained, leading to conditions which are close to full restraint.

Only a few works have been carried out to study restrained shrinkage and the associated eigenstresses development in UHPC [6,7] and in UHPFRC [2,3,8–11]. The effect of shrinkage reducing admixtures and superabsorbent polymers on the early age shrinkage of UHPC was investigated in [12,13]. The effect of specimen thickness on the restrained shrinkage behavior of UHPFRC was studied in [10,11] and it was shown that the cracking risk is reduced as the thickness of the specimen increase. However, to the best of the authors' knowledge, no extensive research has been reported in open literature on the influence of full restraint conditions on the development of the eigenstresses in UHPFRC.

The strain-hardening capacity of UHPFRC helps to mitigate the detrimental effects of the eigenstresses, except in very special cases of unfavorable fiber orientations, in which case the strain-hardening response is limited or lost and the eigenstresses may lead to premature localized cracking, with reduced protective performance. The viscoelastic potential in tension of the UHPFRC also helps to relax the developed eigenstresses, thereby reducing their adverse effects. However, depending on the stress level, the relaxation may be associated to linear viscoelastic or non-linear viscoelastic. Kamen et al. [14] showed that UHPFRC viscous response at early age (3 days) deviates considerably from a linear response when the tensile stress level changes from 32% to 63% of the tensile strength. Because of the interaction of various complex effects like the hydration and ageing, stress level, loading history and their couplings, the time dependent behavior of UHPFRC at early age under high sustained loads is not fully understood.

Only a few studies have been carried out to understand the viscoelastic behavior of UHPFRC in compression [3,15–20] and in tension [8,19,21–23]. It was shown that the compressive creep response of UHPFRC is significantly lower than that of ordinary concretes at a similar loading age and load level [24]. The basic compressive creep coefficient of UHPFRC without thermal treatment, at a loading age of 28 days, for a load level below 40% of the compressive strength, is typically 0.8-1, instead of 2-4 for normal concretes [24]. [25–27] studied the early age tensile creep behavior of concrete and [28] showed that the viscous properties of concrete help to reduce the cracking tendency by reducing the early age eigenstresses by about 50%. [2,8] showed that the response was similar in UHPFRC. Very few studies have been conducted to understand the early age tensile creep of UHPFRC [4,14,29,30]. The TSTM setup developed at MCS-EPFL by Kamen et al. [2,8] was used extensively to investigate the early age tensile response of Strain-hardening UHPFRC under various temperatures and loading conditions, which confirmed a significant creep potential for the material due to its high paste volume [9,21].

In these mixes, because of the low w/c ratio, the overall degree of hydration is much less (about 30% to 40% at 28 days) than that of normal concretes [9]. Because of this, it is advantageous to replace a part of the unhydrated clinker with Supplementary Cementitious Materials (SCMs) like limestone filler. No work has been carried out until now to study the development of autogenous deformations and eigenstresses under restraint for UHPFRC mixes with massive replacement of clinker with limestone fillers. Powers et al. [31] showed that complete hydration of cement can occur only for water/binder ratios of 0.42 in the long term. Waller [32] and Jensen [33] extended this model to systems with silica fume. Using these models, [8,9,34] predicted the maximum degree of hydration of cement in different types of UHPFRC and showed that it is low, around 30% to 50%. Thus if cement (clinker) is progressively replaced by inert particles in a UHPC matrix, such that the overall amount of hydrates stays the same, no detrimental consequences on the mechanical performance of the material should be observed. This effect was shown by many researchers for normal and high strength concrete [6,35,36]. Nehdi et al. [37] studied combinations of limestone filler, cement and silica fume in high performance mortars with cement replacement by filler up to 25% mass. [38–43] showed that it is possible to replace significant amounts of cement in UHPC mixes with low w/b ratios (0.19-0.25) with fillers like fly ash, limestone filler, GGBS and metakaolin, keeping the w/b ratio constant, without significantly decreasing the compressive strength. The same trend was observed by [44,45] with clinker replacement by limestone filler in SH-UHPFRC mixes. Ghafari et al. [46] discusses the effect of SCMs such as FA and GGBS on the porosity and autogenous shrinkage of UHPC. They show that the full or partial replacement of SF by the SCMs lead to a considerable decrease in the finer pores and thereby lead to lower autogenous shrinkage, without much loss in the compressive strength. Schachinger et al. [7] showed that the autogenous deformations in blast furnace cement concretes were lower than that with normal OPC; with values of 0.6‰ and 1.3‰ respectively after 1 day, and 1.3‰ and 1.7‰ respectively after 56 days. Liu et al. [47] showed that the autogenous shrinkage of RPC can be effectively mitigated by addition of SCMs like GGBS along with internal curing by means of super absorbent polymers.

Even though many reporters report a decrease in the autogenous shrinkage with the replacement of fillers in UHPC ($w/b=0.19-0.25$) [46–49], some reporters indicate an increase in the autogenous shrinkage with the addition of GGBS as a filler [48]. [42] showed that the shrinkage of HPC with FA or GGBS reduced by 14.28% and 27.95% respectively at 180 days and that the creep at 180 days reduced by 36.71% and 56.11% respectively, when compared to standard mix with only cement. The knowledge on the shrinkage and creep of UHPFRC with SCMs, along with the development of eigenstresses under restrained shrinkage is scarce in literature. Moreover, according to the best of the authors' knowledge, very few studies have been made to understand the tensile properties of UHPFRC with SCMs like limestone filler, fly ash or GGBS [50].

In the present paper, the eigenstresses development in UHPFRC under full and partial restraint conditions will be investigated for two types of UHPFRC mixes; Mix I with type I cement and silica fume, and Mix II with 50% mass replacement of type I cement with limestone filler. The development of autogenous deformations in these mixes will be studied from the time of casting until one month or more. Vibration resonance frequency tests (VRFT) will be carried out to study the development of dynamic elastic modulus of the two mixes. Isothermal calorimetry tests will also be conducted to understand the kinetics of overall hydration of the mixes.

2 Experimental

2.1 Materials and preparation

Two mixes were used for the present study, both from the CEMTEC_{multiscale}® family. The CEMTEC_{multiscale}® mixes were initially developed at Laboratoire Central des Ponts et Chaussées (LCPC), France [51]. This mix was optimized and modified in the framework of the research works held in MCS/EPFL for rehabilitation and strengthening of existing structures [44,52] to produce Mix I, which is a UHPFRC type CM22_TKK_b. The matrix is composed of cement (CEM I 52.5 HTS from Le Teil, Lafarge), white microsilica (SEPR, BET = 14 m²/gr), superplasticizer (Zementol Zeta Super S from TKK, Slovenia) and water. The matrix is a pure cement paste with no fine sand, to accommodate all the fibers and therefore exhibits excellent rheological properties in the fresh state even though the water/binder ratio is very low, 0.129.

Since the degree of hydration of cement in Mix I is only 30% after 28 days [9], it was decided to replace 50% of the cement with inert limestone filler. The mix, which will be designated as Mix II from here on, contains two types of limestone fillers: Betoflow D® and Betocarb SL® (OMYA), of different gradings. Both mixes were developed based on the concept of packing density, which is the key for obtaining Ultra high-performance cementitious composites. The total water added to the system is divided into two main parts; the void water, which is the amount of water needed to fill the voids and the excess water which is

the rest of the water that gives workability to the mix. Optimizing the packing density with the help of different grain size classes reduces the voids in the matrix and therefore the void water, thereby improving the overall workability-strength performance of the cementitious material. In this study, the generalized CIPM model [53,54] was implemented to optimize the packing density of the mixes. The water film thickness, which is the amount of excess water divided by the surface area of the particle system, was kept similar in both mixes, in order to have similar workability. Figure 1 shows the particle size distribution (PSD) of the individual components used in the formulation of the matrix together with that of the final mixes. The overall PSD of the final mixes were obtained from the mix-design and the PSD of the individual components, which were determined using laser diffraction. More details regarding the procedure adopted for optimizing the packing density could be found in [54].

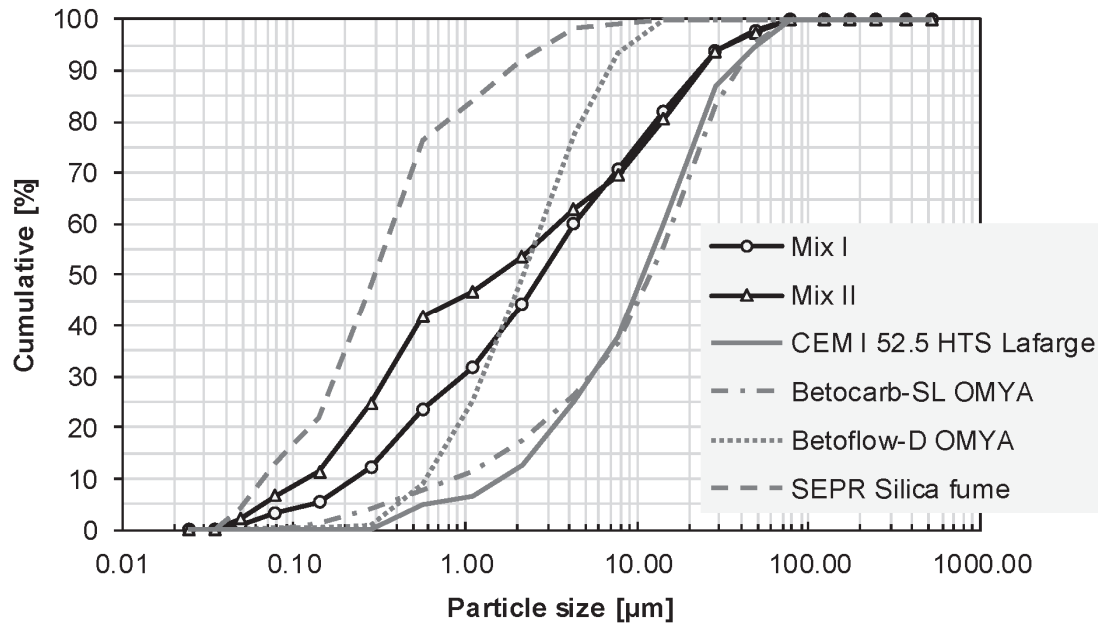


Figure 1: Particle size distribution of the mixes along with that of the individual components.

Both mixes had a fibrous mix containing two types of steel fibers; microfibers and macrofibers, with a total dosage of 9% by volume after the concepts developed by Rossi et al. [51]. The microfibers (steel wool, from Gervois, France) had a semi-circular section with variable dimensions and an irregular aspect ratio. The macrofibers were straight with $l_f = 10$ mm, $d_f = 0.2$ mm and turned out to be slightly torqued after the cutting process of the original wires, produced by Redaelli TECNA, Italy. Both mixes exhibit a significant strain-hardening behavior under tension (1-2 %) [21,55,56]. The detailed compositions of Mix I and II along with those of the corresponding UHPC matrices (without fibers, designated as Mix I_m and Mix II_m) are given in Table 1. The chemical and physical properties of the cement and silica fume used are given in Table 2.

Table 1: Compositions of Mix I and II.

Material	Units	Mix I	Mix II	Mix I _m [*]	Mix II _m [*]
Cement, CEM I 52.5 le Teil	[kg/m ³]	1467.0	733.7	1616.2	809.6
Silica fume, SEPR	[kg/m ³]	381.4	293.5	420.2	323.8
Limestone filler 1 (Betocarb SL [®])	[kg/m ³]	--	223.0	--	246.1
Limestone filler 2 (Betoflow D [®])	[kg/m ³]	--	510.6	--	563.4
Steel fibers (straight macro fibers; l _f = 10 mm, d _f = 0.2 mm and microfibers/steel wool)	[kg/m ³]	706.5	706.5	--	--
Total water	[kg/m ³]	225.8	217.9	248.7	240.4
Superplasticizer from TKK, Slovenia; Zementol zeta super S; polycarboxylate; 25% solid content; (total amount)	[kg/m ³]	20.5	14.7	22.6	16.2
Packing density	[--]	0.815	0.793	--	--
Compaction factor, K	[--]	9.0	9.0		

* corresponds to the compositions of the UHPC matrix without fibers.

The procedure for mixing the components was the same for both mixes. Initially the powders (cement, silica fume, limestone fillers) and the microfibers were mixed for 3 minutes. Water was then added to the mix, while the superplasticizer was added one minute after. The entire composition was mixed for 7-8 minutes after which 50% of the total steel fibers were added and mixed for 45 seconds. The remaining 50% of the fibers were then added and the whole mix was mixed for another two minutes. At the end of mixing, the workability of the mixes was tested following ASTM C1437 [57]. The air content as well as the specific gravity of the mixes were also measured using an air content meter after EN 459-2. The properties of both mixes in the fresh state are shown in Table 3 and that in the hardened state are shown in Table 4.

The compressive strength and modulus of elasticity were determined on 70 mm x 140 mm cylinders, whereas the tensile properties were obtained from uniaxial tensile tests at a strain rate of 10^{-5} 1/s, on dumbbell specimens with a center cross section of 50 mm x 30 mm, following [58]. The sorptivity was also measured for both mixes at an age of 28 days following EN 1925: 99-07.

Table 2: Chemical compositions of cement and SF_{SEPR}.

Components	Chemical composition (%)	
	Cement	SF _{SEPR}
SiO ₂	22.75	94
TiO ₂	-	< 500 ppm
Al ₂ O ₃	2.7	3
Fe ₂ O ₃	1.9	0.15
CaO	67.1	0.02
Na ₂ O	0.15	0.10
K ₂ O	0.2	0.06
MgO	0.75	-
SO ₃	2.1	60 ppm
ZrO ₂	-	2.4
P ₂ O ₅	0.2	-
Cl	< 0.1	-
C	-	40 ppm
CO ₂	1.3	-

Table 3: Properties of Mix I and II in the fresh state (average value from 4 tests).

Property	Units	Mix I	Mix II
Workability (ASTM - spread after 25 blows)	mm	179	146
Specific weight	kg/m ³	2834	2695
Air content	%	3.2	4.7

Table 4: Properties of Mix I and II in the hardened state.

Property	Units	Mix I	Mix II	Age (days)
Tensile first crack strength* (average of 8 tests)	MPa	12.3 ± 1.7	11.1 ± 1.9	14
Uniaxial tensile strength (average of 8 tests)	MPa	18.0 ± 3.1	15.1 ± 2.7	14
Modulus of elasticity in tension (average of 8 tests)	GPa	51.0 ± 2.3	46.3 ± 1.3	14
End of tensile hardening (average of 10 tests)	‰	1.6 ± 0.4	1.3 ± 0.5	14
Compressive strength (average of 3 tests)	MPa	230.5 ± 0.9	169.7 ± 0.5	28
Modulus of elasticity in compression (average of 3 tests)	GPa	48.3 ± 0.8	46.3 ± 0.8	28
Sorptivity (average of 10 tests)	gr/m ² √h	45.0 ± 5.2	32.5 ± 9.5	28

* corresponds to the transition from the elastic behavior to the strain-hardening behavior.

2.2 Vibration Resonance Frequency Test (VRFT)

The development of the dynamic moduli of elasticity of the two mixes was studied using the Vibration Resonance Frequency test method. The automatic test setup for two specimens in parallel was developed by [59] in EPFL following the works of Kazemi [9], after [60]. The tests were carried out on two cylindrical specimens 140 mm in length and 70 mm in diameter, inside a climate room maintained at 20 °C +/- 1 °C. The specimens were weighed and the surfaces were sealed with two layers of aluminum tape in order to prevent the drying and moisture loss. The cylinders were then kept on a support in front of a system consisting of a steel ball suspended using a steel thread. The specimens were hit at their centers, at one end, with the steel ball, that produced longitudinal vibrations in the specimens, which were measured using an accelerometer fixed on the other end of the cylinder. The data acquisition was done at a rate of one measurement per minute.

Using an analytical procedure developed by [60], the dynamic elastic modulus was determined at different ages. The proposed analytical procedure was based on a three-dimensional analysis of the vibration of the cylinder. The two first longitudinal resonance frequencies were determined, from which the elastic modulus and Poisson's ratio were calculated at the different ages investigated.

2.3 Isothermal calorimetry tests

Isothermal calorimetry tests were done in a TAM AIR calorimeter from TA instruments, and the heat flow in the mixes was continuously measured from the time of casting, to follow the kinetics of hydration. The thermostat in the TAM AIR can maintain the temperature in the samples and the surrounding environment within ± 0.02 °C of the chosen isothermal temperature. The mixes used for the isothermal calorimetry tests did not have the micro or macro fibers. Four samples were tested for each of Mix I_m and Mix II_m at 20 °C. Immediately after mixing, about 10 g of the sample was placed into a 20 mL glass ampoule and kept in the calorimeter, along with a reference sample of water in another ampoule, which acted as an inert sample to improve the signal to noise ratio and identify the temperature artefacts and fluctuations. More detailed information regarding the test procedure and sample preparation could be found in [61, 62].

2.4 Temperature Stress Testing Machine (TSTM)

The Temperature Stress Testing Machine was developed at MCS/EPFL during the doctoral thesis of Kamen [8] following the works of [63–65]. It is a thermo-mechanical testing setup situated inside a temperature-controlled room and used to conduct mechanical measurements and tests on cementitious specimens, from a very early age directly after casting, at different temperatures. Quasi-isotherm temperature conditions were ensured in the specimen with the help of a cooling circuit surrounding the molds. A schematic diagram of the TSTM setup is shown in figure 2.

The setup consists of two devices; the Free Setup (FS) helps to measure the free autogenous deformations. The Restrained Setup (RS) helps in measuring the eigenstresses developing under various restraint conditions with the help of a load cell and controlling their development with an electromechanical actuator linked to a closed loop control system. The associated free deformations in the restrained specimen as well as the free deformations in the free system were measured by means of two LVDT in each specimen, attached to a rod inserted in the material, immediately after casting. In the RS setup, two LVDT namely LVDT A and LVDT B with an accuracy range of ± 0.5 mm were placed 750 mm apart, whereas in the FS setup, two LVDT namely LVDT C and LVDT D with an accuracy range of ± 2.5 mm were installed 750 mm apart from each other, as shown in figure 2.

The eigenstresses were calculated by dividing the force measured by the load cell of the RS setup with the cross sectional area of the specimen. In both devices, fully sealed specimens of cross sectional dimensions 50 mm x 100 mm were used. Further details regarding the TSTM setup could be found in [8,9,21,55].

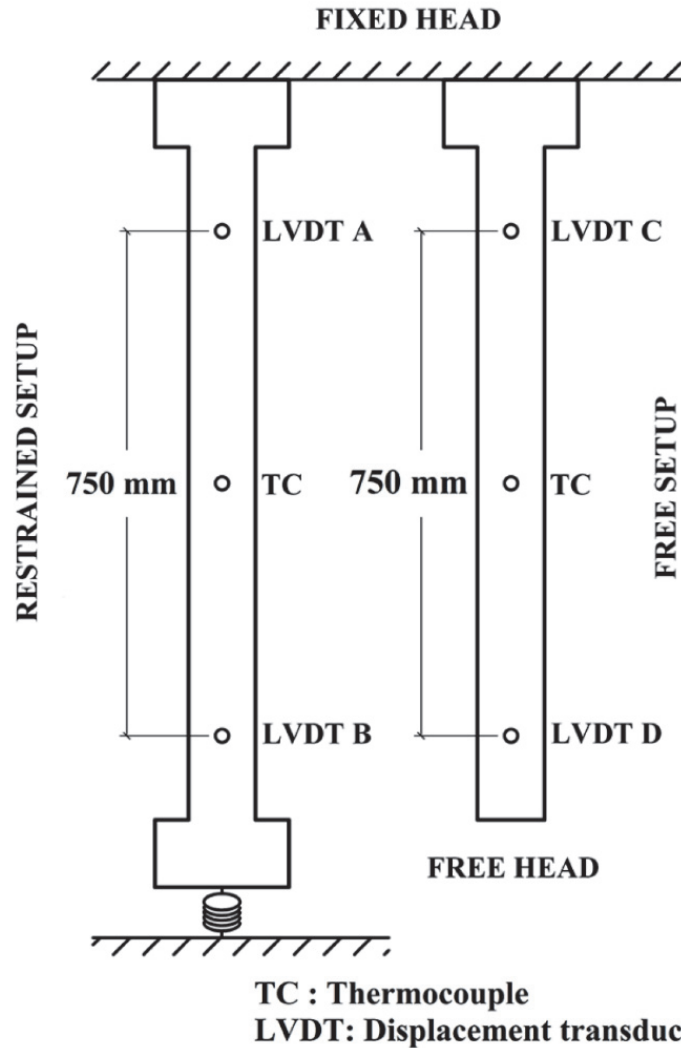


Figure 2: Schematic representation of the TSTM setup (adapted after [8,21]).

2.5 Loading programs for the TSTM tests

Two types of tests were conducted in the TSTM; full restraint tests and partial restraint tests, both at a quasi-isothermal temperature of 20 °C. All measurements were started immediately after casting.

In the full restraint test, the specimen was subjected to fully restrained conditions against any autogenous or thermal deformations, from the time of casting, until a month or more. In order to carry this out, an active control was required to keep at zero the relative displacement between two points A and B 750 mm apart. However, at fresh state and in the very early age close to setting time, the material stiffness was too low to impose a closed loop force or deformation control. As such, the tests were started under stroke control (passive control) with the stroke remaining at the same position as the start of the test. The monitored development of eigenstresses under passive stroke control was used to determine a trigger value to activate the deformation control leading to full restraint condition. A value of 0.2 MPa (corresponding to a force of 100 kg carried by the specimen) was chosen as the trigger value, to be low enough to minimize the discrepancies of the control mode and the impacts on the viscous effects of the loading history, while being high enough to reach a sufficient stiffness of the specimen to respond to a closed loop deformation control without yielding out of control. After the setting of the UHPFRC, when the stress in the material reached 0.2 MPa, the control was automatically switched to deformation control, wherein the relative displacement between the points A and B was kept zero. The control was therefore an active control as the deformations were controlled actively depending on the autogenous deformations occurring in the material, thereby ensuring full restraint conditions in the material.

In the partial restraint test, the entire test was controlled using stroke control and the stroke was kept in the same relative position without any movement, from the beginning of the test until the end. Because of the finite stiffness of the machine parts, due to which there were slight displacements of the machine parts, the specimen was not fully restrained in this case. The partial restraint imposed by the machine in these tests were calculated to be 54% in the Mix I-20C-PR1 test and 60 % in the Mix I-20C-PR2, by comparing the free deformations in the restrained system and the free deformations in the free system. It can then be assumed that the stroke controlled test impose a restraint of about 50-60%.

The temperature evolution in the restrained and free specimens were monitored using thermocouples inserted into the specimens right after casting. No active temperature control was used. The temperature of the samples increased slightly (1 °C – 2.2 °C) due to the heat of hydration, even though the molds contained cooling circuits to maintain the temperature. As such, the tests could not be considered to be fully under isothermal conditions but were under quasi-isothermal conditions.

It was assumed that the autogenous deformation varies linearly from one end to the other in the FS setup. The autogenous shrinkage was calculated by dividing the difference of displacements shown by LVDT C and D by the distance between them, that is, 750 mm. It was assumed that for each test, the restrained specimens exhibited similar autogenous shrinkage as that in the free specimens. For the Mix I, two full restraint tests (Mix I-20C-FR1, Mix I-20C-FR2) and two partial restraint tests (Mix I-20C-PR1, Mix I-20C-PR2) were carried out, whereas for the Mix II, only two full restraint tests were conducted (Mix II-20C-FR1, Mix II-20C-FR2).

3 Results and discussion

3.1 Development of dynamic elastic modulus

The development of the dynamic modulus of elasticity is shown in figure 3 on a semi-log scale. The static elastic moduli determined from compression test, after SIA 262/1- Annex G, on 70 mm x 140 mm cylinders are also shown on the figure 3 for Mix I (7 days) and Mix II (7, 14, 28 days). As expected, the dynamic elastic moduli of the mixes are slightly higher than the static ones. The dynamic elastic modulus of Mix I stabilized around 52 GPa for specimen C1 and about 50 GPa for specimen C2, whereas that of Mix II reached about 50 GPa after 200 hours.

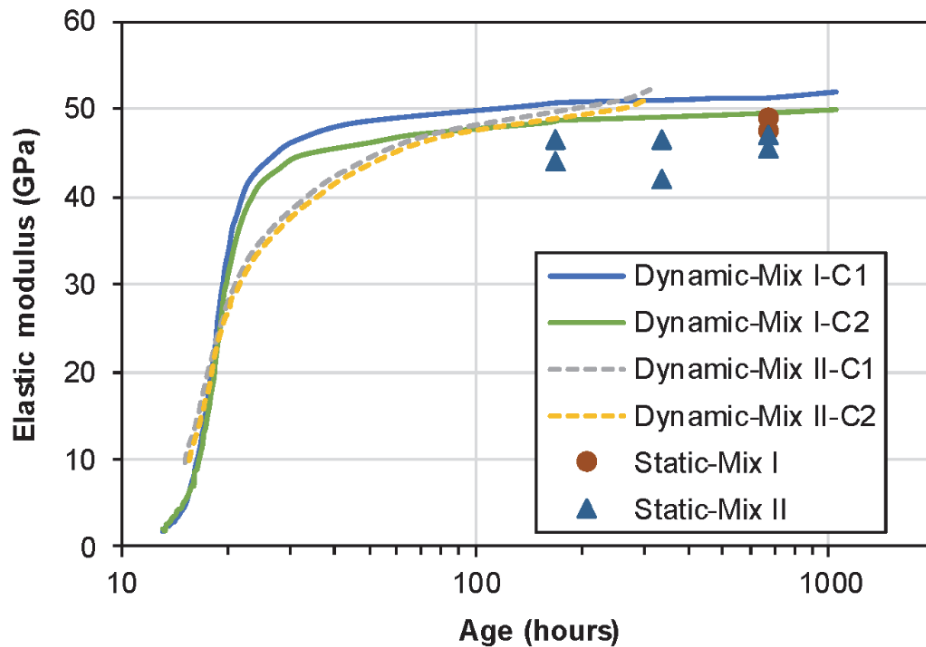


Figure 3: Development of dynamic elastic moduli of Mix I and II obtained from the VRF tests. The static modulus of elasticity of both the mixes are also shown at 7, 14 and 28 days.

The main difference in the development of the dynamic modulus in the mixes occurs around 20 hours as can be seen from the figure 3. At this time, the rate of development of the dynamic elastic modulus becomes much lower in the case of Mix II when compared to that of Mix I. However, at a later age, the trend inverts and the rate of development of the dynamic elastic modulus of Mix I becomes lower than that of Mix II. Eventually the dynamic elastic moduli reach similar values at an age of about 200 hours.

This trend could be explained by the difference in the two main parameters; the silica fume/cement (SF/C) ratio and the water/cement (W/C) ratio. Mix I has a SF/C ratio of 0.26 and Mix II has a SF/C ratio of 0.4, whereas the W/C ratio of Mix I is 0.163 and that of Mix II is 0.310. Jensen [33] has shown the influence of SF/C ratio and the W/C ratio on the rate of drop of relative humidity in cement paste specimens. The kinetics of the changes in the relative humidity is closely related to the kinetics of the rate of hydration in different mixes. As such, even though the relative humidity changes with age were not studied for the mixes in the present study, the expected trends of the same might indicate possible explanations for the kinetics of rate of development of dynamic elastic modulus. According to Jensen [33], as shown in figure 4, an increase in the SF/C ratio leads to an increase in the rate of drop of relative humidity in cement paste specimens in the early age and consequently an increase in the rate of overall hydration in the specimens. However, [32] has shown that only 20% mass of the silica fume contributes to the pozzolanic reaction, as all the $\text{Ca}(\text{OH})_2$ will be consumed and the pozzolanic reaction gets saturated. Since the SF/C ratio for both mixes is higher than 0.2, it can be assumed that it has minimal effect on the trend of hydration. On the other hand, figure 4 also shows a similar trend of increase in the rate of drop of relative humidity with a decrease in the W/C ratio [33]. Hence, the reduced rate of development of dynamic elastic modulus for Mix II in the early age can be attributed predominantly to the dilution effect (effect of higher W/C ratio). Figure 4 shows that the relative humidity drop is much faster as the W/C ratio decreases, but ultimately becomes similar for W/C ratio less than or equal to 0.3. The trend is similar to that of the dynamic elastic modulus in figure 3, in which the development is faster in Mix I with lower W/C ratio, but ultimately becomes similar in both mixes at a later age. Similar trends were also observed in [66,67] in ternary cement binders with SCM.

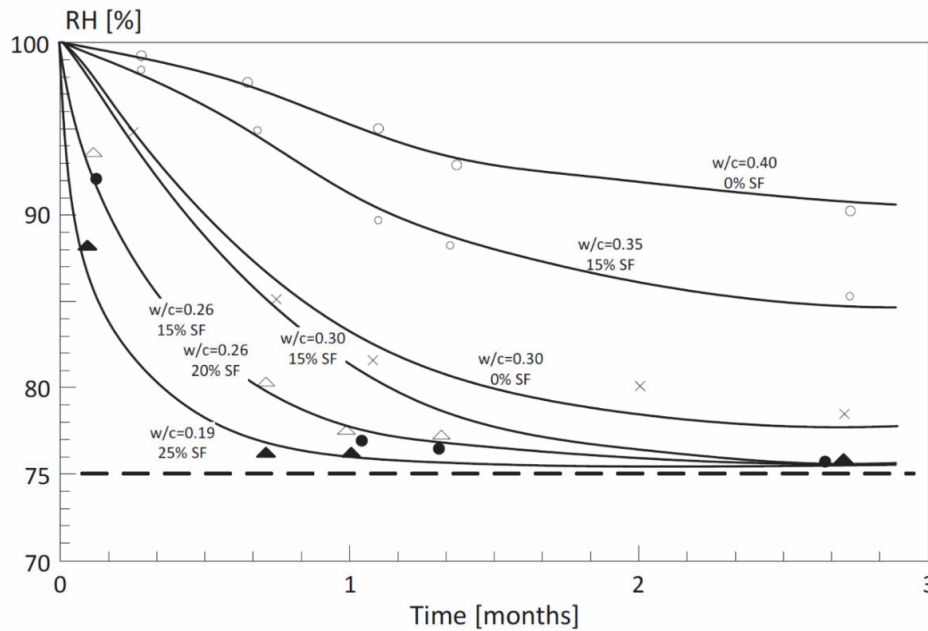


Figure 4: Effect of silica fume content and the water/cement ratio on the relative humidity within various cement paste and mortar specimens (taken from [33] after [68]).

3.2 Heat of hydration

The heat of hydration of both the matrices (without fibers) were obtained from the isothermal calorimetry tests. Figure 5 shows the heat flow per unit volume of both mixes. Four measurements are shown for each mix. However, the scatter between the four tests was very low and therefore the curves were almost superimposed on each other. The volume of the 10g of paste put in the ampoule was calculated using the specific weight of both the mixes (2295.9 kg/m^3 for Mix I_m and 2199.6 kg/m^3 for Mix II_m). Figure 5 shows a higher dormant period for Mix I_m, which is due to the higher amount of superplasticizer needed to reach the minimum workability. Figure 6a shows that the cumulative heat per unit volume of the Mix II_m is lower than that of Mix I_m, which could be explained by the limited reactivity of the limestone filler particles in Mix II_m and also due to the dilution effect in the same. Even though the limestone filler acts as nucleation sites for the hydration of more cement, the dilution effect dominates the nucleation effect and thereby releases less heat in the early age. Similar trends were seen in the case of blended cements in [66,69,70]. In the case of UHPC mixes, it was shown in [71] that the cumulative heat per unit volume of binder were almost similar up to 54% replacement of cement with limestone filler, whereas it was much lesser when the limestone filler replacement reached 74%.

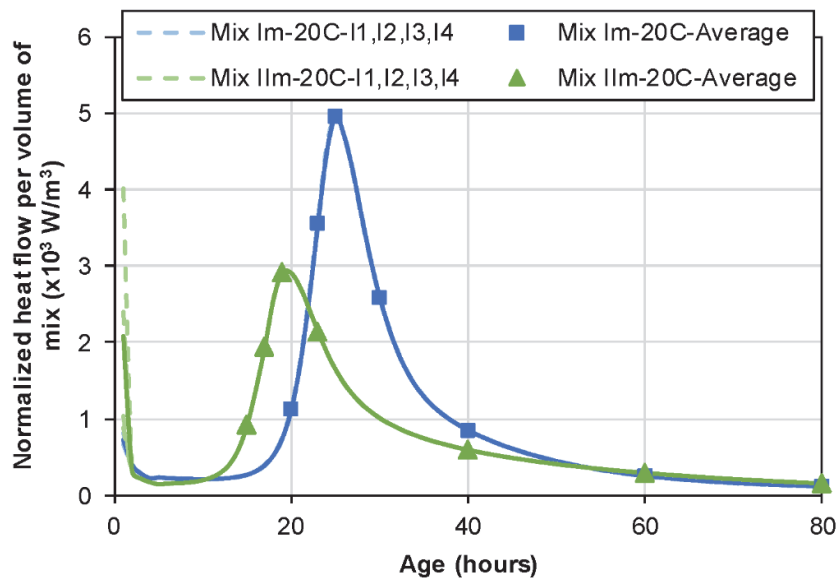


Figure 5: Heat flow per unit volume of Mix I_m and Mix II_m, from isothermal calorimetry tests at 20 °C.

The cumulative heat released can be used to calculate the degree of hydration of the mixes. Table 5 shows the hypothetical value of the total potential heat release for both the mixes, at full hydration, assuming that only cement and silica fume contributes to the release of heat.

Based on literature data [9,32], it was also assumed that only 20% mass of the silica fume will contribute to the heat of hydration, as all the Ca(OH)_2 will be consumed by then and there will not be any more pozzolanic reaction, that is, maximum mass of silica fume reacting is equal to 20% of the mass of the cement. Figure 6b shows the degree of hydration curves for both the mixes, which was obtained by dividing the cumulative heat per unit volume of the mixes (obtained from the isothermal calorimetry tests) by the total potential heat of the respective mix, $\text{Ht}_{100\%}$ at full hydration, as seen in Table 5. Figure 6b shows that the degree of hydration of Mix II_m at 650 hours is about 49.5% whereas that of Mix I_m at 650 hours is only 28.7%.

Table 5: Total potential heat release of Mix I and II at full hydration, $\text{Ht}_{100\%}$.

Mix	Cement reacted (kg/m ³)	Heat release of cement (kJ/kg)	Silica fume reacted (kg/m ³)	Heat release of silica fume (kJ/kg)[32]	Total potential heat at full hydration, $\text{Ht}_{100\%}$ (kJ/m ³)
Mix I	1607.9	452.3	321.6	780	978,085
Mix II	809.6	452.3	161.9	780	492,480

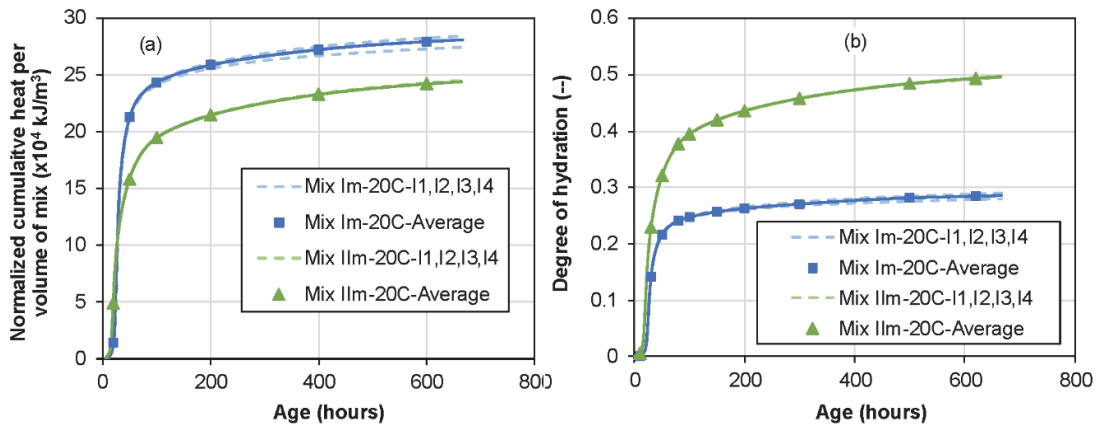


Figure 6: a) Cumulative heat per unit volume of Mix I_m and Mix II_m, from isothermal calorimetry tests at 20 °C, b) Overall degree of hydration of Mix I_m and Mix II_m at 20 °C.

3.3 Temperature evolution in the TSTM

Figure 7 shows the evolution of the temperature in the restrained specimens in the TSTM. The main observations in the evolution of the temperature are summarized in Table 6, which shows that the rise in the temperature in Mix I is higher (1.8 °C – 2.2 °C) than in Mix II (1.0 °C). Since the rise in the temperature in the specimens is small (max of only 2.2 °C), the test can be considered as a quasi-isothermal test.

As discussed later in section 3.4, the eigenstresses start developing at the end of the apparent swelling and therefore the end of apparent swelling could be considered as an apparent setting time. Figure 7 shows the corresponding points on the temperature curves, which is also summarized in the Table 6.

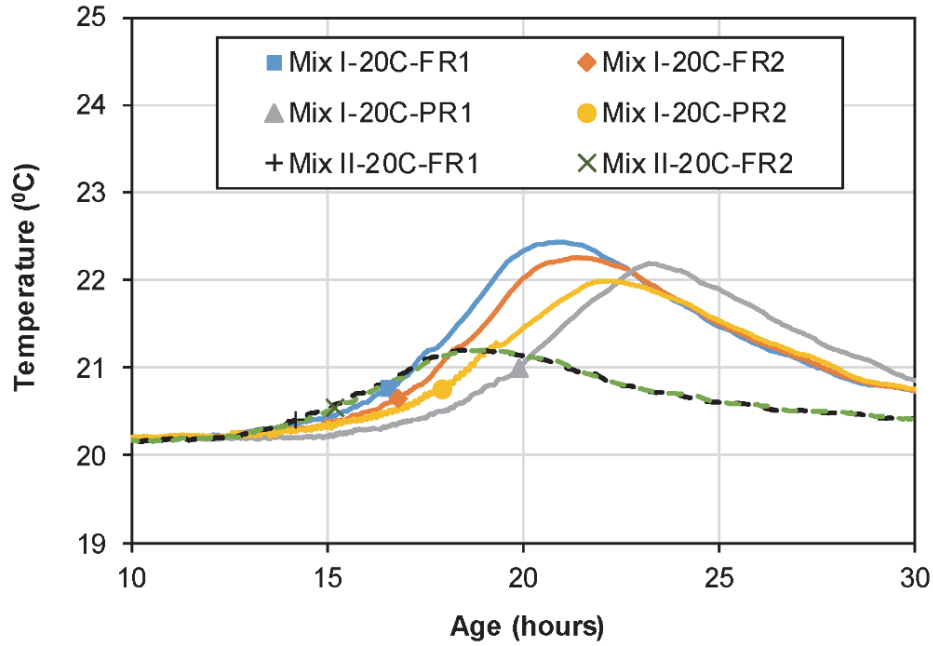


Figure 7: Evolution of temperature in the restrained test specimens in the TSTM setup (focusing near the peak of the temperature curves).

Table 6: Trends of temperature evolution in the TSTM experiments.

Experiment	ΔT_{tot}^* (°C)	t_{peak}^* (hours)	t_{as}^* (hours)	ΔT_{as}^* (°C)	$\Delta T_{as} / \Delta T_{tot}^*$ (%)	σ_{as}^* (MPa)
Mix I-20C-FR1	2.2	20.9	16.6	0.66	30.0	0.06
Mix I-20C-FR2	2.0	21.3	16.8	0.54	27.0	0.04
Mix I-20C-PR1	2.0	23.2	19.9	0.83	41.5	0.12
Mix I-20C-PR2	1.8	22.2	17.9	0.55	30.6	0.04
Mix II-20C-FR1	1.0	18.3	14.2	0.28	28.0	0.01
Mix II-20C-FR2	1.0	18.9	15.2	0.41	41.0	0.06

* ΔT_{tot} : total rise in temperature, t_{peak} : time to peak of the temperature curve, t_{as} : time to the end of apparent swelling of autogenous deformations (apparent setting time), ΔT_{as} : rise in temperature up to the end of apparent setting time, σ_{as} : eigenstress value at the apparent setting time.

It can be seen that the apparent setting time occurs when the rise in temperature is approximately 27%-41.5% of the total rise in temperature in the specimen. The corresponding eigenstresses at these points are also less than or equal to 0.06 MPa, except for Mix I-20C-PR1 where the stress was 0.12 MPa. These values of eigenstresses are very low and therefore the end of apparent swelling can be considered as the apparent setting time in the mixes.

3.4 Development of autogenous deformations

The free autogenous deformations $\epsilon_{\text{free}}^{\text{free}}$ were measured using the FS setup of the TSTM and the autogenous shrinkage was calculated as explained in section 2.5. Figures 8, 9 and 10 show the development of $\epsilon_{\text{free}}^{\text{free}}$ corresponding to the different tests. Figure 8 shows the development of autogenous deformations as measured, whereas figure 9 shows the evolution of autogenous deformations zeroed at the end of swelling. Figure 10 compares the kinetics of the autogenous deformation curves for each mix and defines the different phases in their evolution.

In figure 10, Point A is the time of contact of water with the binders and it is considered as the “zero age” of the material. Point B is the point where the test measurements start. The phase AB is the phase in which the mixing procedure as well as the casting of the mix into the molds take place. It can be seen that there is a swelling phase in all the mixes (phase BC). The point C is the end of the apparent swelling phase of the material, after which the actual shrinkage deformations begin, which lead to the development of eigenstresses in the material. The point C is in the range of 16.5-19.5 hours in the case of Mix I whereas it is in the range of 14.5 – 15.5 hours for Mix II.

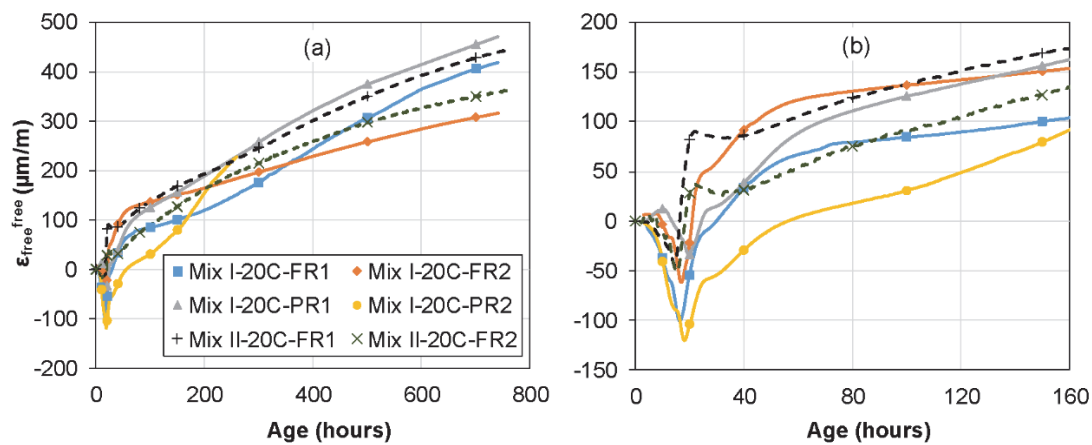


Figure 8: Evolution of free autogenous deformations (increasing deformation represents shrinkage) in the FS setup of the TSTM; a) overall trend, b) early age.

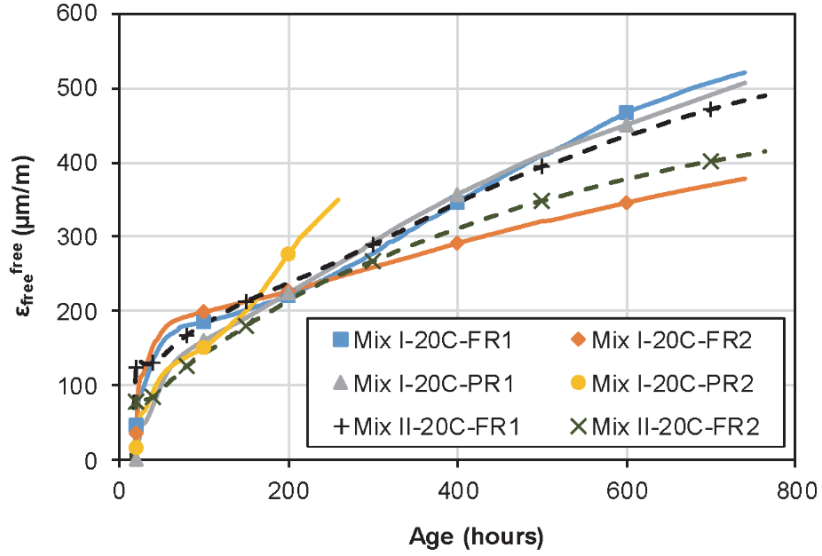


Figure 9: Evolution of autogenous deformations zeroed at the end of the swelling phase.

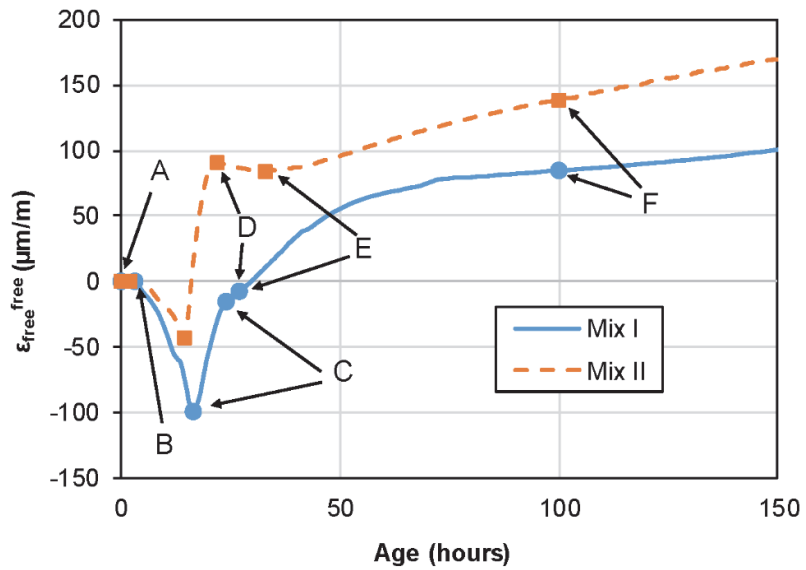


Figure 10: The different phases in the evolution of the autogenous deformations of Mix I and II, in the FS setup of the TSTM.

Point D is the point that shows a major difference in the two mixes. While for Mix I, even though there is a reduction in the rate of shrinkage deformations beyond the point D, the shrinkage deformations are still increasing and there is no reduction (or swelling) in the value of the same; whereas for Mix II, a clear reduction in the autogenous deformations (shoulder effect) can be observed at the point D. Jensen [33] showed a similar trend in the reduction of the relative humidity in cementitious materials with silica fume. Jensen [33] postulated that the discontinuity in the reduction of the relative humidity was due to the initiation of the reaction of the silica fume for pozzolanic reaction.

Kazemi [9] also showed a similar trend using Proton NMR (^1H -NMR). It is assumed that it is around the point D, that the silica fume starts to react which could lead to a change in the rate of hydration, which in turn leads to a change in the rate of autogenous shrinkage occurring in the material. Point E is the point where the temporary swelling ends for the Mix II whereas for Mix I, it is the point where the rate of development of autogenous deformations change slightly. The phase EF is similar in both the mixes, even though there may be slight differences in the rate of development of the autogenous deformations.

Another interesting observation, as shown in figures 11 and 12, is the comparison of the average autogenous shrinkage curves for the two mixes along with their corresponding development of dynamic elastic modulus. The autogenous shrinkage of Mix II shows a reduction around 20-22 hours and it is approximately around this time that the rate of development of dynamic elastic modulus of Mix II deviates from that of Mix I, marked as zone II in figure 12. It can also be seen that the autogenous shrinkage curves of both mixes become almost similar approximately at the same time when the average dynamic elastic modulus of both mixes become similar (zone III in figure 12).

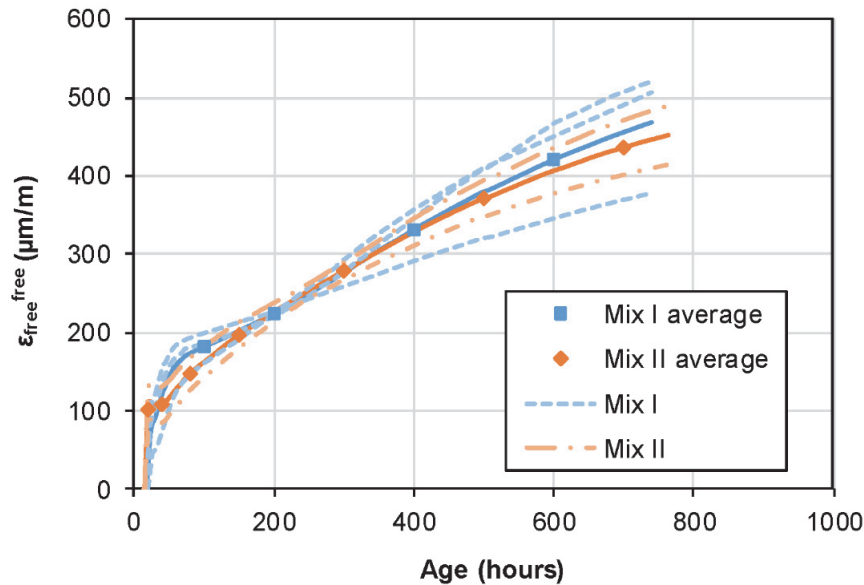


Figure 11: Average shrinkage curves of Mix I and Mix II from the FS setup of the TSTM.

This trend can be explained using the capillary pressure hypothesis [16,72–74], which states that the capillary tension (or depression) in the liquid phase in the pores, exerts a pressure on the solid skeleton (hydrates) formed, which then undergoes a compression and therefore a shrinkage (autogenous). However, the elastic stiffness and the viscous response of the solid skeleton of the matrix help in mitigating the effect of the capillary tension. As the hydration progresses, the pore structure becomes finer, which in turn leads to a higher capillary tension and thereby a higher autogenous shrinkage.

The hydration also leads to the consumption of the water in the pores, which is another reason for the increase in the capillary tension in the liquid phase. In zone II in figure 12, the dynamic elastic modulus of Mix II is slightly lesser than that of Mix I. It can then reasonably be assumed that the pore structure in Mix II will be coarser than the same for Mix I in this zone. As a coarser pore structure leads to a lesser value of capillary stress, the autogenous shrinkage produced will also be lesser. This might be the possible explanation for the slightly lower autogenous shrinkage for Mix II in zone II when compared to Mix I. It also explains why the average autogenous shrinkage values of both mixes become similar when the average dynamic elastic moduli become similar in the zone III.

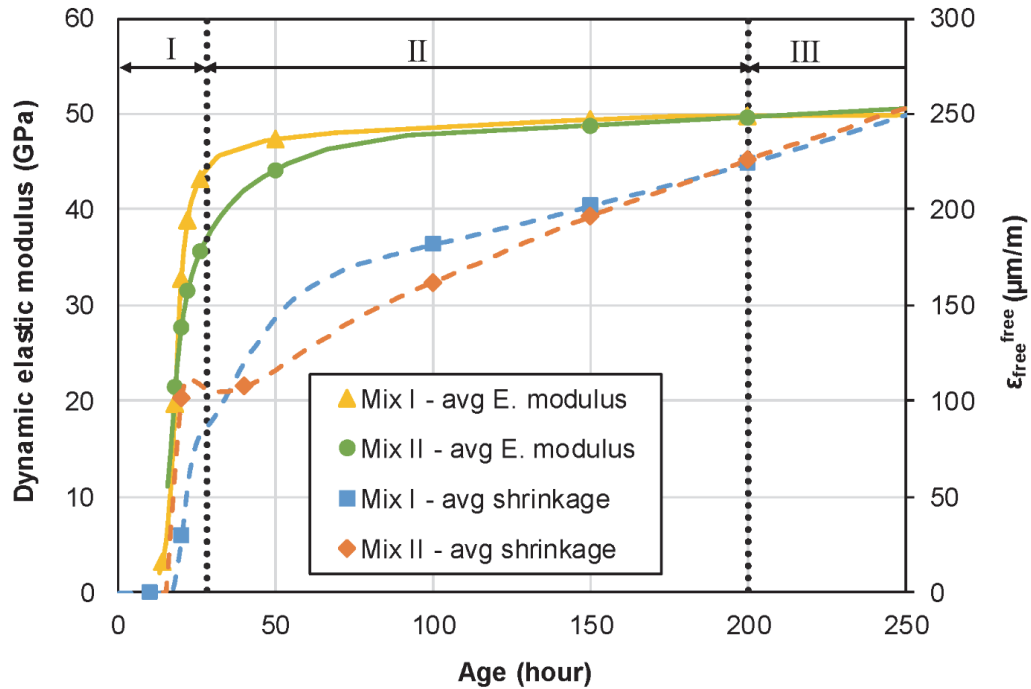


Figure 12: Comparison of the evolution of the autogenous shrinkage in Mix I and II with the corresponding development of elastic modulus.

Figure 8a shows that the long term autogenous shrinkage varies between 376 $\mu\text{m/m}$ and 514 $\mu\text{m/m}$ at 720 hours (one month) for Mix I whereas that for Mix II varies between 405 $\mu\text{m/m}$ and 477 $\mu\text{m/m}$. At an age of 7 days at 20 °C, Kamen [8] reported an autogenous shrinkage, which varied between 105 $\mu\text{m/m}$ and 140 $\mu\text{m/m}$ for a UHPFRC mix similar to Mix I, whereas Switek [21] reported an autogenous shrinkage of 168 $\mu\text{m/m}$ at 7 days. The results in the present study exhibit slightly higher values for the autogenous shrinkage at 7 days with Mix I showing a value ranging from 202 $\mu\text{m/m}$ to 225 $\mu\text{m/m}$ and Mix II from 193 $\mu\text{m/m}$ to 222 $\mu\text{m/m}$. The slightly higher values can be explained by the changes in the dormant period of the mixes in the present study when compared to that of [8,21]. The Mix I in the present study have an approximate dormant period of 11 hours whereas the dormant period of the mixes used in [8,21] varied between 32-33 and 22-24 hours respectively. This is

mainly because of the variation in the quantity of superplasticizer used in the mixes. The Mix I in the present study has a superplasticizer dosage of 1.4%, whereas that in [21] was 2.3% and in [8] was 3.3%. As such, the present mixes have slightly higher autogenous shrinkage at 7 days.

3.5 Development of eigenstresses

Figure 13a shows the displacements of LVDT A and B from the Mix I-20C-FR1 test. It can be seen that both are exact mirror images of each other, ensuring zero relative displacement between the two, thereby ensuring full restraint conditions. Figure 13b shows the displacements of LVDT A and B from the Mix I-20C-PR1 test and unlike that in the full restraint test, the displacements are not mirror images of each other and thereby the relative displacement between them is non-zero and therefore the restraint imposed is only partial.

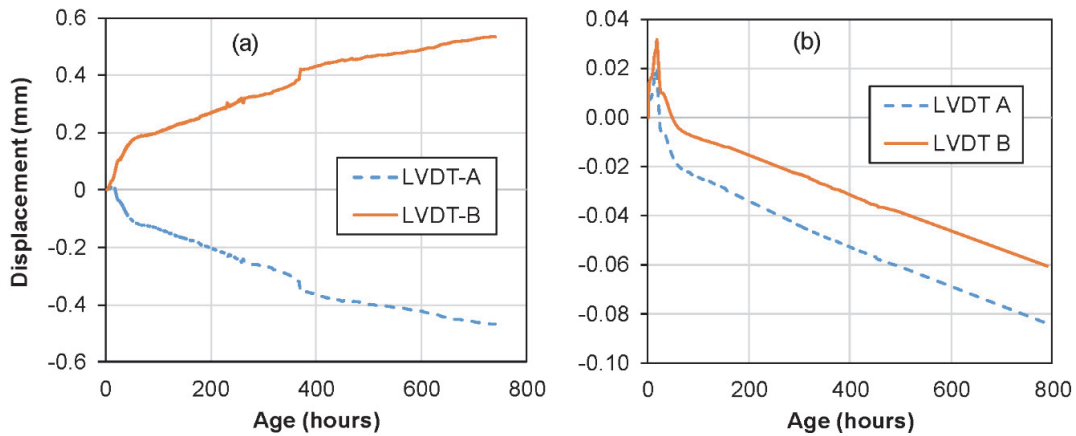


Figure 13: Comparison of LVDTs A and B in the; a) Mix I-20C-FR1 full restraint test, b) Mix I-20C-PR1 partial restraint test.

At this point, it is interesting to compare the procedure for full restraint adopted in the present study, with another commonly used procedure in literature. Following the procedure developed by [75], [2,34,76] had conducted full restraint tests on UHPFRC mixes similar to Mix I in the present study in similar TSTM setups, to study the development of eigenstresses. The procedure was to allow the specimen to shrink from its initial position up to 5-6 μm and then to bring the specimen back to its initial zero position, which induced stresses in the material. The cycle was then repeated again for every 5-6 μm increments. Figure 14a compares the development of eigenstresses using this procedure with that adopted in the present study using deformation control and it can be seen that the stresses at any given age are slightly lesser in the case of the incremental procedure, when compared to that of Mix I.

Figure 14b depicts the development of eigenstresses with the age axis of the mixes in [2, 34] adjusted in such a way so that the stresses start to develop at the same age as that of the Mix I. But even then it can be seen that the stresses are developing much faster in the experiments in the present study, which shows that the incremental procedure adopted in [2, 34] does not guarantee full restraint. However, it should be noted that the difference in the values of eigenstresses between the different procedures is not that large and may be even attributed to the slight difference in the composition of the mixes tested. Nevertheless, the procedure developed in the present study is much easier to carry out and easier to model. On the other hand, the incremental procedure helps in the determination of local estimate of the elastic modulus during the incremental loading steps as the elastic strain and stress could be measured at these loading steps.

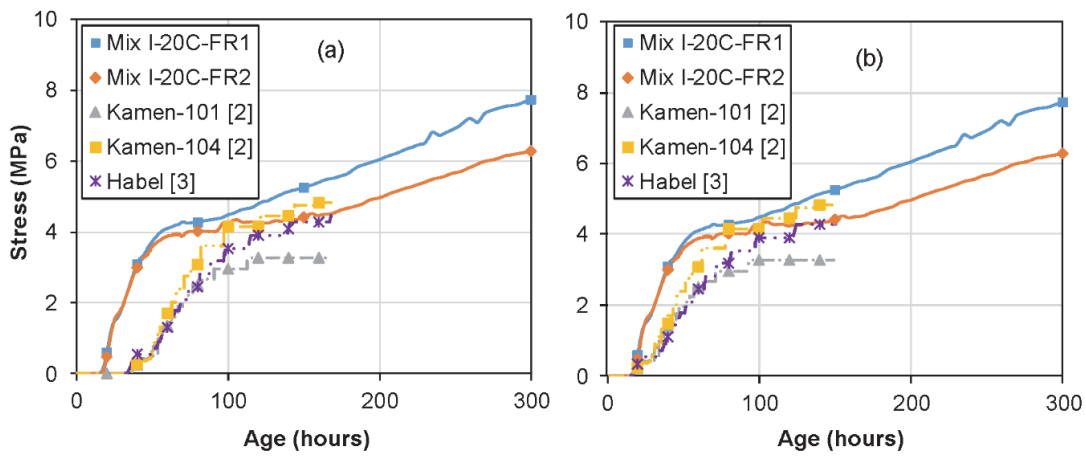


Figure 14: Comparison of the development of eigenstresses in the full restraint tests in the present study and tests using the incremental procedure of [2,3]; a) time scale as measured, b) time scale adjusted.

Figure 15 shows the development of eigenstresses in the two mixes under the different restraint conditions. As expected, the eigenstresses developed in the case of full restraint tests were much higher than that in the partial restraint tests for Mix I. The stresses reached a value of 12.2 MPa and 11.7 MPa at an age of one month (720 hours) in the two full restraint tests for Mix I, whereas the stresses were only about 5.3 MPa in the partial restraint tests for the same age. The rate of development of eigenstresses under full restraint were much slower for Mix II, with the values being only 6.9 MPa and 5.4 MPa for Mix II-20C-FR1 and Mix II-20C-FR2 respectively, at an age of one month. However, the eigenstresses kept on developing even beyond one month, with Mix I-20C-FR2 reaching a stress value above 14 MPa (in the strain-hardening domain) at around 1900 hours (2.6 months) and Mix II-20C-FR2 reaching a stress value of 12.3 MPa (just below the strain-hardening domain) at around 2400 hours (3.3 months). It indicates that even though the rate of eigenstresses development is slower for Mix II, the eigenstresses can still reach values close to the strain-hardening domain at a later age.

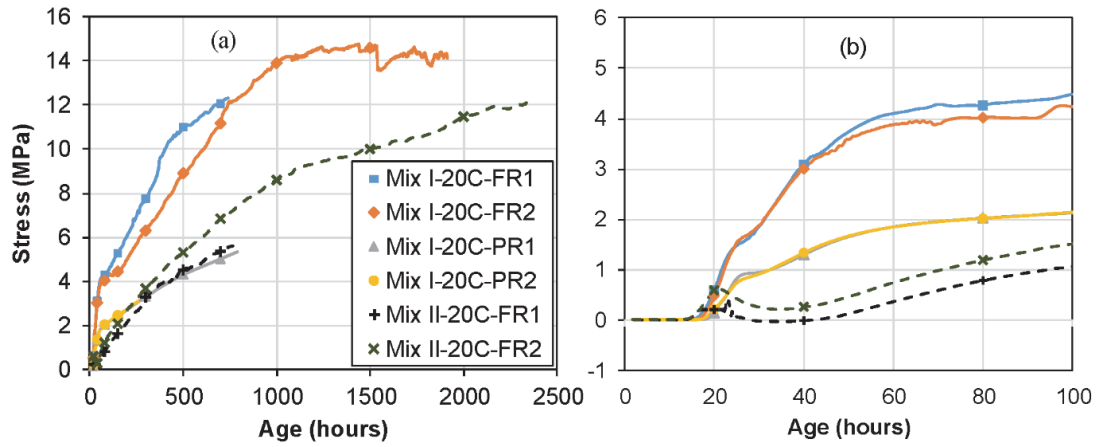


Figure 15: Development of eigenstresses in the full and partial restraint tests in the RS setup of the TSTM; a) overall trend, b) early age behavior.

The lower value of eigenstresses might be explained by a higher viscoelastic response of Mix II, and consequently a higher relaxation potential, which will help in relaxing the developed eigenstresses. This was confirmed by conducting tensile creep tests for both mixes on prismatic specimens of dimensions 1000 mm x 70 mm x 40 mm, at different stress levels. The details regarding the tensile creep rigs and the test setup could be found in [21,30]. Figure 16 shows the average normalized specific creep curves for both mixes under tension, loaded at an age of 14 days, at different stress levels. Mix II exhibits a higher creep response throughout the period of loading, thereby confirming a much higher viscous response, and consequently a higher relaxation potential.

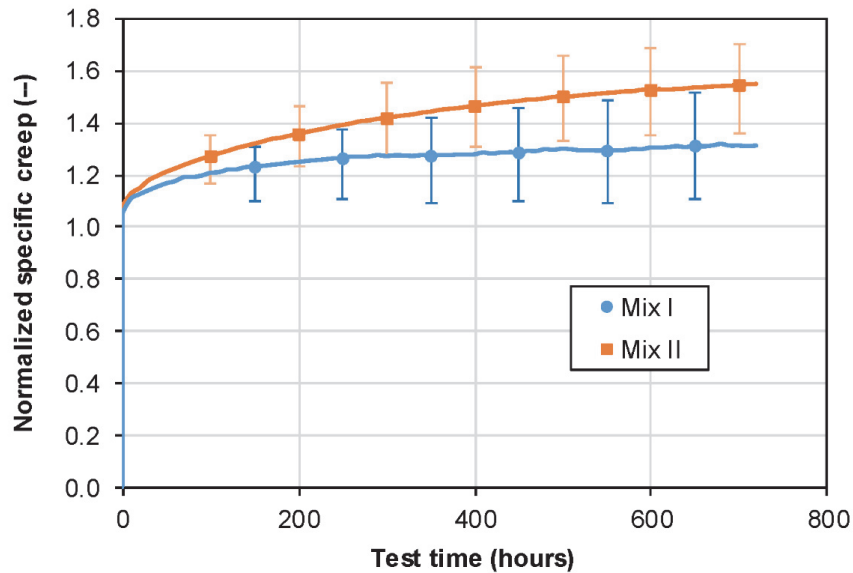


Figure 16: Average normalized specific creep of Mix I and II under tension, loaded at an age of 14 days.

The reduced eigenstresses in Mix II may also be due to slower rate of development of elastic modulus in Mix II, as discussed in section 3.1. A combination of slightly lower elastic modulus as well as lower autogenous shrinkage may have led to a slower development of eigenstresses. The drop in the autogenous shrinkage (point D in figure 10) has also led to a decrease in the eigenstresses in Mix II, as can be seen clearly from figure 15b, whereas a similar drop in autogenous shrinkage and a consequent reduction in eigenstresses were not present in the case of Mix I. Bouasker et al. [66] and Mehdipour et al. [67] observed similar trends in ternary cement binders with limestone filler and reported that the time to cracking was much higher in the case of ternary binders with limestone fillers, when compared to cement binders without limestone filler. As such, the tests show that it is advantageous to use the mix with limestone filler, as the adverse effects of the eigenstresses as well as the cracking risk are considerably reduced.

Fracture tests were later conducted on all the specimens and the tensile strengths are summarized in Table 7. The tensile strength results were consistent with the values shown in [21], who obtained an average tensile strength of 15.5 MPa for specimens of similar dimensions loaded at 10 days for a similar mix. Uniaxial tensile tests were also conducted on dumbbell specimens of Mix I and Mix II, with cross sections of 50 mm x 30 mm, in an electromechanical test setup at very low strain rates of 10^{-8} 1/s. The tests showed average elastic limits of 9.60 MPa and 10.19 MPa and average tensile strengths of 15.79 MPa and 17.17 MPa respectively for Mix I and Mix II at an age of 14 days age.

Table 7 shows that the eigenstresses at 720 hours in the full restraint tests on Mix I, were much higher than the other tests and even higher than the elastic limit of the material. As such, the stress levels had clearly reached the strain-hardening domain of the tensile response of the material. On the other hand, the eigenstresses development was much slower in the Mix II, with the values of the eigenstresses after 720 hours being only about 33-40 % of the tensile strength of the mix and also below the elastic limit. This clearly confirms the advantage of the limestone filler mix in terms of the cracking risk and serviceability.

Table 7: Summary of fracture tests done in the TSTM.

Specimen	Eigenstresses at 720 hours (MPa)	Tensile strength (MPa)	Eigenstresses as a percent of tensile strength after 720 hours (%)
Mix I-20C-FR1	12.23	12.8	95.54
Mix I-20C-FR2	11.71	16.6	70.54
Mix I-20C-PR1	5.07	18.18	27.89
Mix I-20C-PR2	--	17.02	--
Mix II-20C-FR1	5.42	16.02	33.83
Mix II-20C-FR2	6.93	17.38	39.87

4 Conclusions

- Tests on UHPFRC under full restraint conditions were done for the first time and they showed that the eigenstresses could reach values higher than the elastic limit and even close to the ultimate strength of the material.
- A new closed loop deformation controlled method was proposed to carry out tests under full restraint conditions. A value of 0.2 MPa was chosen as the trigger value to activate the closed loop of deformation control, to be low enough to minimize the discrepancies of the control mode and the impacts on the viscous effects of the loading history, while being high enough to demonstrate a sufficient stiffness of the specimen to respond to a closed loop deformation control without yielding out of control.
- Two mixes were investigated; Mix I with pure type I cement and silica fume and Mix II with silica fume and 50% replacement of type I cement with limestone filler.
- The development of the elastic modulus and autogenous shrinkage were almost similar in both Mix I and Mix II, except for changes in the kinetics at certain ages.
- Isothermal calorimetry tests were conducted which showed that the degree of hydration of Mix II at 650 hours is about 49.5% whereas that of Mix I at 650 hours is only 28.7%.
- This study highlighted the necessity of using a strain-hardening material for casting UHPFRC on an existing substrate, in order to avoid localized macrocracking and meet the serviceability criteria associated to the protective function.
- The rate of development of eigenstresses under full restraint conditions were much slower in Mix II when compared to Mix I, with Mix I reaching the strain-hardening domain at around 720 hours (one month), whereas for Mix II the eigenstresses were only approaching the strain-hardening domain, even after 3 months. However, the results indicated that even for Mix II, the eigenstresses might reach the strain-hardening domain at a later age beyond 3 months.

Acknowledgements

The project was financially supported by the Swiss National Science Foundation (grant 200021_153394/1). The authors would like to appreciate the help given by the technicians of GIC-ENAC-EPFL in performing the experimental works with the TSTM. The authors would also like to acknowledge the help given by Ms. Y. Briki, Mr. L. Sofia and Mr. J. D. Rego in conducting the isothermal calorimetry tests at LMC/EPFL.

References

- [1] E. Denarié, E. Brühwiler, Cast-on Site UHPFRC for improvement of existing structures – achievements over the last 10 years in practice and research, in: *High Perform. Fiber Reinf. Cem. Compos.* 7, 2015: pp. 473–480.
- [2] A. Kamen, E. Denarié, H. Sadouki, E. Brühwiler, Thermo-mechanical response of UHPFRC at early age - Experimental study and numerical simulation, *Cem. Concr. Res.* 38 (2008) 822–831. doi:10.1016/J.CEMCONRES.2008.01.009.
- [3] K. Habel, Structural behaviour of elements combining ultra-high performance fibre reinforced concretes (UHPFRC) and reinforced concrete, Doctoral thesis No: 3036, Ecole Polytechnique Fédérale de Lausanne, Switzerland, 2004.
- [4] K. Habel, J.P. Charron, E. Denarié, E. Brühwiler, Autogenous deformations and viscoelasticity of UHPFRC in structures. Part I: experimental results, *Mag. Concr. Res.* 58 (2006) 135–145.
- [5] E. Denarié, J. Silfwerbrand, H. Beushausen, Structural Behaviour, in: *Bond. Cem. Mater. Overlays Repair, Lining or Strength. Slabs or Pavements*, Springer, 2011: pp. 81–106.
- [6] P. Schiessl, K. Beckhaus, I. Schachinger, P. Rucker, New Results on Early-Age Cracking Risk of Special Concrete, *Cem. Concr. Aggregates.* 26 (2004) 1–9.
- [7] I. Schachinger, K. Schmidt, D. Heinz, P. Schießl, Early-age cracking risk and relaxation by restrained autogenous deformation of ultra high performance concrete, in: *6th Int. Symp. High Strength / High Perform. Concr.*, Leipzig, Germany, 2002: pp. 1341–1354.
- [8] A. Kamen, Comportement au jeune âge et différé d'un BFUP écrouissant sous les effets thermomécaniques, Doctoral thesis No: 3827, Ecole Polytechnique Fédérale de Lausanne, Switzerland, 2007.
- [9] M. Kazemi Kamyab, Autogenous Shrinkage and Hydration Kinetics of SH-UHPFRC under Moderate to Low Temperature Curing Conditions, Doctoral thesis No: 5681, Ecole Polytechnique Fédérale de Lausanne, Switzerland, 2013.
- [10] D.-Y. Yoo, J.-J. Park, S.-W. Kim, Y.-S. Yoon, Influence of ring size on the restrained shrinkage behavior of ultra high performance fiber reinforced concrete, *Mater. Struct.* 47 (2014) 1161–1174. doi:10.1617/s11527-013-0119-0.
- [11] D.-Y. Yoo, N. Banthia, Y.-S. Yoon, Geometrical and boundary condition effects on restrained shrinkage behavior of UHPFRC slabs, *KSCE J. Civ. Eng.* 22 (2018) 185–195. doi:10.1007/s12205-017-0587-9.
- [12] A.M. Soliman, M.L. Nehdi, Effect of partially hydrated cementitious materials and superabsorbent polymer on early-age shrinkage of UHPC, *Constr. Build. Mater.* 41 (2013) 270–275. doi:10.1016/J.CONBUILDMAT.2012.12.008.

- [13] J. Liu, Z. Ou, J. Mo, Y. Chen, T. Guo, W. Deng, Effectiveness of Saturated Coral Aggregate and Shrinkage Reducing Admixture on the Autogenous Shrinkage of Ultrahigh Performance Concrete, *Adv. Mater. Sci. Eng.* 2017 (2017) 1–11.
- [14] A. Kamen, E. Denarié, H. Sadouki, E. Brühwiler, UHPFRC tensile creep at early age, *Mater. Struct.* 42 (2008) 113–122. doi:10.1617/s11527-008-9371-0.
- [15] P. Rossi, J.P. Charron, M. Bastien-Masse, J.L. Tailhan, F. Le Maou, S. Ramanich, Tensile basic creep versus compressive basic creep at early ages: comparison between normal strength concrete and a very high strength fibre reinforced concrete, *Mater. Struct.* 47 (2014) 1773–1785.
- [16] P. Acker, Swelling, shrinkage and creep: a mechanical approach to cement hydration, *Mater. Struct.* 37 (2004) 237–243. doi:10.1007/BF02480632.
- [17] A. Loukili, P. Richard, J. Lamirault, A Study on Delayed Deformations of an Ultra High Strength Cementitious Material, *Spec. Publ.* 179 (1998) 929–950.
- [18] M. Cheyrezy, M. Behloul, Creep and shrinkage of ultra-high performance concrete, in: *Creep, Shrinkage Durab. Mech. Concr. Other Quasi-Brittle Mater. (Concreep 6)*, 2001: pp. 527–538.
- [19] V.Y.Y. Garas, K.E.E. Kurtis, L.F.F. Kahn, Creep of UHPC in tension and compression: Effect of thermal treatment, *Cem. Concr. Compos.* 34 (2012) 493–502. doi:10.1016/J.CEMCONCOMP.2011.12.002.
- [20] Y. Xu, J.J. Liu, J.J. Liu, P. Zhang, Q. Zhang, L. Jiang, Experimental studies and modeling of creep of UHPC, *Constr. Build. Mater.* 175 (2018) 643–652. doi:10.1016/J.CONBUILDMAT.2018.04.157.
- [21] A.E. Switek, Time-Dependent Response of Ultra High Performance Fibre Reinforced Concrete (UHPFRC) under Low to High Tensile Stresses, Doctoral thesis No: 4899, Ecole Polytechnique Fédérale de Lausanne, Switzerland, 2011.
- [22] V.Y. Garas, L.F. Kahn, K.E. Kurtis, Short-term tensile creep and shrinkage of ultra-high performance concrete, *Cem. Concr. Compos.* 31 (2009) 147–152. doi:10.1016/J.CEMCONCOMP.2009.01.002.
- [23] V.Y. Garas, A.R. Jayapalan, L.F. Kahn, K.E. Kurtis, Micro- and Nanoscale Characterization of Effect of Interfacial Transition Zone on Tensile Creep of Ultra-High-Performance Concrete, *Transp. Res. Rec.* 2141 (2010) 82–88. doi:10.3141/2141-14.
- [24] P. Acker, M. Behloul, Ductal Technology: A large spectrum of properties, a wide range of applications, in: *Proc. Int. Symp. Ultra High Perform. Concr.*, Kassel, Germany, 2004: pp. 11–23.
- [25] S.A. Altoubat, D.A. Lange, Tensile basic creep: Measurements and behavior at early age, *ACI Mater. J.* 98 (2001) 386–393.

- [26] D.S. Atrushi, Tensile and Compressive Creep of Early Age Concrete: Testing and Modelling, Doctoral thesis, Norwegian University of Science and Technology, Norway, 2003.
- [27] B. Bissonnette, D. Boily, J. Bastien, M. Fafard, Tensile creep of concrete repair materials: recent experimental findings towards optimization, in: *Creep, Shrinkage Durab. Mech. Concr. Other Quasi-Brittle Mater. (Concreep 6)*, 2001: pp. 599–604.
- [28] S.A. Altoubat, D.A. Lange, Creep, Shrinkage and Cracking of Restrained Concrete at Early Age, *ACI Mater. J.* 98(4) (2001) 323–331.
- [29] A. Switek-Rey, E. Denarié, E. Brühwiler, Early age creep and relaxation of UHPFRC under low to high tensile stresses, *Cem. Concr. Res.* 83 (2016) 57–69.
- [30] A. Switek-Rey, E. Denarié, E. Brühwiler, Tensile creep of UHPFRC under low and high stresses, in: *4th Int. Conf. Constr. Mater. – Performance, Innov. Struct. Implic.*, Nagoya, Japan, 2009: pp. 432–437.
- [31] T.C. Powers, T.L. Brownyard, Studies of the Physical Properties of Hardened Portland Cement Paste, *J. Proc.* 43 (1946) 101–132. doi:10.14359/8745.
- [32] V. Waller, “Relations entre composition des bétons, exothermie en cours de prise et résistance à la compression”, thèse de doctorat, LCPC, Nantes, France, 2001.
- [33] O.M. Jensen, Autogenous Phenomena in Cement-Based Materials, Doctoral thesis, Technical University of Denmark, 2005.
- [34] K. Habel, P. Gauvreau, Response of ultra-high performance fiber reinforced concrete (UHPFRC) to impact and static loading, *Cem. Concr. Compos.* 30 (2008) 938–946. doi:10.1016/J.CEMCONCOMP.2008.09.001.
- [35] P.L. Domone, S.M. N., Properties of high-strength concrete mixes containing PFA and GGBS, *Mag. Concr. Res.* 47 (1995) 355–367.
- [36] S.J.J. Barnett, M.N.N. Soutsos, S.G.G. Millard, J.H.H. Bungey, Strength development of mortars containing ground granulated blast-furnace slag: Effect of curing temperature and determination of apparent activation energies, *Cem. Concr. Res.* 36 (2006) 434–440. doi:https://doi.org/10.1016/j.cemconres.2005.11.002.
- [37] M. Nehdi, S. Mindess, P.-C. Aïtcin, Optimization of high strength limestone filler cement mortars, *Cem. Concr. Res.* 26 (1996) 883–893. doi:10.1016/0008-8846(96)00071-3.
- [38] A. Taфраoui, G. Escadeillas, S. Lebailly, T. Vidal, Metakaolin in the formulation of UHPC, *Constr. Build. Mater.* 23 (2009) 669–674. doi:10.1016/J.CONBUILDMAT.2008.02.018.
- [39] H. Yazıcı, H. Yiğiter, A.Ş. Karabulut, B. Baradan, Utilization of fly ash and ground granulated blast furnace slag as an alternative silica source in reactive powder concrete, *Fuel* 87 (2008) 2401–2407. doi:10.1016/J.FUEL.2008.03.005.

- [40] Z. Wu, C. Shi, W. He, Comparative study on flexural properties of ultra-high performance concrete with supplementary cementitious materials under different curing regimes, *Constr. Build. Mater.* 136 (2017) 307–313. doi:10.1016/J.CONBUILDMAT.2017.01.052.
- [41] Z. Jisong, Z. Yinghua, L. Haijiang, Experimental Investigation and Prediction of Compressive Strength of Ultra-High Performance Concrete Containing Supplementary Cementitious Materials, *Adv. Mater. Sci. Eng.* 2017 (2017) 1–8.
- [42] B.A. Gedam, N.M. Bhandari, A. Upadhyay, Influence of Supplementary Cementitious Materials on Shrinkage, Creep, and Durability of High-Performance Concrete, *J. Mater. Civ. Eng.* 28 (2016) 04015173 (1-11). doi:10.1061/(ASCE)MT.1943-5533.0001462.
- [43] R.D.D. Toledo Filho, E.A.B.A.B. Koenders, S. Formagini, E.M.R.M.R. Fairbairn, Performance assessment of Ultra High Performance Fiber Reinforced Cementitious Composites in view of sustainability, *Mater. Des.* 36 (2012) 880–888. doi:<https://doi.org/10.1016/j.matdes.2011.09.022>.
- [44] E. Denarié, Recommendations for the tailoring of UHPFRC recipes for rehabilitation, deliverable ARCHES D06, 2009. <http://arches.fehrl.org>.
- [45] E. Denarié, E. Brühwiler, Strain Hardening Ultra-high Performance Fibre Reinforced Concrete: Deformability versus Strength Optimization, *Int. J. Restaur. Build. Monum.* 17 (2011) 397–410.
- [46] E. Ghafari, S.A. Ghahari, H. Costa, E. Júlio, A. Portugal, L. Durães, Effect of supplementary cementitious materials on autogenous shrinkage of ultra-high performance concrete, *Constr. Build. Mater.* 127 (2016) 43–48. doi:10.1016/J.CONBUILDMAT.2016.09.123.
- [47] J. Liu, Z. Ou, J. Mo, Y. Wang, H. Wu, The effect of SCMs and SAP on the autogenous shrinkage and hydration process of RPC, *Constr. Build. Mater.* 155 (2017) 239–249. doi:10.1016/J.CONBUILDMAT.2017.08.061.
- [48] C. Jiang, Y. Yang, Y. Wang, Y. Zhou, C. Ma, Autogenous shrinkage of high performance concrete containing mineral admixtures under different curing temperatures, *Constr. Build. Mater.* 61 (2014) 260–269. doi:<https://doi.org/10.1016/j.conbuildmat.2014.03.023>.
- [49] Y. Lyu, H. Huang, G. Ye, G. De Schutter, Autogenous shrinkage of low water-binder ratio cement pastes with supplementary cementitious materials, in: *Fourth Int. Conf. Sustain. Constr. Mater. Technol.*, 2016: pp. 1–9.
- [50] A.M.T. Hassan, S.W. Jones, G.H. Mahmud, Experimental test methods to determine the uniaxial tensile and compressive behaviour of ultra high performance fibre reinforced concrete (UHPFRC), *Constr. Build. Mater.* 37 (2012) 874–882. doi:10.1016/J.CONBUILDMAT.2012.04.030.

- [51] P. Rossi, A. Arca, E. Parant, P. Fakhri, Bending and compressive behaviours of a new cement composite, *Cem. Concr. Res.* 35 (2005) 27–33. doi:10.1016/J.CEMCONRES.2004.05.043.
- [52] E. Denarié, K. Habel, J. Wuest, SAMARIS deliverable D13, Report on preliminary studies for the use of HPFRCC for the rehabilitation of road infrastructure components, 2004. <http://samaris.zag.si>.
- [53] S.A.A.M. Fennis, J.C. Walraven, J.A. den Uijl, Compaction-interaction packing model: regarding the effect of fillers in concrete mixture design, *Mater. Struct.* 46 (2013) 463–478. doi:10.1617/s11527-012-9910-6.
- [54] A. Hajiesmaeili, E. Denarié, Next Generation UHPFRC for Sustainable Structural Applications, *Am. Concr. Inst.* 326 (2018) 58.1-58.10.
- [55] M.A. Hafiz, E. Denarié, Experimental Study of Tensile Response of Strain Hardening UHPFRC at Early Age, in: *Strain-Hardening Cem. Compos.*, Springer, Dresden, Germany, 2018: pp. 308–315.
- [56] M.A. Hafiz, E. Denarié, Tensile viscous response of Strain Hardening UHPFRC under high restraint and isothermal conditions, in: *Euro C - 2018 Comput. Model. Concr. Struct.*, 2018: pp. 903–912.
- [57] Standard Test Method for Flow of Hydraulic Cement Mortar BT - Standard Test Method for Flow of Hydraulic Cement Mortar, (15AD).
- [58] SIA (2017), *Cahier Technique 2052, Béton fibré ultra-performant (BFUP): Matériaux, dimensionnement et exécution*, SIA, Zürich., (2017).
- [59] G. Guignet, H. Kazemi-Kamyab, E. Denarié, Internal communication, August 2014, EPFL, Switzerland, (2014) .
- [60] S. Kolluru, J. Popovics, S.P. Shah, Determining Elastic Properties of Concrete Using Vibrational Resonance Frequencies of Standard Test Cylinders, *Cem. Concr. Aggregates.* 22 (2000) 81.
- [61] L. Wadsö, Operational issues in isothermal calorimetry, *Cem. Concr. Res.* 40 (2010) 1129–1137. doi:<https://doi.org/10.1016/j.cemconres.2010.03.017>.
- [62] K. Scrivener, R. Snellings, B. Lothenbach, *A practical guide to microstructural analysis of cementitious materials*, Crc Press, 2018.
- [63] O. Bjontegaard, Thermal dilatation and autogenous deformation as driving forces to self-induced stresses in high performance concrete, Doctoral thesis, The University of Trondheim, Norway, 1999.
- [64] K. Kovler, Testing system for determining the mechanical behaviour of early age concrete under restrained and free uniaxial shrinkage, *Mater. Struct.* 27 (1994) 324–330.

- [65] J.P. Charron, Contribution à l'étude du comportement au jeune âge des matériaux cimentaires en conditions de déformations libre et restreinte, Doctoral thesis, University of Laval, Québec, Canada, 2003.
- [66] M. Bouasker, N.E.H. Khalifa, P. Mounanga, N. Ben Kahla, Early-age deformation and autogenous cracking risk of slag–limestone filler-cement blended binders, *Constr. Build. Mater.* 55 (2014) 158–167.
- [67] I. Mehdipour, K.H. Khayat, Elucidating the Role of Supplementary Cementitious Materials on Shrinkage and Restrained-Shrinkage Cracking of Flowable Eco-Concrete, *J. Mater. Civ. Eng. ASCE*. 30 (2018).
- [68] A.M. Paillere, M. Buil, J.J. Serrano, Effect of Fiber Addition on the Autogenous Shrinkage of Silica Fume, *Mater. J.* 86 (1989). doi:10.14359/2295.
- [69] P. Mounanga, M.I.A. Khokhar, R. El Hachem, A. Loukili, Improvement of the early-age reactivity of fly ash and blast furnace slag cementitious systems using limestone filler, *Mater. Struct.* 44 (2011) 437–453.
- [70] Y. Ballim, P.C. Graham, The effects of supplementary cementing materials in modifying the heat of hydration of concrete, *Mater. Struct.* 42 (2009) 803–811.
- [71] W. Huang, H. Kazemi-Kamyab, W. Sun, K. Scrivener, Effect of cement substitution by limestone on the hydration and microstructural development of ultra-high performance concrete (UHPC), *Cem. Concr. Compos.* 77 (2017) 86–101.
- [72] P. Acker, Micromechanical analysis of creep and shrinkage mechanisms, in: *Cocreep-6 Creep, Shrinkage Durab. Mech. Concr. Other Quasi-Brittle Mater.*, 2001: pp. 15–25.
- [73] P. Acker, Why Does Ultrahigh-Performance Concrete (UHPC) Exhibit Such Low Shrinkage and Such Low Creep?, *Spec. Publ.* (2004) 141–154.
- [74] C. Hua, P. Acker, A. Ehrlacher, Analyses and models of the autogenous shrinkage of hardening cement paste: I. Modelling at macroscopic scale, *Cem. Concr. Res.* 25 (1995) 1457–1468.
- [75] A. Bentur, K. Kovler, Evaluation of early age cracking characteristics in cementitious systems, *Mater. Struct.* 36 (2003) 183–190.
- [76] J.P. Charron, J. Marchand, M. Pigeon, B. Bissonnette, Test Device for Studying the Early-Age Stresses and Strains in Concrete, *Spec. Publ.* 220 (2004) 113–124. doi:10.14359/13153.

Chapter – 3

Paper 2

Tensile response of UHPFRC under very low strain rates and low temperatures

Reference: M.A. Hafiz¹, E. Denarié², Tensile response of UHPFRC under very low strain rates and low temperatures, *submitted to Cement and Concrete Research, April 2019.*

1 – corresponding author of the paper – conducted all the experiments presented in the paper along with the writing of the full article

2 – thesis supervisor

Abstract

This paper addresses the uniaxial tensile response of Strain-Hardening Ultra High-Performance Fiber Reinforced Concretes (SH-UHPFRC) subjected to very low strain rates and moderate to low temperatures. The influence of four different strain rates; 1×10^{-5} , 1×10^{-7} , 1×10^{-8} and 5×10^{-9} 1/s on the tensile properties like elastic limit, elastic modulus, tensile strength, strain at tensile strength and hardening modulus, was studied for two types of SH-UHPFRC mixes; Mix I with type I cement and silica fume, and Mix II with silica fume and 50% mass replacement of type I cement with limestone filler, at three curing temperatures; 20 °C, 10 °C and 5 °C. The tests at strain rates lesser than 1×10^{-6} 1/s are the first of their kind for UHPFRC materials and the results show a considerable impact on the elastic limit of the mixes. Acoustic Emission tests were also carried out for validation of test results of the elastic limit.

Keywords: SH-UHPFRC, tensile response, very low strain rates, temperature, SCM, viscosity, elastic limit, Acoustic Emission.

1 Introduction

Ultra High-Performance Fiber Reinforced Concretes (UHPFRC) are special types of cementitious materials reinforced with short discontinuous steel fibers, which exhibit a high tensile strength (over 12 MPa) and a significant strain-hardening (1-5 ‰) for the best mixes, depending on the different fiber orientation situations encountered in practice. They also have a very low permeability and outstanding durability, making them very good materials for rehabilitation or reinforcement applications (combined with rebars), for the improvement of load carrying capacity and protective functions of existing structures [1].

This paper addresses the strain rate sensitivity of the tensile mechanical properties of UHPFRC and the associated literature. It is well known that the tensile properties like the elastic limit, f_{Ute} (also often referred to as first cracking stress, pre-cracking strength), strain at the elastic limit ϵ_{Ute} , elastic modulus E_{mod} , tensile strength f_{Utu} , the strain at the tensile strength ϵ_{Utu} and the hardening modulus E_{har} are all sensitive to the rate of application of load. In literature, the effect of strain rates is usually described using the Dynamic Increase Factor (DIF), which is the ratio of value of the property of the material at a dynamic strain rate with respect to that at a quasi-static strain rate. The CEB model code [2] recommends a reference quasi-static strain rate of $3 \times 10^{-6} \text{ s}^{-1}$ for the calculation of the DIF.

A schematic diagram showing the tensile response of SH-UHPFRC is shown in figure 1, which can be divided into three main domains;

1. Elastic domain: the region from the beginning until the elastic limit.
2. Hardening domain: the region from the elastic limit until the tensile strength.
3. Softening domain: the region from the tensile strength until full separation of the specimen.

The focus of the present study was on the elastic and hardening domains and the effect of very low strain rates on the mechanical properties in these domains were investigated. In the elastic region, the elastic limit (f_{Ute}) as well as the elastic modulus in tension (E_{mod}) were studied whereas in the hardening domain, the tensile strength (f_{Utu}), the strain at tensile strength (ϵ_{Utu}) and the hardening modulus (E_{har}) were investigated. The f_{Ute} is the stress level until which the tensile stresses are proportional to the strains, with the corresponding strain given by ϵ_{Ute} . The slope of the stress strain curve in the elastic domain is given by the elastic modulus E_{mod} . The f_{Utu} and ϵ_{Utu} correspond to the coordinates of the peak stress in the tensile response. In this paper, E_{har} is defined as the slope of the line joining the stress-strain coordinate corresponding to a strain level of 0.4‰ and that corresponding to the peak stress, as shown in figure 1.

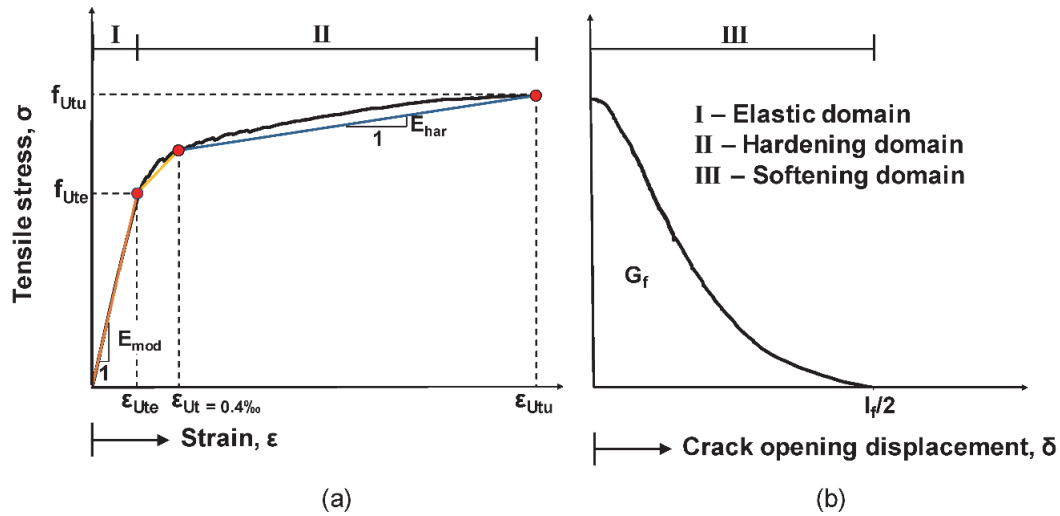


Figure 1: Schematic tensile response of SH-UHPFRC, a) elasto-hardening response, b) softening response including the effect of unloading at tensile strength.

The kinetics of various mechanisms influence the tensile response of UHPFRC as shown in figure 2, which include ageing of the material (hydration of binders), early age volume changes like autogenous shrinkage, drying shrinkage and thermal deformations, viscoelastic phenomena like creep and relaxation, and damage phenomena including microcrack onset and growth.

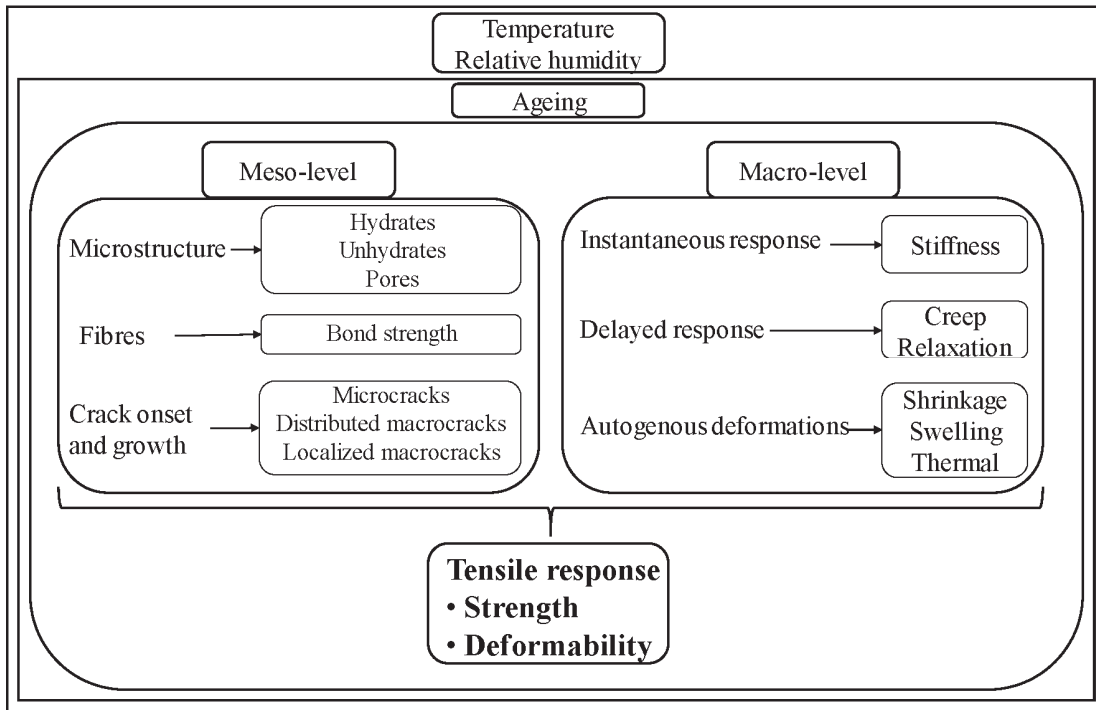


Figure 2: Evolutionary mechanisms affecting the tensile response of UHPFRC.

There is a complex interaction of these phenomena especially under very low strain rates making it challenging to separate the contributions of the individual mechanisms. The phenomenon of ageing is prevalent mainly in the younger material (up to 3-5 days after addition of water), whereas in the long term, the influence of viscoelasticity and damage become dominant. These two phenomena, which produce similar effects (increased deformations and loss of stiffness), interact with each other depending on the stress level. On the one hand, for low strain rate, viscoelasticity plays an important role in the development of microcracks and crack propagation; whereas on the other hand, at high stress levels, the presence of microcracks lead to the development of non-linear viscoelasticity.

Rusch [3] was the first to highlight the effect of time dependent phenomenon on the strength of concrete under compression (static fatigue). Similar effects were shown for concrete under bending and tension by [4–7]. Many authors have shown the effect of monotonic strain rate on the tensile properties of normal concrete, both at high strain rates (1 s^{-1} to 200 s^{-1}) [8–11] and at low strain rates ($1 \times 10^{-7} \text{ s}^{-1}$ to 1 s^{-1}) [12–15]. All the studies showed that the tensile strength of normal concrete increases with an increase in the applied strain rate. [16] showed that direct tensile tests on concrete done by [17] at a strain rate of $3 \times 10^{-7} \text{ s}^{-1}$ showed a significant decrease in the tensile strength when compared to the quasi static strain rate of $3 \times 10^{-6} \text{ s}^{-1}$ as recommended by the CEB model code formulation for concrete in tension [2]. Similar trends were also shown for concrete in compression by [18] for very low monotonic strain rates less than $1 \times 10^{-6} \text{ s}^{-1}$.

Recent studies suggest that the DIF for UHPFRC differ from that of normal concrete [19]. Because of the very high strength and specific fracture energy of these materials, they are very suitable to resist impact loading caused by explosions, vehicle crashes and falling rocks [20]. As such, majority of the studies on the effect of strain rate on the tensile mechanical properties of UHPFRC are concentrated to the dynamic domain ($1 \times 10^{-4} \text{ s}^{-1}$ to $1 \times 10^2 \text{ s}^{-1}$) [20–36]. All of these works discuss the strain rate effect using the direct tension test except [21,30] who had conducted flexural bending tests and [27–29] who had used splitting tension tests to study the strain rate effects in the dynamic domain.

The main fields of application of SH-UHPFRC are the design of new structures and rehabilitation works, for the improvement of load carrying capacity and protective functions of existing structures. In the latter case, when a new layer of UHPFRC is applied on an existing structure, it is subjected to early age volume deformations such as autogenous shrinkage, thermal deformations and drying shrinkage in certain situations. These deformations are restrained to different extents, depending on the relative stiffness of the new layer and the existing substrate and depending on the boundary conditions of the support, leading to the development of tensile eigenstresses in the material. Furthermore, these restrained deformations take place at very low strain rates ($1 \times 10^{-8} \text{ 1/s}$ – $1 \times 10^{-11} \text{ 1/s}$). It is therefore essential to investigate the tensile response of UHPFRC materials at these very low strain rates. To the best of authors' knowledge, the smallest tensile strain rate that was studied for UHPFRC was $1 \times 10^{-6} \text{ s}^{-1}$ [20], and no works have been done until now to understand the effect of very low strain rates ($< 1 \times 10^{-6} \text{ s}^{-1}$) on the tensile behavior of UHPFRC.

At very low strain rates, the couplings between hydration, creep and damage become more dominant. Bazant et al. [37,38] showed the influence of ageing and hydration on the creep phenomenon. Rossi et al. [39] showed that the basic creep of concrete is highly correlated to the acoustic emission and propagation of microcracks, indicating that microcracks play a major role in the creep of concrete at high stress levels. The influence of stress level and microcracking on the relaxation response of concrete was also studied in [5,40,41], which showed a higher relaxation response along the failure envelope (non-linear) when compared to that at lower stress levels, confirming the interaction of damage and non-linear viscoelasticity at higher stress levels. More recently, for UHPFRC, [42–44] studied the interaction of ageing, early age volume changes, stress level and loading history. [45] showed that at an age of 46 hours (13 hours after setting), UHPFRC exhibited non-linear creep under a stress level of 30% whereas at an age of 72 hours (39 hours after setting) it exhibited linear creep at a stress level of 32%. Using incremental relaxation tests in a TSTM, [42] showed that at high stress levels of 60% and 90%, higher relative relaxations were observed indicating a non-linear viscoelastic response.

Furthermore, temperature influences the kinetics of hydration, ageing and viscoelastic behavior. There is a complex interaction between the effect of temperature on the ageing and creep response of cementitious materials. On the one hand, a higher temperature leads to a higher creep response; whereas on the other hand, a higher curing temperature would lead to a higher apparent age (maturity) of the material and consequently a lower creep response [46]. The effect of thermal curing and temperature on the development of autogenous shrinkage and creep deformations were shown in [47–52], while the effect of the same on the mechanical properties were shown in [45,51,53–55]. However, contrary to prefabrication, for cast on site applications of UHPFRC, the local climatological conditions govern. In addition, in winter conditions, the cast on site UHPFRC layers will be subjected to very low temperatures. It is very well known that at low temperatures, the development of hydration is much slower than at ordinary temperatures, and only a few works have been carried out to study the influence of low curing temperatures on the development of hydration and autogenous shrinkage in UHPFRC [44,46]. Therefore, fundamental knowledge regarding the tensile behavior of UHPFRC subjected to low curing temperatures is needed for their successful applications for repair and rehabilitation.

Finally, increasing focus is now being given to the use of Supplementary Cementitious Materials (SCM) in UHPFRC mixes in view of sustainability, to reduce the environmental impact of cement production. Because of the very low water/cement ratio in UHPFRC mixes with pure cement, a significant portion of the cement remain unhydrated and it could advantageously be replaced by inert fillers like limestone filler, fly ash etc [46,53,56]. Depending on the water/cement ratio, many studies have shown that the degree of hydration of cement in UHPFRC mixes with pure cement is as low as 30% after 28 days [44,46,51]. The unhydrated cement and silica fume simply act as fillers (physical effect), and improve the compactness of the matrix at the micro level and thereby lead to the increase of the mechanical properties at the macro level. However, from a sustainability point of view, cement is a very costly material to be used as a filler; not only in terms of monetary cost but also in terms of the environmental impact.

Cement industry accounts for around 5% of the global carbon dioxide (CO₂) emissions. The CO₂ emission is directly proportional to the cement content in the concrete mix; 900 kg of CO₂ are emitted during the manufacture of every ton of cement [57,58]. As such, lesser the cement content in the UHPFRC, lesser will be the impact on the environment. However, not many works have been carried out to investigate the tensile behavior of these type of low clinker UHPFRC mixes, especially under very low strain rates.

In this paper, the effect of very low strains on the tensile response of two types of UHPFRC was investigated; Mix I with pure type I cement, silica fume and steel fibers and Mix II with 50% replacement of cement with limestone filler and a similar steel fibrous mix. Uniaxial direct tensile tests were conducted at four different strain rates; $1 \times 10^{-5} \text{ s}^{-1}$, $1 \times 10^{-7} \text{ s}^{-1}$, $1 \times 10^{-8} \text{ s}^{-1}$ and $5 \times 10^{-9} \text{ s}^{-1}$, and at three different curing temperatures; 20 °C, 10 °C and 5 °C.

2 Experimental

2.1 Material

Two types of SH-UHPFRC mixes were studied in this paper, both from the CEMTEC_{multiscale}® family. The CEMTEC_{multiscale}® mixes were initially developed at Laboratoire Central des Ponts et Chaussées (LCPC), France [59]. This material was optimized and modified in the framework of the research works held in MCS/EPFL for rehabilitation and strengthening of existing structures [60,61] to produce Mix I, which is a SH-UHPFRC of type CM22_TKK_b. The ultra compact cementitious matrix is composed of cement (type CEM I 52.5 HTS from Le Teil, Lafarge), white microsilica (SEPR, BET = 14 m²/gr), superplasticizer (Zementol Zeta Super S from TKK, Slovenia) and water. The material has a very high content of paste to accommodate all the fibers and therefore exhibits excellent rheological properties in the fresh state even though the water/binder ratio is very low, 0.129.

Because of the very low degree of hydration of Mix I (30% after 28 days [62], 50% of the cement in Mix I could be replaced by two types of inert limestone fillers; Betoflow D® and Betocarb SL® (OMYA). Using the concepts of packing density optimization, the composition of the different components like the cement, limestone fillers and the silica fume was designed. The new mix, CM22_TKK_b_LF, will be designated as Mix II from here on in the paper. More details on the mix design of the Mix II could be found in Chapter 2 [62].

Both mixes had a fibrous mix containing two types of steel fibers; microfibers and macrofibers, with a total dosage of 9% by volume. The microfibers (steel wool, from Gervois, France) had a semi-circular section with an average diameter of 0.04 mm and a length of 2-3 mm, and an irregular aspect ratio allowing a high adhesion with a cementitious matrix. The macrofibers were straight, with $l_f = 10 \text{ mm}$, $d_f = 0.2 \text{ mm}$, from Bekaert, Belgium.

The materials exhibit a significant strain-hardening behavior under tension (1-2 %) [63,64]. The detailed compositions of Mix I and II are given in Table 1 and the properties in the fresh state are given in Table 2. More details regarding the properties of the mixes in the hardened state, as well as the chemical compositions of the powders in the mixes could be found in Chapter 2 [62].

Table 1: Compositions of Mix I and II.

Material	Mix I	Mix II
	[kg/m ³]	[kg/m ³]
Cement, CEM I 52.5 le Teil	1467.0	733.7
Silica fume, SEPR	381.4	293.5
Limestone filler 1 (Betocarb SL [®])	--	223.0
Limestone filler 2 (Betoflow D [®])	--	510.6
Steel fibers (straight macro fibers; l _f = 10 mm, d _f = 0.2 mm and microfibers/steel wool)	706.5	706.5
Total water	225.8	217.9
Superplasticizer from TKK, Slovenia; Zementol zeta super S; polycarboxylate; 25% solid content; (total amount)	20.5	14.7

Table 2: Properties of Mix I and II in the fresh state (average value from 4 tests).

Property	Units	Mix I	Mix II
Workability (ASTM - spread after 25 blows)	mm	179	146
Specific weight	kg/m ³	2834	2695
Air content	%	3.2	4.7

2.2 Uniaxial tensile test

The uniaxial tensile test is a difficult test to perform for cementitious materials, both with and without fibers. However, the results obtained from the test give a direct and reliable estimate of the tensile mechanical properties and do not need any complex inverse analyses to obtain the same, as is the case with flexural tests. One of the main difficulties in performing the tensile test is the misalignment of the specimen in the test setup and the eccentricity that arises from it. Even if the alignment is perfect before the test, because of the micro and macro crack formations during the test, the eccentricities may arise again.

In the present experimental campaign, the eccentricity was constantly monitored with the help of four LVDTs in two perpendicular planes as shown in figure 3. Special care was taken to see that the specimens were aligned in such a way that the bending stress due to possible eccentricity was less than 0.6 MPa, at least in the elastic domain of the tensile response.

Another major difficulty is the controlling of the gauge length. For strain controlled tests, if the fracture process zone occurs outside of the gauge length, it may not be possible to control the test anymore. This was minimized by selecting a gauge length of 385 mm, which even included the transition zone in the specimen, where there is a higher probability for crack formation.

The boundary conditions of the test setup also play an important role in performing the tests. [65] has shown that fixed boundary conditions are less favorable for slight eccentricities compared to pinned end conditions, but lead to the only reliable estimation of the tensile response after the onset of cracking. As such, fixed boundary conditions were used for the tests in the present study.

2.3 Specimen shape and preparation

Specimens with dumbbell geometry were used for the study, the transition zone of which was designed using the Neuber's solution [66], which helped to minimize the stress concentrations around the necking. The geometry of the dumbbell specimen is shown in figure 3. The cross section in the middle straight portion of the specimen was 30mm x 50mm. Four LVDTs were placed on the specimen, with LVDT A and B in the XY plane and LVDT C and D in the XZ plane.

After the preparation of the UHPFRC mix, special attention was taken to cast the different specimens in a way as similar as possible from one specimen to the next, in order to avoid the scatter in the tensile responses due to the scatter in the fiber orientations between the individual specimens. The UHPFRC was guided into the molds with a half pipe, from one end and was slowly moved to the other end, so that the fibers follow the direction of flow of the mix and align themselves in the molds. Deformable tape was applied on the molds in the transition zones, to prevent the buildup of eigenstresses due to restrained shrinkage before demolding.

Directly after casting, the specimens were kept in a climate chamber set at the required temperature of 20 °C, 10 °C or 5 °C. They were demolded two days later, but were continuously cured at the respective temperatures. Four circular aluminum discs of 100 mm diameter and 1.5 mm thickness were glued on the ends of the specimens for proper transfer of the loads through the grips. A system was developed to keep the circular plates on either side of the specimen parallel to each other and to have the same thickness of glue between the four different circular plates and the specimen, thereby removing one possible cause for eccentricity while loading. The specimen was coated with a layer of paraffin wax to prevent drying shrinkage while curing.

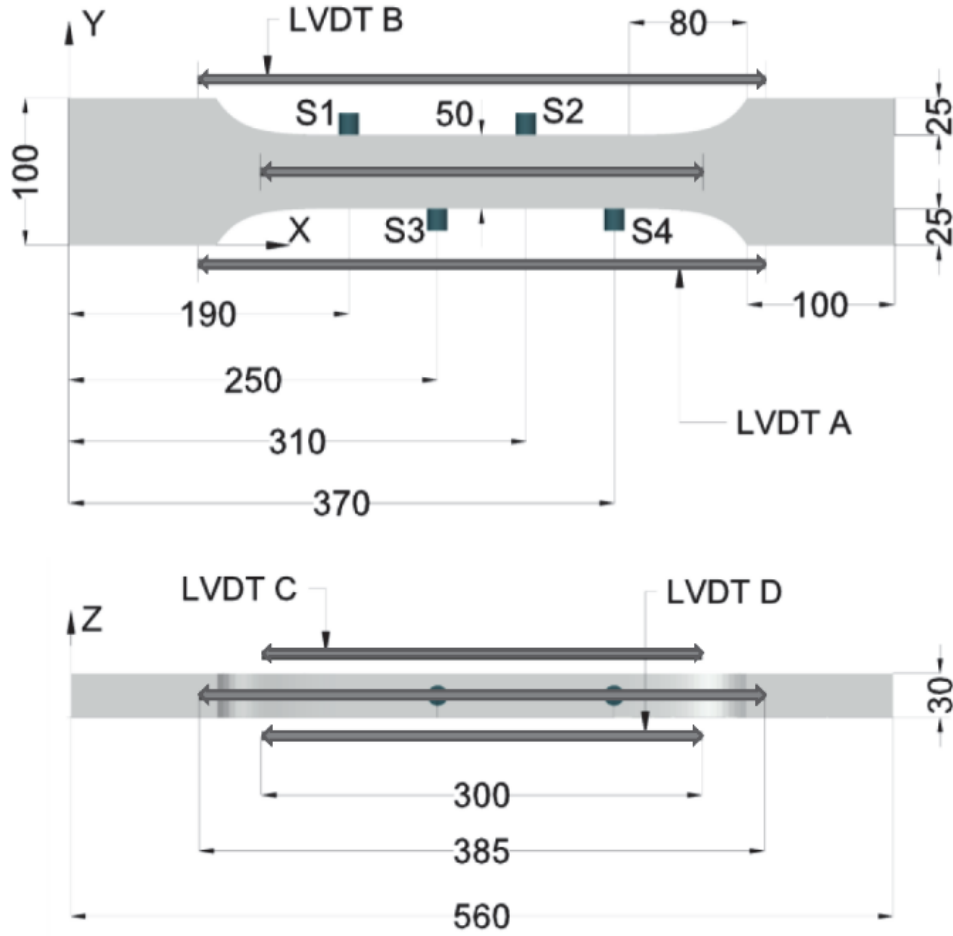


Figure 3: Geometry of the dumbbell specimens, along with the positions of the LVDTs and the Acoustic Emission sensors S1, S2, S3 and S4 (all measurements are in mm).

2.4 Test setup and loading

The tests were carried out in an electromechanical testing machine, KAPPA 250 DS from ZWICK/ROELL with a capacity of 250 kN, with the test setup shown in figure 4. The testing machine was specially designed to carry out controlled tests at very low strain rates, as low as $1 \times 10^{-9} \text{ s}^{-1}$. The boundary conditions were fixed at both ends of the specimen, without hinges before the grips. A cooling chamber was also attached along with the test setup to test the specimens under different curing temperatures; 20 °C, 10 °C and 5 °C. The tests were carried out at four different strain rates; $1 \times 10^{-5} \text{ s}^{-1}$ (quasi static strain rate), $1 \times 10^{-7} \text{ s}^{-1}$ (low strain rate), $1 \times 10^{-8} \text{ s}^{-1}$ and $5 \times 10^{-9} \text{ s}^{-1}$ (very low strain rates) for the two types of UHPFRC mixes; Mix I and Mix II, at an age of 14 days. The average of the displacements of LVDTs A and B was used to control the test and the strain rates were calculated using a gauge length of 385 mm.

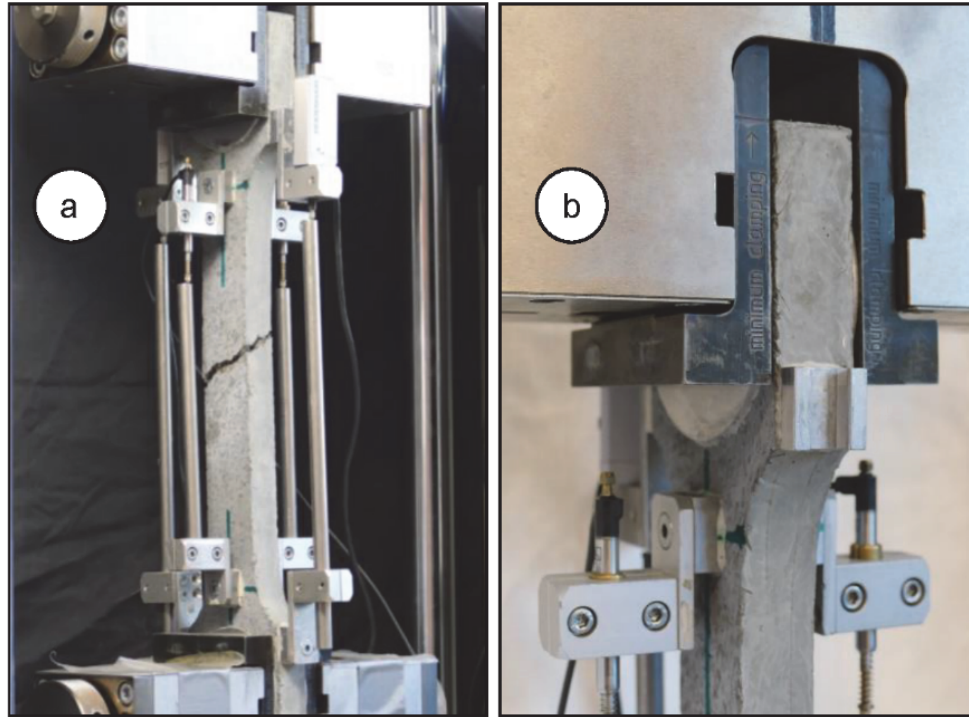


Figure 4: a) Electromechanical KAPPA 250 DS test setup from ZWICK/ROELL with the dumbbell specimen for uniaxial tensile test, b) grips for fixed boundary conditions.

2.5 Acoustic emission tests

An AMSY-6 acoustic emission system from Vallen Systeme was used for detecting the acoustic emission events. Preliminary tests were done on an aluminum plate of the same geometry as that of the dumbbell specimens, for finding out the threshold of noise for the AE events, which were coming from the environment inside the lab as well as from the testing machine. After these tests, a threshold of 40dB was set in the system as the noise threshold. The software VisualAE was used for the analysis of the obtained data and for the localization of the acoustic events in the specimen. The position of the sensors on the specimen is shown in figure 3.

3 Results and Discussions

3.1 Overview of the tests

Table 3 shows the overview of the uniaxial tensile tests that were conducted under different configurations, with 90 tests in total.

Table 3: Overview of the uniaxial tensile tests.

UHPFRC Mix	Curing temperature (°C)	Name of the series	Strain rate (s ⁻¹)	Number of specimens tested
Mix I	20	M1 – 20C	1x10 ⁻⁵	8
			1x10 ⁻⁷	8
			1x10 ⁻⁸	7
	5	M1 – 5C	1x10 ⁻⁵	5
			1x10 ⁻⁷	5
			5x10 ⁻⁹	5
	20	M2 – 20C	1x10 ⁻⁵	13
			1x10 ⁻⁷	6
			1x10 ⁻⁸	3
			5x10 ⁻⁹	3
			1x10 ⁻⁵	4
			1x10 ⁻⁷	4
Mix II	10	M2 – 10C	5x10 ⁻⁹	4
			1x10 ⁻⁵	4
			1x10 ⁻⁷	5
	5	M2 – 5C	5x10 ⁻⁹	6
			1x10 ⁻⁵	4

Figure 5 shows the stress-displacement (average of LVDT A and B) curves from all the tests under different configurations. The effect of the very low strain rates, moderate to low temperatures and mix type on the relevant mechanical properties will be discussed in detail in the coming sections.

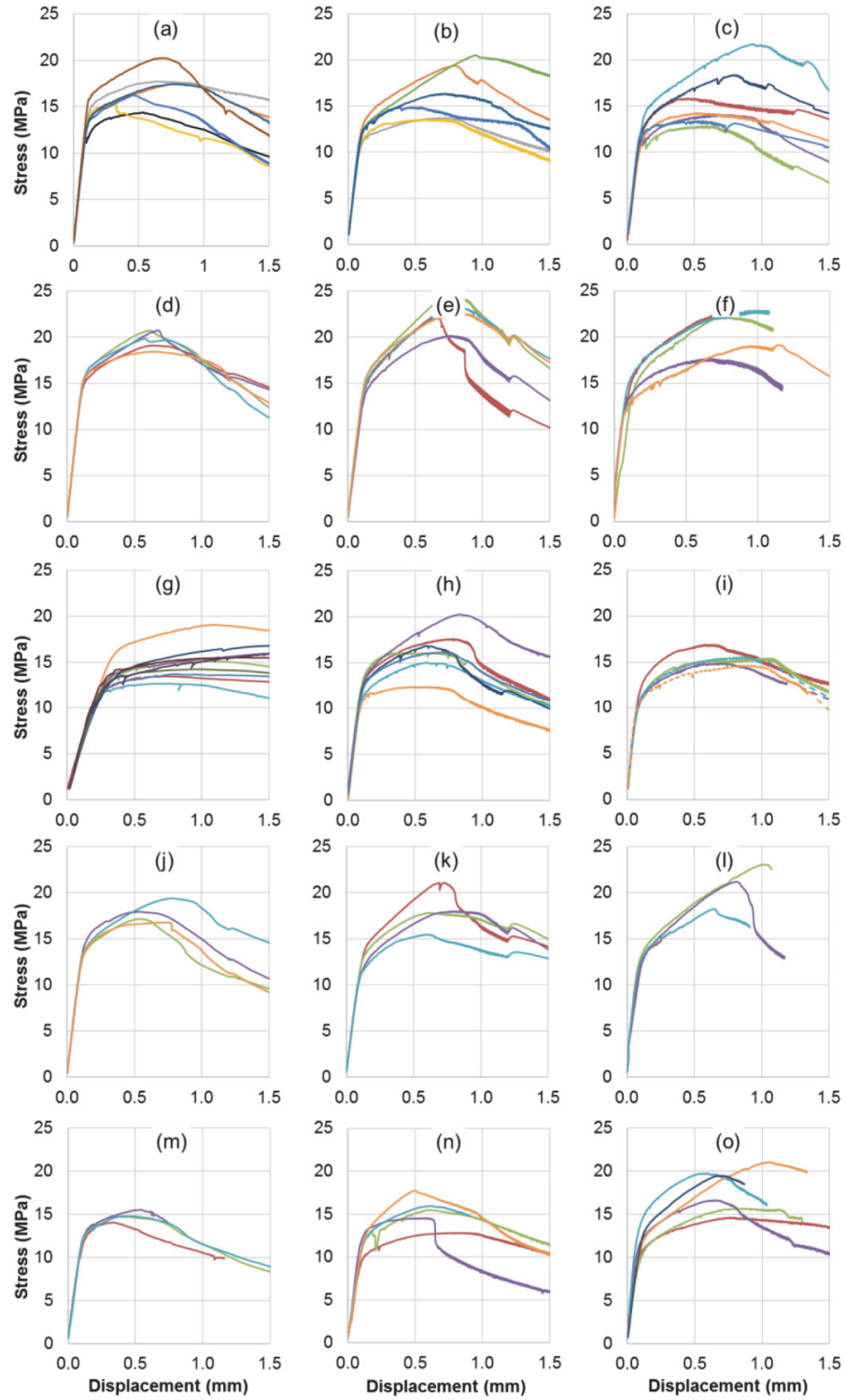


Figure 5: Stress displacement curves for; a) M1-20C at 1×10^{-5} 1/s, b) M1-20C at 1×10^{-7} 1/s, c) M1-20C at 1×10^{-8} 1/s, d) M1-5C at 1×10^{-5} 1/s, e) M1-5C at 1×10^{-7} 1/s, f) M1-5C at 5×10^{-9} 1/s, g) M2-20C at 1×10^{-5} 1/s, h) M2-20C at 1×10^{-7} 1/s, i) M2-20C at 1×10^{-8} 1/s (dashed lines) and M2-20C at 5×10^{-9} 1/s (solid lines), j) M2-10C at 1×10^{-5} 1/s, k) M2-10C at 1×10^{-7} 1/s, l) M2-10C at 5×10^{-9} 1/s, m) M2-5C at 1×10^{-5} 1/s, n) M2-5C at 1×10^{-7} 1/s and o) M2-5C at 5×10^{-9} 1/s.

3.2 Effect of very low strain rates

3.2.1 Elastic limit

The elastic limit or the first cracking strength, f_{Ute} corresponds to the transition from the elastic behavior to the strain-hardening behavior. It roughly corresponds to the strength of the matrix, even though some authors have shown that the fiber geometry or the fiber volume would affect the same [32,67]. For normal concrete without fibers, the elastic limit can be considered as the same as the tensile strength. For strain-hardening cementitious materials, the accurate determination of the elastic limit is a very challenging problem. Different authors discuss different methods for obtaining the elastic limit of UHPFRC materials. In the present paper, the inverse analysis procedure described in SIA 2052 standard for UHPFRC [68,69] was followed for the determination of the elastic limit.

The procedure is graphically explained in figure 6 for a specimen MixI-SR12-S1 at a strain rate of 1×10^{-5} 1/s at 20 °C. From point 1 very close to the beginning on the stress-strain curve, the secant modulus of elasticity at point 2 corresponding to a stress level of 2 MPa was calculated. The calculated secant modulus is shown as point 3 in the figure 6. The secant modulus from the same point 1, along the stress-strain curve was then followed until there is a 10% drop from the same at point 2, and the corresponding point is marked as point 4. The stress level on the stress-strain curve corresponding to the point 4 is chosen as the elastic limit of the material [69].

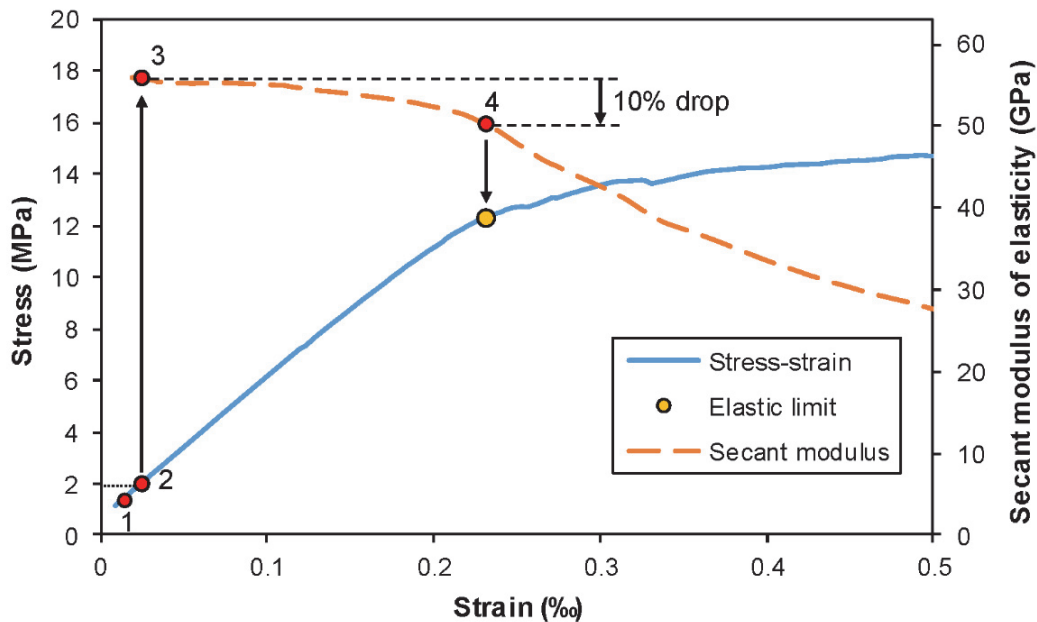


Figure 6: graphical representation of the procedure for determining the elastic limit using the inverse analysis method (specimen MixI-SR12-S1, strain rate 1×10^{-5} 1/s at 20 °C).

Figure 7 shows the average elastic limit calculated using the above procedure, for all the tests, along with the value of one standard deviation. Figure 7 clearly show that the elastic limit for both mixes decrease with the decrease in the strain rate. The trend is similar to what has been reported by many authors for quasi static to dynamic domain for concrete [8–11,13,14,17,70], for UHPFRC [20,32,35,36] and for similar materials like HPFRCC [71] and HSHDC [33]. In the present study, at the respective very low strain rates, the drop in the elastic limit from that at quasi-static strain rate was found to be 22%, 19%, 28%, 22% and 22% respectively for M1–20C, M1–5C, M2–20C, M2–10C and M2–5C. It can be clearly seen that the drop is significant, with its value being consistent between 19%-28%.

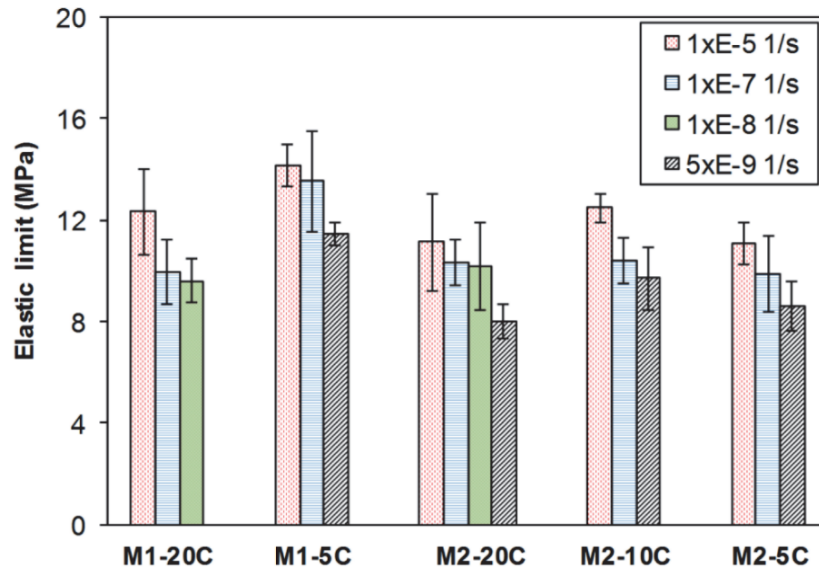


Figure 7: Effect of strain rate on the elastic limit of Mix I and II.

3.2.2 Elastic limit detection using Acoustic Emission measurements

One of the main aims of the acoustic emission technique in this study was to validate the procedure adopted for finding the elastic limit. Figure 8a shows the cumulative AE events in a specimen Mix I-20C-SR13-S1 loaded at a strain rate of $1 \times 10^{-5} \text{ s}^{-1}$ and figure 8b shows the same in a specimen Mix I-20C-SR13-S2 loaded at a strain rate of $1 \times 10^{-7} \text{ s}^{-1}$. In both figures, corresponding to the elastic limit which has been determined using the procedure described in section 3.2.1 [68,69], there is a sudden change in the rate of development of AE events. This clearly indicates that an objective threshold has been reached that can be characterized as elastic limit, and that microcracking is occurring at a faster rate from this point.

However, it should be noted that there are some acoustic events even before this point, thereby indicating that slight microcracking may occur even before the elastic limit.

However, these microcracks were rather isolated as shown in figure 9 and therefore the specimen can still be considered to behave as an elastic material. Another important observation is that the AE events started appearing at a stress level of about 74% of the elastic limit in the specimen loaded at a strain rate of $1 \times 10^{-5} \text{ s}^{-1}$ whereas it appeared at a stress level of about 69% of the elastic limit for a strain rate of $1 \times 10^{-7} \text{ s}^{-1}$.

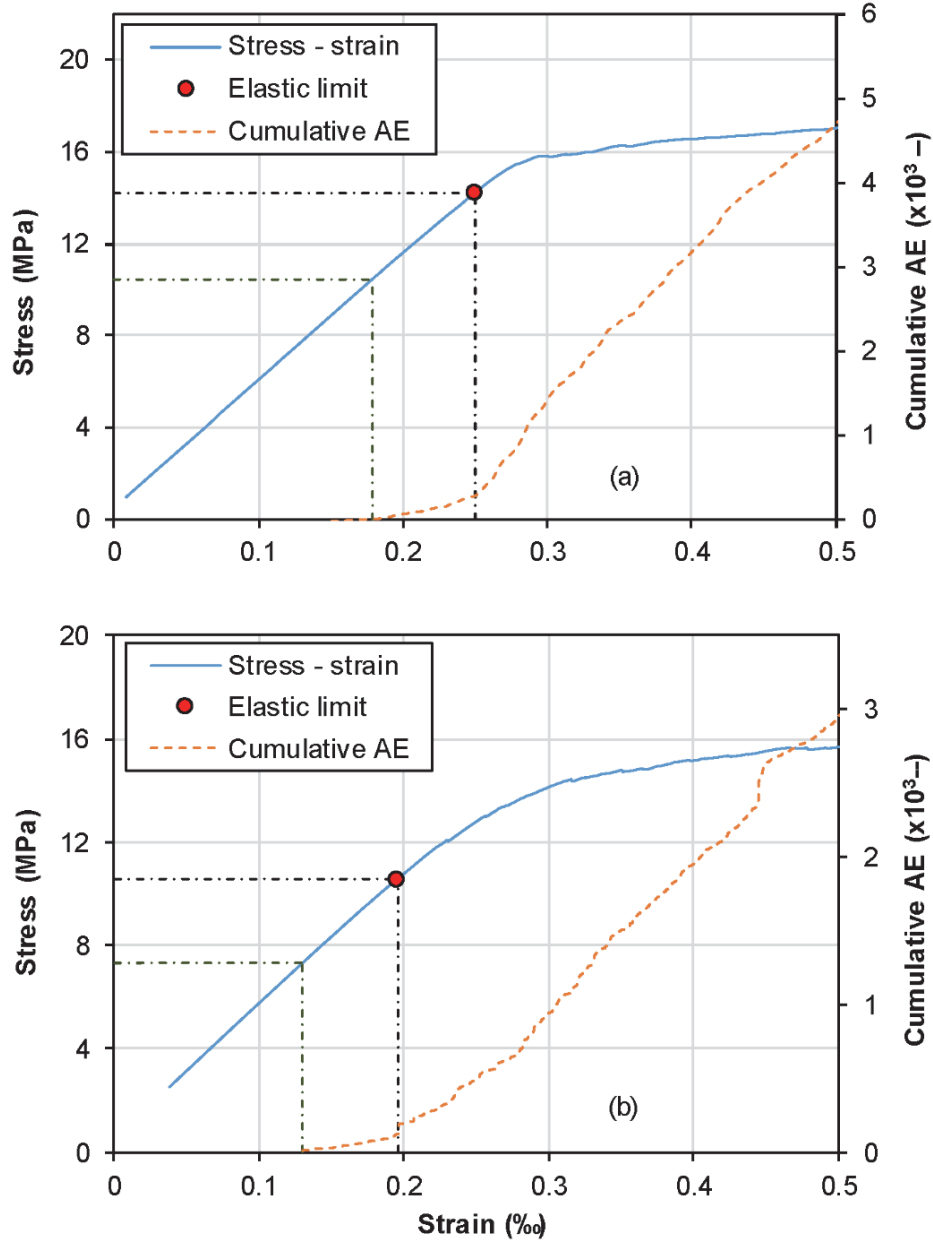


Figure 8: Determination of the elastic limit using the 10% secant modulus drop method, along with the development of cumulative Acoustic Emission events at 20°C, for a) specimen Mix I-20C-SR13-S1, strain rate of $1 \times 10^{-5} \text{ s}^{-1}$, and b) specimen Mix I-20C-SR13-S2, strain rate of $1 \times 10^{-5} \text{ s}^{-1}$.

Figure 9 shows the development of the acoustic events in the tensile test of dumbbell specimen Mix I-20C-SR15-S1. Using the procedure described in section 3.2.1, the elastic limit was found out and is marked as point 3, while the tensile strength is shown by the point 6. The localization of the acoustic events at six different stress levels in the tensile response of the UHPFRC is shown and it can be seen that at point 2 just before the elastic limit, the acoustic events are very negligible and isolated. However, after the elastic limit at point 4, there is a sudden increase in the AE activity, therefore indicating the progression of damage at a much faster rate. Figure 9 also shows a uniform distribution of the acoustic events throughout the gauge length of the specimen, before crack localization at the tensile strength.

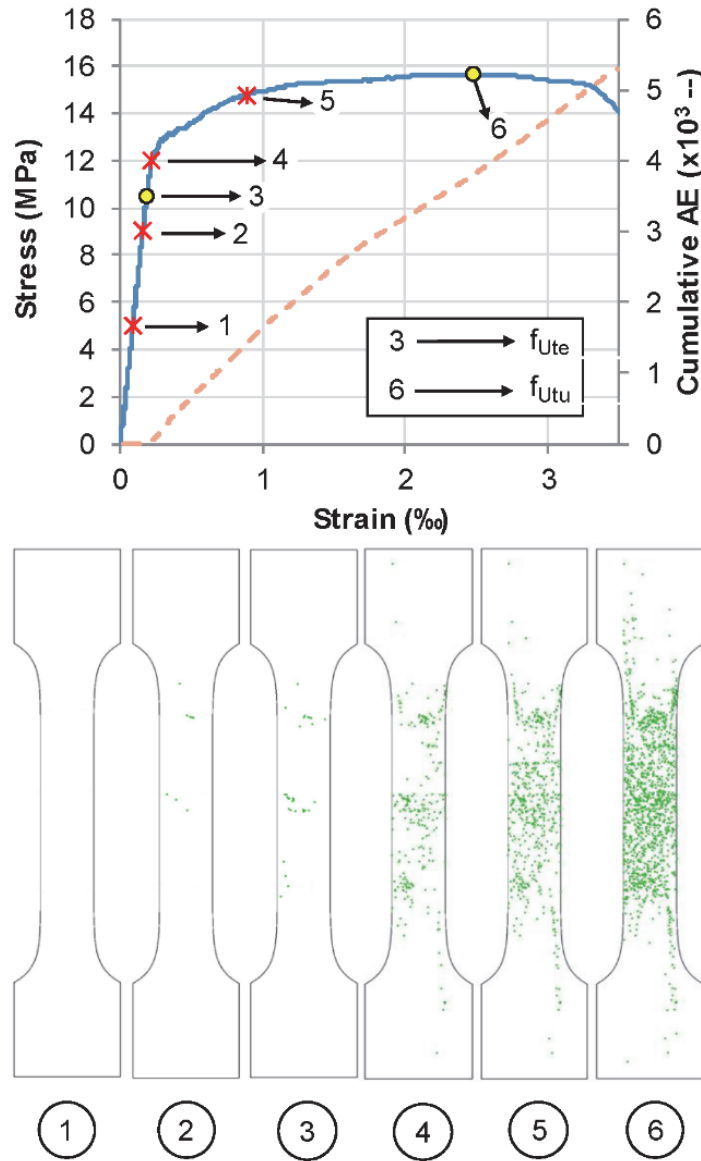


Figure 9: Development of Acoustic Emission events at various stress levels during a uniaxial tensile test in a dumbbell specimen Mix I-20C-SR15-S1 at a strain rate of 1×10^{-5} 1/s at 20 °C.

3.2.3 Elastic modulus

Figure 10 shows the effect of low strain rates on the elastic modulus in tension of the UHPFRC Mix I and Mix II. It can be seen that no proper conclusion could be drawn from the trend of elastic modulus under the different strain rates. Even though except for Mix I at 20 °C, all the other series show a trend wherein the elastic modulus decrease as the strain rate decrease from $1 \times 10^{-5} \text{ s}^{-1}$ to $1 \times 10^{-7} \text{ s}^{-1}$, and then increase again as the strain rate decrease further, the scatter of results, especially for the strain rate of $5 \times 10^{-9} \text{ s}^{-1}$, is huge. It therefore makes it difficult to comment on the effect of strain rate on the elastic modulus of these mixes.

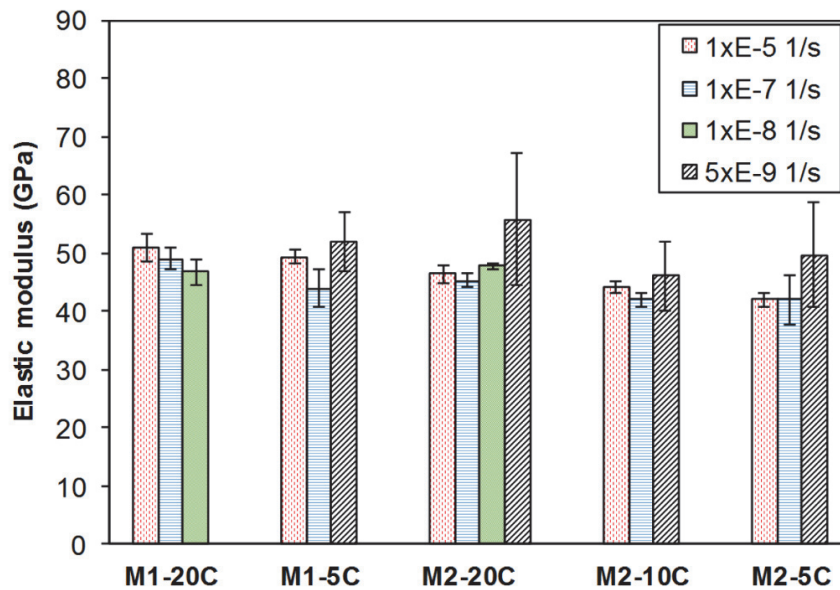


Figure 10: Effect of strain rate on the elastic modulus in tension, of Mix I and II.

However, figure 11 showing the DIF of elastic moduli, shows that except for a few erroneous values at a strain rate of $5 \times 10^{-9} \text{ s}^{-1}$, the other DIF values are very close to 1. This indicates that the elastic modulus of UHPFRC does not appear to be significantly influenced by strain rates for the investigated range.

However, this trend is in contrast to the findings of [72–75] for conventional concrete in the dynamic domain, who found out that the elastic modulus increased with increasing strain rate due to the viscosity of pore water. Even then, [74,75] found that the DIF of elastic modulus showed a very small increase when compared to that of the tensile strength of the concrete. They discussed that the aggregates, which play the major role in the Young's modulus of concrete, were not sensitive to the viscous effects. Therefore, the strain rate sensitivity was much less for elastic modulus when compared to that of the tensile strength.

Furthermore, for UHPFRC materials in the dynamic domain, [19,20,36] reported no strain rate sensitivity for the elastic modulus while [32] was not able to reach a conclusion on the same because of the huge scatter in the results. These findings were similar to that of the present study. Following the same discussion as in [74,75] regarding the negligible viscous response of aggregates in conventional concrete, it can be argued that the steel fibers are even less sensitive to the viscous effects, thereby completely removing the effect of strain rate. Moreover, [36] also attributes the unclear strain rate sensitivity of elastic modulus to the insignificant effect of pore water viscosity at very low w/c ratio and to the homogeneity of the UHPC matrix. Nevertheless, it could also be argued that the strain rates investigated in the present study were still not low enough to exhibit a considerable decrease in the elastic modulus, and that specimens if tested even below a strain rate of 1×10^{-9} 1/s, may exhibit a much more pronounced influence of viscosity and therefore a lesser elastic modulus.

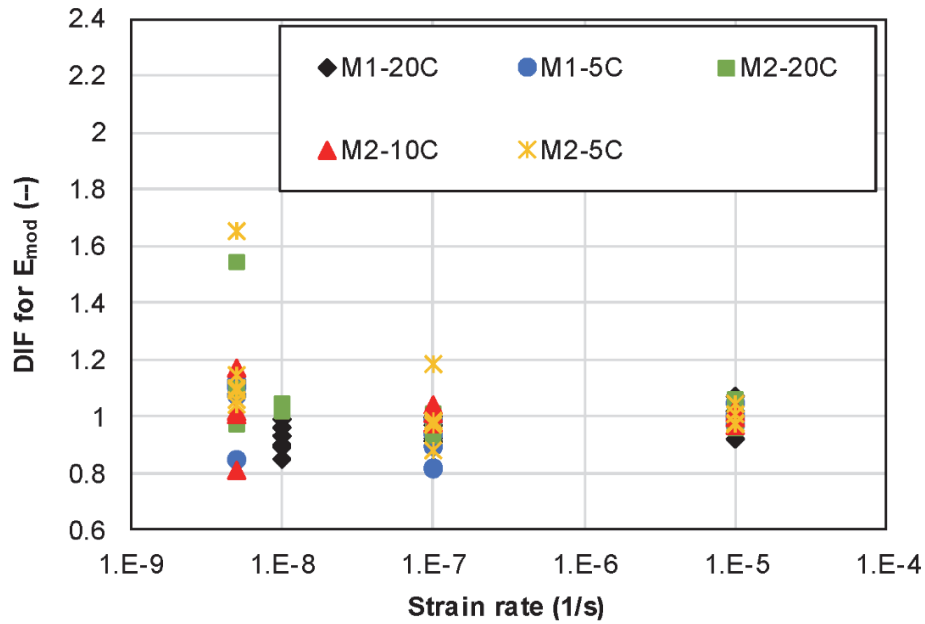


Figure 11: DIF for elastic modulus in tension, of Mix I and II at very low loading rates.

3.2.4 Tensile strength

Figure 12 summarizes the effect of strain rates on the f_{utu} of the two mixes for various curing temperatures. There was no unique trend in the tensile strength as the strain rate decreased. Mix I at 20 °C showed a decrease in the tensile strength with a decrease in the strain rate whereas, Mix II at 10 °C and Mix II at 5 °C exhibited an increase in the tensile strength. A third trend was shown by Mix I at 5 °C and Mix II at 20 °C, with an initial increase and then a decrease in the tensile strength as the strain rates decreased. As such, no proper trend was seen for the effect of strain rate on the tensile strength of the mixes investigated.

This is in contrast to the findings of the studies in the dynamic domain [20,22,23,31–33,35,36] where a clear dependence of tensile strength on the strain rate is reported with the tensile strength increasing with increase in the strain rate. On the other hand, as noted in [23,35], the increase in the DIF is quite steep in the dynamic domain ($> 1 \text{ s}^{-1}$), whereas it was much milder in the quasi-static domain. However, the lack of test data for strain rates lower than $1 \times 10^{-6} \text{ s}^{-1}$ for UHPFRC materials makes the comparison difficult and as a result, no trend in the tensile strength could be established. It could be assumed that the strain rate sensitivity becomes milder and milder as the strain rates decrease and ultimately reaches a state where the tensile strength is no more sensitive to the strain rate.

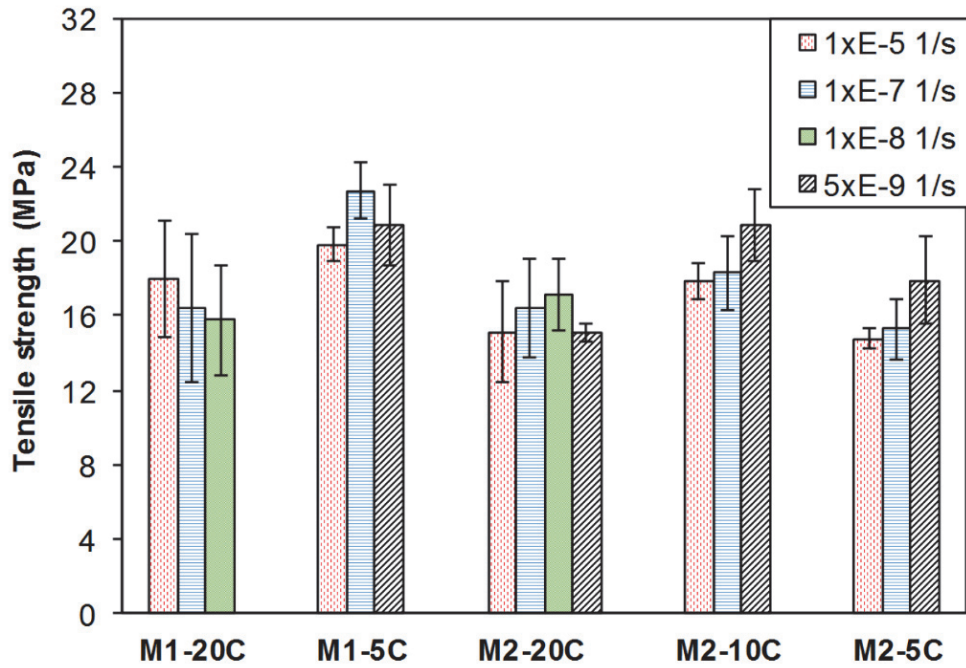


Figure 12: Effect of strain rate on the tensile strength of Mix I and II.

According to Naaman [76], the tensile strength of discontinuous fiber reinforced cementitious composites is given by equation (1), where λ is a factor which accounts for the average pullout length, fiber orientation effects and group reduction effects, τ is the bond strength of the fiber matrix interface, V_f is the fiber volume fraction and l_f/d_f is the aspect ratio of the fibers.

$$f_{utu} = \lambda \tau V_f \left(\frac{l_f}{d_f} \right) \quad (1)$$

In equation (1), the only factor that is rate sensitive is the equivalent bond strength τ . As such, the strain rate sensitivity of the tensile strength very much depends on that of the pullout of fibers from the matrix. However, all studies on the effect of loading rates on the pullout behavior of high strength steel fibers embedded in UHPC matrix has been conducted for the dynamic domain [77–80]. [77] reported a comparatively smaller strain rate dependence of pullout load for straight smooth fibers when compared to that of hooked fibers. It could be argued that the effect becomes even smaller or negligible under very low loading rates, thereby making the bond strength and consequently the tensile strength rate insensitive. Moreover, [71,78] showed that the strain rate sensitivity of single fiber pullout decreased as the compressive strength of the matrix increased beyond 55 MPa. The very high compressive strength of the matrices in the present study could therefore make the pullout response strain insensitive for the range of strain rate investigated.

If however, at very slow loading rates, the pullout of the single straight smooth fibers in the present study shows a strain rate sensitivity, it could be argued that the factor λ , including the effect of grouping of fibers or fiber orientation, counters the fiber pullout strain rate sensitivity, thereby making the overall composite action, strain rate insensitive. The results in [23,71] indicated a higher rate sensitivity of fiber pullout for mixes with lower fiber volume fraction, and the authors attributed this behavior to the group effect, wherein, the strain rate sensitivity is eliminated when a group of fibers interact together during pullout. The same effect may be present for the mixes in the present study as the fiber volume dosage is 9%. The scatter in the fiber orientation between individual specimens may also contribute to the scatter in the tensile strength [22], which can be another possible explanation for the strain rate insensitivity of the tensile strength, as seen in the present study. As such, it could be argued either that the strain rate insensitivity of tensile strength at very low strain rates, could be because of the strain rate insensitivity of the fiber pullout at these loading rates, or that the factors like fiber grouping and fiber orientation make the overall composite response strain rate insensitive.

3.2.5 Strain at tensile strength

Figure 13 shows the trend of ϵ_{Utu} under varying strain rates for two mixes and three curing temperatures. Except for M1-20C at $1 \times 10^{-8} \text{ s}^{-1}$ and M2-20C at $5 \times 10^{-9} \text{ s}^{-1}$, one can notice an increase in ϵ_{Utu} with a decrease in the loading rates.

The trend is different from what many authors have reported for UHPFRC in the dynamic domain [23,24,31,32,35,36], wherein an increase in ϵ_{Utu} is reported with an increase in the strain rate of loading. The increase in ϵ_{Utu} was attributed mainly to the increase in the number of cracks within the gauge length as the strain rate increased [23,31]. However, [33] reported a decrease in the ϵ_{Utu} with an increase in the strain rate, similar to the findings in the present study. They showed that the average crack width decreased from 160 μm at 0.0001 s^{-1} to 120 μm at 0.1 s^{-1} , and attributed the same to the trend observed. Similar trend of decrease in ϵ_{Utu} with increasing strain rates were also observed by [81,82], who described it as the effect of fiber breakage at higher strains.

In the present study, at very low strain rates, it could be argued that the observed trend is also dependent on the trends of f_{Ute} and f_{Utu} as discussed in sections 3.2.1 and 3.2.4. Even though the f_{Ute} decreases with decrease in strain rate, the fibrous mix remains the same and therefore becomes more efficient in achieving strain-hardening. Due to the lower f_{Ute} at very low strain rates, microcracks would have started to appear much earlier and as a result, the number of cracks until f_{Utu} could be much larger. Moreover, as shown by [33], the crack width would be larger at lower strain rates. These trends could therefore explain the trend of ϵ_{Utu} under very low strain rates in the present study.

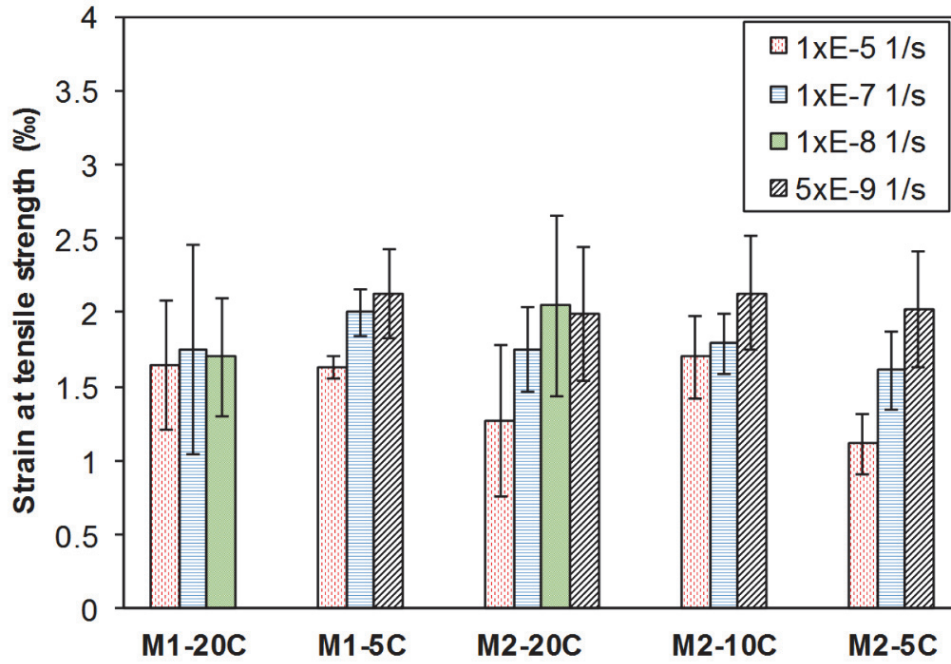


Figure 13: Effect of strain rate on the strain at tensile strength of Mix I and II.

3.2.6 Hardening modulus

Using the average values and scatter of f_{Ute} , E_{mod} , stress corresponding to a strain of 0.4‰, f_{Utu} and ϵ_{Utu} , a trilinear curve was built to synthesize the tensile response for each configuration, as shown in figure 14.

The hardening moduli E_{har} were calculated as described in figure 1 for each configuration and are shown in figure 15. No unique trend was seen for E_{har} with the varying strain rates, which is similar to the trend reported in [36]. Just like the explanations in section 3.2.4, E_{har} might have been influenced by the factor λ in equation (1), comprising of the effects of fiber orientation and fiber grouping, thereby making it strain rate insensitive.

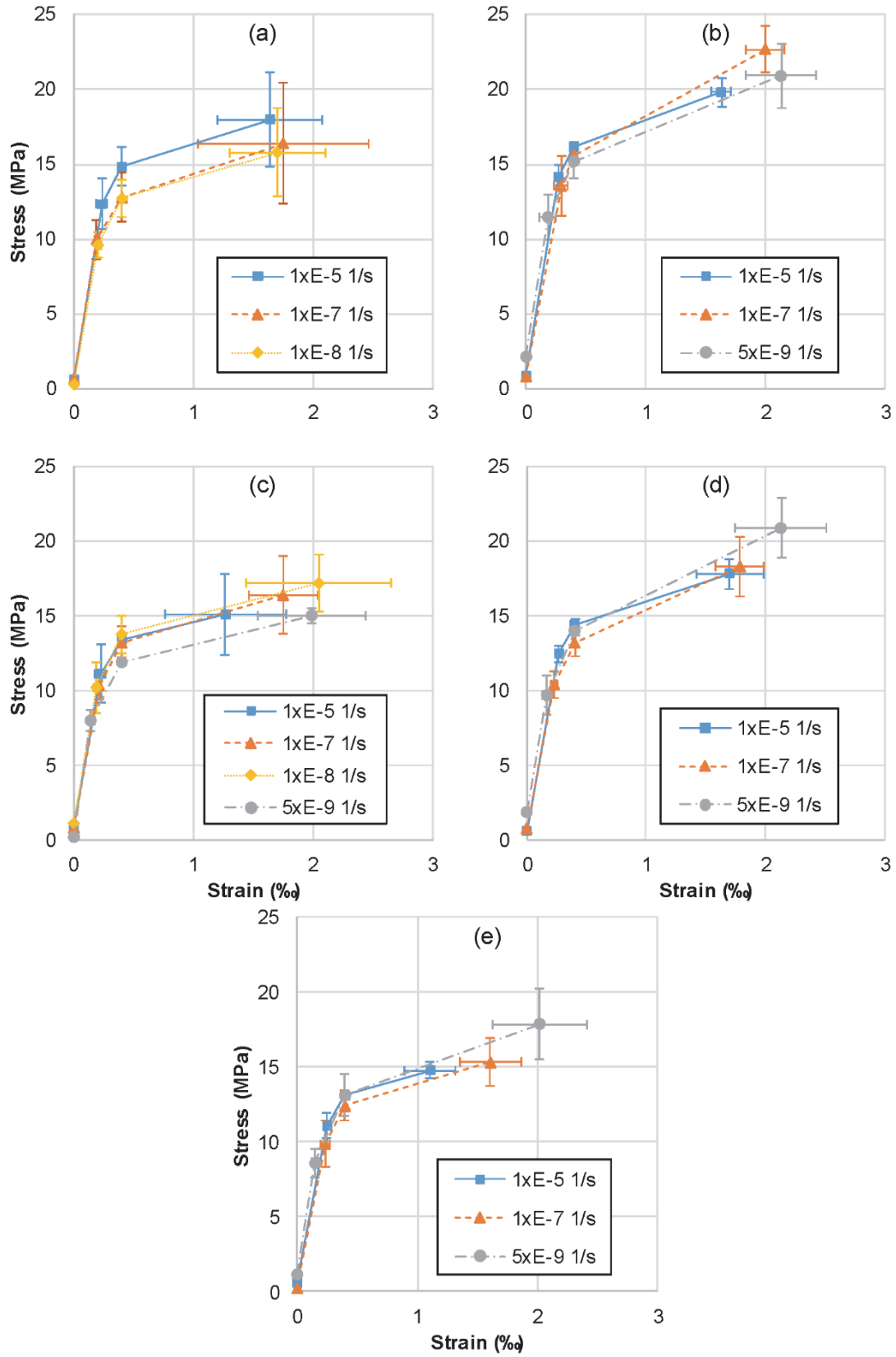


Figure 14: Trilinear tensile response from the average values of E_{mod} , f_{Ute} , f_{Utu} and ϵ_{Utu} for; a) M1-20C, b) M1-5C, c) M2-20C, d) M-10C and e) M2-5C.

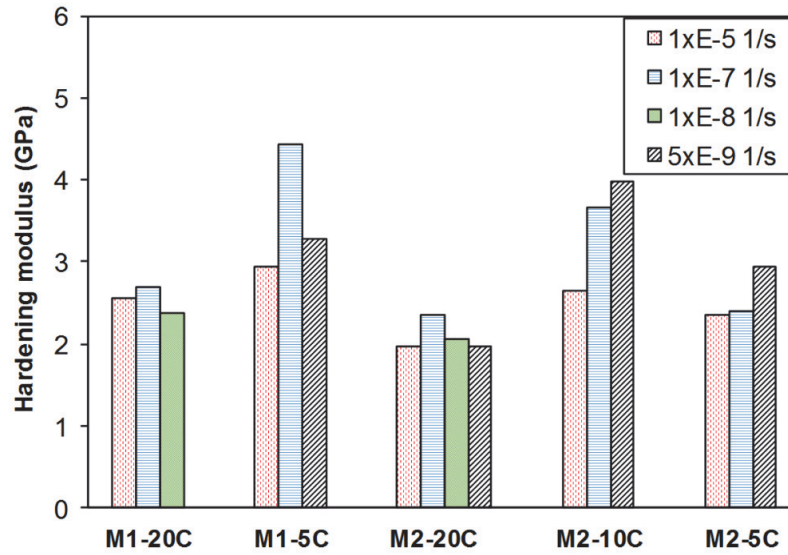


Figure 15: Effect of strain rate on the hardening modulus of Mix I and II, loaded at an age of 14 days.

3.3 Effect of moderate to low temperatures

3.3.1 Age vs Maturity

Lower temperatures slow down the hydration reaction and ageing of the material. The Arrhenius equation and the apparent activation energy could be used to find out the maturity of the mixes to indicate the extent of hydration processes and its sensitivity to temperature. [46] found out the apparent activation energy for a UHPFRC mix CM22_TKK which was the predecessor of the Mix I in the present study. The value of $E_a/R = 3300$ K from that study [46], where E_a is the apparent activation energy in J/mol.K and R is the ideal gas constant, with a value of 8.314 J/mol.K, was assumed for the Mix I in the present case. For Mix II, a value of 4000 K was found out after conducting isothermal calorimetry tests at three different temperatures (not shown here). The maturity of the mixes corresponding to an age of 14 days is shown in Table 4.

Table 4: Maturity at the time of testing under different temperatures.

Temperature	Age at the time of testing	Maturity at the time of testing for Mix I	Maturity at the time of testing for Mix II
°C	hours (days)	hours (days)	hours (days)
20	336 (14)	336 (14)	336 (14)
10	336 (14)	226 (9.4)	207 (8.6)
5	336 (14)	183 (7.6)	161 (6.7)

3.3.2 Elastic limit

Figure 16 shows the effect of temperature on the elastic limit for both the mixes under different strain rates. Mix I shows higher elastic limits at a temperature of 5 °C than at 20 °C, even though the maturity of the former is lesser than that of the latter. One possible explanation for this trend could be the denser microstructure under low temperatures, with significantly decreased quantity and size of capillary pores as indicated in [83]. Another possible explanation could be the crisscross effect seen in cumulative heat developed in isothermal calorimetry tests for similar UHPFRC mix under different temperatures as shown by [46]. It was seen that the cumulative heat developed at a temperature of 5 °C crossed that at 10 °C, at an age of approximately 10 days, but didn't cross that at 20 °C. It could be argued that at a later age for Mix I, the cumulative heat and consequently the hydration can be higher for a curing temperature of 5 °C, following similar discussion.

However, for Mix II, the trend was slightly different as can be seen in figure 16, with a higher elastic limit at 10 °C, except at a strain rate of 1×10^{-7} 1/s. Nevertheless, this could be also be explained with the microstructure and crisscross effect, along with the development of hydration in Mix II. It was shown in Chapter 2 [62] that the development of elastic modulus and hydration at 20 °C in Mix II was much slower than that of Mix I, and it took more time for Mix II to reach the final asymptotic value of elastic modulus or degree of hydration. As such, it may need more time to form the microstructure especially under lower temperatures, thereby delaying the two effects previously discussed. In figure 16, it could be argued that at 10 °C, the two effects have already occurred, thereby showing a higher elastic limit (except for strain rate of 1×10^{-7} 1/s), whereas it needs more time for the effects to be seen at 5 °C.

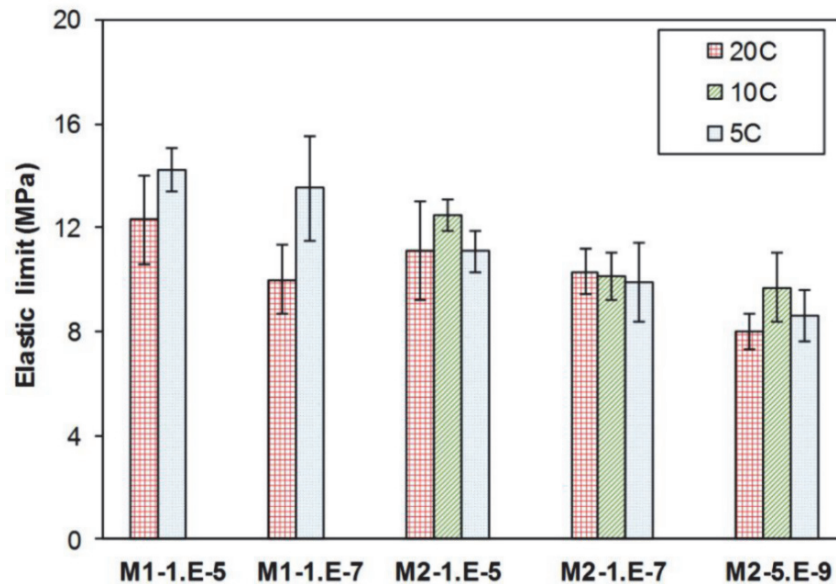


Figure 16: Effect of temperature on the elastic limit for different mix type and loading rates [X-axis - "Mix type-strain rate (1/s)"].

3.3.3 Elastic modulus

Figure 17 shows the effect of temperature on the elastic modulus for both the mixes under different strain rates. Except at a strain rate of 5×10^{-9} 1/s for Mix II at 5 °C, all the other configurations showed a uniform trend of decrease in the elastic modulus with a decrease in the temperature. However, the difference is really small ($< 4\%$), and therefore the effect could be considered negligible.

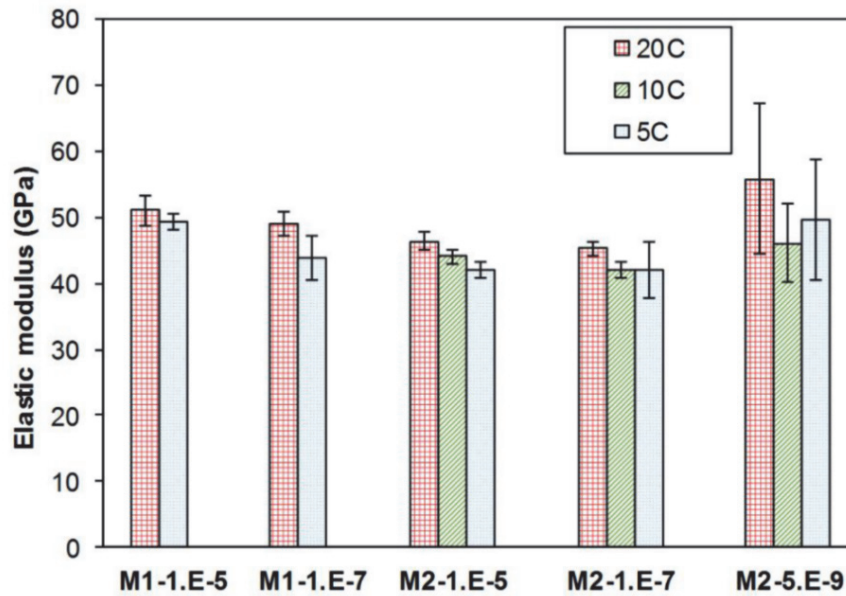


Figure 17: Effect of temperature on the elastic modulus for different mix type and loading rates [X-axis - "Mix type-strain rate (1/s)".]

3.3.4 Tensile strength

Figure 18 shows the effect of temperature on the tensile strength for both the mixes under different strain rates. It can be seen that the trend is very similar to that of the elastic limit. The behavior could therefore be attributed to the same effects as described in the case of f_{Ute} . A similar trend of higher tensile strength at lower temperatures was reported by [7] for steel fiber concrete. [84] showed that the pullout of single fibers from cement pastes with and without microsilica showed a higher bond stress at a temperature of 38 °C compared to that at 2 °C at 7 days, whereas the trend was inverted when tested at 90 days. The higher bond stress at lower temperatures can also be attributed to the better microstructure under these conditions.

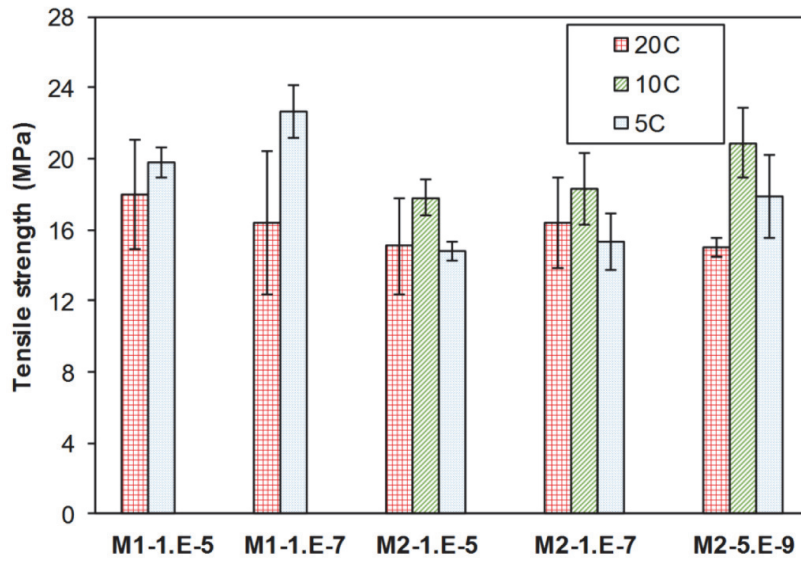


Figure 18: Effect of temperature on the tensile strength for different mix type and loading rates [X-axis - "Mix type -strain rate (1/s)"].

3.3.5 Strain at tensile strength

Figure 19 shows the effect of temperature on ϵ_{Utu} for the different configurations tested, in which no particular trends were seen. The complex interaction of creep and temperature as indicated earlier could be the reason for the observed independence. Moreover, the effects of fiber orientation and fiber grouping add to the complexity of the response making it apparently temperature independent in the present case.

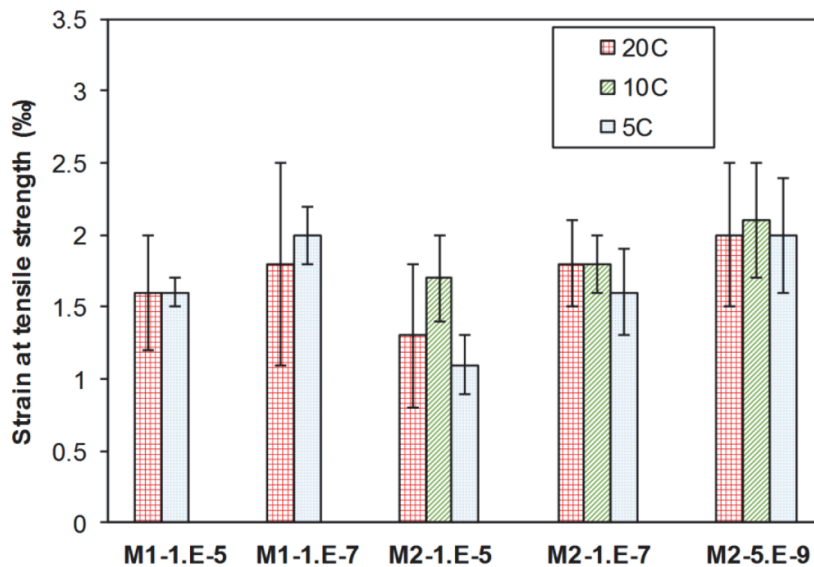


Figure 19: Effect of temperature on the strain at tensile strength for different mix type and loading rates [X-axis - "Mix type -strain rate (1/s)"].

3.4 Effect of mix type

3.4.1 Elastic limit and tensile strength

Figures 20 and 21 show the effect of the mix type on the elastic limit and tensile strength under different configurations.

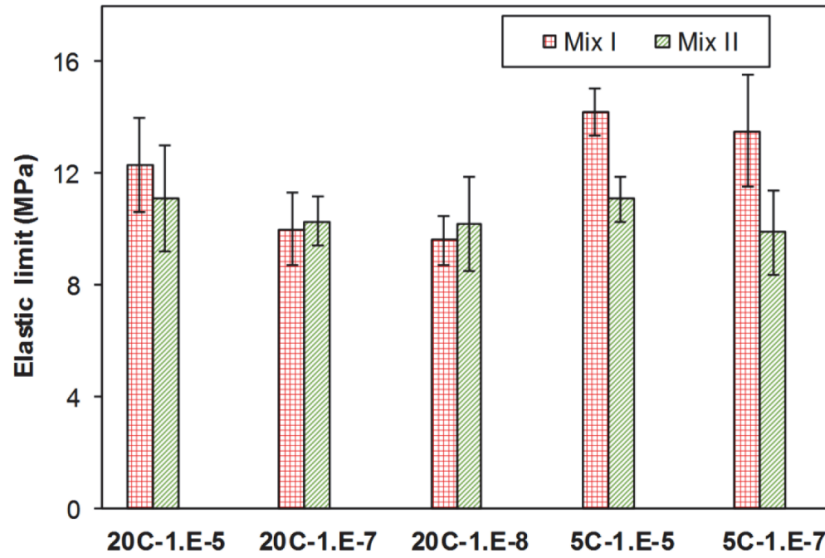


Figure 20: Effect of mix type on the elastic limit for different strain rates and curing temperatures [X-axis - "temperature-strain rate (1/s)"].

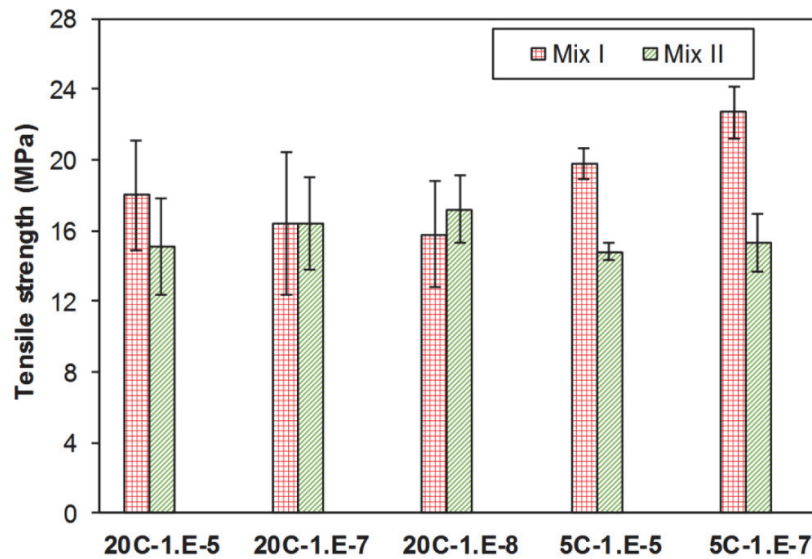


Figure 21: Effect of mix type on the tensile strength for different strain rates and curing temperatures [X-axis - "temperature-strain rate (1/s)"].

It can be seen that in both the cases, the values are more or less similar at a temperature of 20 °C, whereas Mix I shows considerably higher elastic limit and tensile strength at 5 °C. This can be explained using the fact that development of elastic modulus and hydration in Mix II was much slower than that of Mix I, and it took more time to for Mix II to reach the final asymptotic value of elastic modulus or degree of hydration, as shown in Chapter 2 [62], which becomes even more delayed under lower temperatures. As such, at 20 °C, the properties were more or less similar at the testing age of 14 days whereas it may take more time for Mix II to reach similar or higher values at a temperature of 5 °C.

3.4.2 Elastic modulus

Figure 22 shows the effect of mix type on the elastic modulus under different configurations. Except for a strain rate of 1×10^{-8} 1/s at 20 °C, Mix I shows a higher elastic modulus than Mix II. In Mix I, the unhydrated cement acts as filler whereas in Mix II, they were replaced by limestone powder. Using the hydration model developed by Waller [85], the theoretical ultimate degree of hydration was calculated to be 0.30 and 0.52 for Mix I and II respectively. Unhydrated cement fillers can produce a higher stiffness compared to that of limestone filler, leading to a higher elastic modulus for Mix I. Another possible explanation is the higher viscous potential of Mix II as shown by creep tests at 14 days under different stress levels, Chapter 2 [62]. However, this is only visible at very low strain rates, and the trend observed at 20 °C at a strain rate of 1×10^{-8} is contradictory. Nevertheless, it can also be possible that the effect of higher viscous potential of Mix II will be seen only at even lower strain rates. On the contrary, it could also be argued that the difference in the elastic modulus in the different configurations is negligible in terms of percentage decrease, just as in the case of temperature effect on elastic modulus.

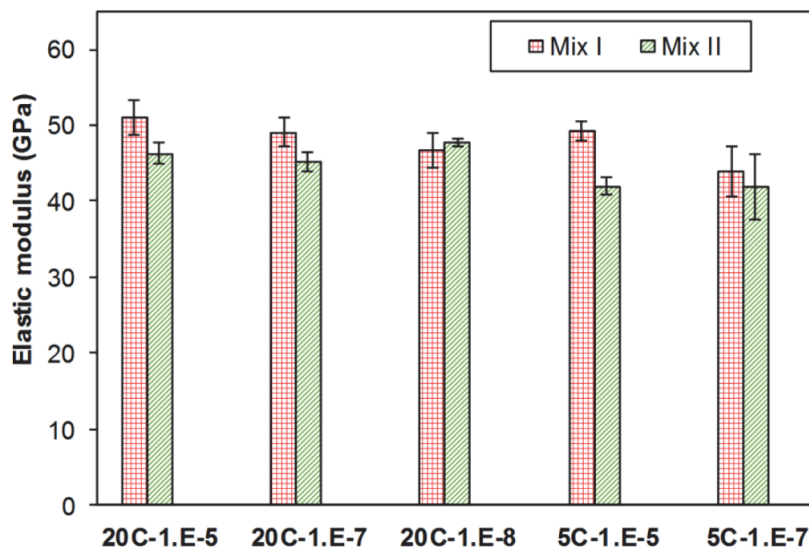


Figure 22: Effect of mix type on the elastic modulus for different strain rates and curing temperatures [X-axis - "temperature-strain rate (1/s)"].

3.4.3 Strain at ultimate strength

Figure 23 shows the effect of mix type on the strain at tensile strength, and it can be seen that just as in the case of effect of temperature, there is no particular trend on the effect of mix type on the strain at tensile strength. The huge scatter in the data also makes any conclusion impossible.

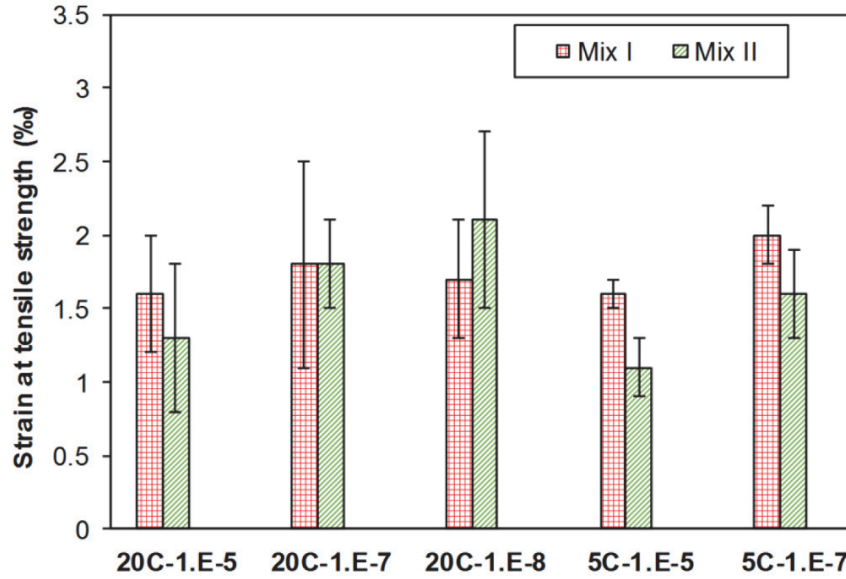


Figure 23: Effect of mix type on the strain at tensile strength for different strain rates and curing temperatures [X-axis - "temperature-strain rate (1/s)"].

4 Analytical models

4.1 Overview

The CEB model code [2] recommends a quasi-static strain rate of $3 \times 10^{-6} \text{ s}^{-1}$ for the calculation of the DIF. However, not every studies on the effect of strain rate on the tensile response of UHPFRC or similar materials consider this as a quasi-static strain rate, but instead considers $1 \times 10^{-5} \text{ s}^{-1}$ or $1 \times 10^{-6} \text{ s}^{-1}$. This is not ideal for comparative and modelling purposes, but as pointed out in [19], the dynamic strength increase is minimal in this range of strain rates and therefore the DIF from different studies could be compared. As such, for the experimental tests in the present study, the DIF was calculated using a quasi-static strain rate of $1 \times 10^{-5} \text{ 1/s}$. The DIF for the different tensile properties were compared with analytical models in the literature, the general format of which is shown in equation (2) [86].

$$DIF_{property} = \begin{cases} \left(\frac{\dot{\epsilon}}{\epsilon_s} \right)^{A*\delta}, & \dot{\epsilon} \leq t \text{ s}^{-1} \\ \beta \left(\frac{\dot{\epsilon}}{\epsilon_s} \right)^B, & \dot{\epsilon} > t \text{ s}^{-1} \end{cases} \quad (2)$$

where property refers to the relevant tensile property studied; A, B, β , δ are the parameters of the model and t refers to the strain rate in s^{-1} at which the transition occurs. In the following sections, existing analytical models along with new best fitting models will be used to analyze the DIF for f_{Ute} and ϵ_{Utu} . No models were developed for E_{mod} , f_{Utu} or E_{har} as these properties did not exhibit a clear strain rate sensitivity in the present study.

4.2 Effect of strain rate on f_{Ute}

The CEB model code parameters for f_{Ute} are given in Table 5, where f'_c is the quasi-static compressive strength and $f'_{c,0} = 10$ MPa. For the ease of comparison, it could be assumed that the elastic limit of fiber reinforced cementitious materials is the same as the tensile strength of the matrix, and therefore the CEB model could be used to compare the f_{Ute} of these materials. Malvar and Ross [16] compiled fifteen studies on the effect of strain rate on the tensile strength of conventional concrete at strain rates in the range of $1 \times 10^{-6} \text{ s}^{-1}$ to $1 \times 10^2 \text{ s}^{-1}$ and formulated the model as shown in Table 5 for the prediction of the DIF. They used the same quasi-static strain rate as that of the CEB formulation.

Both the models were used to predict the DIF only until the quasi-static strain rate of $3 \times 10^{-6} \text{ s}^{-1}$, at which the DIF value is 1. The tests in the present study are done at strain rates lower than this quasi-static strain rate. Using regression analysis, a new best fitting model similar to that of equation (2) has been proposed for the DIF of f_{Ute} . The model was developed only for strain rates less than $1 \times 10^{-5} \text{ s}^{-1}$, and therefore includes only the first part of equation (2), the parameters of which are shown in Table 5. The quasi-static strain rate for the new model was chosen as the same as that of the other models for better comparison. It should be noted that the terminology of Dynamic Increase Factor is maintained, even though the factor is less than 1 for lower strain rates.

Figure 24 shows the predictions of the three models and the values of the calculated DIF for f_{Ute} from the five series of tensile tests in the present study. It can be seen that the CEB model as well as the Malvar and Ross model predict the response at low strain rates reasonably well, but a much higher drop in the elastic limit was seen in the tests as shown by the new best fitting model.

Table 5: Parameters of the analytical models for the prediction of effect of strain rate on the DIF for f_{Ute} .

Property	Model	$\dot{\epsilon}_s$ (s ⁻¹)	A (--)	B (--)	β (--)	δ (--)	t (s ⁻¹)
	CEB [2]	3x10 ⁻⁶	1.016	0.333	$\log \beta = 7.11\delta - 2.33$	$\delta = \frac{1}{10 + 6 \frac{f'_c}{f_{c,0}}}$	30
DIF f_{Ute}	Malvar and Ross [16]	3x10 ⁻⁶	1.016	0.333	$\log \beta = 6\delta - 2$	$\delta = \frac{1}{1 + 8 \frac{f'_c}{f_{c,0}}}$	1
	New best fitting model	3x10 ⁻⁶	5.535	--	--	$\delta = \frac{1}{1 + 8 \frac{f'_c}{f_{c,0}}}$	1x10 ⁻⁵

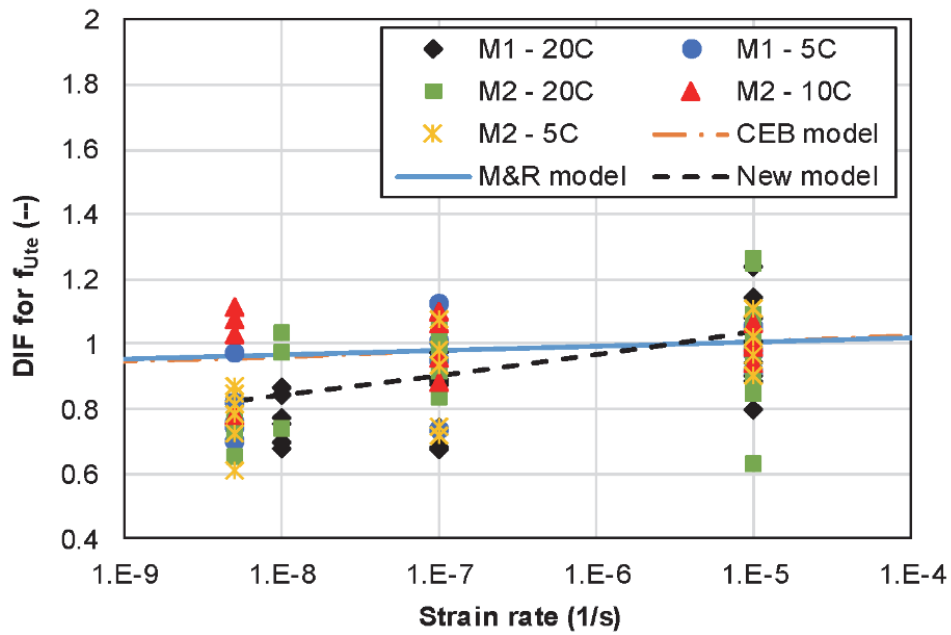


Figure 24: DIF for elastic limit of Mix I and II at very low loading rates, along with the predictions of analytical models (M&R - Malvar and Ross).

4.3 Effect of strain rate on ϵ_{Utu}

Many authors have reported the effect of strain rates in the dynamic domain on ϵ_{Utu} for UHPFRC [23–25,31–33,35]. All these studies were compiled by Thomas et al. [19] and a model for DIF was proposed similar to equation (2). A similar model was also proposed by Park et al. [23] for the trend of ϵ_{Utu} . The parameters of both models are shown in Table 6. Figure 25 shows the predictions of the Thomas model and the Park model at very low strain rates, along with the test results in the present study.

Table 6: Parameters of the analytical models for the prediction of effect of strain rate on the DIF for ϵ_{Utu} .

Property	Model	ϵ_s (s ⁻¹)	A (--)	B (--)	β (--)	δ (--)	t (s ⁻¹)
DIF ϵ_{Utu}	Thomas et al. [19]	3x10 ⁻⁶	1	1.5	1.2847x10 ¹¹	8.26x10 ⁻³	20
	Park et al. [23]	3x10 ⁻⁶	1	0.3286	0.003998	0.01465	25
	New best fitting model	3x10 ⁻⁶	9.925	--	--	$\delta = \frac{1}{1 + 8 \frac{f_c'}{f_{c,0}'}}$	1x10 ⁻⁵

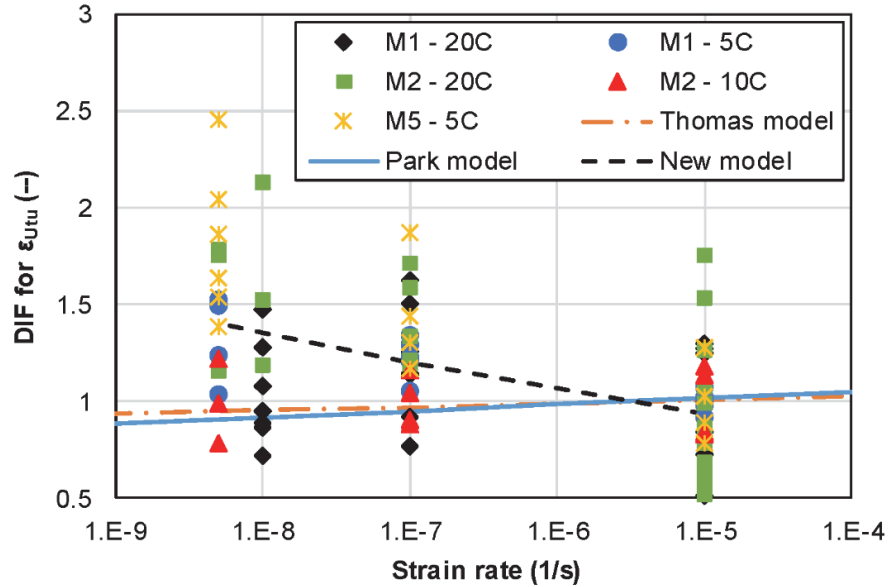


Figure 25: DIF for strain at tensile strength of Mix I and II at very low loading rates, along with the predictions of analytical models.

It can be seen that the general predictions of the models, is a decrease in ϵ_{Utu} with a decrease in the strain rate, which is in contrast to the findings of the present study. As such, a new best fitting model for the test results was proposed, as seen in Table 6, which is also shown in figure 25 for strain rates less than $1 \times 10^{-5} \text{ s}^{-1}$. However, more test results are needed at very low strain rates to confirm the validity of this model.

5 Conclusions

- Uniaxial tensile tests were performed at different loading rates from quasi-static to very low, for two types of mixes; Mix I with pure type I cement and silica fume and Mix II with silica fume and 50% replacement of type I cement with limestone filler, under three different curing temperatures; 20 °C, 10 °C and 5 °C. The tests at strain rates less than $1 \times 10^{-6} \text{ s}^{-1}$ were the first of their kind for UHPFRC materials.
- Effect of strain rate
 - The elastic limit was found to decrease considerably with the decrease in the strain rate. At very low loading rates, the elastic limit showed a drop of 19%-28% when compared to that at quasi-static strain rates. The results are even more interesting for softening UHPFRC or less robust SH-UHPFRC.
 - Acoustic emission measurements on uniaxial tensile tests confirmed the validity of the inverse analysis procedure used for the determination of the elastic limit in tension.
 - The elastic modulus in tension was found to be insensitive to the varying strain rates.
 - The tensile strength was also found to be insensitive to the strain rates at strain rates less than $1 \times 10^{-6} \text{ s}^{-1}$. It was concluded that the strain rate insensitivity of tensile strength at very low strain rates, could be either because of the strain rate insensitivity of the fiber pullout at these loading rates, or because of the factors like fiber grouping and fiber orientation, which offset the intrinsic rate sensitivity.
 - The strain at tensile strength increased as the strain rate decreased. It was attributed to the fact that even at lower strain rates, when the f_{Ute} is lower, the fibrous mix remains the same and therefore becomes more efficient in achieving strain-hardening.
 - The hardening modulus was found to be insensitive to the strain rates.
- Effect of temperature
 - The elastic limit and tensile strength were both found to increase with a decrease in curing temperature, which was attributed to the formation of denser microstructure with lesser quantities and sizes of capillary pores, and a better fiber matrix bond at lower temperatures.

- The elastic modulus and strain at tensile strength were found to be insensitive to the curing temperature.
- Effect of mix type
 - The elastic limit and tensile strength were found to be dependent on the kinetics of hydration in the mixes. It took more time for Mix II to reach the same properties as that of Mix I, because of the slower development of hydration.
 - The elastic modulus was found to be smaller in Mix II, and it was mainly attributed to the presence of limestone powder as inert filler, which reduced the overall stiffness of the mix.
 - The strain at tensile strength was found to be insensitive to the type of mix used in the study.
- Analytical modelling
 - Existing DIF models for f_{Ute} in the dynamic domain of strain rate were extended to the very low strain rate domain and the predictions were compared. A new best fitting model for strain rates less than $1 \times 10^{-5} \text{ s}^{-1}$ was proposed. The results could be used for the development of new guidelines for serviceability for UHPFRC materials.
 - A new best fitting model was developed to predict the trend of ε_{Utu} , which requires further validation using test results.

Acknowledgements

The project was financially supported by the Swiss National Science Foundation (grant 200021_153394/1). The authors would like to gratefully acknowledge the help given by the technicians of GIC-ENAC-EPFL Mr. S. Despont, Mr. G. Guignet and Mr. S. Demierre and Mr. A. Hajiesmaeili in performing the experimental works in the laboratory. Mix II was developed by Mr. A. Hajiesmaeili.

References

- [1] E. Denarié, E. Brühwiler, Cast-on Site UHPFRC for improvement of existing structures – achievements over the last 10 years in practice and research, in: High Perform. Fiber Reinf. Cem. Compos. 7, (2015): pp. 473–480.
- [2] “Comité Euro-International du Béton,” CEB-FIP Model Code 1990, Trowbridge, Wiltshire, UK, (1993).

- [3] H. Rüsç, Research toward a general flexural theory for structural concrete, *ACI J.* 57 (1960) 1–28.
- [4] H.W. Reinhardt, H.A.W. Cornelissen, *Zeitstandzugversuche an Beton*, Baustoffe, Bauverlag, Wiesbad. (1985) 162–167.
- [5] F.P. Zhou, Time dependent crack growth and fracture in concrete, Doctoral Thesis, Report TVBM-1011, Division of Building Materials, Lund Institute of Technology, Sweden., (1992).
- [6] A.E. Hansen, Time Dependent Tensile Fracture of Concrete, Doctoral Thesis, Norwegian Institute of Technology, Division of Concrete Structures, University of Trondheim (1991).
- [7] H.A. Körmeling, Strain Rate and Temperature Behaviour of Steel Fiber Concrete in Tension, Doctoral Thesis, Delft University of Technology, (1986).
- [8] P.Y.T.N. C. Allen Ross and J. W. Tedesco, Split-Hopkinson Pressure-Bar tests on Concrete and Mortar in Tension and Compression, *Mater. J.* 86 (1989) 475–481. doi:10.14359/2065.
- [9] J.W. Tedesco, C.A. Ross, P.B. McGill, B.P. O’Neil, Numerical analysis of high strain rate concrete direct tension tests, *Comput. Struct.* 40 (1991) 313–327. doi:10.1016/0045-7949(91)90357-R.
- [10] F.M. Mellinger, D.L. Birkimer, Measurement of Stress and Strain on Cylindrical Test Specimens of Rock and Concrete under Impact Loading, (1966).
- [11] R. John, T. Antoun, A.M. Rajendran, Effect of strain rate and size on tensile strength of concrete, *Shock Compression Condens. Matter–1991.* (1992) 501–504. doi:10.1016/B978-0-444-89732-9.50115-1.
- [12] A.J. Zielinski, H.W. Reinhard, H.A. Körmeling, Experiments on concrete under repeated uniaxial impact tensile loading, *Matériaux Constr.* 14 (1981) 163–169. doi:10.1007/BF02473920.
- [13] W.L. Cowell, Dynamic Properties of Plain Portland Cement Concrete, Naval Civil Engineering Laboratory, Port Hueneme, CA, (1966).
- [14] J. Takeda, H. Tachikawa, Deformation and Fracture of Concrete Subjected to Dynamic Load, in: *Proc. Int. Conf. Mech. Behav. Mater. V*, Kyoto, Japan, (1971).
- [15] O.P. Kvirikadze, Determination of the Ultimate Strength and Modulus of Deformation of Concrete at Different Rates of Loading, in: *Int. Symp. Test. Situ Concr. Struct.*, Budapest, Hungary, (1977): pp. 109–117.
- [16] L.J. Malvar and C.A. Ross, Review of Strain Rate Effects for Concrete in Tension, *Mater. J.* 95 (1998) 735–739. doi:10.14359/418.
- [17] J.W.T. C. Allen Ross and Steven T. Kuennen, Effects of Strain Rate on Concrete Strength, *Mater. J.* 92 (1995) 37–45. doi:10.14359/1175.

- [18] D. Tasevski, M.F. Ruiz, A. Muttoni, Compressive Strength and Deformation Capacity of Concrete under Sustained Loading and Low Stress Rates, *J. Adv. Concr. Technol.* 16 (2018) 396–415. doi:10.3151/jact.16.396.
- [19] R.J. Thomas, A.D. Sorensen, Review of strain rate effects for UHPC in tension, *Constr. Build. Mater.* 153 (2017) 846–856. doi:10.1016/J.CONBUILDMAT.2017.07.168.
- [20] K. Fujikake, T. Senga, N. Ueda, T. Ohno, M. Katagiri, Effects of Strain Rate on Tensile Behavior of Reactive Powder Concrete, *J. Adv. Concr. Technol.* 4 (2006) 79–84. doi:10.3151/jact.4.79.
- [21] P.R. Edouard Parant Eric Jacquelin, and Claude Boulay, Strain Rate Effect on Bending Behavior of New Ultra-High-Performance Cement-Based Composite, *Mater. J.* 104 (2007). doi:10.14359/18901.
- [22] E. Cadoni, D. Forni, Experimental analysis of the UHPFRCs behavior under tension at high stress rate, *Eur. Phys. J. Spec. Top.* 225 (2016) 253–264. doi:10.1140/epjst/e2016-02639-2.
- [23] S.H. Park, D.J. Kim, S.W. Kim, Investigating the impact resistance of ultra-high-performance fiber-reinforced concrete using an improved strain energy impact test machine, *Constr. Build. Mater.* 125 (2016) 145–159. doi:10.1016/J.CONBUILDMAT.2016.08.027.
- [24] J.K. Park, S.-W. Kim, D.J. Kim, Matrix-strength-dependent strain-rate sensitivity of strain-hardening fiber-reinforced cementitious composites under tensile impact, *Compos. Struct.* 162 (2017) 313–324. doi:10.1016/J.COMPSTRUCT.2016.12.022.
- [25] N.T. Tran, D.J. Kim, Synergistic response of blending fibers in ultra-high-performance concrete under high rate tensile loads, *Cem. Concr. Compos.* 78 (2017) 132–145. doi:10.1016/J.CEMCONCOMP.2017.01.008.
- [26] A.M. Soliman, M.L. Nehdi, Effect of partially hydrated cementitious materials and superabsorbent polymer on early-age shrinkage of UHPC, *Constr. Build. Mater.* 41 (2013) 270–275. doi:10.1016/J.CONBUILDMAT.2012.12.008.
- [27] Y. Su, J. Li, C. Wu, P. Wu, Z.-X. Li, Effects of steel fibres on dynamic strength of UHPC, *Constr. Build. Mater.* 114 (2016) 708–718. doi:10.1016/J.CONBUILDMAT.2016.04.007.
- [28] Y. Su, J. Li, C. Wu, P. Wu, Z.-X. Li, Influences of nano-particles on dynamic strength of ultra-high performance concrete, *Compos. Part B Eng.* 91 (2016) 595–609. doi:10.1016/J.COMPOSITESB.2016.01.044.
- [29] M. Nöldgen, W. Riedel, K. Thoma, E. Fehling, Properties of ultra high performance concrete (UHPC) in tension at high strain rates, in: *VIII Int. Conf. Fract. Mech. Concr. Concr. Struct.*, (2013).

- [30] S.G. Millard, T.C.K. Molyneaux, S.J. Barnett, X. Gao, Dynamic enhancement of blast-resistant ultra high performance fibre-reinforced concrete under flexural and shear loading, *Int. J. Impact Eng.* 37 (2010) 405–413. doi:10.1016/J.IJIMPENG.2009.09.004.
- [31] N.T. Tran, T.K. Tran, D.J. Kim, High rate response of ultra-high-performance fiber-reinforced concretes under direct tension, *Cem. Concr. Res.* 69 (2015) 72–87. doi:10.1016/J.CEMCONRES.2014.12.008.
- [32] S. Pyo, K. Wille, S. El-Tawil, A.E. Naaman, Strain rate dependent properties of ultra high performance fiber reinforced concrete (UHP-FRC) under tension, *Cem. Concr. Compos.* 56 (2015) 15–24. doi:10.1016/J.CEMCONCOMP.2014.10.002.
- [33] R. Ranade, V.C. Li, W.F. Heard, Tensile Rate Effects in High Strength-High Ductility Concrete, *Cem. Concr. Res.* 68 (2015) 94–104. doi:10.1016/J.CEMCONRES.2014.11.005.
- [34] M. Xu, K. Wille, Fracture energy of UHP-FRC under direct tensile loading applied at low strain rates, *Compos. Part B Eng.* 80 (2015) 116–125. doi:10.1016/J.COMPOSITESB.2015.05.031.
- [35] S. Pyo, S. El-Tawil, A.E. Naaman, Direct tensile behavior of ultra high performance fiber reinforced concrete (UHP-FRC) at high strain rates, *Cem. Concr. Res.* 88 (2016) 144–156. doi:10.1016/J.CEMCONRES.2016.07.003.
- [36] K. Wille, M. Xu, S. El-Tawil, A.E. Naaman, Dynamic impact factors of strain hardening UHP-FRC under direct tensile loading at low strain rates, *Mater. Struct.* 49 (2016) 1351–1365. doi:10.1617/s11527-015-0581-y.
- [37] Z.P. Bazant, S. Prasannan, Solidification Theory for Concrete Creep. I: Formulation, *J. Eng. Mech.* 115 (1989) 1691–1703.
- [38] Z.P. Bažant, S. Prasannan, Solidification Theory for Concrete Creep: I: Verification and Application, *ASCE J. Eng. Mech.* 115 (1989) 1704–1725.
- [39] P. Rossi, N. Godart, J.L. Robert, J.P. Gervais, D. Bruhat, Investigation of the Basic Creep of Concrete by Acoustic Emission, in: *Proceedings, Creep Shrinkage Concr.*, (1993): pp. 33–38.
- [40] Z.P. Bažant, R. Gettu, Rate Effects and Load relaxation in Static Fracture of Concrete, *ACI Mater. J.* 89 (1992) 456–468.
- [41] E. Denarié, Etude expérimentale des couplages Viscoelasticite - Croissance des fissures dans les betons de ciment, Doctoral thesis No: 2195, Ecole Polytechnique Fédérale de Lausanne, (2000).
- [42] A. Switek-Rey, E. Denarié, E. Brühwiler, Early age creep and relaxation of UHPFRC under low to high tensile stresses, *Cem. Concr. Res.* 83 (2016) 57–69.

- [43] A.E. Switek, Time-Dependent Response of Ultra High Performance Fibre Reinforced Concrete (UHPFRC) under Low to High Tensile Stresses, Doctoral thesis No: 4899, Ecole Polytechnique Fédérale de Lausanne, Switzerland, (2011).
- [44] A. Kamen, Comportement au jeune âge et différé d'un BFUP écrouissant sous les effets thermomécaniques, Doctoral thesis No: 3827, Ecole Polytechnique Fédérale de Lausanne, Switzerland, 2007.
- [45] A. Kamen, E. Denarié, H. Sadouki, E. Brühwiler, Evaluation of UHPFRC activation energy using empirical models, *Mater. Struct.* 42 (2009) 527–537. doi:10.1617/s11527-008-9400-z.
- [46] M. Kazemi Kamyab, Autogenous Shrinkage and Hydration Kinetics of SH-UHPFRC under Moderate to Low Temperature Curing Conditions, Doctoral thesis No: 5681, Ecole Polytechnique Fédérale de Lausanne, Switzerland, (2013).
- [47] V.Y. Garas, K.E. Kurtis, L.F. Kahn, Creep of UHPC in tension and compression: Effect of thermal treatment, *Cem. Concr. Compos.* 34 (2012) 493–502. doi:10.1016/J.CEMCONCOMP.2011.12.002.
- [48] W. Li, Z. Huang, G. Hu, W. Hui Duan, S.P. Shah, Early-age shrinkage development of ultra-high-performance concrete under heat curing treatment, *Constr. Build. Mater.* 131 (2017) 767–774. doi:10.1016/J.CONBUILDMAT.2016.11.024.
- [49] V.Y. Garas, A.R. Jayapalan, L.F. Kahn, K.E. Kurtis, Micro- and Nanoscale Characterization of Effect of Interfacial Transition Zone on Tensile Creep of Ultra-High-Performance Concrete, *Transp. Res. Rec.* 2141 (2010) 82–88. doi:10.3141/2141-14.
- [50] V.Y. Garas, L.F. Kahn, K.E. Kurtis, Short-term tensile creep and shrinkage of ultra-high performance concrete, *Cem. Concr. Compos.* 31 (2009) 147–152.
- [51] A. Kamen, E. Denarié, E. Brühwiler, Thermal effects on physico-mechanical properties of ultra-high-performance fiber-reinforced concrete, *ACI Mater. J.* 104 (2007) 415–423.
- [52] A. Kamen, E. Denarié, H. Sadouki, E. Brühwiler, Thermo-mechanical response of UHPFRC at early age — Experimental study and numerical simulation, *Cem. Concr. Res.* 38 (2008) 822–831. doi:10.1016/J.CEMCONRES.2008.01.009.
- [53] H. Yiğiter, S. Aydın, H. Yazıcı, M.Y. Yardımcı, Mechanical performance of low cement reactive powder concrete (LCRPC), *Compos. Part B Eng.* 43 (2012) 2907–2914. doi:10.1016/J.COMPOSITESB.2012.07.042.
- [54] P.R. Prem, B.H. Bhaskar Kumar, N.R. Iyer, Influence of curing regimes on compressive strength of ultra high performance concrete, *Sadhana.* 38 (2013) 1421–1431. doi:10.1007/s12046-013-0159-8.

- [55] T. (Tess) M. Ahlborn, D.K. Harris, D.L. Misson, E.J. Peuse, Characterization of Strength and Durability of Ultra-High-Performance Concrete under Variable Curing Conditions, *Transp. Res. Rec.* 2251 (2011) 68–75. doi:10.3141/2251-07.
- [56] W. Huang, H. Kazemi-Kamyab, W. Sun, K. Scrivener, Effect of cement substitution by limestone on the hydration and microstructural development of ultra-high performance concrete (UHPC), *Cem. Concr. Compos.* 77 (2017) 86–101.
- [57] N. Mahasenan, S. Smith, K. Humphreys, The Cement Industry and Global Climate Change: Current and Potential Future Cement Industry CO₂ Emissions, *Greenh. Gas Control Technol. - 6th Int. Conf.* (2003) 995–1000. doi:10.1016/B978-008044276-1/50157-4.
- [58] M.A. Nisbet, M.L. Marceau, M.G. VanGeem, Environmental Life Cycle Inventory of Portland Cement Concrete, (2002).
- [59] P. Rossi, A. Arca, E. Parant, P. Fakhri, Bending and compressive behaviours of a new cement composite, *Cem. Concr. Res.* 35 (2005) 27–33. doi:10.1016/J.CEMCONRES.2004.05.043.
- [60] E. Denarié, Recommendations for the tailoring of UHPFRC recipes for rehabilitation, deliverable ARCHES D06, (2009). <http://arches.fehrl.org>.
- [61] E. Denarié, K. Habel, J. Wuest, SAMARIS deliverable D13, Report on preliminary studies for the use of HPFRCC for the rehabilitation of road infrastructure components, (2004). <http://samaris.zag.si>.
- [62] M.A. Hafiz, A. Hajiesmaeili, E. Denarié, Tensile response of low clinker UHPFRC subjected to fully restrained shrinkage, *Cem. Concr. Res.* 124 (2019). doi:<https://doi.org/10.1016/j.cemconres.2019.105804>.
- [63] M.A. Hafiz, E. Denarié, Experimental Study of Tensile Response of Strain Hardening UHPFRC at Early Age, in: *Strain-Hardening Cem. Compos.*, Springer, Dresden, Germany, (2018): pp. 308–315.
- [64] A. Switek-Rey, E. Denarié, E. Brühwiler, Tensile creep of UHPFRC under low and high stresses, in: *4th Int. Conf. Constr. Mater. – Performance, Innov. Struct. Implic.*, Nagoya, Japan, (2009): pp. 432–437.
- [65] T. Kanakubo, Tensile Characteristics Evaluation Method for Ductile Fiber-Reinforced Cementitious Composites, *J. Adv. Concr. Technol.* 4 (2006) 3–17. doi:10.3151/jact.4.3.
- [66] H. Neuber, Der zugbeanspruchte flachstab mit optimalem querschnittsubergang, *Forsch. Im Ingenieurwes.* 35 (1969) 29–30.
- [67] S.-T. Kang, J.-I. Choi, K.-T. Koh, K.S. Lee, B.Y. Lee, Hybrid effects of steel fiber and microfiber on the tensile behavior of ultra-high performance concrete, *Compos. Struct.* 145 (2016) 37–42. doi:10.1016/J.COMPSTRUCT.2016.02.075.

- [68] SIA (2017), Cahier Technique 2052, Béton fibré ultra-performant (BFUP): Matériaux, dimensionnement et exécution, SIA, Zürich., (2017).
- [69] E. Denarié, “Recommendations for the improvement of Annexes D and E of SIA CT 2052”, private communication to Prof. Dr. Cornelius Oesterlee (Bern University of Applied Sciences, also chair of SIA CT 2052 committee), email from E. Denarié from 6.12.2016., (2016).
- [70] M.K. McVay, Spall Damage of Concrete Structures, (1988).
- [71] D. joo Kim, S. El-Tawil, A.E. Naaman, Rate-dependent tensile behavior of high performance fiber reinforced cementitious composites, *Mater. Struct.* 42 (2009) 399–414. doi:10.1617/s11527-008-9390-x.
- [72] C.A. Ross, J.W. Tedesco, M.L. Hughes, D.M. Jerome, Moisture and Strain Rate Effects on Concrete Strength, *ACI Mater. J.* 93 (1996) 293–300. doi:10.14359/9814.
- [73] H.W. Reinhardt, P. Rossi, J.G.M. van Mier, Joint investigation of concrete at high rates of loading, *Mater. Struct.* 23 (1990) 213–216. doi:10.1007/BF02473020.
- [74] P. Rossi, F. Toutlemonde, Effect of loading rate on the tensile behaviour of concrete: description of the physical mechanisms, *Mater. Struct.* 29 (1996) 116. doi:10.1007/BF02486201.
- [75] D. Yan, G. Lin, Dynamic properties of concrete in direct tension, *Cem. Concr. Res.* 36 (2006) 1371–1378. doi:10.1016/J.CEMCONRES.2006.03.003.
- [76] A.E. Naaman, Engineered Steel Fibers with Optimal Properties for Reinforcement of Cement Composites, *J. Adv. Concr. Technol.* 1 (2003) 241–252. doi:10.3151/jact.1.241.
- [77] M. Xu, B. Hallinan, K. Wille, Effect of loading rates on pullout behavior of high strength steel fibers embedded in ultra-high performance concrete, *Cem. Concr. Compos.* 70 (2016) 98–109. doi:10.1016/J.CEMCONCOMP.2016.03.014.
- [78] Kim, D. J., S. El-Tawil, A.E. Naaman, Loading rate effect on pullout behavior of deformed steel fibers, *ACI Mater. J.* 105 (2008) 576–584.
- [79] Y.-S. Tai, S. El-Tawil, T.-H. Chung, Performance of deformed steel fibers embedded in ultra-high performance concrete subjected to various pullout rates, *Cem. Concr. Res.* 89 (2016) 1–13. doi:10.1016/J.CEMCONRES.2016.07.013.
- [80] Y.-S. Tai, S. El-Tawil, High loading-rate pullout behavior of inclined deformed steel fibers embedded in ultra-high performance concrete, *Constr. Build. Mater.* 148 (2017) 204–218. doi:10.1016/J.CONBUILDMAT.2017.05.018.
- [81] K.S. Douglas, S.L. Billington, Strain rate dependence of HPFRCC cylinders in monotonic tension, *Mater. Struct.* 44 (2011) 391–404.

- [82] E. Yang, V.C. Li, Rate dependence in engineered cementitious composites, in: Int. RILEM Work. High Perform. Fiber Reinf. Cem. Compos. Struct. Appl., RILEM Publications SARL, (2006): pp. 83–92.
- [83] E. Gallucci, X. Zhang, K.L. Scrivener, Effect of temperature on the microstructure of calcium silicate hydrate (C-S-H), *Cem. Concr. Res.* 53 (2013) 185–195. doi:10.1016/j.cemconres.2013.06.008.
- [84] N. Banthia, J.-F. Trottier, Effects of curing temperature and early freezing on the pull-out behavior of steel fibres, *Cem. Concr. Res.* 19 (1989) 400–410. doi:[https://doi.org/10.1016/0008-8846\(89\)90029-X](https://doi.org/10.1016/0008-8846(89)90029-X).
- [85] V. Waller, “Relations entre composition des bétons, exothermie en cours de prise et résistance à la compression”, thèse de doctorat, LCPC, Nantes, France, (2001).
- [86] H. Mihashi, F.H. Wittmann, Stochastic Approach to Study the Influence of Rate of Loading on Strength of Concrete, *HERON*. 25 (1980) 1–55.

Chapter – 4

Paper – 3

Modelling of the tensile behavior of SH-UHPFRC at low and high stress levels, under very low loading rates

Reference: M.A. Hafiz¹, E. Denarié², Modelling of the tensile behavior of SH-UHPFRC at low and high stress levels, under very low loading rates, *submitted to Journal of Engineering Mechanics*, July 2019.

1 – corresponding author of the paper – conducted all the experiments presented in the paper as well as the calibration of the model presented, along with the writing of the full article

2 – thesis supervisor

Abstract

The tensile behavior under low loading rates governs largely the mechanical response of Strain-Hardening Ultra High Performance Fiber Reinforced Concretes (SH-UHPFRC) at early age and long term, in applications of rehabilitation. A viscoelastic-viscohardening model was developed and applied to predict the tensile response of two types of SH-UHPFRC; Mix I with pure type I cement, silica fume and steel fibers and Mix II with 50% replacement of cement with limestone filler and a similar fibrous mix, and compare their time-dependent responses. Different tensile loading conditions were investigated, including the behavior under restrained shrinkage deformations, the effect of very low monotonic strain rates, and linear and non-linear relaxation and creep tests. The predictions of the model were also compared with experimental results from literature. The interaction of ageing, hydration, early age volume changes, viscoelastic phenomena and damage and their influence on the overall tensile behavior of UHPFRC was discussed.

Keywords: UHPFRC, Strain-hardening, viscoelastic-viscohardening model, restrained shrinkage, eigenstresses, low strain rates, creep, relaxation, ageing.

1 Introduction

Strain-Hardening Ultra High Performance Fiber Reinforced Concretes (SH-UHPFRC) are very effective for rehabilitation or reinforcement applications of existing RC structures, due to their outstanding mechanical and durability properties (high tensile strength over 12 MPa, significant strain-hardening, robust in the range between 1-5‰, and sorptivity most often below $50 \text{ g/m}^2\text{h}^{0.5}$). In composite UHPFRC-concrete structures, a new layer of UHPFRC applied on existing reinforced concrete is subjected to early age volume changes such as autogenous shrinkage deformations, thermal deformations and drying shrinkage in certain situations, leading to the development of tensile eigenstresses in the material, under the restraint of the underlying substrate. These deformations, which take place at very low strain rates of about $1 \times 10^{-8} \text{ 1/s} - 1 \times 10^{-11} \text{ 1/s}$, are restrained to different extents, depending on the relative stiffness of the new layer and of the existing substrate and depending on the boundary conditions of the support. More generally, the asymptotic tensile properties of SH-UHPFRC under very low loading rates are also of primary importance for applications where deadweight dominates (buildings), without significant fatigue loading.

The tensile response of SH-UHPFRC subjected to very slow rates of deformation is influenced by various mechanisms as shown in figure 1.

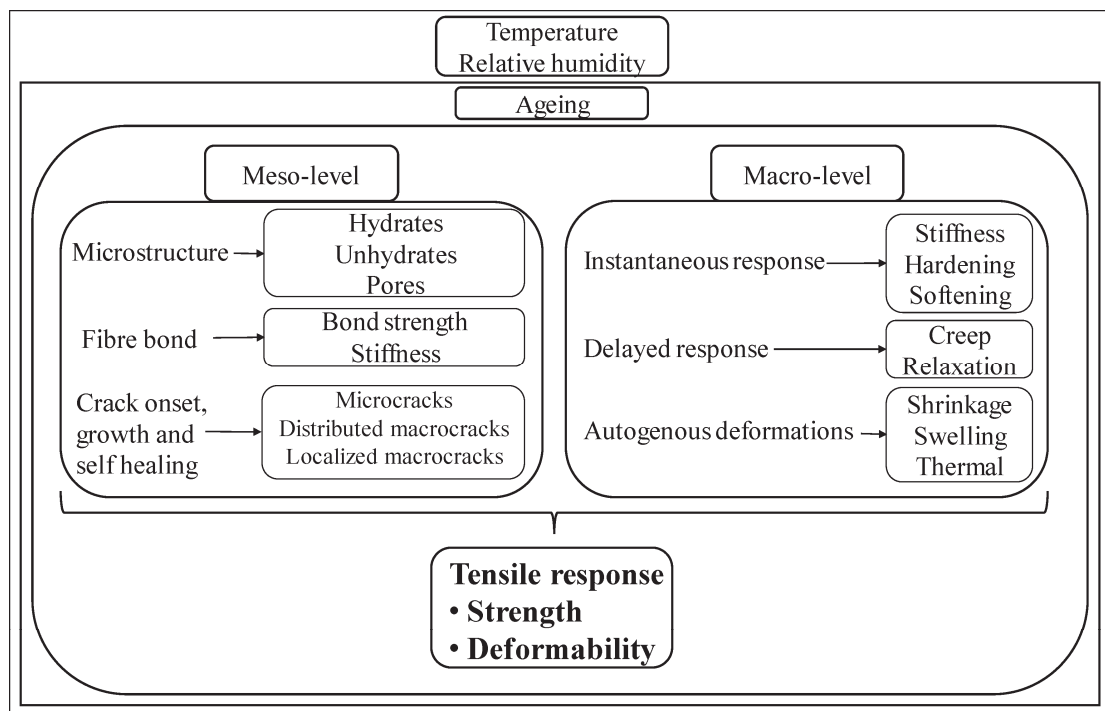


Figure 1: Mechanisms affecting the overall tensile response of UHPFRC.

The mechanism of ageing of the material influences the development of the microstructure, the bond strength between the fibers and the matrix and the onset and growth of microcracks. These meso-scale changes, in turn affect the response at the macro scale, including the development of stiffness of the material, the time dependent phenomena of creep and relaxation and the autogenous deformations like shrinkage, swelling and thermal deformations. However, these mechanisms are interdependent and their complex couplings influence the overall tensile response of the material.

Ageing is more prevalent in the younger material and [1,2] showed that most of the evolution of the degree of hydration of UHPFRC of types CM22 and CM22_TKK occurred during the first 8 days after contact of binders with water. The ongoing hydration in the early age significantly influences the early age autogenous shrinkage and viscoelastic response. [3,4] showed that the application of a thermal treatment which accelerated the hydration reactions, also led to a significant acceleration in the development of autogenous shrinkage and creep deformations, thereby confirming the influence of hydration on the autogenous shrinkage and viscoelastic response. Moreover, [5] showed that the viscoelastic response of UHPFRC of type CM22_TKK was much higher at an age of 2 days when compared to that at 7 days, and attributed this behavior to an “early age hydration induced” non-linearity. The influence of time dependent phenomena on the strength and deformability of cementitious materials was shown by [6–9] for normal concrete and more recently for SH-UHPFRC under tension by [10], with the general conclusion that the strength properties increase with an increase in the rate of loading. However, the trend of effect of strain/stress rate on the strain at tensile strength (deformability) is not fully understood. [11–16] reported an increase in the strain at tensile strength with an increase in the strain rate whereas [6,10,17] reported a decrease. Furthermore, at higher stress levels, the non-linear viscoelasticity is influenced by damage [18–22], thereby exhibiting a much higher relaxation response along the failure envelope (non-linear) when compared to that at lower stress levels. Using single step and incremental loading tests, [5] showed that SH-UHPFRC of type CM22_TKK showed non-linear creep/relaxation responses for a stress level of more than 60% of the tensile strength. Moreover, [5] also showed a much higher non-linear viscous response at a stress level of 90% when compared to that at 60%, thereby confirming the pronounced influence of damage on the non-linear viscoelasticity.

Using the solidification theory, Bazant et al. [23,24] showed the influence of ageing and hydration on the viscous behavior of normal concrete. Mazzotti et al. [25] proposed an isotropic damage model, where the combined effects of non-linear and viscous strain evolution and crack nucleation and propagation at high stresses was considered, by introducing the concepts of stress rate reduction factor and effective strain for creep damage after [26]. Similar approach was followed by [27,28] for the modelling of interaction of creep and damage. Some other works that considered the interaction of creep and damage include [29,30]. Another common way to model the viscoelastic behavior of cementitious materials is using rheological models with springs and dashpots in series or parallel. De Schutter [31] considered that depending on the development of hydration, the parameters of the spring and dashpot of a Kelvin-Voigt model evolve and can be used to predict the creep behavior of

early age concrete. The use of this model was extended by [32] by using several Kelvin-Voigt chains in series with different springs and dashpots.

In literature, the viscoplastic response of cementitious materials is mainly dealt, using two types of modelling approaches; the Perzyna model [33] and the Duvaut Lions model [34]. The interaction of creep and damage was modelled using a viscoelastic-viscoplastic rheological model by [35] using the concepts of the Duvaut Lions model, whereas similar studies were carried out using the Perzyna approach by [36,37]. [38,39] used an affinity hypothesis to compare the linear and non-linear compressive creep responses for normal concrete. Some first efforts in the modelling of viscoelastic response of UHPFRC were carried out in [1,27,40–43]. Modelling of the basic creep response of UHPC was carried out in [43–45] and that of the autogenous shrinkage of UHPC was discussed in [46,47]. A hygro-thermo-chemo-mechanical model for the prediction of the early age behavior of UHPC was discussed in [48,49]. However, the interaction of effects like ageing, stress levels, loading history and their couplings were not considered in these models for UHPFRC.

In this paper, a new viscoelastic-viscohardenening model is presented and applied to predict the tensile response of two types of SH-UHPFRC; Mix I with pure type I cement, silica fume and steel fibers and Mix II with 50% replacement of cement with limestone filler and a similar steel fibrous mix. The parameters of the model were calibrated using three different types of tests; full restraint tests in the Temperature Stress Testing Machine (TSTM), uniaxial tensile tests at three different strain rates (1×10^{-5} 1/s, 1×10^{-7} 1/s and 1×10^{-8} 1/s) and relaxation tests in the non-linear (hardening) domain. After calibration, the model was used to study the effect of different degrees of restraint on the eigenstresses development, to compare the linear viscoelastic behavior of Mix I and II and to predict the experimental tests under creep loading. The predictions of the model were also compared with experimental results from literature. The interaction of the various mechanisms like ageing, hydration, early age volume changes, viscoelastic phenomena and damage and their influence on the overall tensile behavior of UHPFRC was discussed.

2 Viscoelastic – viscohardenening model

2.1 Overview

Many studies in literature consider a viscoplastic behavior of cementitious materials in the domain after the elastic limit. However, most of these works are done for non-hardening materials like normal concrete where the viscoplasticity mainly occurs in the softening domain [35,36]. To the best of author's knowledge, not many works have been done to predict the tensile viscous response in the hardening domain of strain-hardening fiber reinforced cementitious materials [37]. The hardening response in [37] has been simplified as a linear hardening one.

For stress development under very low strain rates, as in the case of eigenstresses development under restrained shrinkage, the influence of viscosity is expected even in the hardening domain of cementitious materials, and therefore needs to be considered. The effect of ageing on the non-linear viscous response could also be implemented depending on the age at testing and duration of the tests.

As such, an ageing viscoelastic-viscoshardening model based on generalized Maxwell schemes (VE-VH model) was developed to predict the tensile response of the material under different loading conditions. The material was assumed to behave as homogenous both in the elastic domain as well as in the hardening domain. Two sets of Maxwell chains were used to predict the overall behavior of the material, as shown in figure 2, with a trilinear tensile response. Note that the two sets act neither in series nor in parallel, but act one after the other. Below the elastic limit, only the first set of chains (M1) was active, which captures the ageing viscoelastic behavior, whereas above the elastic limit, only the second set of chains (M2) was active which predicts the viscous hardening behavior. The model can be considered as a generalized version of the Duvaut-Lions scheme [34], with generalized Maxwell models before and after the elastic limit (5 chains each in the present study). Additionally, to represent the progressive change of the hardening slope after the elastic limit, the hardening modulus (E_i) in M2 were made strain dependent. Moreover, for simplification of the model, the history effect on the stresses before the elastic limit (in M1) was not considered on the stresses after the elastic limit (in M2).

However, the presented model is only a combination of two linear models one after the other. The model does not contain any plasticity conditions, and therefore cannot be considered as a fully viscoplastic model in the hardening domain. Moreover, the model does not include the effect of damage in the hardening domain, and does not consider the effect of the same on the unloading slopes in the hardening domain. It might be possible to simplify the model into a more physical visco-damage model by considering the unloading slopes, for which the Maxwell parameters evolve with the microcrack damage.

The elastic limit f_{Ute} is the stress level until which the tensile stresses are proportional to the strains. The f_{Utu} and ϵ_{Utu} correspond to the coordinates of the peak stress in the tensile response. Figure 2 shows that in the elastic domain before f_{Ute} the tensile response has a single slope, which correspond to the elastic modulus of the material, whereas in the hardening domain after f_{Ute} , two slopes are considered depending on the strain level, both of which are generalized as hardening slope in this study, to adequately represent the investigated materials. The tensile properties like f_{Ute} , f_{Utu} and ϵ_{Utu} are sensitive to the applied strain rate/ stress rate. The influence of very low strain rates on the tensile properties of the mixes in the present study was discussed in detail in Chapter 3 [10]. The elastic limit is the point that separates the activation of M1 and M2, and therefore it is very important to include the effect of strain rates on the elastic limit in the model. This was done by using experimental results from Chapter 3 [10] as discussed later in section 4.4. The influence of strain rates on the other mechanical properties and the possible effects in the model are also discussed in section 4.4.

In figure 2,

E_k = stiffness of the spring element in Maxwell unit k in M1;

E_l = stiffness of the spring element in Maxwell unit l in M2;

τ_k = retardation time of the dashpot element in Maxwell unit k in M1;

τ_l = retardation time of the dashpot element in Maxwell unit l in M2;

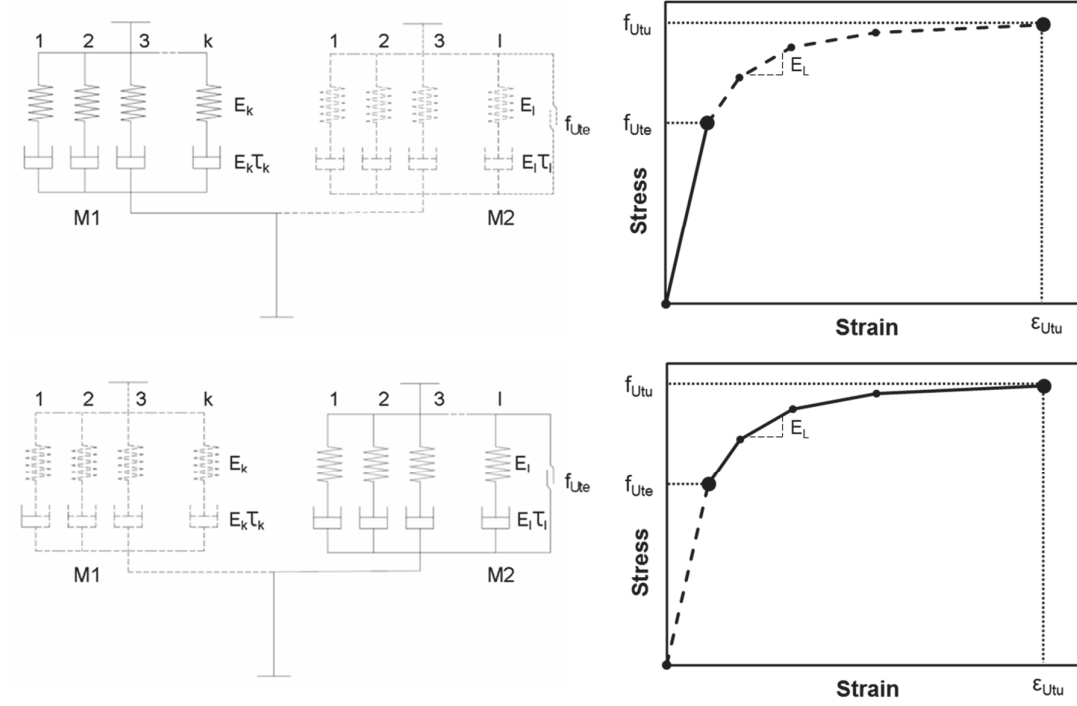


Figure 2: Schematic representation of the Viscoelastic-Viscohardenening model with M1 acting below the elastic limit and M2 acting above the elastic limit.

In the VE-VH model, if \mathcal{E} , $\mathcal{E}_{VE(M1)}$ and $\mathcal{E}_{VH(M2)}$ represent the total strain, viscoelastic strain in M1 and viscohardenening strain in M2 respectively and if σ , $\sigma_{VE(M1)}$ and $\sigma_{VH(M2)}$ represent the total stress, stress in M1 and stress in M2 respectively, then the total strain and stress at any point is given by,

$$\mathcal{E} = \mathcal{E}_{VE(M1)} + \mathcal{E}_{VH(M2)} \quad (1)$$

$$\sigma = \sigma_{VE(M1)} + \sigma_{VH(M2)} \quad (2)$$

Below the elastic limit, $\epsilon_{VH(M2)}=0$ and $\sigma_{VH(M2)}=0$; therefore,

$$\epsilon = \epsilon_{VE(M1)} \quad (3)$$

$$\sigma = \sigma_{VE(M1)} \quad (4)$$

Above the elastic limit, $\epsilon_{VE(M1)}= \epsilon_{Ute}$ and $\sigma_{VE(M1)}=f_{Ute}$; therefore,

$$\epsilon = \epsilon_{Ute} + \epsilon_{VH(M2)} \quad (5)$$

$$\sigma = f_{Ute} + \sigma_{VH(M2)} \quad (6)$$

2.2 Incremental constitutive relationship

An incremental constitutive relationship after [50] was used to predict the development of the eigenstresses, by applying Boltzmann's superposition principle. Equation (7) shows the stress development in a single Maxwell chain using the incremental procedure. Assuming a constant incremental strain rate of $\Delta\epsilon^i$ in a time interval from t^i to t^{i+1} , the stress at the end of the interval is given by the sum of the stress at the beginning of step i , decaying according to a Maxwell model, and the stress due to the effect of a strain increment $\Delta\epsilon^i$ applied linearly from time t^i to time t^{i+1} .

$$\sigma_k^{i+1} = \frac{\tau_k}{\Delta t} \cdot \left(\frac{E_k^{i+1} + E_k^i}{2} \right) \cdot \left(1 - e^{-\frac{\Delta t}{\tau_k}} \right) \cdot \Delta\epsilon^i + \sigma_k^i \cdot e^{-\frac{\Delta t}{\tau_k}} \quad (7)$$

where,

σ_k^{i+1} = stress in Maxwell unit k at the end of the time interval Δt ;

σ_k^i = stress in Maxwell unit k at the beginning of the time interval Δt ;

E_k^{i+1} = stiffness of the spring element in Maxwell unit k at the end of the time interval Δt ;

E_k^i = stiffness of the spring element in Maxwell unit k at the beginning of the time interval Δt ;

$\Delta \varepsilon^i$ = strain increment in time Δt ;

Δt = duration of the time interval;

Hence, for a generalized Maxwell model with m Maxwell units, the total stress is given by,

$$\sigma^{i+1} = \sum_{k=1}^m \left[\frac{\tau_k}{\Delta t} \cdot \left(\frac{E_k^{i+1} + E_k^i}{2} \right) \cdot \left(1 - e^{-\frac{\Delta t}{\tau_k}} \right) \right] \cdot \Delta \varepsilon^i + \sum_{k=1}^m \sigma_k^i \cdot e^{-\frac{\Delta t}{\tau_k}} \quad (8)$$

2.2.1 Below the elastic limit

Below the elastic limit, the material behaves as viscoelastic and only M1 is active. Due to a strain increment of $\Delta \varepsilon^i = \Delta \varepsilon_{VE(M1)}^i$ in time interval Δt , the total stress at the end of the time interval Δt , σ^{i+1} is given by,

$$\sigma^{i+1} = \sum_{k=1}^m \left[\frac{\tau_k}{\Delta t} \cdot \left(\frac{E_k^{i+1} + E_k^i}{2} \right) \cdot \left(1 - e^{-\frac{\Delta t}{\tau_k}} \right) \right] \cdot \Delta \varepsilon_{VE(M1)}^i + \sum_{k=1}^m \sigma_k^i \cdot e^{-\frac{\Delta t}{\tau_k}} \quad (9)$$

2.2.2 Above the elastic limit

The stress development in M2 can be derived in the same way as that of M1 and is shown in equation (10). In this domain, the strain increment in any time interval Δt is given by, $\Delta \varepsilon^i = \Delta \varepsilon_{VH(M2)}^i$. Using equations (6) and (8), the total stress, in the domain above the elastic limit is given by,

$$\sigma^{i+1} = f_{Ute} + \sum_{l=1}^n \left[\frac{\tau_l}{\Delta t} \cdot \left(\frac{E_l^{i+1} + E_l^i}{2} \right) \cdot \left(1 - e^{-\frac{\Delta t}{\tau_l}} \right) \right] \cdot \Delta \varepsilon_{VH(M2)}^i + \sum_{l=1}^n \sigma_l^i \cdot e^{-\frac{\Delta t}{\tau_l}} \quad (10)$$

2.3 Summary

Equation (9) can be used to predict the viscoelastic behavior under the elastic limit and equation (10) can be used to predict the viscohardening behavior above the elastic limit. The model was extended to include the effect of degree of restraint acting on the system, as shown in Appendix B and discussed in section 5.1. The calibration of the parameters of the model for the mixes in the present study will be described in detail in section 4.

3 Materials

The developed model was used to predict the tensile response of two types of Strain-Hardening UHPFRC mixes; Mix I and Mix II both from the CEMTEC_{multiscale}[©] family. Mix I was a UHPFRC of type CM22_TKK_b, which has a matrix composed of cement (CEM I 52.5 HTS from Le Teil, Lafarge), white microsilica (SEPR, BET = 14 m²/gr), superplasticizer (Zementol Zeta Super S from TKK, Slovenia) and water. However, the degree of hydration of Mix I was only about 30% after one month [2,51], and therefore 50% of the cement in Mix I was replaced with inert limestone filler to produce Mix II, which was a UHPFRC of type CM22_TKK_LF. Mix II contains two types of limestone fillers: Betoflow D[®] and Betocarb SL[®] (OMYA), of different gradings. Both mixes had a fibrous mix containing two types of steel fibers; microfibers and macrofibers, with a total dosage of 9% by volume after the concepts developed by Rossi et al. [52]. The detailed compositions of Mix I and II are given in Table 1 and the properties in the fresh state are given in Table 2. More details regarding the mechanical properties and the chemical compositions of the mixes could be found in Chapter 2 [51].

Table 1: Compositions of Mix I and II.

Material	Mix I	Mix II
	[kg/m ³]	[kg/m ³]
Cement, CEM I 52.5 le Teil	1467.0	733.7
Silica fume, SEPR	381.4	293.5
Limestone filler 1 (Betocarb SL [®])	--	223.0
Limestone filler 2 (Betoflow D [®])	--	510.6
Steel fibers (straight macro fibers; l _f = 10 mm, d _f = 0.2 mm and microfibers/steel wool)	706.5	706.5
Total water	225.8	217.9
Superplasticizer from TKK, Slovenia; Zementol zeta super S; polycarboxylate; 25% solid content; (total amount)	20.5	14.7

Table 2: Properties of Mix I and II in the fresh state (average value from 4 tests).

Property	Units	Mix I	Mix II
Workability (ASTM - spread after 25 blows)	mm	179	146
Specific weight	kg/m ³	2834	2695
Air content	%	3.2	4.7

4 Calibration of the model

4.1 Overview

The experimental tests that were used for the calibration of these parameters are shown in Table 3 and explained in sections 4.2 – 4.6.

Table 3: The list of parameters of the VE-VH model and the tests used for their calibration.

Parameter	Test used for calibration
Stiffness of the material, $E_{tot,M1}$	Vibration resonance frequency tests (VRFT)
M1 parameters; E_k and τ_k	Full restraint tests in Temperature Stress Testing Machine (TSTM)
Hardening modulus, $E_{L,M2}$	Uniaxial tensile tests in KAPPA 250 DS electromechanical test setup from ZWICK/ROELL
M2 parameters; E_l and τ_l	Relaxation tests in the hardening domain in KAPPA 250 DS electromechanical test setup from ZWICK/ROELL
Strain rate sensitivity of elastic limit	Uniaxial tensile tests in KAPPA 250 DS electromechanical test setup from ZWICK/ROELL

From equations (9) and (10), the parameters for the prediction of the stresses in the material include, at a given age,

- a) The development of the stiffness of the material, $E_{tot,M1}$ for M1 such that

$$E_{tot,M1} = \sum_{k=1}^n E_k$$

- b) The Maxwell chain parameters E_k and τ_k for M1
- c) The slope of the response in the hardening domain or hardening modulus, $E_{L,M2}$ for M2 such that $E_{L,M2} = \sum_{l=1}^n E_l$
- d) The Maxwell chain parameters E_l and τ_l for M2, where E_l is considered to be dependent on the strain level in the hardening domain.

The calibrated parameters are given in Appendix A at the end of the chapter.

4.2 Calibration of $E_{tot,M1}$ – Vibration resonance frequency tests (VRFT)

The development of stiffness or elastic modulus of the mixes were studied using the Vibration Resonance Frequency test. The automatic setup was developed by [2,53] following the works of [54]. Cylindrical specimens 140 mm in length and 70 mm in diameter, kept in a climate room maintained at 20 °C +/- 1 °C, were used for the tests. The specimens were hit at their centers, at one end, with a spherical steel ball, that produced longitudinal vibrations in the specimens, which were measured using an accelerometer fixed on the other end of the cylinder. Using an analytical procedure developed by [54], the elastic modulus was determined at different ages. Two tests were conducted for each mix and the respective average curves were considered to obtain the values of $E_{tot,M1}$. Figure 3 shows the development of the elastic modulus for both mixes. Detailed discussion regarding the trends of the same could be found in Chapter 2 [51].

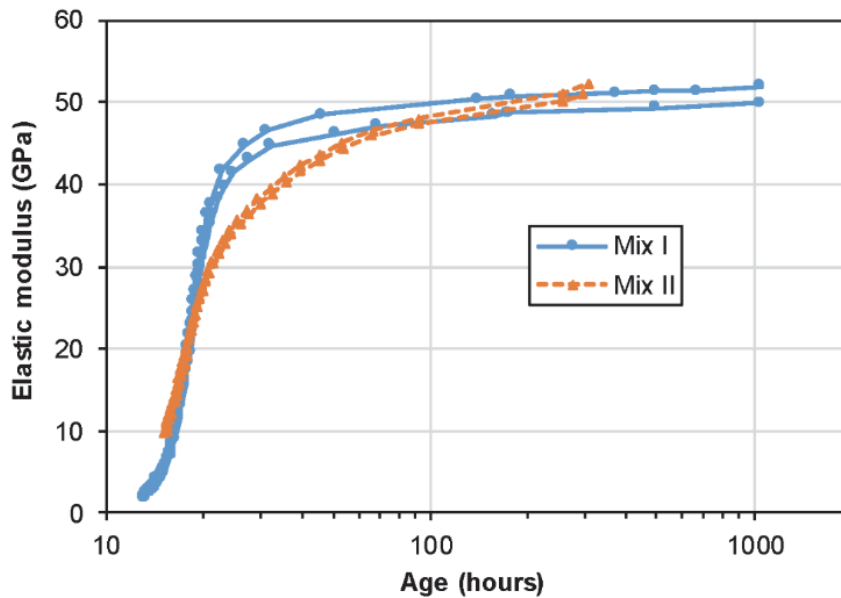


Figure 3: Development of elastic modulus for Mix I and II at 20 °C from the VRF tests.

4.3 Calibration of M1 parameters, E_k and τ_k – Full restraint tests in TSTM

In order to determine the ageing viscoelastic parameters of M1, tests under full restraint of shrinkage deformations were performed using a Temperature Stress Testing Machine (TSTM). More details regarding the test setup could be found in [5,55]. A closed loop procedure was developed, to impose full restraint conditions on the material, and to measure the corresponding development of eigenstresses. Two full restraint tests were conducted for each mix (Mix I-20C-FR1, Mix I-20C-FR2, Mix II-20C-FR1, Mix II-20C-FR2) in the RS setup and the associated free autogenous deformations were measured in the FS setup. The average elastic limit in the eigenstresses development for Mix I was calculated as 12.5 MPa, whereas for Mix II the eigenstresses did not reach the strain-hardening domain even at the end of three months, but only approached it. Figure 4 shows the development of autogenous deformations in the TSTM.

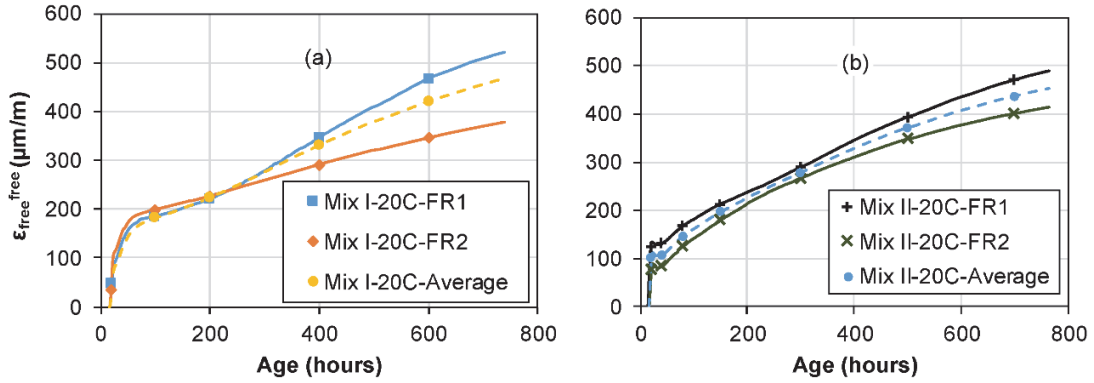


Figure 4: Evolution of autogenous deformations (zeroed at the end of swelling) in the FS setup of TSTM at 20 °C for a) Mix I, b) Mix II.

The average of the eigenstresses development in the full restraint tests below the elastic limit, was considered for the calibration of the respective parameters of M1; E_k and τ_k for both mixes. The values of the retardation times τ_k were considered in such a way so as to cover the entire duration of the tests. As such, five Maxwell chains were selected with the respective retardation times of 1, 10, 100, 1000 and 10000 hours, which cover the entire duration of the tests. The calibration of E_k was done using a least square fit regression analysis so that the development of eigenstresses in the TSTM tests were closely predicted

by the model using equation (9), with the condition $E_{tot,M1} = \sum_{k=1}^5 E_k$, where $E_{tot,M1}$ was

obtained as explained in section 4.2. The $\Delta \varepsilon_{VE(M1)}^i$ in equation (9) for the full restraint tests was obtained from the average development of the autogenous shrinkage as shown in figure 4. Figures 5 and 6 show the development of the eigenstresses under full restraint in Mix I and II respectively, along with the predictions of the viscoelastic part of the VE-VH model (below the elastic limit).

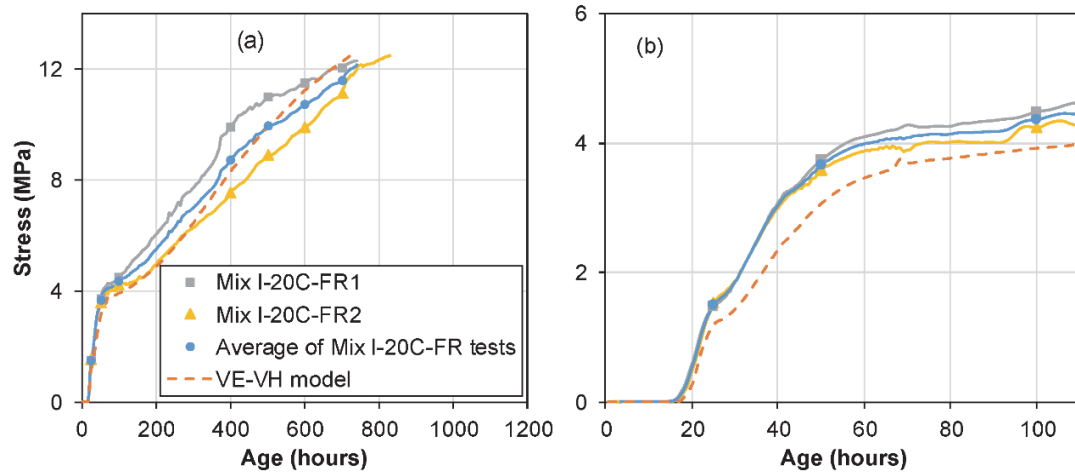


Figure 5: Model prediction of the development of eigenstresses in Mix I under full restraint conditions below the elastic limit, along with the experimental full restraint tests for Mix I at 20 °C; a) overall trend, b) early age behavior.

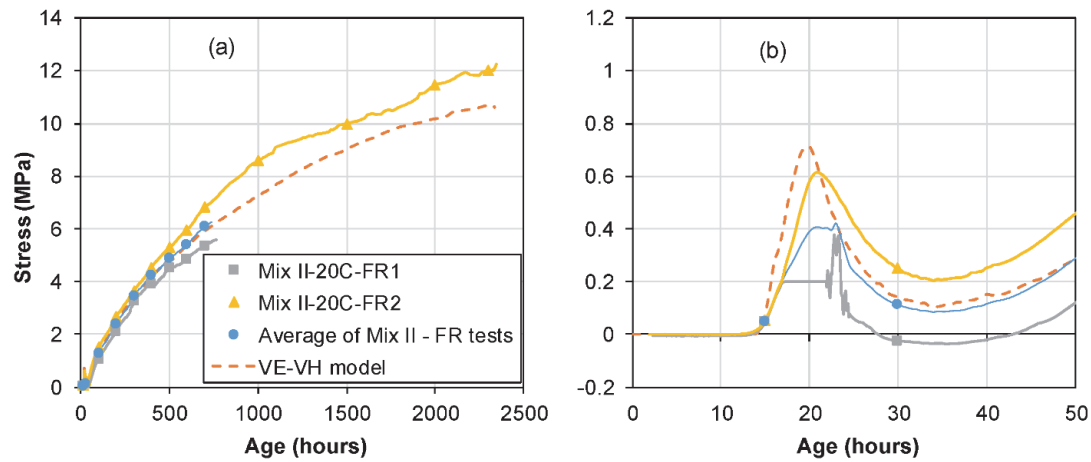


Figure 6: Model prediction of the development of eigenstresses in Mix II under full restraint conditions below the elastic limit, along with the experimental full restraint tests for Mix II at 20 °C; a) overall trend, b) early age behavior.

4.4 Calibration of $E_{L,M2}$ and the influence of strain rates– uniaxial tensile tests

For the calibration of slope of the tensile response in the hardening domain $E_{L,M2}$, uniaxial tensile tests under different monotonic strain rates were used. These tests were chosen for the calibration of $E_{L,M2}$ as the tests were done until the end of hardening domain unlike the full restraint tests. The tests were carried out on dumbbell specimens with a center cross section of 50 mm x 30 mm, at three different strain rates; $1 \times 10^{-5} \text{ s}^{-1}$ (quasi static strain rate), $1 \times 10^{-7} \text{ s}^{-1}$ (low strain rate) and $1 \times 10^{-8} \text{ s}^{-1}$ (very low strain rates), at an age of 14 days. More details regarding the test setup and specimen preparation could be found in Chapter 3 [10].

Table 4 summarizes the results of the uniaxial tensile tests and the overall response of both mixes under different strain rates were simplified into trilinear responses as shown in figure 7. With a decrease in the strain rate, the elastic limit was found to decrease whereas the strain at tensile strength was found to increase. The elastic modulus and tensile strength were found to be insensitive to the strain rate. More details and discussions regarding the test results could be found in Chapter 3 [10].

Table 4: Tensile mechanical properties of Mix I and II under different strain rates.

Mix	Strain rate (1/s)	Elastic limit, f_{Ute} (MPa)	Stress at 0.4‰ of strain (MPa)	Tensile strength, f_{Utu} (MPa)	Strain at tensile strength, ϵ_{Utu} (‰)
Mix I at 20 °C	1×10^{-5}	12.3 ± 1.7	14.8 ± 1.3	18.0 ± 3.1	1.64 ± 0.44
	1×10^{-7}	10.0 ± 1.3	12.8 ± 1.6	16.4 ± 4.0	1.70 ± 0.71
	1×10^{-8}	9.6 ± 0.9	12.7 ± 1.2	15.8 ± 3.0	1.75 ± 0.40
Mix II at 20 °C	1×10^{-5}	11.1 ± 1.9	13.4 ± 1.7	15.1 ± 2.7	1.27 ± 0.51
	1×10^{-7}	10.3 ± 0.9	13.2 ± 1.1	16.4 ± 2.7	1.75 ± 0.29
	1×10^{-8}	10.2 ± 1.7	13.8 ± 1.3	17.2 ± 1.9	2.05 ± 0.61

Using the experimental results of elastic limit at different strain rates in Table 4, general equations were proposed for the elastic limit of both mixes, given by equations (11) and (13), Table 5. A similar equation was also proposed for ϵ_{Utu} of Mix I, as given by equation (12). However, a general equation was not proposed for ϵ_{Utu} of Mix II, even though it showed a trend of increasing values with decreasing strain rate, due to the very large scatter in the results. Because of the observed strain rate insensitivity of elastic modulus and tensile strength in the studied range of strain rate, no general equations were proposed.

Table 5: General equations for the elastic limit and strain at tensile strength for Mix I and II.

Mix	Property	General equation
Mix I	Elastic limit	$f_{Ute} = 0.412 * \ln(\dot{\epsilon}) + 16.957$ (11)
	Strain at tensile strength	$\epsilon_{Utu} = -0.016 * \ln(\dot{\epsilon}) + 1.459$ (12)
Mix II	Elastic limit	$f_{Ute} = 0.140 * \ln(\dot{\epsilon}) + 12.696$ (13)

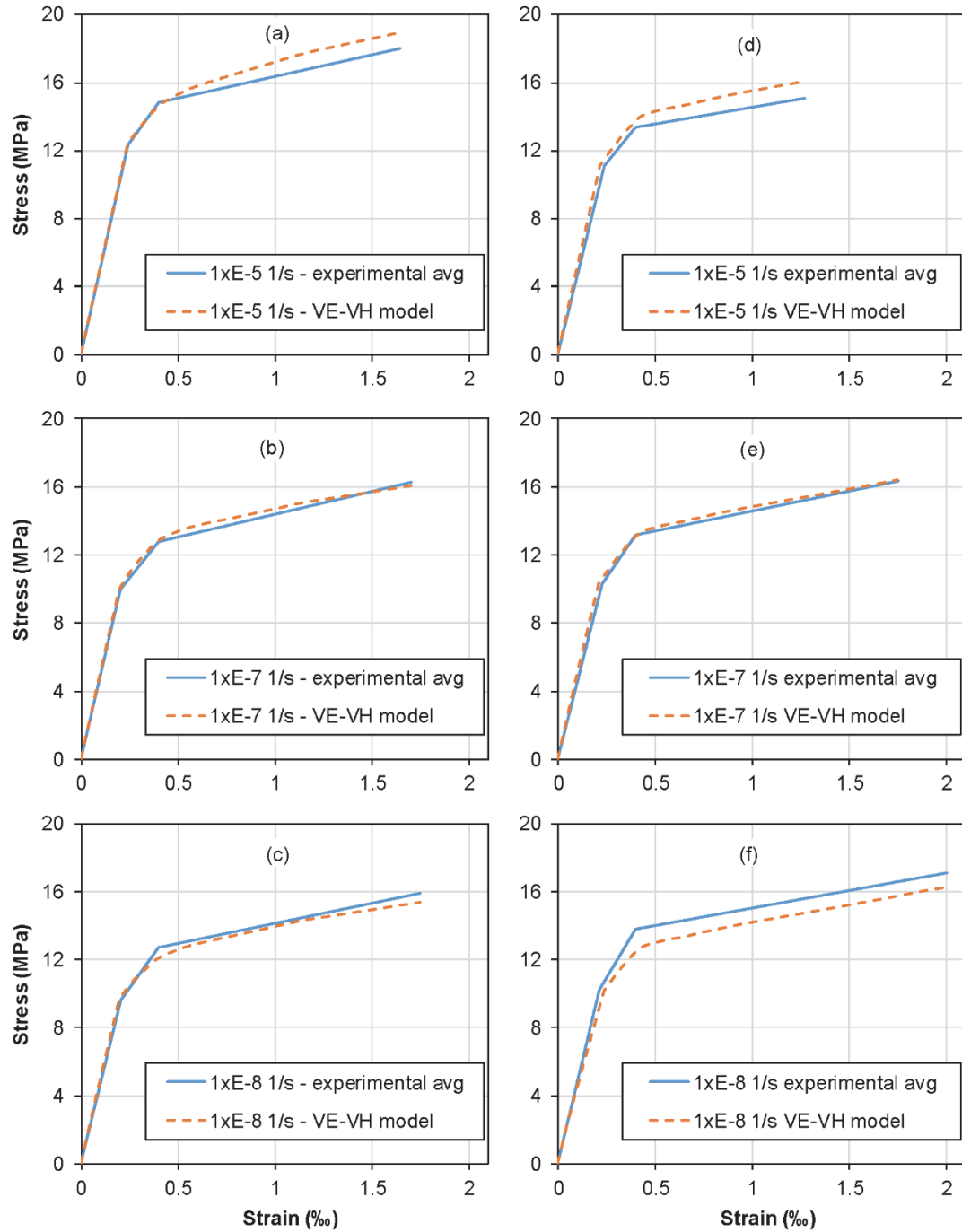


Figure 7: Prediction of the tensile response under different strain rates for; a,b,c) Mix I and d,e,f) Mix II.

As indicated earlier, $E_{L,M2}$ accounts for the slope of the tensile response in the hardening domain after the elastic limit. Due to the formation of microcracks after the elastic limit, the stiffness of the material is reduced. The damage and the corresponding reduction in the stiffness become more as the strain level (or stress level) increases along the hardening domain, and as such $E_{L,M2}$ was considered as a function of the strain level, in the model.

However, for the ease of implementation in equation (10), the time corresponding to a particular strain level was found out using linear interpolation. $E_{L,M2}$ was calibrated using a least square fit regression analysis, so that the experimental tensile responses of the mixes in the hardening domain at three different strain rates (1×10^{-5} 1/s, 1×10^{-7} 1/s and 1×10^{-8} 1/s), as shown in figure 7, were closely predicted. However, since these tests were conducted only at an age of 14 days, the observed parameters are applicable only after this age. More discussions regarding the observed trends at different strain rates will be carried out in sections 5.6 and 5.7, along with a parametric study at strain rates lower than 1×10^{-8} 1/s.

4.5 Calibration of M2 parameters, E_I and τ_I – Non-linear relaxation tests in the hardening domain

For the calibration of the M2 parameters; E_I and τ_I , non-linear relaxation tests were carried out in the electromechanical testing machine, KAPPA 250 DS from ZWICK/ROELL. The specimen used was the same as that of the uniaxial tests, with a center cross section of 50 mm x 30 mm. A monotonic strain rate of 1×10^{-5} 1/s was applied on the specimen until a strain level of 0.8 ‰, which is in the strain-hardening domain of the tensile response. The specimen was then kept at the same strain level of 0.8 ‰ and the relaxation in the stresses was measured. Two tests were carried out only for Mix I at an age of 14 days, out of which one test had to be stopped abruptly due to a power failure.

The values of τ_I were considered one order smaller than that of the M1 in order to predict the higher viscous responses. Five Maxwell chains of retardation times 0.1, 1, 10, 100 and 1000 hours were considered. The values of the parameter E_I were determined using a least square fit regression analysis such that the experimental non-linear relaxation test as shown in figure 8 was closely predicted.

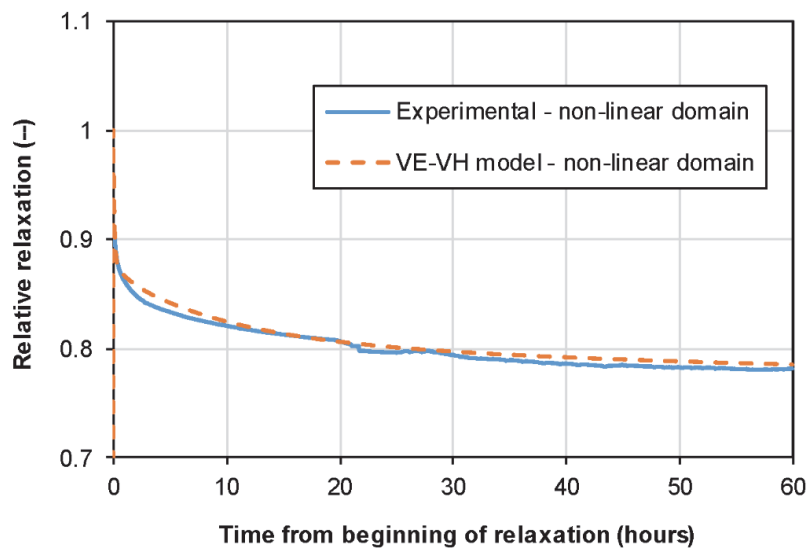


Figure 8: Experimental test and prediction of relaxation response of Mix I in the non-linear domain, loaded at an age of 14 days to a strain level of 0.8‰.

However, the test was conducted only for Mix I at an age of 14 days and a strain level of 0.8 ‰. Due to the lack of experimental results, it was assumed that the parameters are the same for other strain levels along the hardening domain. It should be noted that, if experiments were done at other strain levels in the hardening domain and the corresponding parameters were calibrated as before, the changing trend of non-linear relaxation along the hardening domain at different strain levels could also be predicted using the model. Furthermore, since no experimental tests were done to study the relaxation behavior in the non-linear domain for Mix II, the same parameters as obtained for Mix I were assumed for Mix II, as a very crude approximation.

4.6 Combination of M1 and M2 applied to TSTM results

Figure 9 shows the development of eigenstresses under full restraint for Mix I at 20°C, along with the prediction of both M1 and M2 of the VE-VH model. For the test Mix I-20C-FR2, the eigenstresses development has crossed the elastic limit of 12.5 MPa, and has proceeded further into the hardening domain. As such, the prediction of the eigenstresses have a combination of the predictions from M1 (below 12.5 MPa) and M2 (above 12.5 MPa). There is a close correlation between the experimental results and the model prediction.

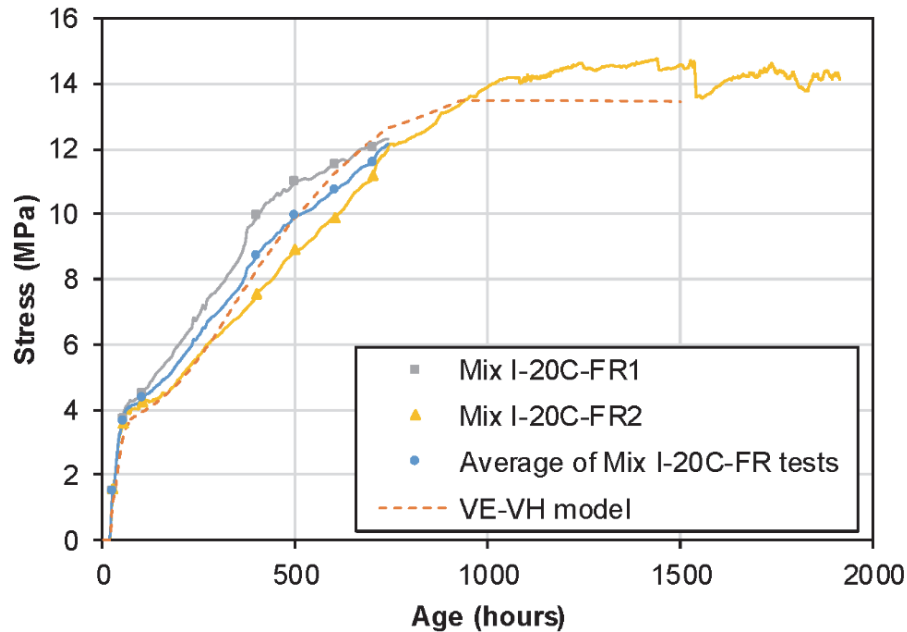


Figure 9: Prediction of the eigenstresses development under full restraint for Mix I at 20 °C, above and below the elastic limit using M1 and M2 of the VE-VH model.

5 Applications and discussions

5.1 Effect of degree of restraint on the development of eigenstresses

5.1.1 Modelling of tests with partial restraint

The effect of different degrees of restraint acting on the specimens was implemented in the VE-VH model using an additional restraint spring with a stiffness of E_0 , which acts in series with both sets of Maxwell chains, as shown in figure B.1 in Appendix B. The derivation of the incremental constitutive relations for the same is detailed in Appendix B.

The predictions of the model were compared to experimental results under a finite restraint, two partial restraint tests were also conducted using the TSTM for Mix I at 20 °C; Mix I-20C-PR1 and Mix I-20C-PR2. The partial restraint tests were conducted using a passive stroke control method as explained in detail in Chapter 2 [51]. Using equation (14), the degree of restraint in a partial restraint test in the TSTM was calculated, where ϵ_{free}^{free} is the free deformation measured in the FS setup and ϵ_{res}^{free} is the free deformations measured in the RS setup in a partial restraint test. More details regarding the derivation of equation (14) could be found in [56]. The degree of restraint acting in the two partial restraint tests were calculated to be $50\% \pm 6\%$.

$$\mu = 1 - \frac{\epsilon_{res}^{free}(t)}{\epsilon_{free}^{free}(t)} \quad (14)$$

In order to predict these experimental results, the stiffness of the restraint spring E_0 was chosen such that the value of μ in equation (B.7) becomes 50%. Figure 10 shows the predictions of the model under the average degree of restraint of 50% along with the scatter band. The experimental results from the Mix I-20C-PR1 and Mix I-20C-PR2 tests are also shown in the figure. Figure 10 shows that the results from the experimental tests fall well inside the scatter band of the prediction of the model. However, the kinetics of the eigenstresses development is slightly different, which can be attributed to the possible difference in the kinetics of development of autogenous deformations in the FS and RS setup of the TSTM. In the full restraint tests (which were used to calibrate the model), the entire autogenous shrinkage contributes to the development of the eigenstresses so that the kinetics of development of eigenstresses follow that of the autogenous deformations. This is evident from figure 6b, where the eigenstresses even show a decrease just after 20 hours, which corresponds to the decrease in the autogenous shrinkage at a similar age. However, in the partial restraint tests, only a part of the autogenous shrinkage contributes to the development of the eigenstresses, and as such, the kinetics of eigenstresses development is different from that of the autogenous shrinkage, and therefore also different from the kinetics of the eigenstresses development in full restraint tests.

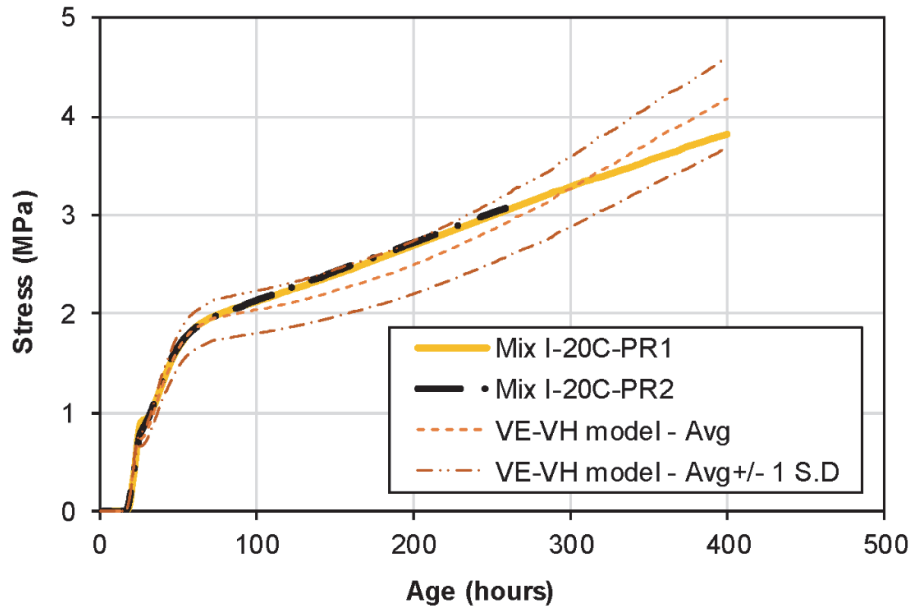


Figure 10: Model prediction of the development of eigenstresses under partial restraint conditions, along with the experimental partial restraint tests for Mix I at 20 °C.

5.1.2 Parametric study – effect of degree of restraint

A parametric study was made to predict the eigenstresses development under various degrees of restraint. [57] showed that depending on the stiffness of the existing structure, the degree of restraint in the new layer of UHPFRC will vary from about 40% to 90% and more. Figure 11 shows the predictions of the model under these restraint conditions for both Mix I and II.

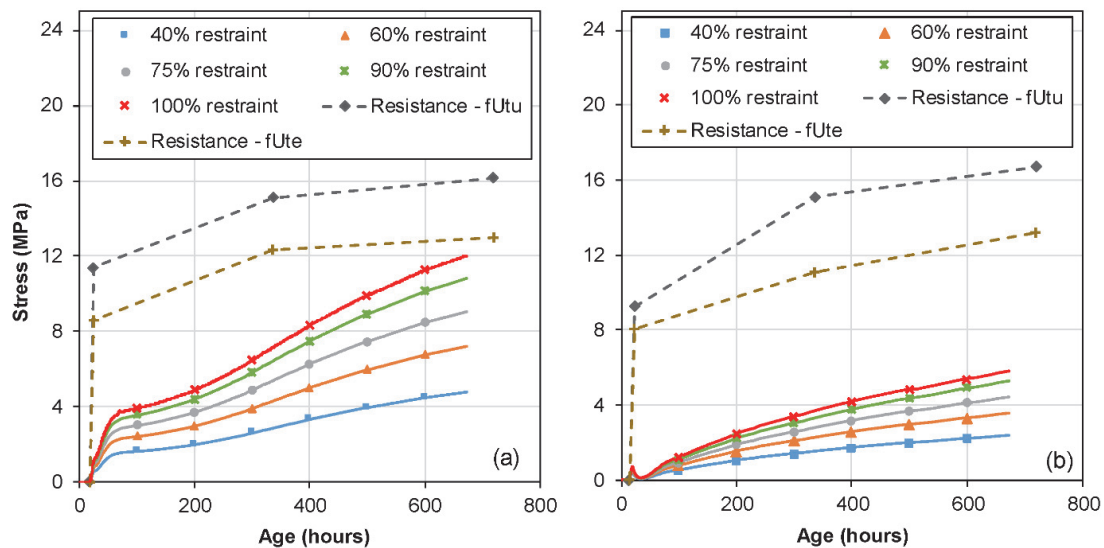


Figure 11: Prediction of the development of eigenstresses under different restraint conditions for; a) Mix I, b) Mix II. The resistance curves of f_{Ute} and f_{Utu} are also shown.

The resistance curves of elastic limit as well as the tensile strength, measured from experimental fracture tests at 1, 14 and 30 days are also shown. The eigenstresses after one month for Mix I are much higher than that of Mix II, and even reaching close to the quasi-static resistance curve of the elastic limit for a degree of restraint of 90%. However, for Mix II, even at a degree of restraint of 90%, the developed eigenstresses are much lower than the resistance curves at the end of one month.

5.2 Relaxation behavior before the elastic limit

5.2.1 Comparison with literature

The predictions of the VE-VH model were compared with experimental relaxation test results, for tests done in the linear domain by [5]. The UHPFRC used in [5] of type CM22_TKK, was closely related to Mix I in the current study (with the exceptions of very small quantity of sand and slightly higher dosage of superplasticizer in CM22_TKK). The relaxations were done at an age of 3 days at a stress level of 30% of the tensile strength at that age. The experimental results are shown in figure 12 along with the predictions of the current VE-VH model, which shows a good correlation. The scatter in the relaxation response in the experiments is evident, with specimen FL_19 and FL_22 showing a relative relaxation of 18% and 35% respectively at an age of 24 hours after loading.

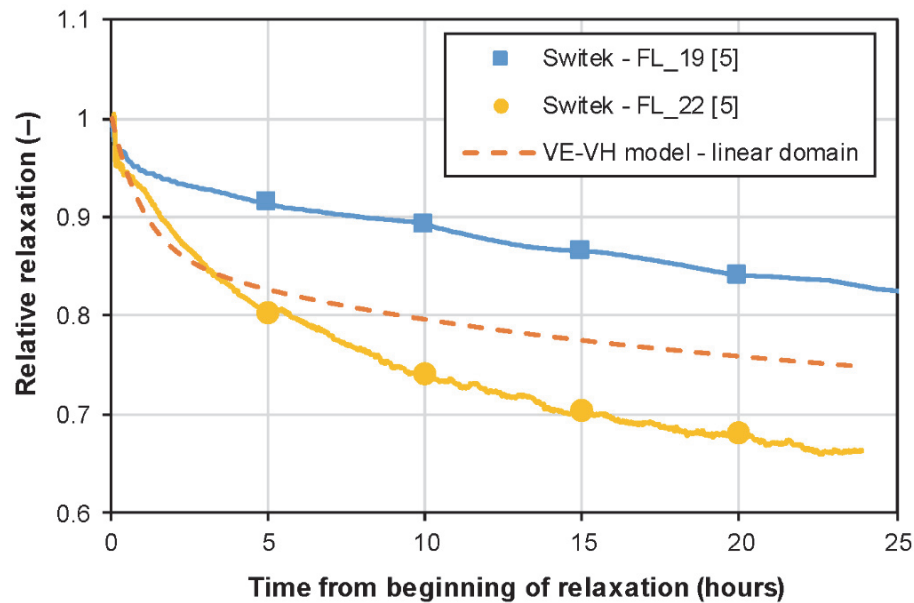


Figure 12: Experimental results of linear relaxation response of CM22_TKK, for a loading age of 3 days to a stress level of 30% of the tensile strength [5], along with the prediction of the VE-VH model.

5.2.2 Parametric study

In order to compare the relaxation responses at different ages of loading for Mix I and II, a parametric study was carried out. Figure 13 shows the comparison of the relaxation responses of Mix I and II at different loading ages, which shows a significantly higher relaxation for Mix II at every age. The trend is similar to that observed in tensile creep tests wherein Mix II shows a much higher creep response than Mix I, when loaded under similar stress levels, as discussed in Chapter 2 [51]. The relaxation of Mix II is considerably higher than Mix I in the early ages, whereas the difference between the two reduces as the loading age increases.

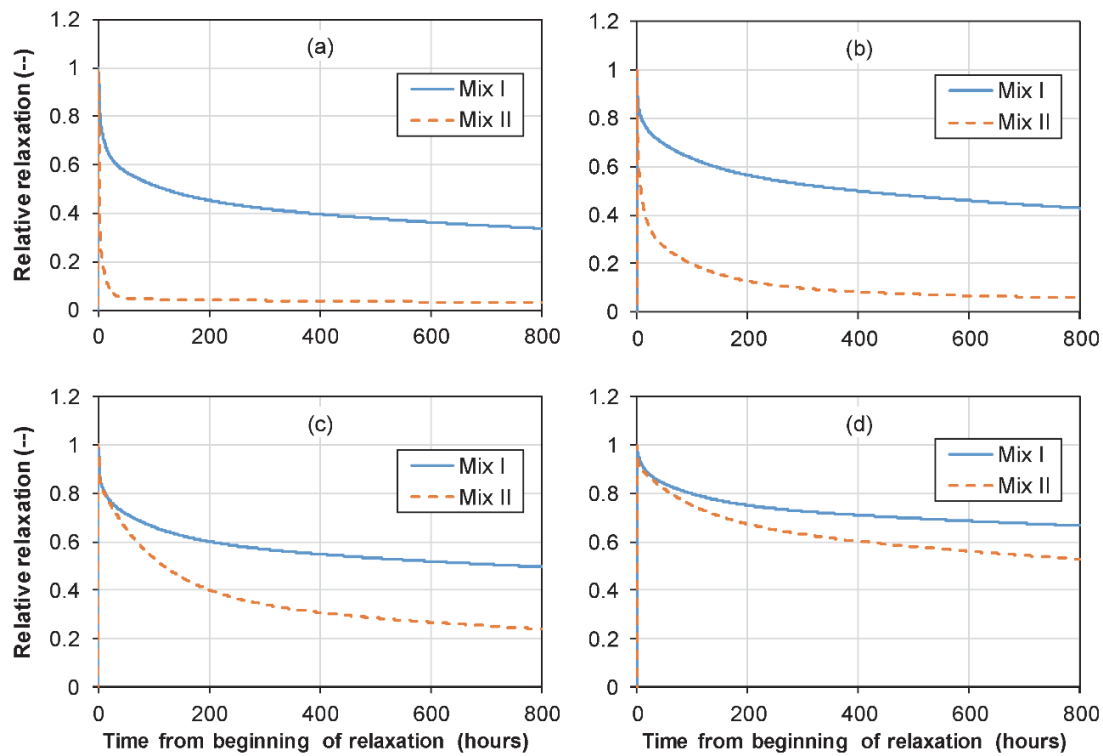


Figure 13: Comparison of the linear relaxation response of Mix I and II at a loading age of; a) 24 hours, b) 48 hours, c) 168 hours and d) 672 hours.

Figure 14 shows the model predictions of the relaxation responses in the linear domain of Mix I and II at different loading ages. The relaxation decreases as the loading age increases, which could be attributed to the ongoing hydration process and the ageing effect that leads to a gradual reduction in the viscous response over time.

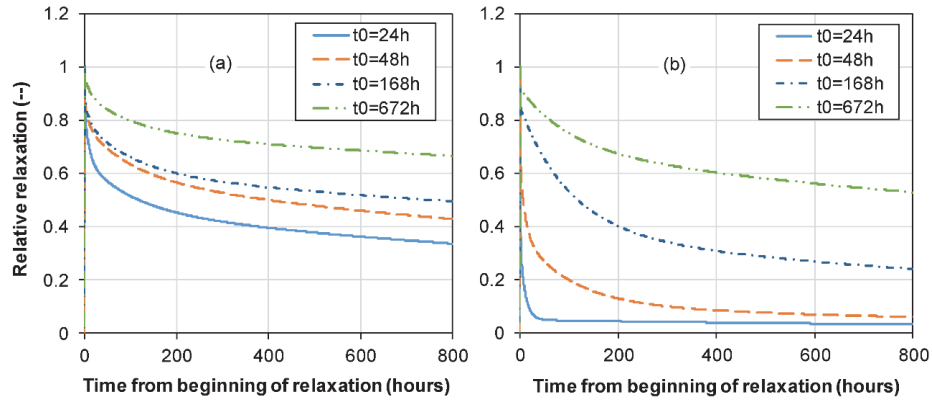


Figure 14: Prediction and comparison of the linear relaxation response at different ages of loading for; a) Mix I, b) Mix II (t_0 represents the loading age).

5.3 Relaxations in the linear and non-linear domain

Figure 15 shows the model predictions of the relative relaxations in the linear and non-linear domain, along with the experimental test data in the non-linear domain. Since the test for calibrating the model was done at an age of 336 hours (14 days) and also only at a strain level of 0.8%, the prediction of the model is shown only for this loading age and strain level. The gradual increase in the relaxation response in the non-linear domain could be included in the model by obtaining the parameters for relaxation tests at different strain levels in the hardening domain. The model predicts a significantly higher relaxation in the non-linear domain when compared to that in the linear domain, with a very steep drop in the beginning as was seen in the experimental test.

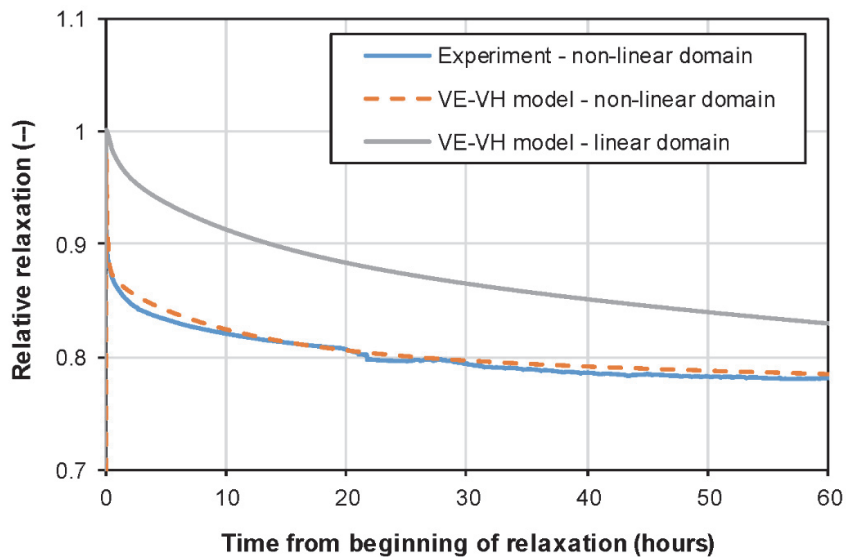


Figure 15: Comparison of the relative relaxations in the linear and non-linear domains of the tensile response.

5.4 Tensile creep

The developed models were used to predict the tensile creep responses of both mixes. In order to validate the predictions of the model, tensile creep tests were conducted on prismatic specimens of dimensions 1000 mm x 70 mm x 40 mm, at different stress levels at an age of 14 days. The details regarding the tensile creep rigs and the test setup could be found in [41,58]. The linear creep curves from the tests were transformed into linear relaxation curves with the help of Bazant's algorithm [59], for comparing with the results from the developed VE-VH model. Figure 16 shows the predictions of the model for both mixes along with the transformed linear relaxation curves from the respective creep tests (stress level of 5.4 MPa, linear domain), and it can be seen that the model predicts the creep response reasonably well. The slight difference in the prediction and the experimental results could be attributed to the difference in the specimens used in the TSTM (from which the model was calibrated) and in the tensile creep rigs. The difference could also be because of the fact that for the TSTM specimens, the LVDTs for deformation measurements were inserted into the specimen whereas for the creep specimens the deformations were measured on the surface of the specimens [41]. The results were similar to that of [5] who showed that in a similar TSTM setup, for low load levels in the viscoelastic domain, the viscous potential from both relaxation and creep tests were in the same scatter band (20% to 35% relaxation after 24 hours) for a loading age of 3 days.

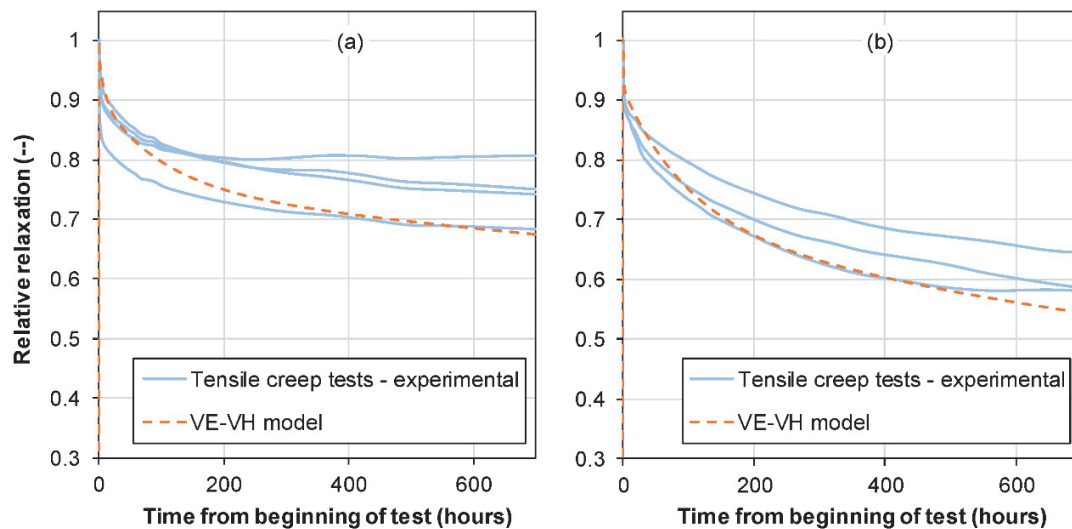


Figure 16: Transformed relaxation curves from tensile creep tests (stress level of 5.4 MPa) using the Bazant algorithm [59], along with the predictions of the model for; a) Mix I, b) Mix II.

5.5 Incremental relaxation tests and loading history effect

Switek et al. [5] conducted incremental relaxation tests on UHPFRC mix of type CM22_TKK, which is the predecessor of Mix I in the present study. Due to the difference in the volumes of the superplasticizer used in both mixes, the setting time of CM22_TKK was approximately 24 hours, whereas it was 17 hours for Mix I. The loading pattern of the incremental relaxation test is shown in figure 17 and the experimental and predicted relaxation responses are shown in figure 18.

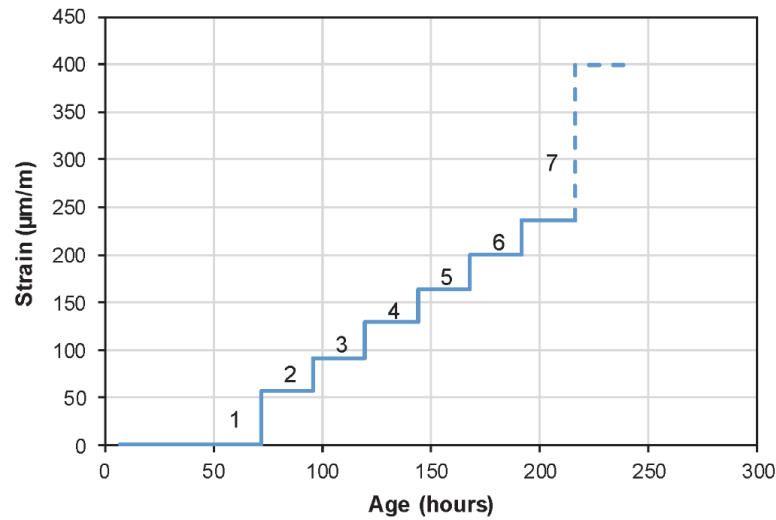


Figure 17: Loading pattern in the incremental relaxation tests.

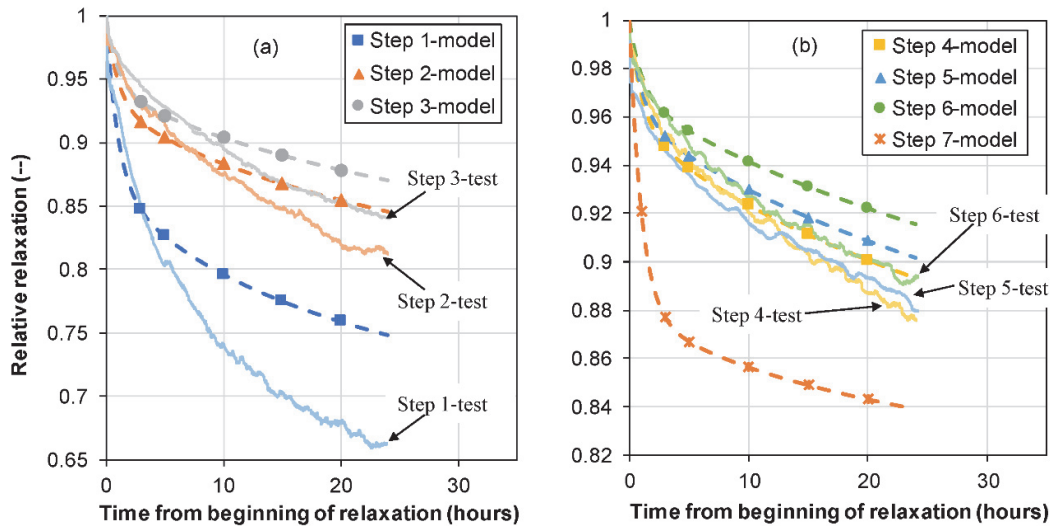


Figure 18: Experimental relaxation response at each step of loading in the incremental relaxation test along with the predictions of the VE-VH model; a) shows the first three steps of loading, b) shows the final four steps of loading.

Figure 18 shows that the trend of the relaxation response is very well predicted by the model, except for a slight shift in the values of the relative relaxation, with the model predicting slightly lower relative relaxation at every step of loading. This can be attributed to the slight difference in the setting time of the mixes with Mix I, used for calibration, having an earlier setting time leading to a lower relaxation response at every loading step because of a higher “apparent age after setting”. The difference could also be attributed to the changes in the viscous potential of both mixes due to the slight changes in the composition or to the possible scatter in the relaxation response in the experiments as discussed in section 5.2. Nevertheless, the trend of the relaxation was captured well by the model showing a decrease in the relative relaxation as the load level increases, which is attributed to the combined effect of ageing and history of loading [5]. Even though the experimental loading in [5] was not continued into the non-linear domain, the model was used to predict the relaxation response, had the loading been continued further into the non-linear domain. It can be seen that the same model, which predicted a gradually decreasing relaxation response until the 6th step of loading in the linear domain because of the ageing and history effect, predicts a much higher relaxation during the 7th step as it was loaded into the non-linear domain, because of the influence of damage on the non-linear viscoelasticity.

5.6 Effect of early age hydration on the tensile response

In this section, the interaction of early age hydration and the viscous phenomena will be discussed with the help of the model, without considering the influence of the early age autogenous deformations. The model was used to predict the tensile responses of Mix I at an age 1 hour after the setting time of 17 hours under different strain rates, which is shown in figure 19. Since the elastic limit at an age 1 hour after setting was not known, only the domain under a stress level of 7 MPa was considered, assuming that the elastic limit may not be reached at or below this stress level.

When loaded at an age of 1 hour after the setting time, at a strain rate of 1×10^{-5} 1/s, the stiffness of the tensile response was very low, reaching a stress of 5.3 MPa at a strain of 2%. This is because the elastic modulus of the mix is still very low as can be seen from the VRF tests in figure 3. For strain rates of 1×10^{-7} 1/s and 1×10^{-8} 1/s, there is a “hydration induced non-linearity” in the tensile response, which is attributed to similar shape of the elastic modulus development at that age as can be seen in figure 3. The eigenstresses vs shrinkage strain responses of the full restraint tests for Mix I also shows a similar trend in the beginning, as seen in figure 20. However, as the strain rate decrease further below 1×10^{-9} 1/s, this effect becomes negligible as the elastic modulus development becomes faster than the stress development under the imposed slow loading rates. As the strain rates decrease further below, the viscous effects start to appear, leading to the gradual reduction in the elastic modulus just as discussed in detail in section 5.7.

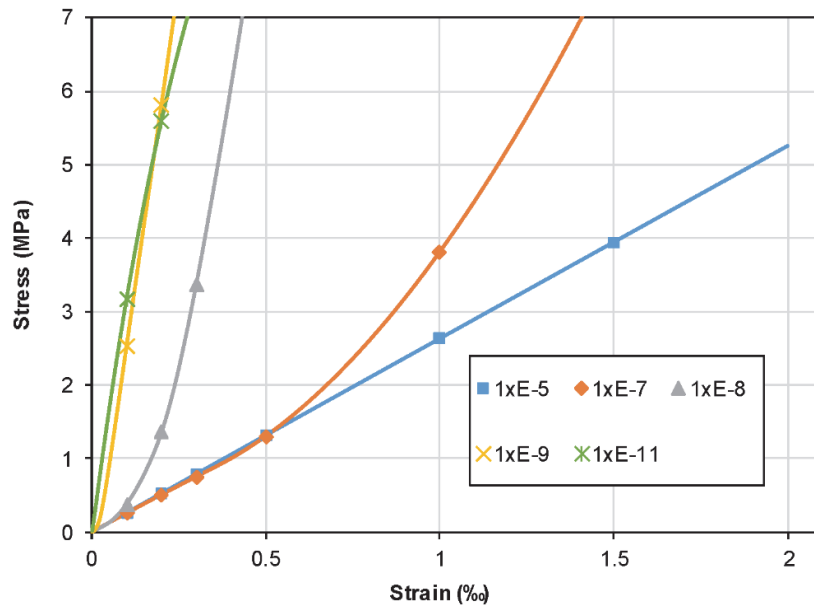


Figure 19: Predictions of the tensile response of Mix I, under different strain rates, loaded at an age 1 hour after the setting time.

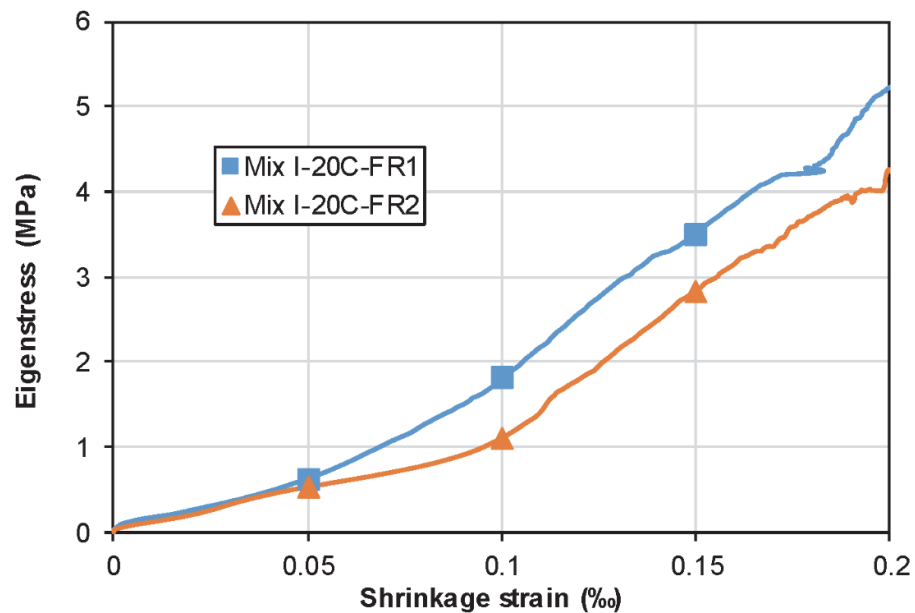


Figure 20: Eigenstresses vs shrinkage strain curves for the full restraint tests of Mix I.

5.7 Parametric study on the effect of very low strain rates on the tensile response.

The model can also be used to predict the effect of very low strain rates on the tensile response of both mixes at an age of 14 days (14 days correspond to an age where the development of elastic modulus is almost over).

In Chapter 3 [10], the influence of very low strain rates on the tensile mechanical properties of Mix I and Mix II was studied. However, the minimum strain rate that was investigated was 5×10^{-9} 1/s. With the current VE-VH model, the tensile response for strain rates even lower than 5×10^{-9} 1/s can be predicted. Since the retardation times of the 5th chains of M1 and M2 were 10000 hours and 1000 hours respectively, they can predict the tensile response until 100000 hours (11.4 years) and 10000 hours (1.1 years respectively). Table 6 shows the times needed to reach a strain level of 2‰ under different strain rates.

Table 6: Table showing the time needed to reach a strain level of 2‰ under various strain rates

Strain rate (1/s)	Time to reach a strain level of 2‰
1×10^{-5}	3.6 minutes
1×10^{-7}	5.6 hours
1×10^{-8}	2.3 days
1×10^{-9}	23 days
1×10^{-10}	230 days
1×10^{-11}	6.3 years

In order to calculate the rate dependency on the elastic limit, which is the transition point from M1 to M2 in the model, the elastic limit at various strain rates were calculated using equations (11) and (13) for Mix I and II respectively. It was also assumed that the elastic limit for any strain rate might not drop below 75% of that corresponding to a quasi-static strain rate. The strains at tensile strength under different strain rates were calculated using equation (12) for Mix I. However, as explained in section 4.4, because of the significant difference in the strains at tensile strength of Mix II at the three different strain rates, no general equation was proposed for the same and the tensile responses were predicted until a strain of 2‰.

The CEB model code [60] recommends a quasi-static strain rate of 3×10^{-6} 1/s for a uniaxial tensile test. Using equations (13) and (15), the elastic limits for Mix I and II at a strain rate of 3×10^{-6} 1/s were found to be 11.72 MPa and 10.91 MPa respectively and the corresponding 75% lower limits were calculated to be 8.79 MPa and 8.18 MPa respectively. Figure 21 shows the effect of very low strain rates on the tensile behavior of mixes I and II.

For Mix I, figure 21a shows that the elastic modulus is almost similar until a strain rate of 1×10^{-8} 1/s and starts to decrease for lower strain rates. This was similar to the trends found in Chapter 3 [10], where the elastic modulus was found to be insensitive to the investigated strain rate range of 1×10^{-5} 1/s to 1×10^{-8} 1/s. The model shows that for Mix I, the strain rate sensitivity of elastic modulus due to the viscous effects will start to appear only if tested at strain rates lesser than or equal to 1×10^{-9} 1/s. This explains the trend in the locus of the elastic limit, with the tests up to 1×10^{-9} 1/s showing a slightly lower strain at the elastic limit.

However, the case was different for Mix II, wherein a clear change in the elastic modulus was seen even at a strain rate of 1×10^{-8} 1/s. This could be attributed to the higher viscous potential of Mix II, as discussed earlier in Chapter 2 [51].

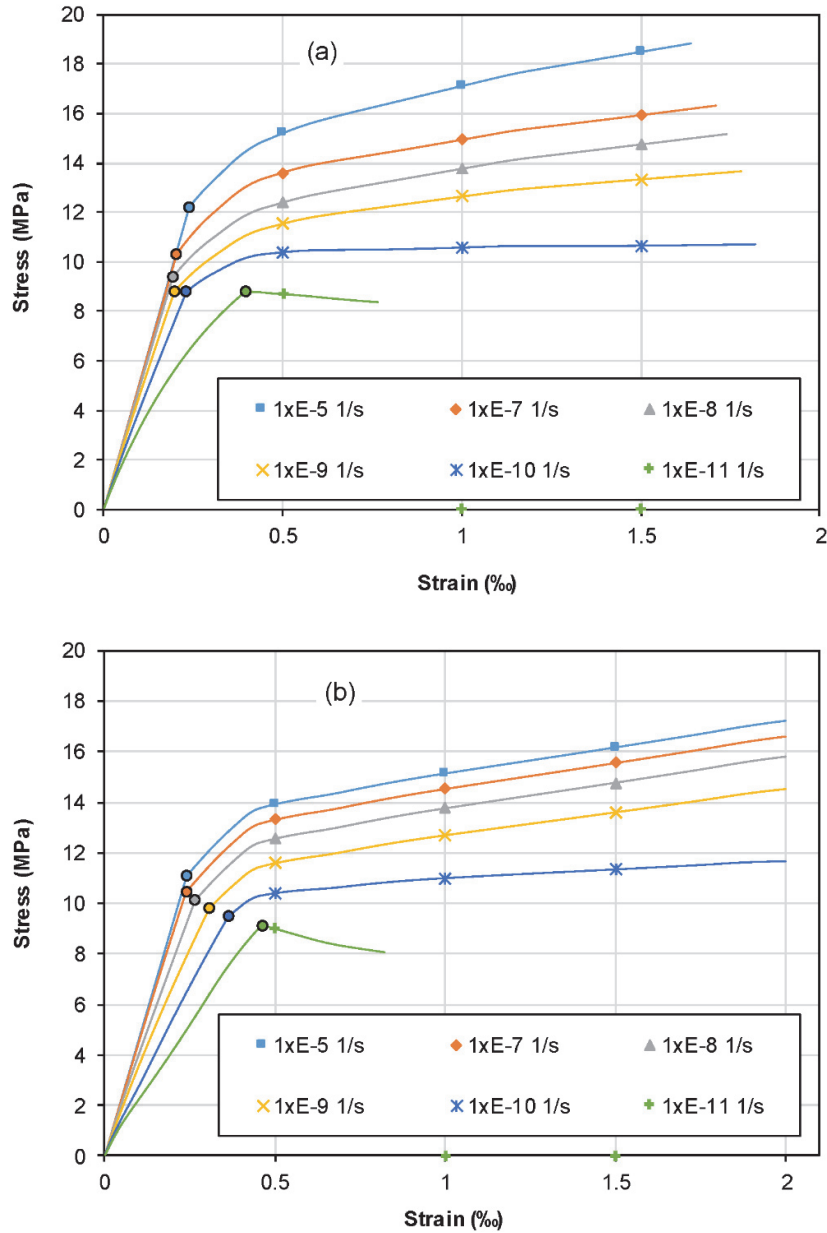


Figure 21: Predictions of the tensile response of a) Mix I, b) Mix II, under different strain rates, loaded at an age of 14 days.

Another interesting observation is the effect of non-linear viscosity on the hardening moduli (slope of response in the hardening domain) at different strain rates for both mixes. Figure 21 shows that for both mixes, the hardening moduli decrease with a decrease in the strain rate.

This is contradictory to the experimental results found in Chapter 3 [10], where the hardening modulus was found to be strain rate insensitive in the range of strain rates tested. As the strain rate decreases, the relaxation due to non-linear viscosity becomes more dominant, thereby reducing the hardening moduli. For both mixes, at a strain rate of 1×10^{-11} 1/s, the tensile response resembles that of a softening UHPFRC. It should be noted that the maximum retardation time in M2 is 1000 hours and therefore it can predict the tensile response in the hardening domain only up to 10000 hours. For the predictions at a strain rate of 1×10^{-11} 1/s, it will require more than 10000 hours to reach the strain level of 2‰, and therefore the predictions were not done until the same, but were done only until the strain level at 10000 hours (from the elastic limit in M2). At these very low strain rates, the relaxation due to non-linear viscosity becomes more dominant than the hardening, thereby reducing the stresses immediately as the material enters the “hardening domain”. As such, it is the combined effect of hardening and a more dominant non-linear viscous relaxation, which makes the overall response resemble that of a strain softening material. This trend might indicate that under extremely low loading rates, similar to static fatigue, the strain-hardening response of UHPFRC might vanish in unfavorable cases.

However, the present approach is based on the assumption that the material would remain homogenous even in the hardening domain, and a decrease in the strain rate would lead to an increase in the viscous response, which even leads to a “softening case” under extremely low strain rates. However, as discussed in Table 4 and in Chapter 3 [10], the tensile strength and the hardening modulus did not show a significant sensitivity to the strain rates investigated. Just as in the dynamic domain, one would assume that a decrease in the strain rate might lead to a decrease in not only the elastic limit, but also the tensile strength and hardening modulus as well. However, it is possible that this assumption does not hold true when the strain rates studied are significantly lower than the quasi-static strain rate, as seen in the experimental results in Chapter 3 [10]. The first major explanation of the strain rate insensitivity of the tensile strength is the possible influence of fiber orientation and grouping, which counteract the effect of strain rate thereby making the final response strain rate insensitive. However, another explanation for the strain rate insensitivity as pointed out by [61], is the possible difference in the imposed strain rate on the overall specimen and the strain rate imposed along the crack planes for the pullout of the fibers, in the hardening domain. It is possible that the strain rates imposed on the fiber pullout is much higher than that imposed overall on the specimen, thereby leading to a cancellation of the effect of strain rate as assumed apriori. This effect, if present, becomes more significant as the strain rates decrease, as the corresponding reduction in the elastic limit, makes the fibrous response in the hardening domain more efficient. Therefore, it is also possible that with the reduction in the elastic limit, the hardening modulus could increase, as the overall strain rate effects are biased with more and more crack planes along the specimen.

This effect was also visible in the full restraint tests as shown in figure 9. It can be seen that after about 900 hours, the model predicts an almost zero hardening slope under the imposed restrained shrinkage strain rates whereas the experiment shows a slightly higher hardening slope. As such, a closer look into the fracture domain to determine the “actual strain rates” acting across the crack planes would be needed as a next step in the modelling.

6 Conclusions

A viscoelastic-viscohardening model was developed using generalized ageing Maxwell models for two types of SH-UHPFRC mixes; Mix I with pure type I cement, silica fume and steel fibers and Mix II with 50% replacement of cement with limestone filler and a similar steel fibrous mix. The model was calibrated using three independent sets of experiments; full restraint tests in the TSTM, uniaxial tensile tests under different monotonic strain rates and relaxation tests in the non-linear domain.

- The model was able to accurately predict the experimental eigenstresses development under a degree of restraint of 50%. A parametric study on the development of eigenstresses under different restraint conditions revealed that for Mix II, the eigenstresses developed after one month, even at a degree of restraint of 90%, was significantly lower than the resistance envelopes of the elastic limit and tensile strength.
- The model was able to predict the experimental linear relaxation responses at an age of 3 days [5], and was well within the scatter band of experimental results. It predicted a much higher relative relaxations in the non-linear domain when compared to that in the linear domain.
- The model closely predicted the experimental creep response of the mixes loaded at an age of 14 days in tensile creep rigs, by converting the creep curves into corresponding relaxation curves using the Bazant's [59] algorithm.
- The ageing and history effects in incremental relaxation tests from [5] were predicted reasonably well by the model, with the model showing a decreasing relaxation response for every consecutive loading step in the linear domain.
- The influence of very low strain rates on the tensile behavior of both mixes were predicted. It was seen that at a strain rate of 1×10^{-11} 1/s, the model predicted an apparent strain softening response, attributed to the combined effect of hardening and a more dominant non-linear viscous relaxation. However, it was also suggested that it might be possible to have a higher hardening modulus at lower strain rates because of the difference in the strain rates being applied on the overall specimen and the crack planes where fibers are pulled out.
- The tensile response of the mixes exhibited a “fast hydration rate induced non-linearity” when loaded under the strain rates in the range of 1×10^{-7} 1/s- 1×10^{-8} 1/s at an age 1 hour after setting, which was attributed to the non-linearity in the development of elastic modulus at the same age. This effect became negligible as the strain rates were reduced further below 1×10^{-9} 1/s.

Acknowledgements

The project was financially supported by the Swiss National Science Foundation (grant 200021_153394/1). The authors would like to gratefully acknowledge the help given by the technicians of GIC-ENAC-EPFL Mr. S. Despont, Mr. G. Guignet and Mr. S. Demierre and Mr. A. Hajiesmaeili in performing the experimental works in the laboratory. Mix II was developed by Mr. A. Hajiesmaeili.

References

- [1] A. Kamen, Comportement au jeune âge et différé d'un BFUP écroutissant sous les effets thermomécaniques, Doctoral thesis No: 3827, Ecole Polytechnique Fédérale de Lausanne, Switzerland (2007).
- [2] M. Kazemi Kamyab, Autogenous Shrinkage and Hydration Kinetics of SH-UHPFRC under Moderate to Low Temperature Curing Conditions, Doctoral thesis No: 5681, Ecole Polytechnique Fédérale de Lausanne, Switzerland (2013).
- [3] A. Loukili, Etude du retrait et du fluage de Bétons à Ultra-Hautes Performances, Ph. D. thesis Ecole Centrale de Nantes, France (1996).
- [4] V.Y.Y. Garas, K.E.E. Kurtis, L.F.F. Kahn, Creep of UHPC in tension and compression: Effect of thermal treatment, *Cem. Concr. Compos.* 34 (2012) 493–502. doi:10.1016/J.CEMCONCOMP.2011.12.002.
- [5] A. Switek-Rey, E. Denarié, E. Brühwiler, Early age creep and relaxation of UHPFRC under low to high tensile stresses, *Cem. Concr. Res.* 83 (2016) 57–69.
- [6] H. Rüsch, Research toward a general flexural theory for structural concrete, *ACI J.* 57 (1960) 1–28.
- [7] H.W. Reinhardt, H.A.W. Cornelissen, *Zeitstandzugversuche an Beton*, Baustoffe, Bauverlag, Wiesbad. (1985) 162–167.
- [8] H.A. Körmeling, Strain Rate and Temperature Behavior of Steel Fiber Concrete in Tension, Doctoral Thesis, Delft University of Technology, Netherlands (1986).
- [9] A.E. Hansen, Time Dependent Tensile Fracture of Concrete, Doctoral Thesis, Norwegian Institute of Technology, Division of Concrete Structures, University of Trondheim (1991).
- [10] M.A. Hafiz, E. Denarié, Tensile response of UHPFRC under very low strain rates and low temperatures, submitted to *Cement and Concrete Research*, April (2019).

- [11] N.T. Tran, T.K. Tran, D.J. Kim, High rate response of ultra-high-performance fiber-reinforced concretes under direct tension, *Cem. Concr. Res.* 69 (2015) 72–87. doi:10.1016/J.CEMCONRES.2014.12.008.
- [12] S. Pyo, K. Wille, S. El-Tawil, A.E. Naaman, Strain rate dependent properties of ultra high performance fiber reinforced concrete (UHP-FRC) under tension, *Cem. Concr. Compos.* 56 (2015) 15–24. doi:10.1016/J.CEMCONCOMP.2014.10.002.
- [13] S.H. Park, D.J. Kim, S.W. Kim, Investigating the impact resistance of ultra-high-performance fiber-reinforced concrete using an improved strain energy impact test machine, *Constr. Build. Mater.* 125 (2016) 145–159. doi:10.1016/J.CONBUILDMAT.2016.08.027.
- [14] S. Pyo, S. El-Tawil, A.E. Naaman, Direct tensile behavior of ultra high performance fiber reinforced concrete (UHP-FRC) at high strain rates, *Cem. Concr. Res.* 88 (2016) 144–156. doi:10.1016/J.CEMCONRES.2016.07.003.
- [15] K. Wille, M. Xu, S. El-Tawil, A.E. Naaman, Dynamic impact factors of strain hardening UHP-FRC under direct tensile loading at low strain rates, *Mater. Struct.* 49 (2016) 1351–1365. doi:10.1617/s11527-015-0581-y.
- [16] J.K. Park, S.-W. Kim, D.J. Kim, Matrix-strength-dependent strain-rate sensitivity of strain-hardening fiber-reinforced cementitious composites under tensile impact, *Compos. Struct.* 162 (2017) 313–324. doi:10.1016/J.COMPSTRUCT.2016.12.022.
- [17] R. Ranade, V.C. Li, W.F. Heard, Tensile Rate Effects in High Strength-High Ductility Concrete, *Cem. Concr. Res.* 68 (2015) 94–104. doi:10.1016/J.CEMCONRES.2014.11.005.
- [18] P. Rossi, N. Godart, J.L. Robert, J.P. Gervais, D. Bruhat, Investigation of the Basic Creep of Concrete by Acoustic Emission, in: *Proceedings, Creep Shrinkage Concr.* (1993): pp. 33–38.
- [19] E. Denarié, Etude expérimentale des couplages Viscoelasticite - Croissance des fissures dans les betons de ciment, Doctoral thesis No: 2195, Ecole Polytechnique Fédérale de Lausanne (2000).
- [20] Z.P. Bažant, R. Gettu, Rate Effects and Load relaxation in Static Fracture of Concrete, *ACI Mater. J.* 89 (1992) 456–468.
- [21] F.P. Zhou, Time dependent crack growth and fracture in concrete, Doctoral Thesis, Report TVBM-1011, Division of Building Materials, Lund Institute of Technology, Sweden. (1992).
- [22] E. Denarié, C. Cécot, C. Huet, Characterization of creep and crack growth interactions in the fracture behavior of concrete, *Cem. Concr. Res.* 36 (2006) 571–575. doi:https://doi.org/10.1016/j.cemconres.2005.11.011.
- [23] Z.P. Bazant, S. Prasannan, Solidification Theory for Concrete Creep. I: Formulation, *ASCE J. Eng. Mech.* 115 (1989) 1691–1703.

- [24] Z.P. Bažant, S. Prasannan, Solidification Theory for Concrete Creep: I: Verification and Application, *ASCE J. Eng. Mech.* 115 (1989) 1704–1725.
- [25] C. Mazzotti, M. Savoia, A. Tralli, An isotropic damage model for non linear creep behavior of concrete in compression, in: *FraMCoS-4* (2001): pp. 255–262.
- [26] J. Mazars, A description of micro- and macroscale damage of concrete structures, *Eng. Fract. Mech.* 25 (1986) 729–737. doi:[https://doi.org/10.1016/0013-7944\(86\)90036-6](https://doi.org/10.1016/0013-7944(86)90036-6).
- [27] A. Loukili, M. Omar, G. Pijaudier-Cabot, Basic creep of Ultra High strength Concrete - experiments and modeling, in: *Concreep 6* (2001) pp. 545–550.
- [28] J.M. Torrenti, Basic creep of concrete-coupling between high stresses and elevated temperatures, *Eur. J. Environ. Civ. Eng.* 22 (2018) 1419–1428. doi:[10.1080/19648189.2017.1280417](https://doi.org/10.1080/19648189.2017.1280417).
- [29] A. Sellier, S. Multon, L. Buffo-Lacarrière, T. Vidal, X. Bourbon, G. Camps, Concrete creep modelling for structural applications: non-linearity, multi-axiality, hydration, temperature and drying effects, *Cem. Concr. Res.* 79 (2016) 301–315. doi:<https://doi.org/10.1016/j.cemconres.2015.10.001>.
- [30] L. Zhaoxia, Effective creep Poisson's ratio for damaged concrete, *Int. J. Fract.* 66 (1994) 189–196. doi:[10.1007/BF00020083](https://doi.org/10.1007/BF00020083).
- [31] G. De Schutter, Degree of hydration based Kelvin model for the basic creep of early age concrete, *Mater. Struct.* 32 (1999) 260. doi:[10.1007/BF02479595](https://doi.org/10.1007/BF02479595).
- [32] F. Benboudjema, J.M. Torrenti, Early-age behavior of concrete nuclear containments, *Nucl. Eng. Des.* 238 (2008) 2495–2506. doi:<https://doi.org/10.1016/j.nucengdes.2008.04.009>.
- [33] P. Perzyna, Fundamental Problems in Viscoplasticity, in: G.G. Chernyi, H.L. Dryden, P. Germain, L. Howarth, W. Olszak, W. Prager, R.F. Probstein, H.B.T.-A. in A.M. Ziegler (Eds.), Elsevier, (1966) pp. 243–377. doi:[https://doi.org/10.1016/S0065-2156\(08\)70009-7](https://doi.org/10.1016/S0065-2156(08)70009-7).
- [34] G. Duvaut, J.L. Lions, *Les inéquations en mécanique et en physique*, Dunod, Paris (1972).
- [35] A. Berthollet, Contribution à la modélisation du béton vis-à-vis du vieillissement et de la durabilité: interaction des déformations de fluage et du comportement non-linéaire du matériau, Doctoral thesis, L'institut National des Sciences Appliquées de Lyon (2003).
- [36] R.R. Pedersen, A. Simone, L.J. Sluys, An analysis of dynamic fracture in concrete with a continuum visco-elastic visco-plastic damage model, *Eng. Fract. Mech.* 75 (2008) 3782–3805. doi:<https://doi.org/10.1016/j.engfracmech.2008.02.004>.
- [37] G.P.A.. Van Zijl, Computational modeling of SHCC, ISE Report ISI2009-20 (2009).

- [38] R. Miguel Fernandez, A. Muttoni, P.G. Gambarova, Relationship between Nonlinear Creep and Cracking of Concrete under Uniaxial Compression, *J. Adv. Concr. Technol.* 5 (2007) 1–11.
- [39] D. Tasevski, M.F. Ruiz, A. Muttoni, Compressive Strength and Deformation Capacity of Concrete under Sustained Loading and Low Stress Rates, *J. Adv. Concr. Technol.* 16 (2018) 396–415. doi:10.3151/jact.16.396.
- [40] A. Kamen, E. Denarié, H. Sadouki, E. Brühwiler, UHPFRC tensile creep at early age, *Mater. Struct.* 42 (2008) 113–122. doi:10.1617/s11527-008-9371-0.
- [41] A.E. Switek, Time-Dependent Response of Ultra High Performance Fiber Reinforced Concrete (UHPFRC) under Low to High Tensile Stresses, Doctoral thesis No: 4899, Ecole Polytechnique Fédérale de Lausanne, Switzerland (2011).
- [42] H.S. Müller, I. Burkart, H. Budelmann, J. Ewert, V. Mechtcherine, L. Dudziak, C. Müller, S. Eppers, Time-dependent behavior of ultra high performance concrete (UHPC), in: 3rd Int. Fib Congr. Exhib. Inc. PCI Annu. Conv. Bridg. Conf. Think Glob. Build Locally, Proc. (2010).
- [43] T. Stengel, Viscoelasticity of UHPC-Computation of Maxwell Chain Relaxation Spectra Based on Creep Experiments, in: CONCREEP 10 (2015). doi:10.1061/9780784479346.060.
- [44] R. Le Roy, F. Le Maou, J.M. Torrenti, Long term basic creep behavior of high performance concrete: data and modelling, *Mater. Struct.* 50 (2016) 85. doi:10.1617/s11527-016-0948-8.
- [45] Y. Xu, J.J. Liu, J.J. Liu, P. Zhang, Q. Zhang, L. Jiang, Experimental studies and modeling of creep of UHPC, *Constr. Build. Mater.* 175 (2018) 643–652. doi:10.1016/J.CONBUILDMAT.2018.04.157.
- [46] D.Y. Yoo, S. Kim, M.-J. Kim, Comparative shrinkage behavior of ultra-high-performance fiber-reinforced concrete under ambient and heat curing conditions, *Constr. Build. Mater.* 162 (2018) 406–419. doi:10.1016/J.CONBUILDMAT.2017.12.029.
- [47] Z. Hu, Prediction of autogenous shrinkage in fly ash blended cement systems, Doctoral thesis No: 7829, EPFL (2017).
- [48] L. Wan, R. Wendner, G. Cusatis, A Hygro-Thermo-Chemo Mechanical Model for the Simulation of Early Age Behavior of Ultra-High-Performance Concrete, in: CONCREEP 10 (2015) doi:10.1061/9780784479346.020.
- [49] L. Wan, R. Wendner, B. Liang, G. Cusatis, Analysis of the behavior of ultra high performance concrete at early age, *Cem. Concr. Compos.* 74 (2016) 120–135. doi:10.1016/J.CEMCONCOMP.2016.08.005.
- [50] FEMMASSE, MLS FEM analysis, ver. 8.6, (2006). <http://femmasse.com/tools/mls>.

- [51] M.A. Hafiz, A. Hajiesmaeili, E. Denarié, Tensile response of low clinker UHPFRC subjected to fully restrained shrinkage, *Cem. Concr. Res.* 124 (2019). doi:<https://doi.org/10.1016/j.cemconres.2019.105804>.
- [52] P. Rossi, A. Arca, E. Parant, P. Fakhri, Bending and compressive behaviors of a new cement composite, *Cem. Concr. Res.* 35 (2005) 27–33. doi:10.1016/J.CEMCONRES.2004.05.043.
- [53] G. Guignet, H. Kazemi-Kamyab, E. Denarié, Internal communication, August 2014, EPFL, Switzerland (2014) .
- [54] S. Kolluru, J. Popovics, S.P. Shah, Determining Elastic Properties of Concrete Using Vibrational Resonance Frequencies of Standard Test Cylinders, *Cem. Concr. Aggregates*. 22 (2000) 81.
- [55] A. Kamen, E. Denarié, H. Sadouki, E. Brühwiler, Thermo-mechanical response of UHPFRC at early age - Experimental study and numerical simulation, *Cem. Concr. Res.* 38 (2008) 822–831. doi:10.1016/J.CEMCONRES.2008.01.009.
- [56] M.A. Hafiz, E. Denarié, Tensile viscous response of Strain Hardening UHPFRC under high restraint and isothermal conditions, in: *Euro C - 2018 Comput. Model. Concr. Struct.* (2018): pp. 903–912.
- [57] E. Denarié, Deliverable D25b “Guidance for the use of UHPFRC for rehabilitation of concrete highway structures,” (2006).
- [58] A. Switek-Rey, E. Denarié, E. Brühwiler, Tensile creep of UHPFRC under low and high stresses, in: *4th Int. Conf. Constr. Mater. – Performance, Innov. Struct. Implic.*, Nagoya, Japan (2009): pp. 432–437.
- [59] Z.P. Bažant, Numerical determination of long-range stress history from strain history in concrete, *Matériaux Constr.* 5 (1972) 135–141. doi:10.1007/BF02539255.
- [60] “Comité Euro-International du Béton,” CEB-FIP Model Code 1990, Trowbridge, Wiltshire, UK (1993).
- [61] E. Denarie, Internal communication, MCS, EPFL, March (2019).

Appendix A

The parameters of the viscoelastic-viscohardening model for both mixes are given below. For Mix I, table A.1 shows the parameters of the first set of Maxwell chains (M1), whereas table A.2 shows the same for the second set of Maxwell chains (M2). For Mix II, the parameters of M1 and M2 are shown in tables A.3 and A.4 respectively.

Table A.1: Parameters of first set of Maxwell chains for Mix I.

Mix I		τ_1	τ_2	τ_3	τ_4	τ_5
First set of chains, M1		(hours)	(hours)	(hours)	(hours)	(hours)
		1	10	100	1000	10000
Age	$E_{tot,M1}$	$\frac{E_{1(M1)}}{E_{tot(M1)}}$	$\frac{E_{2(M1)}}{E_{tot(M1)}}$	$\frac{E_{3(M1)}}{E_{tot(M1)}}$	$\frac{E_{4(M1)}}{E_{tot(M1)}}$	$\frac{E_{5(M1)}}{E_{tot(M1)}}$
(hours)	(GPa)					
0	0.05	0.20	0.18	0.17	0.20	0.25
16	2.8	0.20	0.18	0.17	0.20	0.25
20	14.2	0.20	0.18	0.17	0.20	0.25
22	26.5	0.20	0.18	0.17	0.20	0.25
24	34.7	0.20	0.18	0.17	0.20	0.25
26	38.1	0.17	0.08	0.18	0.24	0.33
28	40.6	0.17	0.08	0.18	0.24	0.33
30	42.2	0.17	0.08	0.18	0.24	0.33
36	44.9	0.17	0.08	0.18	0.24	0.33
48	46.7	0.17	0.08	0.18	0.24	0.33
60	47.4	0.17	0.08	0.18	0.24	0.33
72	48.0	0.15	0.08	0.18	0.14	0.45
84	48.6	0.15	0.08	0.18	0.14	0.45
96	49.2	0.15	0.08	0.18	0.14	0.45
168	50.6	0.15	0.08	0.18	0.14	0.45
336	51.2	0.04	0.07	0.14	0.07	0.68
672	52.0	0.04	0.07	0.14	0.07	0.68
87600	53.0	0.04	0.07	0.14	0.07	0.68

Table A.2: Parameters of second set of Maxwell chains for Mix I.

Mix I			τ_1	τ_2	τ_3	τ_4	τ_5
Second set of chains, M2			(hours)	(hours)	(hours)	(hours)	(hours)
			0.1	1	10	100	1000
Age	Strain level	$E_{L,M2}$	$\frac{E_{1(M2)}}{E_{L(M2)}}$	$\frac{E_{2(M2)}}{E_{L(M2)}}$	$\frac{E_{3(M2)}}{E_{L(M2)}}$	$\frac{E_{4(M2)}}{E_{L(M2)}}$	$\frac{E_{5(M2)}}{E_{L(M2)}}$
(hours)	‰	(GPa)					
t0.2‰	0.2	21.0	0.50	0.03	0.23	0.17	0.07
t0.3‰	0.3	14.0	0.50	0.03	0.23	0.17	0.07
t0.4‰	0.4	10.0	0.50	0.03	0.23	0.17	0.07
t0.5‰	0.5	6.0	0.50	0.03	0.23	0.17	0.07
t0.6‰	0.6	4.0	0.50	0.03	0.23	0.17	0.07
t0.7‰	0.7	3.5	0.50	0.03	0.23	0.17	0.07
t1.1‰	1.1	3.5	0.50	0.03	0.23	0.17	0.07
t1.2‰	1.2	2.5	0.50	0.03	0.23	0.17	0.07
t2.0‰	2	2.5	0.50	0.03	0.23	0.17	0.07

Table A.3: Parameters of first set of Maxwell chains for Mix II.

Mix II		τ_1	τ_2	τ_3	τ_4	τ_5
First set of chains, M1		(hours)	(hours)	(hours)	(hours)	(hours)
		1	10	100	1000	10000
Age	$E_{tot,M1}$	$\frac{E_{1(M1)}}{E_{tot(M1)}}$	$\frac{E_{2(M1)}}{E_{tot(M1)}}$	$\frac{E_{3(M1)}}{E_{tot(M1)}}$	$\frac{E_{4(M1)}}{E_{tot(M1)}}$	$\frac{E_{5(M1)}}{E_{tot(M1)}}$
(hours)	(GPa)					
0	0.05	0.70	0.26	0.00	0.02	0.02
16	12.4	0.70	0.26	0.00	0.02	0.02
20	27.1	0.70	0.26	0.00	0.02	0.02
22	31.0	0.70	0.26	0.00	0.02	0.02
24	33.5	0.70	0.26	0.00	0.02	0.02
26	35.2	0.40	0.26	0.24	0.08	0.02
28	36.6	0.40	0.26	0.24	0.08	0.02
30	37.7	0.40	0.26	0.24	0.08	0.02
36	40.2	0.40	0.26	0.24	0.08	0.02
48	43.4	0.40	0.26	0.24	0.08	0.02
60	45.2	0.18	0.26	0.36	0.12	0.08
72	46.3	0.18	0.26	0.36	0.12	0.08
84	46.9	0.18	0.26	0.36	0.12	0.08
96	47.5	0.18	0.26	0.36	0.12	0.08
168	48.6	0.18	0.00	0.45	0.24	0.13
336	51.2	0.18	0.00	0.45	0.24	0.13
672	52.0	0.10	0.00	0.22	0.24	0.44
87600	53.0	0.10	0.00	0.22	0.24	0.44

Table A.4: Parameters of second set of Maxwell chains for Mix II.

Mix II			τ_1	τ_2	τ_3	τ_4	τ_5
Second set of chains, M2			(hours)	(hours)	(hours)	(hours)	(hours)
			0.1	1	10	10	1000
Age (hours)	Strain level ‰	$E_{L,M2}$ (GPa)	$\frac{E_{1(M2)}}{E_{L(M2)}}$	$\frac{E_{2(M2)}}{E_{L(M2)}}$	$\frac{E_{3(M2)}}{E_{L(M2)}}$	$\frac{E_{4(M2)}}{E_{L(M2)}}$	$\frac{E_{5(M2)}}{E_{L(M2)}}$
t0.2‰	0.2	17.0	0.50	0.03	0.23	0.17	0.07
t0.3‰	0.3	15.0	0.50	0.03	0.23	0.17	0.07
t0.4‰	0.4	11.8	0.50	0.03	0.23	0.17	0.07
t0.5‰	0.5	3.0	0.50	0.03	0.23	0.17	0.07
t0.6‰	0.6	2.5	0.50	0.03	0.23	0.17	0.07
t0.8‰	0.8	2.5	0.50	0.03	0.23	0.17	0.07
t1.1‰	1.1	2.0	0.50	0.03	0.23	0.17	0.07
t2.0‰	2.0	1.5	0.50	0.03	0.23	0.17	0.07

Appendix B

In section 2, the VE-VH model was presented without considering any effect of the degree of restraint acting on the system. In this section, an additional restraint spring with a stiffness E_0 is considered acting in series with M1/ M2 as shown in figure B.1. Incremental constitutive relations are derived for the same, below and above the elastic limit, as discussed in the sections below.

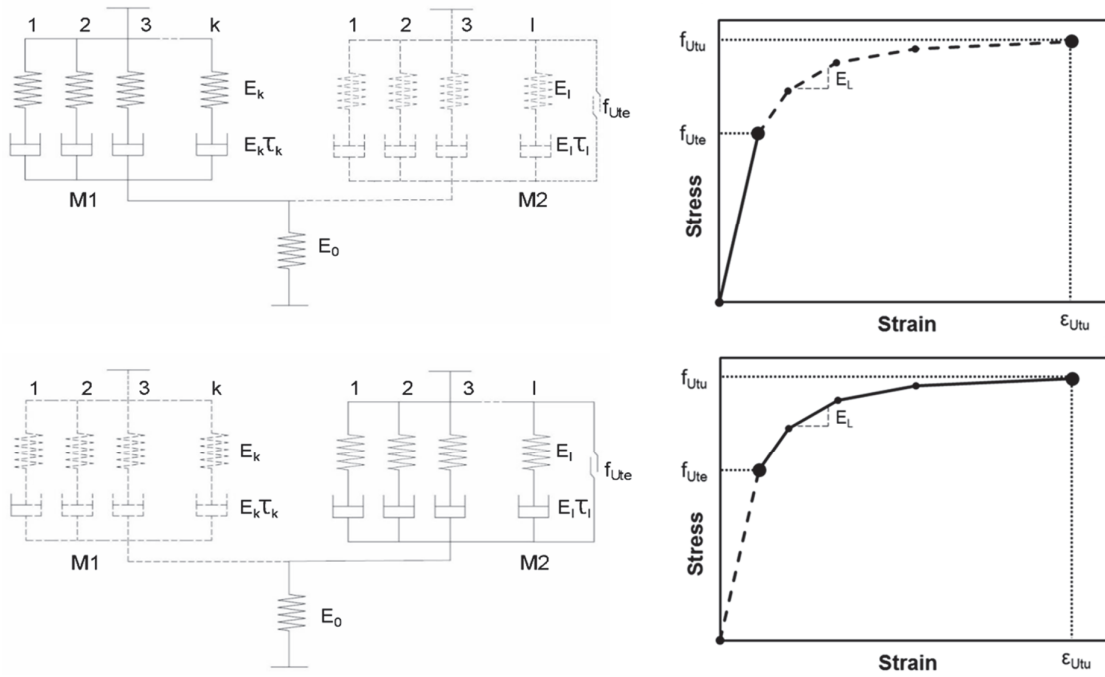


Figure B.1: Schematic representation of the Viscoelastic-Viscohardenig model with the restraint spring with stiffness E_0 acting in series with M1 or M2.

Below the elastic limit:

Below the elastic limit, the material behaves as viscoelastic and only M1 is active, coupled in series with the restraint spring E_0 . Assuming that the strains induced in M1 and the restraint spring E_0 , due to the strain increment $\Delta \varepsilon^i = \Delta \varepsilon_{VE(M1)}^i$ in time interval Δt , are $\Delta \varepsilon_1^i$ and $\Delta \varepsilon_0^i$ respectively, if σ_0^i and σ_0^{i+1} are the stresses in the additional spring E_0 at t^i and t^{i+1} respectively and σ_1^i and σ_1^{i+1} the same in M1, then,

$$\Delta \varepsilon^i = \Delta \varepsilon_1^i + \Delta \varepsilon_0^i \quad (\text{B.1})$$

$$\sigma_0^{i+1} = \sigma_1^{i+1} = \sigma^{i+1} \quad (\text{B.2})$$

From equations (B.1) and (B.2), for the spring E_0 ,

$$\sigma_0^{i+1} = E_0 \cdot \Delta \varepsilon_0^i = \sigma_1^{i+1} \quad (\text{B.3})$$

$$\Delta \varepsilon_0^i = \frac{\sigma_1^{i+1}}{E_0} \quad (\text{B.4})$$

The total stress at the end of the time interval Δt in M1 is therefore given by,

$$\sigma_1^{i+1} = \sum_{k=1}^m \left[\frac{\tau_k}{\Delta t} \cdot \left(\frac{E_k^{i+1} + E_k^i}{2} \right) \cdot \left(1 - e^{-\frac{\Delta t}{\tau_k}} \right) \right] \cdot (\Delta \varepsilon^i - \Delta \varepsilon_0^i) + \sum_{k=1}^m \sigma_k^i \cdot e^{-\frac{\Delta t}{\tau_k}} \quad (\text{B.5})$$

From equations (B.2), (B.4) and (B.5),

$$\sigma^{i+1} = \frac{\sum_{k=1}^m \left[\frac{\tau_k}{\Delta t} \cdot \left(\frac{E_k^{i+1} + E_k^i}{2} \right) \cdot \left(1 - e^{-\frac{\Delta t}{\tau_k}} \right) \right] \cdot \Delta \varepsilon^i + \sum_{k=1}^m \sigma_k^i \cdot e^{-\frac{\Delta t}{\tau_k}}}{1 + \frac{\sum_{k=1}^m \left[\frac{\tau_k}{\Delta t} \cdot \left(\frac{E_k^{i+1} + E_k^i}{2} \right) \cdot \left(1 - e^{-\frac{\Delta t}{\tau_k}} \right) \right]}{E_0}} \quad (\text{B.6})$$

Comparing equations (8) and (B.6), it can be seen that, the stress in a finite restraint system can be obtained by multiplying the stress in the case of an infinitely restrained system by a factor μ corresponding to the age dependent uniaxial degree of restraint, given by,

$$\mu = \frac{1}{1 + \frac{\sum_{k=1}^m \left[\frac{\tau_k}{\Delta t} \cdot \left(\frac{E_k^{i+1} + E_k^i}{2} \right) \cdot \left(1 - e^{-\frac{\Delta t}{\tau_k}} \right) \right]}{E_0}} \quad (\text{B.7})$$

By varying the stiffness E_0 of the restraint spring, the development of tensile stresses under various degrees of restraint can be predicted.

Above the elastic limit:

The stress development in M2 can be derived in the same way as that of M1, and an equation similar to (B.6) can be used to predict the stresses in M2,. If σ_2^i and σ_2^{i+1} are the stresses in M2 at time t^i and t^{i+1} respectively, then,

$$\sigma_2^{i+1} = \sigma^{i+1} = f_{ute} + \frac{\sum_{l=1}^n \left[\frac{\tau_l}{\Delta t} \cdot \left(\frac{E_l^{i+1} + E_l^i}{2} \right) \cdot \left(1 - e^{-\frac{\Delta t}{\tau_l}} \right) \right] \Delta \epsilon^i + \sum_{l=1}^n \sigma_l^i \cdot e^{-\frac{\Delta t}{\tau_l}}}{1 + \frac{\sum_{l=1}^n \left[\frac{\tau_l}{\Delta t} \cdot \left(\frac{E_l^{i+1} + E_l^i}{2} \right) \cdot \left(1 - e^{-\frac{\Delta t}{\tau_l}} \right) \right]}{E_0}} \quad (\text{B.8})$$

The equations (B.6) and (B.8) can be used to predict the effect of degree of restraint on the development of eigenstresses as discussed in section 5.1.

Chapter – 5

Paper – 4

Influence of low curing temperatures on the tensile response of low clinker Strain-Hardening UHPFRC under full restraint

Reference: M.A. Hafiz¹, Jørgen Skibsted², E. Denarié³, Influence of low curing temperatures on the tensile response of low clinker Strain-Hardening UHPFRC under full restraint, *to be submitted to Cement and Concrete Research*, May 2019.

1 – corresponding author of the paper – conducted all the experiments presented in the paper (except the ²⁹Si MAS NMR tests) along with the writing of the full article

2 – conducted the ²⁹Si MAS NMR tests and deconvolutions of results at Aarhus University, Denmark

3 – thesis supervisor

Abstract

The tensile response of Strain-Hardening UHPFRC under full restraint, subjected to curing temperatures of 20 °C, 10 °C, 5 °C, was investigated for two types of mixes with silica fume; Mix I with pure type I cement and Mix II with 50% replacement of cement with limestone filler, both having a similar steel fibrous mix. The development with age of the elastic modulus, tensile strength, autogenous shrinkage and eigenstresses were put into perspective with the hydration kinetics. Two phases of pozzolanic reaction with different rates of consumption of silica fume were identified. A systematic increase of the autogenous shrinkage and eigenstresses with the curing temperatures was observed. The development of eigenstresses with the degree of reaction was similar for the two mixes for all curing temperatures. The eigenstresses were much lower in the case of Mix II, owing to its larger relaxation potential. After one month, the eigenstresses under full restraint reached the tensile hardening domain only for Mix I cured at 20 °C.

Keywords: UHPFRC, Strain-Hardening, low curing temperature, isothermal calorimetry, Solid state ²⁹Si MAS NMR, autogenous shrinkage, eigenstresses, full restraint, silica fume.

1 Introduction

Strain-Hardening Ultra High Performance Fiber Reinforced Concretes (SH-UHPFRC) are very well adapted for rehabilitation or reinforcement (combined with rebars) applications of reinforced concrete structures because of their optimal properties (high tensile strength, over 12 MPa, significant strain-hardening, up to 5%, very low permeability to liquids and gases, and outstanding durability) [1–3]. When a new layer of UHPFRC is applied on an existing structure, early age deformations and drying shrinkage (upon final exposure of the UHPFRC free surfaces), lead to the development of tensile eigenstresses in the UHPFRC. The eigenstresses can reach high stress levels at early age, and might develop further over the long term in the case of drying shrinkage, for mixes where the latter dominates over the autogenous deformations (such as mixes without silica fume). More generally, a major motivation to use Strain-Hardening UHPFRC in structures is to make use of their potential under tensile loading, with tensile stresses at serviceability (under eigenstresses, live loads and deadweight) as high as possible, still preserving their outstanding protective properties. As such, an in-depth understanding of the factors governing the development of eigenstresses and their interaction with the tensile resistance and deformability envelope of these materials is of major importance.

The resistance and deformability offered by UHPFRC is age as well as temperature and moisture curing dependent [4–9]. It also depends largely on the orientation of the fibers in the practical applications [3]. Strain-Hardening UHPFRC with a constant tensile response under any situation of application, is an idealistic vision. A more realistic goal is to have "robust" mixes that exhibit a tensile hardening response in a wide range of applications, such as that classified in the French standard as "strongly hardening – T3" after material tests characterizations [10]. However, even the best mix in the lab, if improperly placed, with an inappropriate workability, or in confined conditions with too narrow rebar spacing or clearance with formwork surfaces can lose its strain-hardening character and lead to premature cracking, compromising the expected protective properties that motivate its use. The knowledge about the development of the tensile resistance and deformability properties like stiffness, elastic modulus and post elastic limit deformability under low temperature curing conditions for UHPFRC materials, is very scarce in literature Chapter 3 [11].

The magnitude and development of eigenstresses in cast-on site applications depend on structural factors (restraint governed by the relative stiffness of new layer and substrate as well as boundary conditions – static system and support of the substrate), and material related factors of the new layer (development of microstructure and pore structure, ageing elastic and viscoelastic properties, autogenous deformations, drying shrinkage). These factors can be related to the hydration kinetics of the binders and external curing and long term ambient conditions [12,13].

The influence of curing temperatures on the kinetics of the development of eigenstresses, especially the effect of low temperatures representative of in-situ casting conditions in winter, are not very well understood for UHPFRC materials [5,14,15]. Very few works have

been carried out to study restrained shrinkage and the associated eigenstresses development in UHPC [16,17] and in UHPFRC [4,5,14,18–21]. Some works has also been carried out under non-isothermal conditions, with the temperature varying according to the development of heat of hydration in the UHPFRC mixes [5,22]. However, to the best of the authors' knowledge, no extensive research has been reported in open literature on the influence of full restraint conditions on the development of the eigenstresses in UHPFRC, under low temperatures. Moreover, studies on the development of autogenous deformations and eigenstresses under restraint for UHPFRC mixes with massive replacement of clinker with limestone fillers are very scarce [21,23].

Many authors showed that the autogenous shrinkage in cementitious materials is driven by capillary stresses that develop in the pore structure due to the decrease of relative humidity as the hydration progresses in systems with partial hydration of binders [24–30]. The capillary stresses, which can be represented by the Kelvin-Laplace equations, are temperature dependent and as such, many studies [14,28,29,31,32] have shown that the autogenous deformations cannot be represented using a maturity function unlike the other macro mechanical properties like compressive strength and elastic modulus [14]. Many studies have been carried out to understand the effect of curing temperatures on the development of autogenous shrinkage in cement based materials [25,29,31,33]. However, very few investigations have considered the same effect for HPC [34,35], UHPC [15,36] or UHPFRC [5,7,8,14]. Moreover, most of these studies focus on curing temperatures higher than 20 °C and investigations on the effect of curing temperatures lower than 20 °C is very scarce [14,15].

Curing temperatures affect the development of the microstructure and the pore network in cementitious materials, which in turn affect the induced capillary stresses and the associated autogenous shrinkage. Many studies have shown that, even though the rate of hydration is much slower at lower curing temperatures, the developed microstructure at a later age has a more uniform distribution of the hydration products, with lesser pores [37–43]. However, there is a disagreement in the ultimate degree of hydration at different temperatures. While many studies show that the ultimate degree of hydration is higher when the curing temperature is lower [38,40,41,44], some others show that the ultimate degree of hydration remain the same at different curing temperatures [37].

The viscoelastic properties of the solid skeleton help in mitigating the development of eigenstresses in cementitious materials. Very few studies have been carried out to investigate the viscoelastic behavior of UHPFRC in compression [4,27,45–49] and in tension [6,18,48,50–55], especially at early age. The compressive creep response of UHPFRC is significantly lower than that of ordinary concretes at a similar loading age and load level [56]. The basic compressive creep coefficient of UHPFRC without thermal treatment, at a loading age of 28 days, for a load level below 40% of the compressive strength, is typically 0.8-1, instead of 2-4 for normal concretes [56]. Not many works have been carried out to study the viscous response of UHPFRC mixes with partial replacement of cement clinker with supplementary cementitious materials.

However, similar studies on cementitious materials other than UHPFRC mixes, report contradictory viscous responses. On the one hand, many authors have reported an increase in the creep response in mixes with partial replacement of cement clinker with fly ash [57–60], blast furnace slag [58–60] or limestone filler [57]. On the other hand, some others have reported a decrease in the creep response in mixes with fly ash [61–64] and Ground Granulated Blast Furnace Slag [61]. However, it should be noted that the observed trends of the viscous response in all these studies were very dependent on the age of loading. In short, the viscous response of mixes with SCM, especially that of UHPFRC mixes, is not fully understood.

Moreover, except the investigations in Chapter 3 [11], no studies have reported the development with age of tensile resistance parameters like strength and deformability under low temperatures for UHPFRC mixes. Fundamental research is needed in this field to make sure that the eigenstresses developed under these curing conditions are lower than the resistance of the material, in order to meet the required serviceability and durability criteria, or to study the couplings between the development of eigenstresses and the tensile hardening response.

This paper investigates the influence of moderate to low curing temperatures, 20 °C, 10 °C and 5 °C, on the development of mechanical properties (elastic modulus and tensile strength), autogenous shrinkage and associated eigenstresses under full restraint, for two types of SH-UHPFRC mixes. Mix I with pure type I cement, silica fume and steel fibers and Mix II with 50% replacement of cement with limestone filler and a similar steel fibrous mix. In a first step, the kinetics of hydration of the two mixes are characterized by means of isothermal calorimetry and ^{29}Si MAS NMR to determine the evolution of the overall degree of hydration, the activation energies of the mixes, and the degree of hydration of cement and degree of reaction of silica fume with age. The development of elastic modulus, autogenous deformations and eigenstresses with age, maturity and degree of hydration are then presented and discussed. Finally, the structural response of the materials, represented by the development of autogenous shrinkage and eigenstresses under full restraint, is classified into three domains. The domains are put into perspective with the material level of kinetics of hydration and reaction of the binders and evolution of elastic modulus, taking into consideration the evolution of the resistance of the two materials at different ages and for different curing temperatures.

2 Experimental

2.1 Materials

Two types of SH-UHPFRC mixes were used in the present study; Mix I and Mix II, both from the CEMTEC^{multiscale}® family, which were initially developed at Laboratoire Central des Ponts et Chaussées (LCPC), France [65]. These mixes were optimized and modified in the framework of the research works held in MCS/EPFL for rehabilitation and strengthening of existing structures [66,67].

Mix I was a SH-UHPFRC of type CM22_TKK_b, composed of an ultra-compact cementitious matrix containing cement (type CEM I 52.5 HTS from Le Teil, Lafarge), white microsilica (SEPR, BET = 14 m²/gr), superplasticizer (Zementol Zeta Super S from TKK, Slovenia) and water. However, since the degree of hydration of Mix I was only about 28-30% after one month [14,21], 50% of the cement in Mix I could advantageously be replaced with two types of inert limestone fillers: Betoflow D[®] and Betocarb SL[®] (OMYA), of different gradings, to produce Mix II, which is a UHPFRC of type CM22_TKK_LF, with improved sustainability. Both mixes had a fibrous mix containing two types of steel fibers; microfibers and macrofibers, with a total dosage of 9% by volume after the concepts developed by Rossi et al. [65]. The detailed compositions of Mix I and II are given in Table 1 where the compositions of the mixes with fibers (Mix I, Mix II) and that of the UHPC matrix without fibers (Mix I_m and Mix II_m) are shown.

Table 1: Compositions of Mixes I and II.

Material	Mix I [kg/m ³]	Mix II [kg/m ³]	Mix I _m * [kg/m ³]	Mix II _m * [kg/m ³]
Cement, CEM I 52.5 le Teil	1467.0	733.7	1616.2	809.6
Silica fume, SEPR	381.4	293.5	420.2	323.8
Limestone filler 1 (Betocarb SL [®])	--	223.0	--	246.1
Limestone filler 2 (Betoflow D [®])	--	510.6	--	563.4
Steel fibers (straight macro fibers; l _f = 10 mm, d _f = 0.2 mm and microfibers/steel wool)	706.5	706.5	--	--
Total water	225.8	217.9	248.7	240.4
Superplasticizer from TKK, Slovenia; Zementol zeta super S; polycarboxylate; 25% solid content; (total amount)	20.5	14.7	22.6	16.2

*corresponds to the compositions of the UHPC matrix without fibers.

Table 2 shows the tests that were carried out only on the UHPC matrix and those conducted on the UHPFRC mixes.

Table 2: Type of mixes used for different tests.

Mix used	Type of test
UHPFRC - Mix I, Mix II	Elastic modulus – VRF tests
	Autogenous deformations – TSTM
	Eigenstresses development – TSTM
	Uniaxial tensile tests
UHPC - Mix I _m , Mix II _m	Isothermal calorimetry
	²⁹ Si MAS NMR

The properties in the hardened state and fresh state are given in Table 3 and Table 4, respectively. The compressive strength and modulus of elasticity were determined on 70 mm x 140 mm cylinders, whereas the tensile properties were obtained from uniaxial tensile tests at a strain rate of 10^{-5} 1/s, on dumbbell specimens with a center cross section of 50 mm x 30 mm, following [68]. The sorptivity was also measured for both mixes at an age of 28 days following EN 1925: 99-07. More details regarding the mechanical properties and the chemical composition of the components could be found in Chapter 2 [21].

Table 3: Properties of Mix I and II in the hardened state, cured at 20 °C.

Property	Units	Mix I	Mix II	Age (days)
Tensile first crack strength* (average of 8 tests)	MPa	12.3 ± 1.7	11.1 ± 1.9	14
Uniaxial tensile strength (average of 8 tests)	MPa	18.0 ± 3.1	15.1 ± 2.7	14
Modulus of elasticity in tension (average of 8 tests)	GPa	51.0 ± 2.3	46.3 ± 1.3	14
End of tensile hardening (average of 10 tests)	‰	1.6 ± 0.4	1.3 ± 0.5	14
Compressive strength (average of 3 tests)	MPa	230.5 ± 0.9	169.7 ± 0.5	28
Modulus of elasticity in compression (average of 3 tests)	GPa	48.3 ± 0.8	46.3 ± 0.8	28
Sorptivity (average of 10 tests)	gr/m ² √h	45.0 ± 5.2	32.5 ± 9.5	28

* corresponds to the transition from the elastic behavior to the strain-hardening behavior.

Table 4: Properties of Mix I and II in the fresh state (average value from 4 tests).

Property	Units	Mix I	Mix II
Workability (ASTM - spread after 25 blows)	mm	179	146
Specific weight	kg/m ³	2834	2695
Air content	%	3.2	4.7

2.2 Isothermal calorimetry tests

Isothermal calorimetry tests were performed in a TAM AIR calorimeter from TA instruments, and the heat flow in the mixes was continuously measured from the time of casting. The thermostat in the TAM AIR can maintain the temperature in the samples and the surrounding environment within ± 0.02 °C of the chosen isothermal temperature. The mixes used for the isothermal calorimetry tests did not have the micro or macro fibers. Four samples were tested for each of Mix I_m and Mix II_m at 20 °C, whereas three samples were tested for each mix at 10 °C and 5 °C. Immediately after mixing, about 10 g of the sample was placed into a 20 mL glass ampoule and kept in the calorimeter, along with a reference sample of water in another ampoule, which acted as an inert sample to improve the signal to noise ratio and identify the temperature artefacts and fluctuations. More detailed information regarding the procedure could be found in [14,69].

2.3 Degree of hydration from ²⁹Si MAS NMR

The development of cement hydration were investigated in both mixes at three different curing temperatures; 20 °C, 10 °C and 5 °C using ²⁹Si MAS NMR (solid-state Magic-Angle Spinning Nuclear Magnetic Resonance), which provides information about the degree of hydration for alite and belite and the fraction of silica fume consumed in pozzolanic reactions. Three master samples of each mix were made and cured separately at the respective temperatures. Similar to that in the isothermal calorimetry tests, the mixes used for the ²⁹Si NMR experiments did not have the micro or macro fibers. On the desired age of hydration, a small slice of the master sample was cut and ground into very fine powder. Isopropanol was then added to the powder to stop the hydration in the sample. The sample was kept in isopropanol for 3 days, after which it was filtered out and stored in a vacuum desiccator until the day of testing. More details regarding the specimen preparation could be found in Chapter 1 of [70].

The ²⁹Si MAS NMR spectra were recorded at 59.6 MHz on a Varian-INOVA 300 MHz (7.05 T) spectrometer, using a home-built CP/MAS probe for 5 mm outer diameter (o.d.) partially sintered zirconia (PSZ) or Si₃N₄ rotors (130 µl sample volume) and a spinning speed of 10.0

kHz. Single-pulse excitation with a 2.5 μ s pulse width ($\sim 45^\circ$ flip angle) for a radio frequency field strength of $\gamma B_1/2\pi \approx 50.0$ kHz was employed along with a 30 s repetition delay and typically around 8.000 – 12.000 scans. The rather high spinning speed of 10.0 kHz was chosen, as no spinning sidebands occur under these conditions in the NMR spectra, which improves the precision of the deconvolution analysis. Furthermore, the relaxation delay of 30 s corresponds to full relaxation under the present conditions, as judged from an array of spectra obtained with different relaxation delays. Neat tetramethyl silane (TMS) was used as the ^{29}Si chemical shift reference, employing larnite ($\beta\text{-Ca}_2\text{SiO}_4$, $\delta = -71.33$ ppm) as a secondary standard.

The deconvolutions of the ^{29}Si NMR spectra were performed with the Varian VnmrJ software, using procedures described elsewhere for anhydrous [71,72] and hydrated Portland cements [73,74]. This approach gives relative intensities for ^{29}Si in alite, belite, silica fume and the for Q^1 , Q^2 , and $Q^2(1A1)$ resonances of the C-(A-)S-H phase. The degrees of hydration (H) for the anhydrous phases were calculated as described in section 3.2.

2.4 Dynamic and static modulus of elasticity

The dynamic modulus of elasticity was determined on cylinders of dimensions 140 mm x 70 mm, using Vibration Resonance Frequency Tests (VRFT) [14,75], right after the setting of the specimens. A steel ball of 1 cm was made to hit the center of one of the circular faces of the cylinders, which produced longitudinal vibrations in the specimen. The vibrations were captured by a miniature accelerometer attached in the center of the circular face at the other end of the cylinder. Using a LABVIEW program, the measured signal was converted into a FFT domain to obtain the first two resonance frequencies in the frequency spectrum. Using an analytical procedure as mentioned in [75], the dynamic elastic modulus of the specimens were calculated. The tests were carried out in a climate chamber where the samples were cured under three different temperatures; 20 $^\circ\text{C}$, 10 $^\circ\text{C}$ and 5 $^\circ\text{C}$, for both mixes. The measurements were started from the setting time until one month or more, at a frequency of one measurement per minute. Even though the measured elastic modulus was the elastic modulus in compression, it was assumed to be the same as elastic modulus in tension.

The static modulus of elasticity was determined on cylindrical samples of 140 mm height and 70 mm diameter, following SIA 262/1 – Annex G [76]. The tests were carried out on samples cured at three different temperatures; 20 $^\circ\text{C}$, 10 $^\circ\text{C}$ and 5 $^\circ\text{C}$, right after casting until the day of testing.

2.5 Uniaxial tensile tests

Uniaxial tensile tests until fracture were carried out on specimens of both mixes to investigate the tensile resistance parameters like elastic limit, f_{Ute} and tensile strength f_{Utu} under different curing temperatures. The tests were performed at different ages as summarized in Table 5.

The tests at 1 day and 28 days were carried out on specimens cast directly in the RS setup of the TSTM (cross section 100 mm x 50 mm) at a stroke rate of 0.2 mm/min, whereas the tests at 14 days were conducted on dumbbell specimens of dimensions 50 mm x 30 mm in an electromechanical test setup KAPPA 250 DS from ZWICK/ROELL at a strain rate of 1×10^{-5} 1/s. More details regarding the electromechanical test setup and specimen preparation could be found in Chapter 3 [11].

Table 5: Summary of uniaxial tensile tests to determine the resistance parameters like f_{Ute} and f_{Utu} .

Age (days)	Mixes	Temperature	Test setup
1	Mix I	20 °C	TSTM
	Mix II	20 °C	TSTM
14	Mix I	20 °C, 5 °C	KAPPA 250 DS
	Mix II	20 °C, 10 °C, 5 °C	KAPPA 250 DS
30	Mix I	20 °C, 5 °C	TSTM
	Mix II	20 °C, 10 °C, 5 °C	TSTM
80	Mix I	20 °C	TSTM

2.6 Development of Autogenous deformations

A Temperature Stress Testing Machine (TSTM) was used to measure the autogenous deformations in the mixes right after casting, at different curing temperatures. The machine which was developed during the doctoral thesis of [18], following the works of [77–79], consists of two parts; the Free Setup (FS), which was used to measure the free autogenous deformations $\varepsilon_{free}^{free}$ in the specimen, and the Restrained setup (RS), which was used to measure the eigenstresses under different restraint conditions with the help of a load cell. More details on the test setup and measurements could be found in [5,9,21]. The cross sectional dimensions of the specimen used in both setup were 100 mm x 50 mm. The tests were carried out for both mixes at three different temperatures; 20 °C, 10 °C and 5 °C, as summarized in Table 6.

2.7 Development of eigenstresses under full restraint

The RS setup of the TSTM was used to conduct full restraint tests at different quasi-isothermal curing temperatures. The relative displacements between two LVDTs 750 mm apart, were kept at zero in order to ensure the full restraint conditions in the specimen.

However, this was not possible in the fresh state, as the material stiffness was too low to impose a close loop deformation control. As such, the tests were started under a passive control by keeping the stroke at the same initial position, until the eigenstresses reached a value of 0.2 MPa. When the trigger value of 0.2 MPa was reached, the control was shifted to deformation control, ensuring full restraint conditions from thereon. The trigger value of 0.2 MPa (corresponding to a force of 100 kg carried by the specimen) was chosen so that it is low enough to minimize the discrepancies of the control mode and the impacts on the viscous effects of the loading history. However, it is still high enough to reach a sufficient stiffness of the specimen to respond to a closed loop deformation control without yielding out of control. The tests were carried out for both mixes at three different temperatures; 20 °C, 10 °C and 5 °C, as summarized in Table 6.

Table 6: Summary of tests carried out in the TSTM.

Mix type	Temperature	Number of tests	Test name
Mix I	20 °C	2	Mix I-20C-FR1
			Mix I-20C-FR2
	5 °C	1	Mix I-5C-FR1
Mix II	20 °C	2	Mix II-20C-FR1
			Mix II-20C-FR2
	10 °C	1	Mix II-10C-FR1
	5 °C	2	Mix II-5C-FR1
			Mix II-5C-FR2

3 Results and discussions

3.1 Isothermal calorimetry

3.1.1 Heat of hydration

Figure 1a shows the average normalized heat flow per volume of the mixes Mix I_m and Mix II_m and figure 1b shows the normalized cumulative heat per volume of the same. Only the average curves are shown as the scatter between different tests at each temperature were less than 0.01%. The normalization was performed by calculating the volume of 10 g of paste that was put in the ampoule using the specific weight of both mixes (2295.9 kg/m³ for Mix I_m and 2199.6 kg/m³ for Mix II_m).

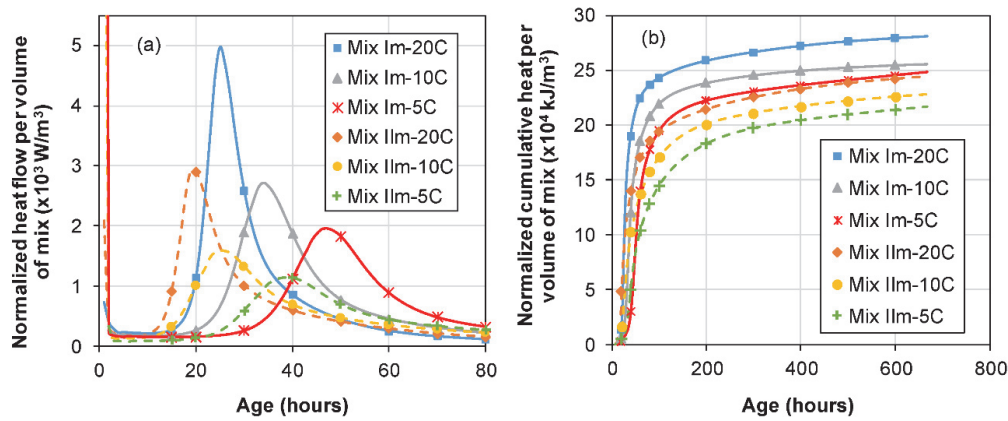


Figure 1: (a) Average cumulative heat per unit volume and (b) average heat flow per unit volume of Mix I_m and II_m from isothermal calorimetry tests at different temperatures.

Comparing the two mixes, figure 1a shows that Mix II_m exhibited a lower dormant period than Mix I_m, at similar temperatures. This could be attributed to the difference in the dosages of the superplasticizer used in the mixes to reach the minimum workability, with Mix I_m having a superplasticizer content of 20.5 kg/m³ and Mix II_m having the same at 14.7 kg/m³. However, it could also reflect a greater nucleation of C-S-H on the surfaces of the limestone filler in Mix II_m. Berodier and Scrivener [80] showed that C-S-H nucleate preferentially on the limestone surface and the amount of C-S-H nuclei formed on the limestone filler surface was much higher than that on the surface of the cement grains. They also postulated that the lower induction period might be caused by the slight dissolution of limestone, which was indicated by a higher concentration of calcium in the solution at the end of the induction period. Moreover, using TEM images, Bazzoni [81] showed a different morphology of C-S-H nuclei on the surfaces. The C-S-H were in the form of individual needles perpendicular to the surface on the limestone grains, whereas the orientation was much different on the cement grains. This also indicated that the C-S-H nucleate preferentially on the surfaces of the limestone filler. Furthermore, figure 1a also shows that a higher curing temperature results in a higher heat flow rate, a lower induction period and a narrower hydration peak in the isothermal calorimetry curves. Similar trends were also reported in [82–86]. The higher peak and lower induction period at higher temperature result from the higher rate of hydration, whereas at lower temperatures, the rate of hydration is slower and gradual. This also leads to the development of better microstructure with fewer and lesser number of pores at low temperatures [37].

Comparing the same mix at different temperatures in figure 1, it can be seen that both the heat flow and the cumulative heat is higher at a temperature of 20 °C than those at 10 °C and 5 °C. This could be attributed to the faster rate of hydration at higher temperatures. However, many authors reported that the cumulative heat of hydration at lower temperatures become higher than that at higher temperatures at later ages of hydration [38,39,83,85], owing to higher degree of hydration at later ages for lower temperatures.

Even though this trend was not seen until 650 hours in the present study, it was seen that the difference between the cumulative heats of hydration for both mixes was reduced at later ages especially for tests at 10 °C and 5 °C. Similar trends were seen by Kazemi Kamyab [14] for UHPC mixes similar to those in the present study, who attributed this difference to the presence of silica fume in the mixes as compared to that of [38,39]. However, Gallucci et al. [37] showed that the degree of hydration at 1 year remains the same for cement pastes tested at different temperatures varying from 5 °C to 60 °C, thereby indicating that the cumulative heat of hydration may also become similar at a later age. Figure 1b also shows a lesser cumulative heat of hydration for Mix II_m when compared to Mix I_m at any temperature. It seems that compared to Mix I_m, slightly lesser volumes of cement are hydrating in Mix II_m (same for silica fume). This may be because of the very dense nucleation of C-S-H in the presence of limestone filler, as discussed earlier, which prevents the water from reaching the unhydrated cement grains, as the microstructure develop. However, further studies using SEM micrographs are needed to validate this argument.

3.1.2 Maturity and activation energy

Different methods could be used to find the activation energy of cumulative heat of hydration from isothermal calorimetry tests as could be found in [14,87–89]. In this study, the master curve method using the maturity equation (1) as reported in [14] was used to determine the apparent activation energy, E_a , corresponding to the development of the cumulative heat of hydration from the isothermal calorimetry tests for both mixes. The apparent activation energy (E_a) in equation (2) was changed until the cumulative heat of hydration curves at different temperatures converged in the maturity domain. The cumulative heat of hydration curves in the age domain as well as in the maturity domain are shown in figure 2.

$$M(t) = \int_0^t e^{\frac{E_a}{R} \left(\frac{1}{273+T_{ref}} - \frac{1}{273+T(t)} \right)} dt \quad (1)$$

where $M(t)$ is the maturity function in hours, E_a is the apparent activation energy in J/mol, R is the ideal gas constant = 8.314 J/(mol.K), T_{ref} = 20 °C is the reference temperature and $T(t)$ is the development of temperature in the specimen in centigrade. In an isothermal case, equation (1) simplifies into a scalar multiplied by time as shown in equation (2),

$$M(t) = t \cdot e^{\frac{E_a}{R} \left(\frac{1}{273+T_{ref}} - \frac{1}{273+T(t)} \right)} \quad (2)$$

Using a least-squares regression analysis, the E_a/R values for Mix I_m and Mix II_m were found to be 3300 K and 4000 K, respectively. The E_a/R for Mix I_m was the same as that reported by [14], who had conducted isothermal calorimetry tests on a similar UHPC matrix of type CM22_TKK, which is the predecessor of Mix I in the present study. Figure 2 shows that the cumulative heat of hydration curves at different temperatures converge in the maturity domain into nearly one curve, except for the slight variations in the values of cumulative heat of hydration of Mix I_m at a later maturity.

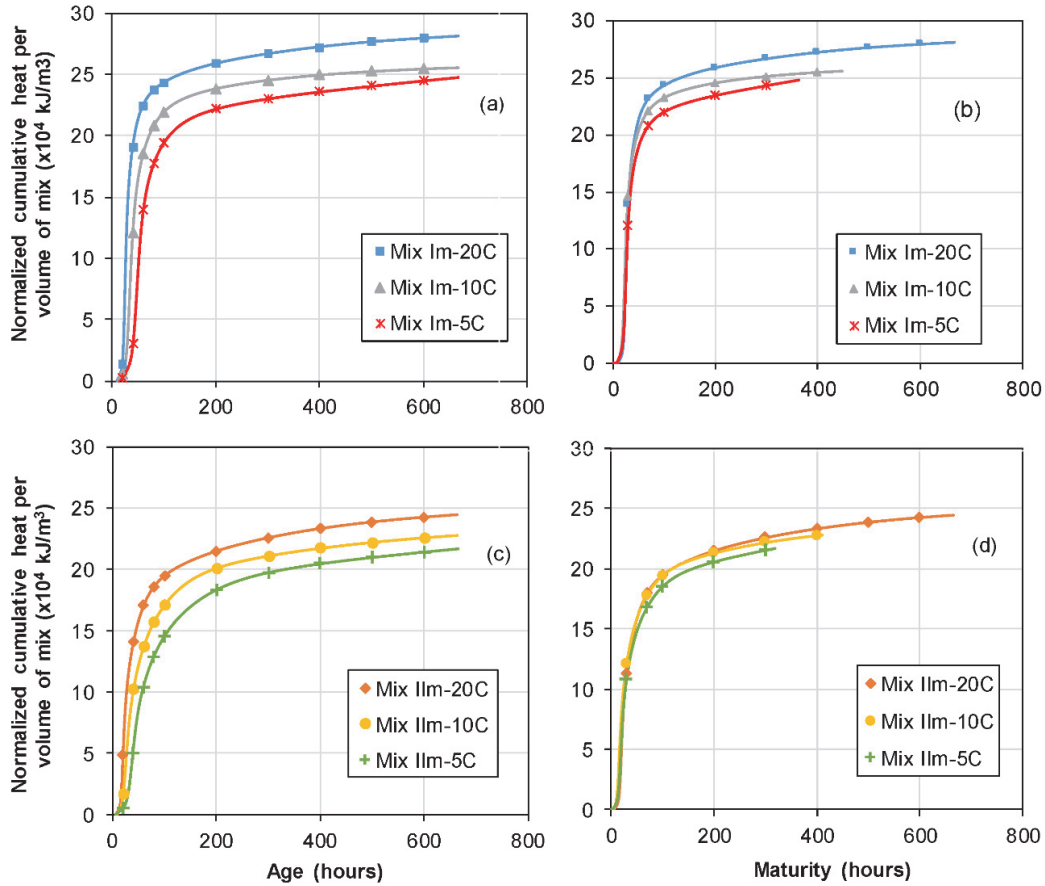


Figure 2: Average cumulative heat per unit volume of Mix I_m in the (a) age domain (b) maturity domain and for Mix II_m in the (c) age domain and (d) maturity domain.

3.1.3 Double Danish model

Even though the conventional ‘Danish model’ introduced by Hansen and Pedersen [90] predicts the development of cumulative heat of hydration for conventional cementitious materials, [14] showed that it cannot predict the behavior of mixes with extensive amounts of silica fume and supplementary cementitious materials. As such, a ‘Double Danish model’, as suggested by Denarié [91], was used to predict the behavior of the present UHPC mixes.

It was assumed that the main heat release from the formation of C-S-H during the hydration of cement was represented by the first term and the remaining heat release associated with the pozzolanic reaction of silica fume was covered by the second term. The double Danish model is given in equation (3).

$$H_T(t) = H_{T_1} \cdot e^{-\left(\frac{\tau_1}{t}\right)^{\beta_1}} + H_{T_2} \cdot e^{-\left(\frac{\tau_2}{t}\right)^{\beta_2}} \quad (3)$$

$$H_{T_\infty} = H_{T_1} + H_{T_2} \quad (4)$$

Here, $H_T(t)$ is the development of cumulative heat of hydration in kJ/m^3 , H_{T1} and H_{T2} are the primary and secondary contributions respectively to the heat of hydration, τ_1 and τ_2 are the hydration time parameters of the first and second terms of the double Danish model in hours, β_1 and β_2 are the hydration slope parameters of the first and second terms of the model, and H_{T_∞} is the asymptotic value of the cumulative heat of hydration of the mixes.

Instead of developing multiple models for different temperatures, a representative cumulative heat of hydration curve was developed for each mix as shown in figure 3. Using a least-squares regression analysis, the parameters of the double Danish model were determined for both mixes, such that the responses of the representative cumulative heat of hydration curves were closely predicted. Figure 3 shows the representative curves along with their predictions for both mixes. The parameters of the model for both mixes are shown in Table 7.

Table 7: Parameters of the double Danish model for Mix I and II.

	Parameter	Units	Mix I _m	Mix II _m
Activation energy	E_a/R	K	3300	4000
	H_{T1}	kJ/m^3	192,000	144,000
	τ_1	hours	25.3	20.0
	β_1	--	3.99	2.28
Double Danish model parameters	H_{T2}	kJ/m^3	95,000	105,000
	τ_2	hours	81.2	69.0
	β_2	--	0.64	0.77
	H_{T_∞}	kJ/m^3	287,000	249,000

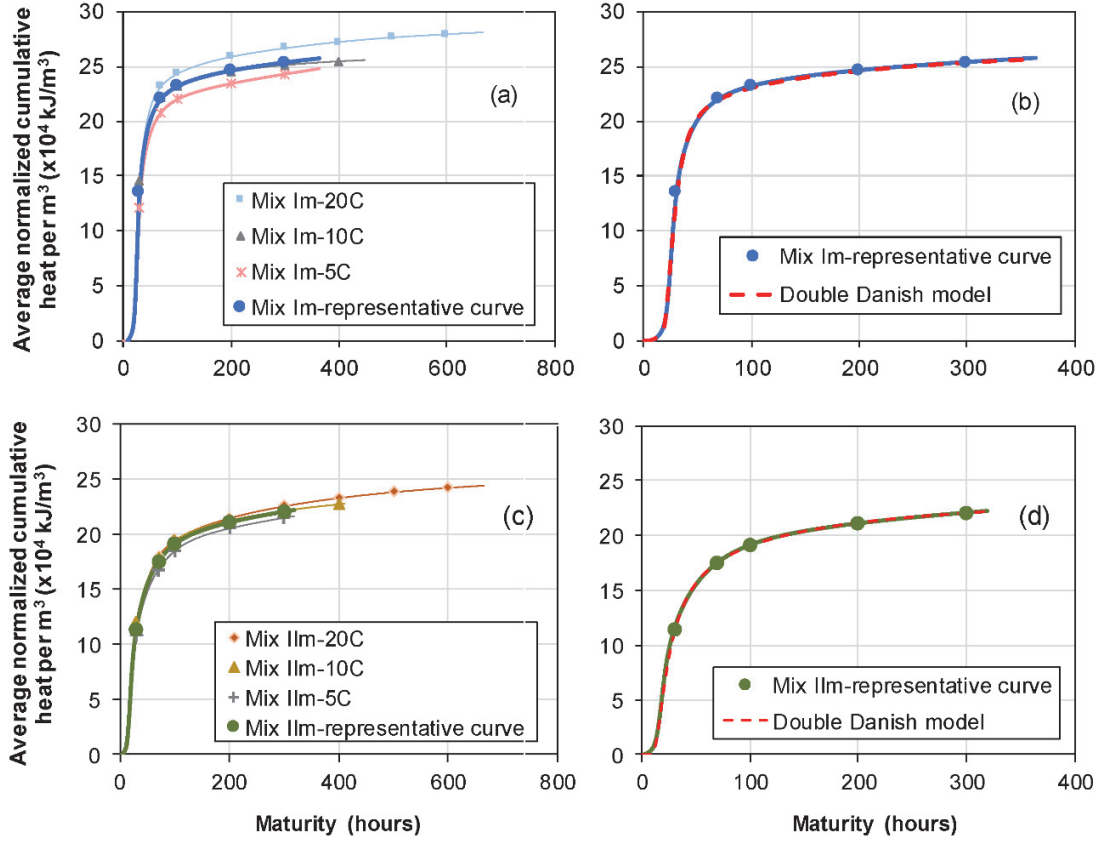


Figure 3: (a) Representative cumulative heat per unit volume of Mix I_m, (b) Double Danish model prediction of Mix I_m, (c) representative cumulative heat per unit volume of Mix II_m, and (d) Double Danish model prediction of Mix II_m.

3.1.4 Degree of hydration

The degree of hydration at any time, $\alpha(t)$, can be estimated by dividing the cumulative heat of hydration per unit volume of the mixes $H_T(t)$ by the theoretical total potential heat of hydration that would have been released if there was full hydration, $H_{T100\%}$, as shown in equation (5) [38].

$$\alpha(t) = \frac{H_T(t)}{H_{T100\%}} \quad (5)$$

The theoretical total heat released can be obtained by considering the individual contributions of total heat of hydration for full hydration of both cement and silica fume in the mixes, as the contributions of the other components are negligible. Moreover, [14,92] have shown that only a maximum of 20% mass of silica fume ($SF/C=0.2$) contributed to the heat of hydration, as all the $Ca(OH)_2$ produced by cement hydration will be consumed by then and there will be no more pozzolanic reaction. Table 8 shows the total potential release of both mixes at full hydration.

Table 8: Total potential heat release of Mix I_m and Mix II_m at full hydration, $H_{T100\%}$.

Mix	Cement reacted (kg/m ³)	Heat release of cement (kJ/kg)	Silica fume reacted (kg/m ³)	Heat release of silica fume (kJ/kg)[92]	Total potential heat at full hydration, $H_{T100\%}$ (kJ/m ³)
Mix I	1607.9	452.3	321.6	780	978,085
Mix II	809.6	452.3	161.9	780	492,480

The degree of hydration at any age for both mixes can be obtained by equation (5). Figure 4 shows the development of degree of hydration with respect to the age and maturity of the material at different temperatures. Using the ultimate heat of hydration, $H_{T\infty}$ from Table 7 and equation (5), the ultimate degrees of hydration of Mix I_m and Mix II_m were calculated to be 29% and 51%, respectively. The maturity as well as the degree of hydration can be used as domains alternative to the age of the material and the responses under different temperatures could be compared for various mechanical properties in these domains as discussed in the upcoming sections.

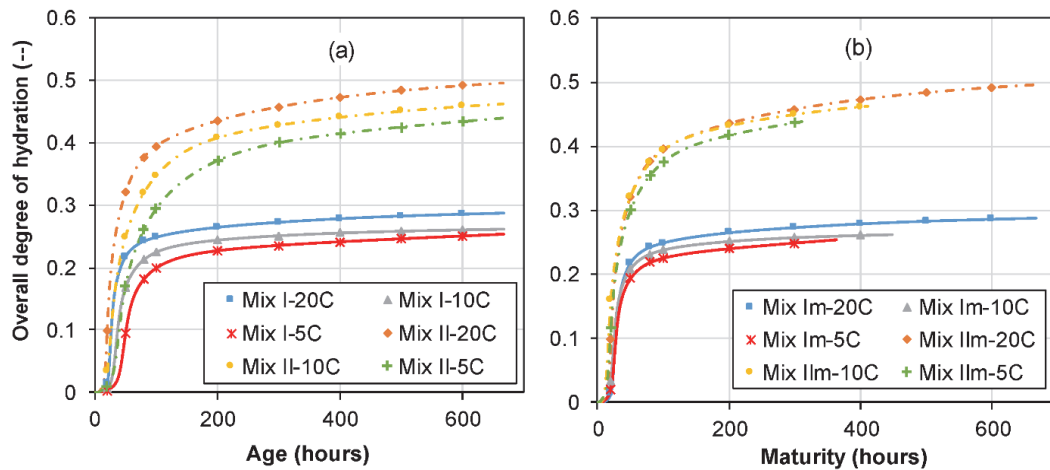


Figure 4: Development of overall degree of hydration of Mix I_m and Mix II_m at different temperatures, calculated using equation (5), from the cumulative heat of hydration curves from isothermal calorimetry tests in the (a) age domain and (b) maturity domain.

3.2 Degree of hydration from ^{29}Si MAS NMR

Figure 5 shows typical ^{29}Si MAS NMR spectra of the hydrated samples (Mix I_m cured at 20 °C) and each spectrum has been analyzed in a semi-quantitative manner, using the same procedures for spectral deconvolution of ^{29}Si MAS NMR spectra, as described in [71–74]. The analysis of the ^{29}Si NMR spectrum of the anhydrous Portland cement gives an alite/belite intensity ratio of 10.9 (molar ratio), and combining this ratio with the bulk SiO_2 content of the cement (22.75 wt%) gives quantities of 5.5 wt.% Ca_2SiO_4 and 79.2 wt.% Ca_3SiO_5 , assuming stoichiometric phases. If the Taylor compositions are used [71,72], which consider the most common guest-ion incorporations, the calculated quantities for belite and alite are 6.6 wt.% and 83.1 wt.%, respectively.

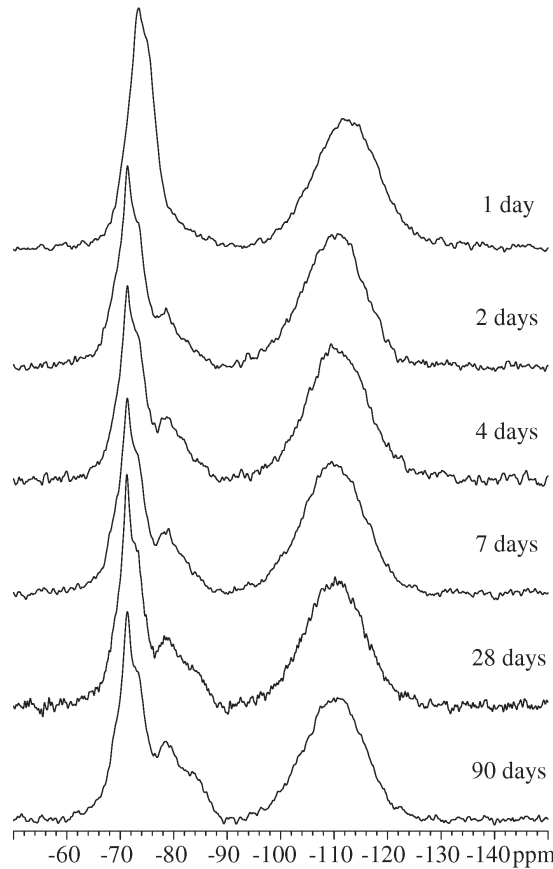


Figure 5: ^{29}Si MAS NMR spectra of the hydrated samples of Mix I_m cured at a temperature of 20 °C.

The relative ^{29}Si NMR intensities (I) and degrees of hydration (H) for alite and belite and the percentage of silica fume reacted (α_{SF}) from the deconvolutions of the ^{29}Si MAS NMR spectra of Mix I_m and Mix II_m respectively, at different temperatures are shown in the Appendix A, Tables A1 and A2. The error limits associated with the degrees of hydration for alite, belite and silica fume are estimated to $\pm 1.5\%$, $\pm 4.0\%$ and $\pm 1.2\%$, respectively.

The higher error limit for belite reflects the low intensity of the belite peak and as such, a small change may lead to a higher effect on the degree of reaction. The degrees of hydration of alite and belite and the percentage of silica fume reacted are given by equations (6), (7) and (8), respectively. The overall degree of hydration of the cement including the contributions of alite and belite is calculated using equation (9), where 0.055 and 0.792 are fractions of alite and belite determined from the analysis of the ^{29}Si NMR spectrum of the anhydrous Portland cement.

$$H_{C_2S} = \left(1 - \frac{I(C_2S)_t}{I(C_2S)_{t=0}} \right) \cdot 100\% \quad (6)$$

$$H_{C_3S} = \left(1 - \frac{I(C_3S)_t}{I(C_3S)_{t=0}} \right) \cdot 100\% \quad (7)$$

$$\alpha_{SF} = \left(1 - \frac{I(SF)_t}{I(SF)_{t=0}} \right) \cdot 100\% \quad (8)$$

$$\alpha_{cem} = H_{C_2S} \cdot \frac{0.055}{0.055 + 0.792} + H_{C_3S} \cdot \frac{0.792}{0.055 + 0.792} \quad (9)$$

Figure 6 shows the development of the degree of cement hydration, α_{cem} , calculated using equation (9) for both mixes in the age domain along with a comparison of that of the matrix of CM22_TKK (CM22_TKK_m) which is the predecessor of Mix I in the present study.

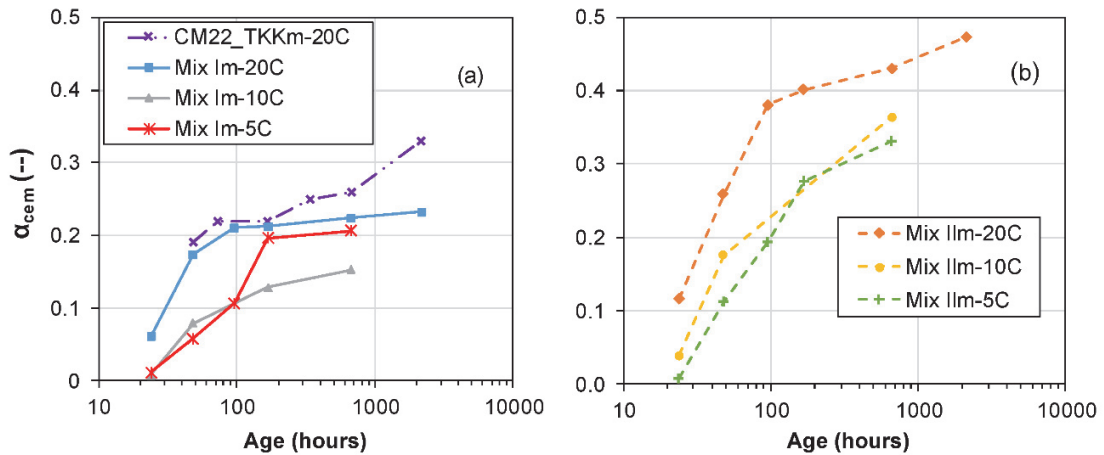


Figure 6: Development of the degree of cement hydration (α_{cem}) at different temperatures in the age domain for (a) Mix I_m and (b) Mix II_m.

The α_{cem} of Mix I_m at 20 °C was almost similar to that of CM22_TKK_m until an age of 28 days, but shows a deviation at 90 days with Mix I_m showing a α_{cem} of 0.23 while CM22_TKK_m shows a value of 0.33. This significant difference may reflect differences in the sample preparations or errors associated with the test measurements. Moreover, both the Waller model [92] and the Jensen model [93] predicted a value of 0.30 as the ultimate α_{cem} of Mix I_m. Mix II_m shows a much higher value of 0.47 at 90 days, whereas the predictions of Waller model and Jensen model were respectively 0.47 and 0.5. For both mixes, the influence of thermal activation of hydration is evident, with higher curing temperature leading to a higher α_{cem} at any particular age, except for Mix I_m at 10 °C at an age of 7 days (168 hours) and 28 days (672 hours). Even though earlier research [38,44] have shown that lower curing temperature may lead to a higher degree of hydration at later ages, it still does not fully explain why at 7 days and 28 days, the α_{cem} of Mix I_m cured at 5 °C was almost similar to that at 20 °C, but that in the case of 10 °C, it was much lower. For Mix II_m, the influence of thermal activation is clear, with α_{cem} at any age decreasing with the decrease in temperature. However, it is possible that at a much later age, α_{cem} becomes the same [37] or even higher for lower temperatures [38,44]. Figure 7 shows the percentage of silica fume reacted (α_{SF}) as a function of age. The only clear trend is the thermal activation of the pozzolanic reaction, which leads to a higher α_{SF} at any particular age at higher temperatures. Figure 8 shows the development of α_{cem} in a maturity domain, which shows almost a similar trend as seen in the case of the age domain.

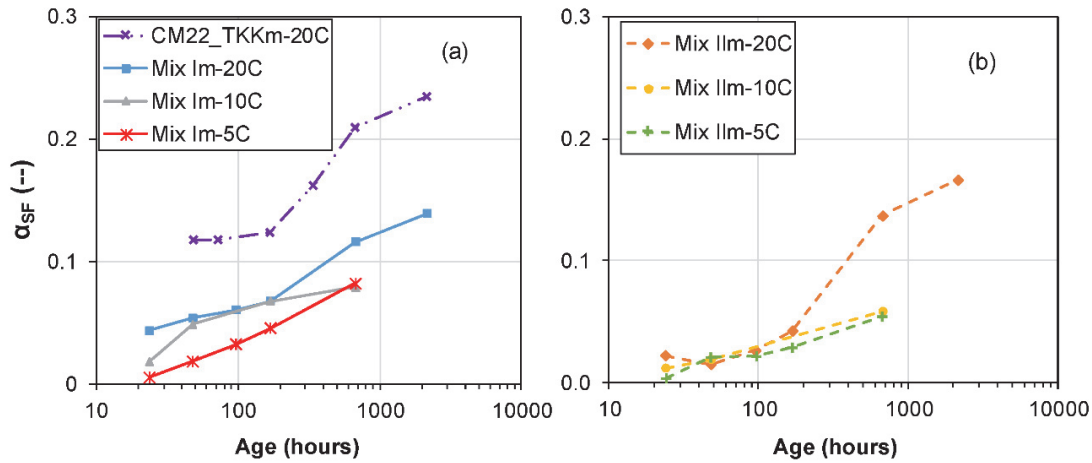


Figure 7: Development of degree of silica fume reaction (α_{SF}) at different temperatures in the age domain for (a) Mix I_m and (b) Mix II_m.

However, a comparison of α_{cem} , α_{SF} and the ratio α_{SF}/α_{cem} in the maturity domain shows an interesting trend, as can be seen in figure 8. Even though, individually the development of α_{cem} and α_{SF} does not show any particular trend other than the higher thermal activation at higher temperatures, the development of α_{SF}/α_{cem} along the maturity domain shows an initial decrease followed by an increase.

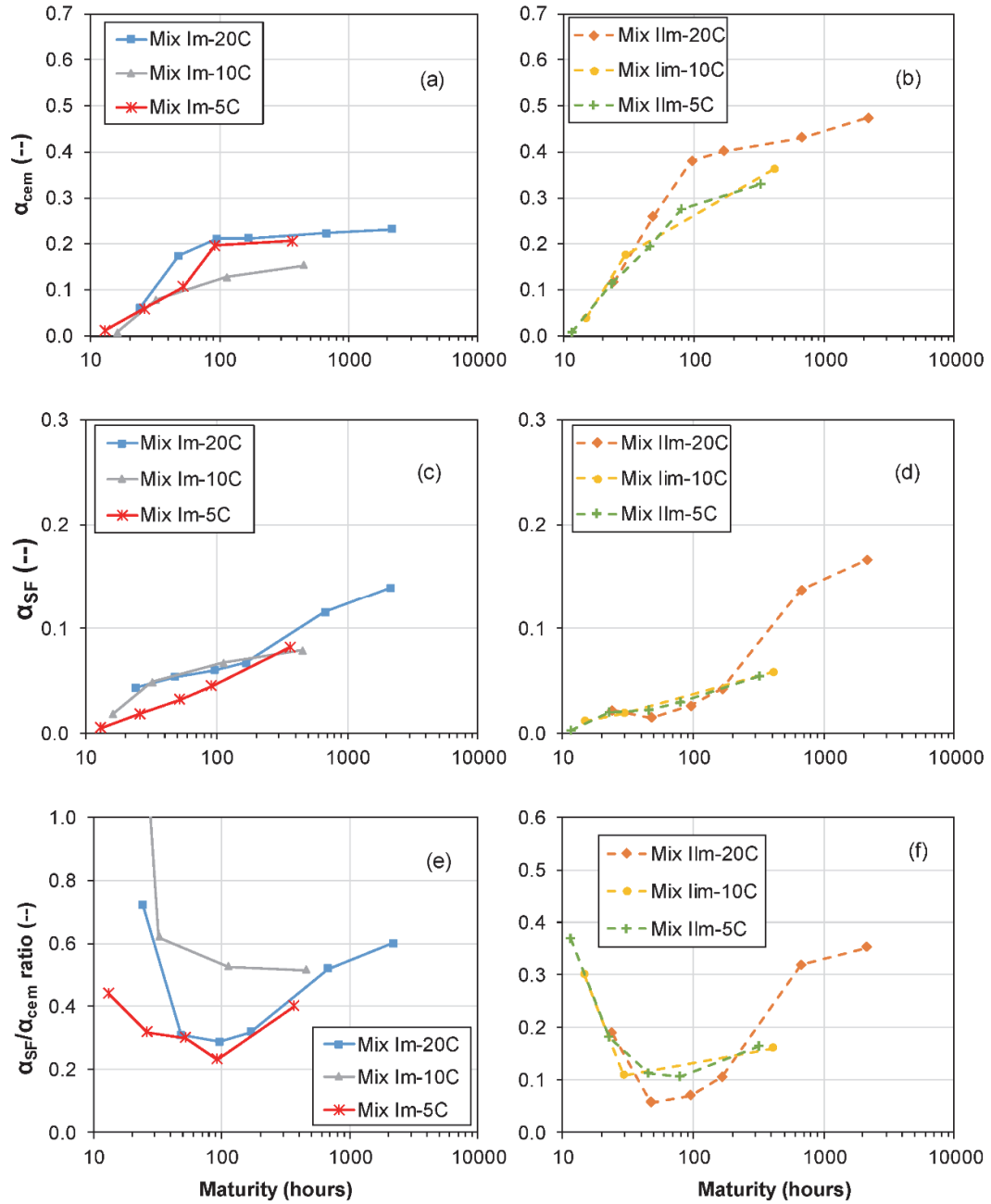


Figure 8: Development of α_{cem} in the maturity domain for (a) Mix I_m and (b) Mix II_m. Development of α_{SF} in the maturity domain for (c) Mix I_m and (d) Mix II_m. Variation in the α_{SF}/α_{cem} ratio in the maturity domain for (e) Mix I_m and (f) Mix II_m.

The trend was not shown by Mix I_m at 10 °C, and as explained earlier, it was the same Mix I_m at 10 °C that showed unexplainable lower values of α_{cem} at ages of 7 days and 28 days, leading to a conclusion that there might have been errors either in the measurement or the preparation of these samples. Nevertheless, the observed trend of an initial decrease in the α_{SF}/α_{cem} followed by an increase gives an indication that in the beginning, even though there

is a limited reaction of the silica fume, the major contribution to the overall degree of hydration of the mixes is that from the cement. However, in the second stage there is a more pronounced reaction of the silica fume, leading to an increase in the α_{SF}/α_{cem} ratio. This indicates that the pozzolanic reaction is also taking place in two stages; an initial stage where the rate of pozzolanic reaction is smaller than that of the direct formation of the C-S-H and a second stage where the trend is reversed.

It is also interesting to note the value of average maturity at which the trend of α_{SF}/α_{cem} is changing from a decreasing rate to an increasing rate. For Mix I, this value was approximately 90 hours (excluding the Mix I-10C test) whereas for Mix II it was approximately 70 hours (note that this is an approximate average value derived from the limited number of points in the test). It is interesting to observe that these values were similar to the hydration time parameters of the second term τ_2 in the double Danish model as shown in Table 7 with Mix I and II having values of 81.2 hours and 69.0 hours, respectively. This clearly indicates that the additional accelerated pozzolanic reaction in the second stage contributes to the heat release predicted by the second term of the Double Danish model.

According to the Waller model [92], the ultimate values of α_{cem} , α_{SF} and α_{SF}/α_{cem} were respectively 0.3, 0.28 and 0.93 for Mix I and 0.47, 0.29 and 0.62 for Mix II. Figure 8 reveals that at an age of 90 hours, the experimental results show values of 0.23, 0.14 and 0.6 for Mix I, and 0.47, 0.17 and 0.35 for Mix II for the same. The huge difference in the α_{SF}/α_{cem} values were mainly because the values of α_{SF} were considerably lower than the Waller predictions, but they may reach similar values at a much later age. The values of α_{cem} was lower for Mix I, probably due to errors in the specimen preparation, whereas α_{cem} of Mix II was similar to the prediction of the Waller model.

3.3 Development of elastic modulus

The development of the dynamic elastic moduli from the VRF tests, along with the static elastic moduli for both mixes at different temperatures are shown in figure 9. For each mix at a particular temperature, two tests were performed using the VRF and since both the curves almost merged together with minimum scatter, the average of the two curves is shown for each mix and temperature in figure 9. For each mix at different temperatures, the dynamic elastic moduli are higher than the corresponding static moduli, as expected. Moreover, the static elastic moduli showed almost similar values at temperatures of 10 °C and 5 °C, which were slightly lesser than those at 20 °C for both mixes. It may be possible that at a much later age, the values of the static moduli become similar under all the temperatures, just as in the case of the dynamic elastic moduli as discussed below.

For the dynamic elastic moduli, the development started earlier for 20 °C because of the thermal activation of hydration as in the case of the isothermal calorimetry tests. However, the trend of development of the dynamic moduli at all temperatures is such that the ultimate dynamic elastic moduli reach a similar value at a later age, slightly higher than 50 GPa.

There is a contrast in literature regarding the degree of hydration and the corresponding development of mechanical properties at different temperatures for cementitious materials. On the one hand, some studies show that the degree of hydration is higher at a later age for lower temperatures [38,39,44], whereas on the other hand, other investigations show that the ultimate degree of hydration remains the same under different temperatures [37]. In any case, the present study shows a trend to have a similar elastic modulus at a later age, but whether it will be higher for lower temperatures at a much later age cannot be concluded.

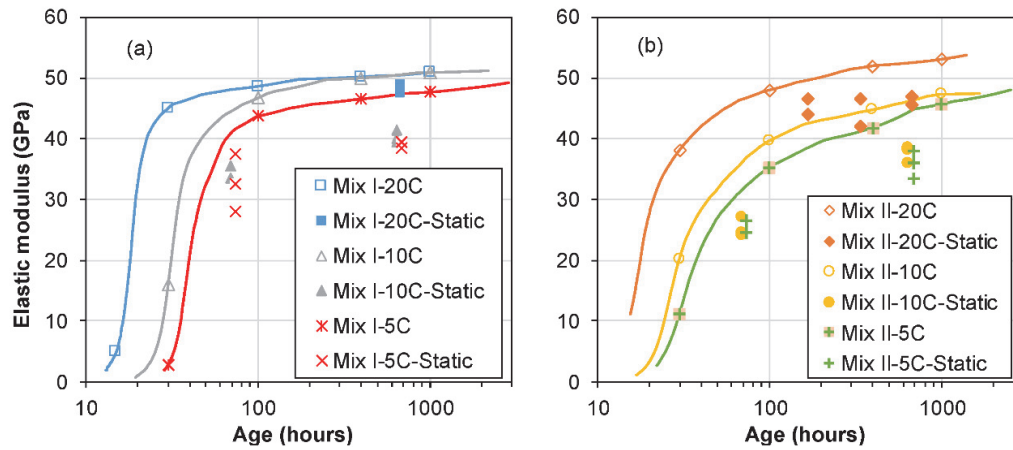


Figure 9: Development of dynamic and static elastic moduli at different temperatures in the age domain for (a) Mix I and (b) Mix II.

Figure 10 shows the comparison of the dynamic elastic moduli development in Mix I and II at different temperatures.

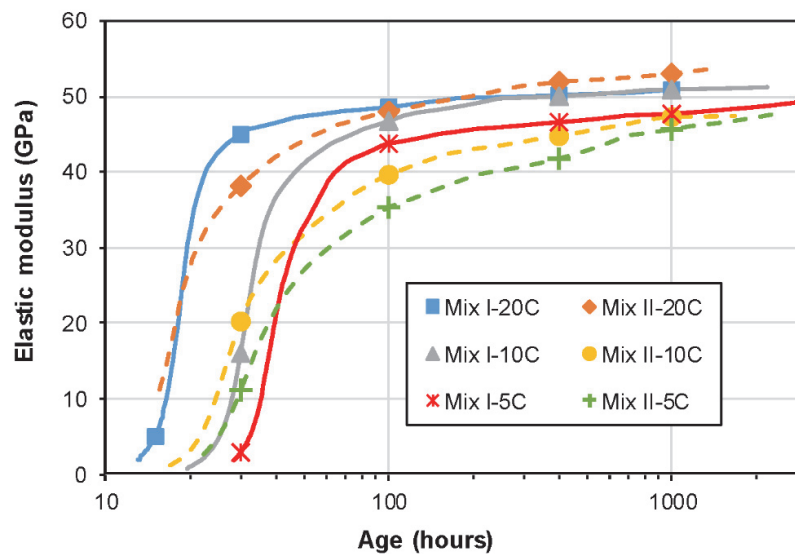


Figure 10: Comparison of the development of average dynamic elastic modulus of Mix I and II at different curing temperatures in the age domain.

At any particular temperature, the dynamic elastic moduli of Mix I and II are comparable in the beginning, whereas at around an elastic modulus of 20 GPa, the rate of development becomes much slower in Mix II for all the curing temperatures. Moreover, the trend inverts at around an elastic modulus of 40 GPa, and the values for both mixes start converging again. This trend was discussed in detail in the framework of two main parameters; the silica fume/cement (SF/C) ratio and the water/cement (w/c) ratio in Chapter 2 [21]. More details could be found in Appendix B.

Following the concepts developed in section 3.1.2 and 3.1.4, the development of elastic moduli at different temperatures was studied in the maturity domain as well as in the degree of hydration domain. Figure 11 shows the development in the maturity domain whereas figure 12 shows the same in the degree of hydration domain. In the maturity domain, a single activation energy ($E_a/R = 3300$ K for Mix I_m and 4000 K for Mix II_m, section 3.1.2) can more or less capture the influence of temperature on the development of the elastic modulus except for slight discrepancies for the mixes at 20 °C. In figure 11a, the development of elastic modulus for Mix I at 20 °C begins at a slightly earlier maturity, which may be attributed to the relatively higher increase in the temperature in the VRF test cylinders at 20 °C during the hydration of the main components. The maturity axis in figure 11 was calculated based on the assumption of isothermal temperature conditions from section 3.1.2, which is not the case in the VRF samples. Even though this trend is not seen in the Mix II samples in figure 11b, the slightly higher values of Mix II at 20 °C at a later age could be attributed either to a better fiber orientation in these mixes or to the fact that the elastic moduli of the other samples at 10 °C and 5 °C may eventually reach these values at a much later age.

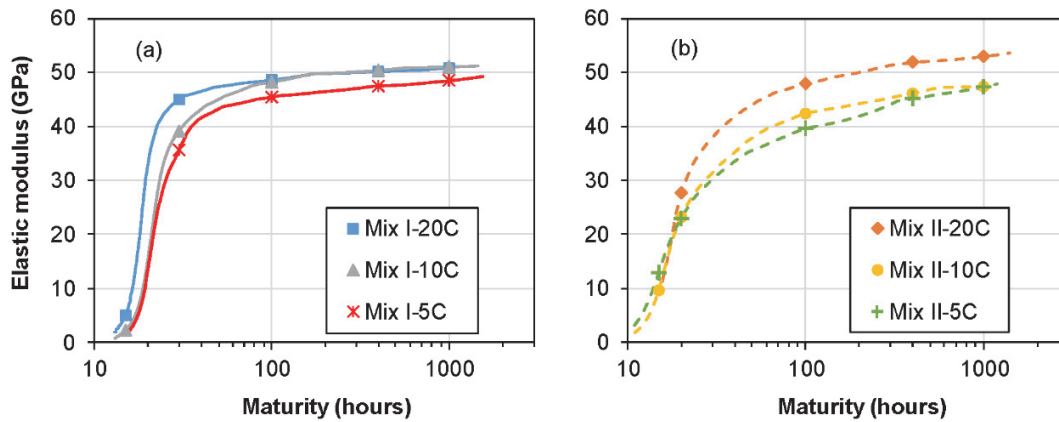


Figure 11: Development of dynamic elastic moduli at different temperatures in the maturity domain for (a) Mix I and (b) Mix II.

The trend is more or less similar in the degree of hydration domain as seen in figure 12 with Mix I at 20 °C showing an entirely different trend when compared to that of the other cases.

This difference may be linked to the calculation of degree of hydration based on the isothermal calorimetry tests where the specimen used is entirely different from that used for the VRF tests. Moreover, the difference could also be attributed to the different mixes used in the tests; mixes with fibers in the VRF tests and mixes without fibers in the isothermal calorimetry tests. Nevertheless, the values of elastic moduli reach almost similar values for Mix I at a degree of hydration of 0.2. The values are similar for Mix II at 10 °C and 5 °C, but shows a slightly higher value at 20 °C for similar degrees of hydration, which could reflect different fiber orientations in the specimens as discussed earlier.

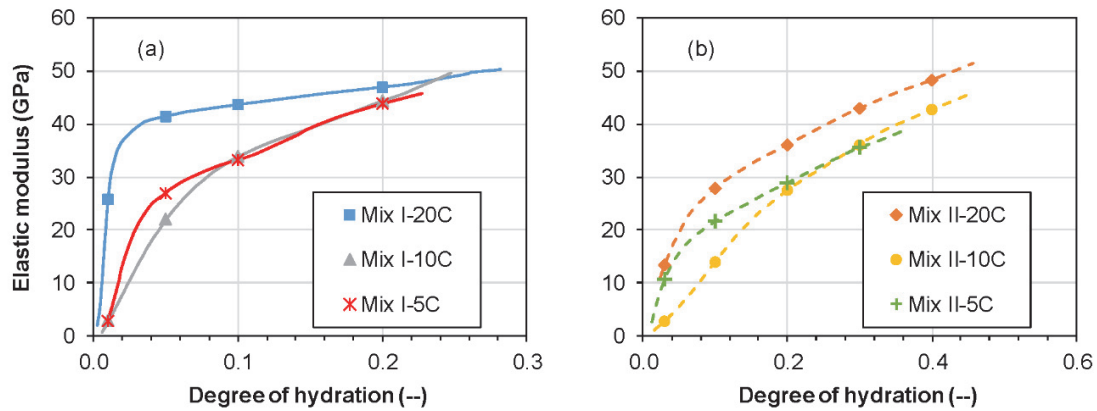


Figure 12: Development of dynamic and static elastic moduli at different temperatures in the degree of hydration domain for (a) Mix I and (b) Mix II.

3.4 Tensile resistance from uniaxial tensile tests

Table 9 summarizes the average values of elastic limit, f_{Ute} , and tensile strength, f_{Utu} , at different ages and under different curing temperatures for both mixes. The standard deviation associated with the measurements are also shown, except for certain tests where only one specimen was tested. A decrease can be seen for f_{Ute} and f_{Utu} for certain test series (Mix I-5C- f_{Ute} , Mix I-5C- f_{Utu} and Mix II-10C- f_{Utu}) as the age increases from 336 hours (14 days) to 720 hours (30 days). This may be because of the smaller cross sectional area of the specimens tested on 14 days (50mm x 30 mm), which may lead to a more favorable orientation of the fibers when compared to the specimens with a cross sectional area of 100mm x 50mm. The trend could also be attributed to the scatter in the test results at different ages. More discussion on the test results is given in section 3.6.

Table 9: Summary of uniaxial tensile tests

Mix	Temperature	Age (hours)	Average f_{Ute} (MPa)	Average f_{Utu} (MPa)
Mix I	20 °C	24	8.6 ± 0.3	11.4 ± 0.5
		336	12.3 ± 1.7	15.1 ± 2.3
		720	13.0 ± 1.2	16.2 ± 2.0
		1920	13.2	18.1
	5 °C	336	14.2 ± 0.8	19.8 ± 0.9
		720	14.0	16.6
Mix II	20 °C	24	8.1 ± 0.2	9.3 ± 0.2
		336	11.1 ± 1.9	15.1 ± 2.7
		800	13.2 ± 0.5	16.7 ± 0.7
	10 °C	336	12.5 ± 0.6	17.8 ± 1.0
		720	13.2	16.1
	5 °C	336	11.1 ± 0.8	14.8 ± 0.5
		720	12.7 ± 0.8	17.9 ± 1.5

3.5 Development of autogenous deformations

The development of autogenous deformations is shown in figure 13, wherein an increasing deformation represents autogenous shrinkage. All the curves have an initial swelling phase in the beginning, as also observed by other researchers for UHPFRC [5,14,55]. However, as indicated in Chapter 2 [21], it is the autogenous deformation after the swelling phase that lead to the development of eigenstresses. As such, figure 14 shows the development of autogenous deformations zeroed at the end of swelling (autogenous shrinkage). For the ease of comparison, an average response of each mix at a particular curing temperature is shown in figure 15. From figure 15, as the curing temperature decreases, the autogenous shrinkage also decreases for both mixes, even though the decrease is much less when the temperature changes from 10 °C to 5 °C for Mix II. Just as in the case of the isothermal calorimetry and elastic modulus, the autogenous shrinkage (after swelling) also starts developing earlier at a temperature of 20 °C, but it is delayed as the temperature decreases.

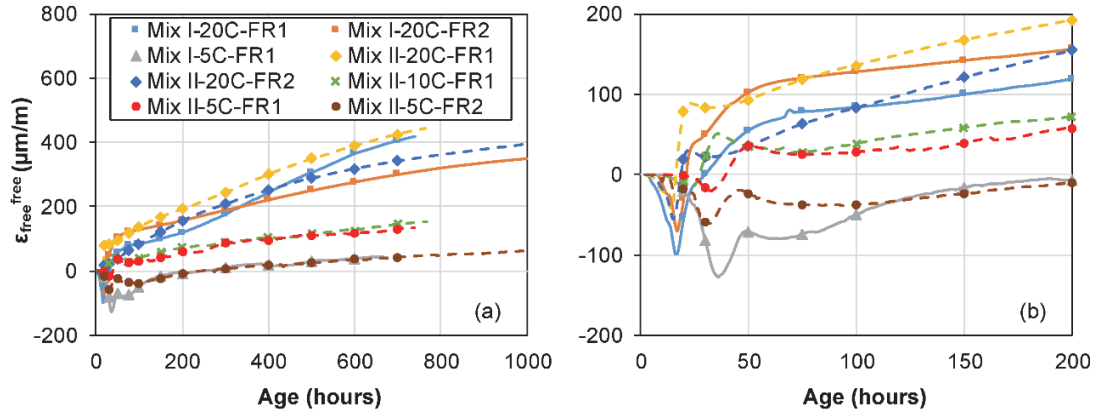


Figure 13: Development of autogenous deformations as measured (with an initial swelling phase) in the FS setup of TSTM for Mix I and II at different quasi-isothermal temperatures in the age domain; (a) overall behavior and (b) early-age behavior.

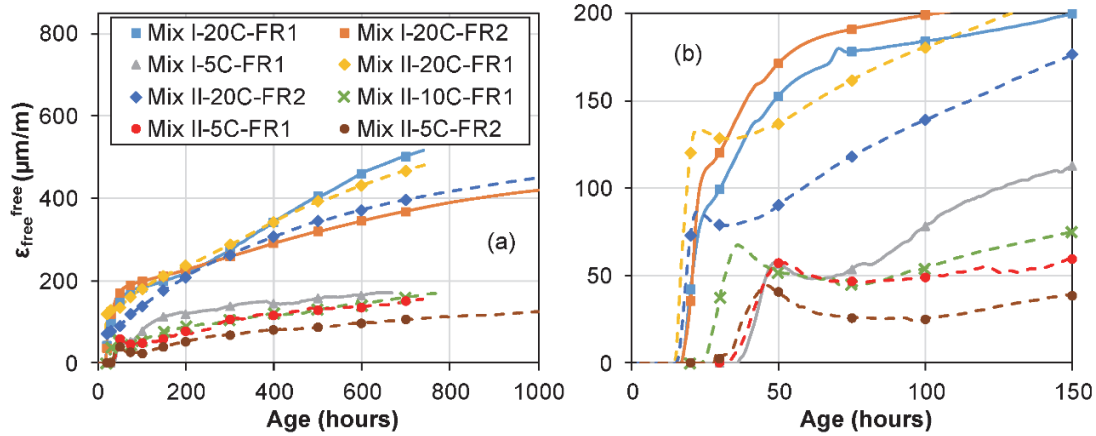


Figure 14: Development of autogenous deformations zeroed after the swelling for Mix I and II at different quasi-isothermal temperatures in the age domain; (a) overall behavior and (b) early-age behavior.

The reduction in the value of the autogenous shrinkage even after an age of 1 month is similar to the trends seen in [7,14,31], while some others have reported non-systematic trends in the development of autogenous shrinkage under different curing temperatures. Kamen et al. [5] showed that the autogenous deformation at 10 °C for a UHPFRC of type CM22, was already higher than the same at 20 °C at an age of 4 days. Lura et al. [35] showed a non-systematic effect of curing temperature on the autogenous shrinkage, but found out that the autogenous shrinkage reached similar asymptotic values at a very later age. Bjontegaard [77] reported an increase in the autogenous shrinkage with both a decrease as well as an increase in the temperature when compared to that at a temperature of 20 °C. Many authors have reported that even though the rate of shrinkage is significantly influenced by the temperature, the magnitude of the shrinkage at a very later age becomes almost similar for all temperatures [29,35].

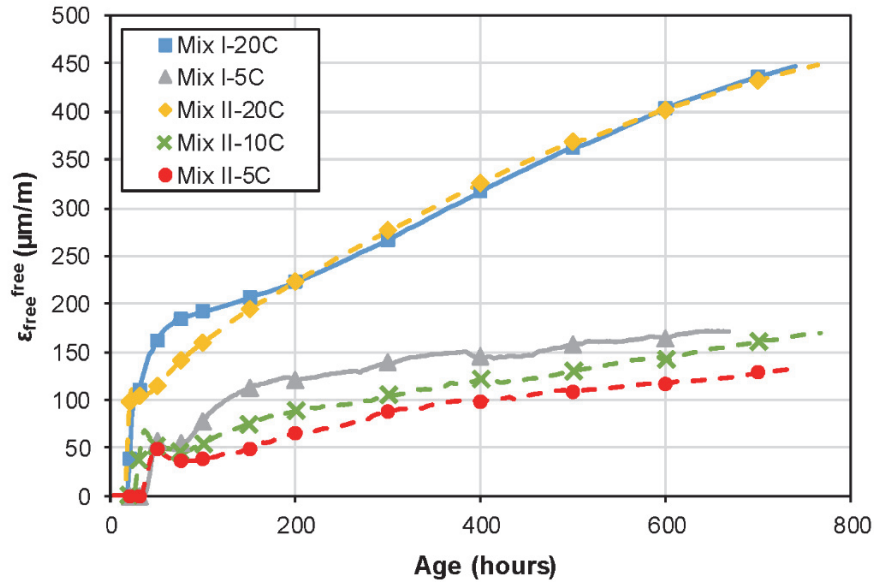


Figure 15: Comparison of the average autogenous deformations zeroed after swelling at different quasi-isothermal temperatures for Mix I and II in the age domain.

Figure 16 shows the development of autogenous shrinkage in the maturity domain. It can be seen that the maturity domain does not provide anything additional over the age domain, and therefore does not eliminate the influence of the temperature. This was shown by many researchers previously [14,29,31,35] who attributed this to the dependence of the driving force of the autogenous shrinkage, the capillary stress, on the temperature, as shown by the Kelvin-Laplace equation, i.e., equation (10).

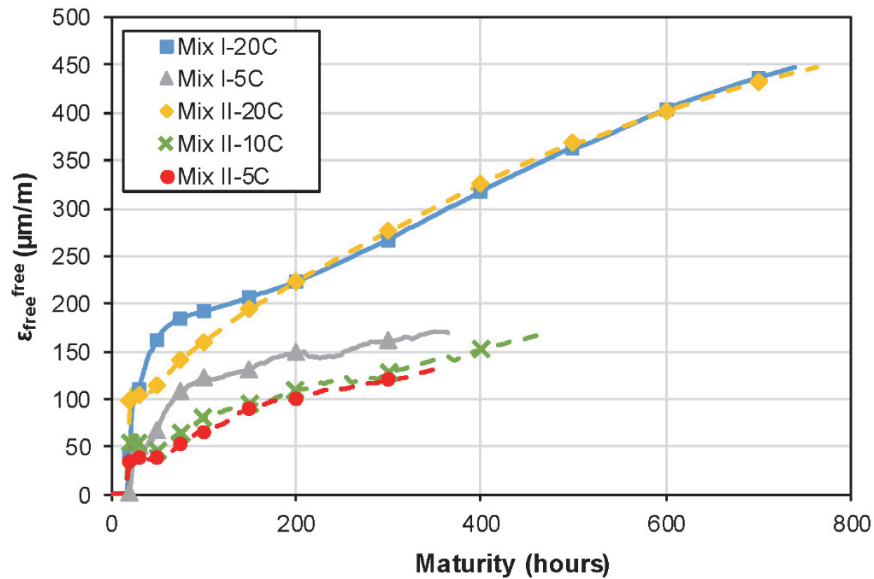


Figure 16: Comparison of the average autogenous deformations zeroed after swelling at different quasi-isothermal temperatures for Mix I and II in the maturity domain.

As such, the degree of hydration calculated from the isothermal calorimetry tests were used to compare the autogenous shrinkage developments under different curing temperatures, as shown in figure 17.

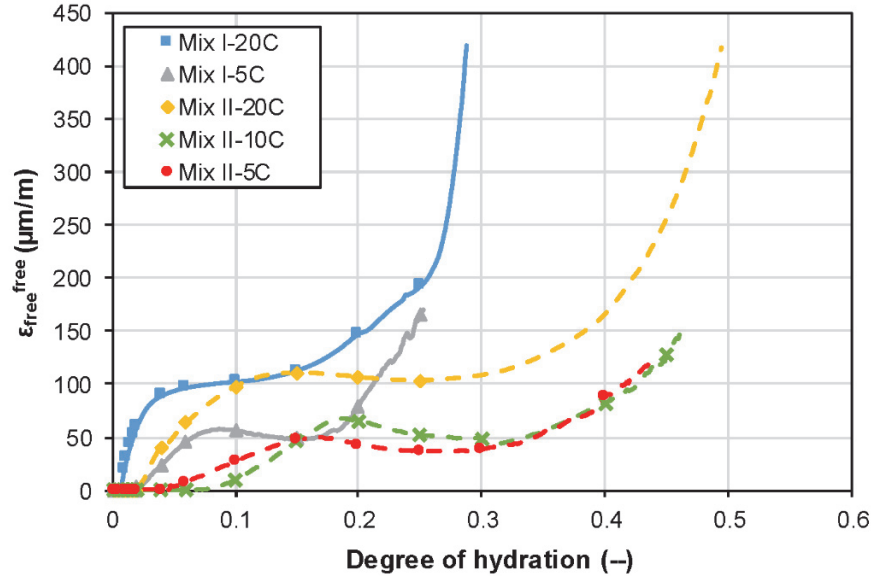


Figure 17: Comparison of the average autogenous deformations zeroed after swelling at different quasi-isothermal temperatures for Mix I and II in the DOH domain.

The comparison between Mix I and II becomes impossible in the degree of hydration domain as both have different ultimate degrees of hydration. Therefore, the results were compared in a degree of reaction (DOR) domain, which is defined as the percentage at any time of the ultimate degree of hydration at any time. While the degree of hydration ($\alpha(t)$ in Equation (5)) can vary only from 0 to 0.29 for Mix I and 0 to 0.51 for Mix II, the degree of reaction can vary from 0 to 1 for both mixes. For example, a degree of hydration of 0.29 for Mix I is equivalent to a degree of reaction of 1 for the same. Figure 18 shows the comparison of the autogenous shrinkage development for both mixes in the DOR domain.

The kinetics of development of autogenous shrinkage are similar for both mixes at different temperatures. All the tests show an initial increase in the autogenous shrinkage until a DOR of 0.2 - 0.3 followed by a plateau or slight decrease until a DOR of about 0.6, after which there is again an increase in the autogenous shrinkage. The difference between the values of the autogenous shrinkage at different temperatures at any degree of reaction is considerably less than the difference at any particular age in the age domain. The slightly higher values of the mixes at 20 °C may reflect scatter in the measurements. Nevertheless, the trend at 20 °C is identical to that in the case of elastic modulus development of Mix I at 20 °C, figure 12, which shows higher values when compared to those at 10 °C and 5 °C at similar degrees of hydration.

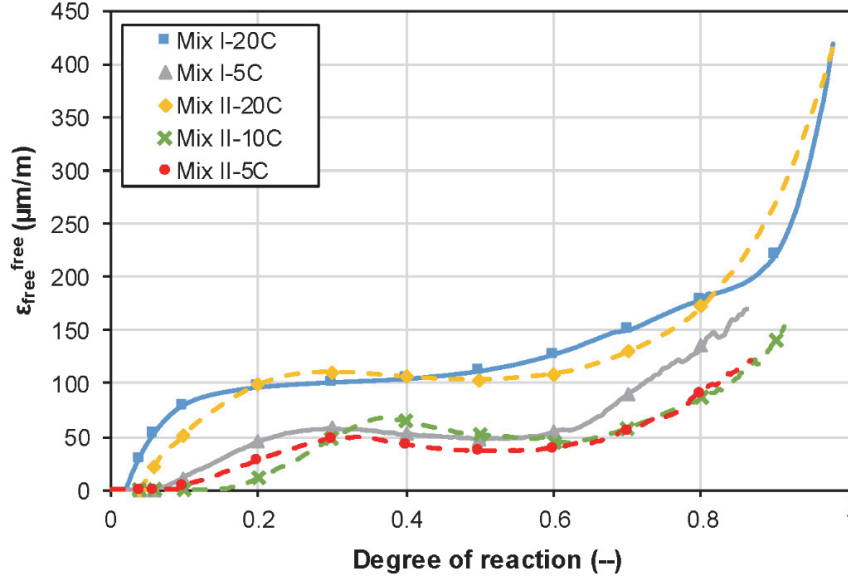


Figure 18: Comparison of the average autogenous deformations zeroed after swelling at different quasi-isothermal temperatures for Mix I and II in the DOR domain.

The reduction in the autogenous deformations at lower temperatures can be explained using the capillary stress that develops within the pore fluid [24]. After setting, the self-desiccation in the cement paste produces a negative pressure in the pore fluid, which leads to a tensile capillary shrinkage induced stress. This capillary stress can be described using the Kelvin-Laplace equation as shown in equation (10) [24,94],

$$\sigma_{capillary} = -\frac{2\sigma}{r} \cos \theta = -\frac{RT}{M_v} \ln(h) \quad (10)$$

where σ is the surface tension of the water/vapor interface, θ is the moistening angle, r is the radius of the liquid vapor meniscus, M_v is the molar volume of water, R is the ideal gas constant, T is the temperature and h is the relative humidity. Earlier studies [94,95] have shown that when the pore network and the degree of hydration are similar, the main factor that affects the capillary stresses is the change in the surface tension or the internal relative humidity with a change in the temperature. Sant et al. [28] showed that the surface tension of water reduced with an increase in the temperature, which should translate to a corresponding decrease in the capillary stress and thereby the autogenous shrinkage. However, at lower temperatures there is a considerable decrease in the rate of depression of the relative humidity in cement-based samples as shown by Jensen and Hansen [31]. As such following equation (10), the expected slight increase in the capillary stress because of the increase in the surface tension of the water/vapor interface, is offset by the reduction in the rate of cement hydration at lower temperatures [29]. This leads to a reduction in the rate of

autogenous relative humidity decrease, therefore resulting in a higher internal relative humidity on an age scale. Therefore, the capillary stress and the corresponding autogenous shrinkage are reduced at lower temperatures. A similar explanation was also given by [25], who showed that temperature dependency of the surface tension is negligible when compared to the thermal activation of the processes. This also explains the reduced difference in the autogenous deformations in the DOR domain when compared to that in the age or the maturity domain.

3.6 Development of eigenstresses

Figure 19 shows the development of eigenstresses in the mixes at different temperatures. Except in the case of Mix I at 20 °C, all the other tests showed an initial increase in the stress which was followed by a slight decrease (shoulder effect), and then an increase again. The trend was similar to that in the autogenous shrinkage, as seen in figure 14b, wherein all the tests except those of Mix I at 20 °C, showed a similar shoulder effect. Moreover, all tests show a further increase in the rate of development of eigenstresses after the shoulder effect, except for Mix I at 5 °C, which shows a plateau in the stress development around a stress value of 4 MPa. Similar stabilization of the eigenstresses were also found in [14] for a UHPFRC of type CMM22_TKK, which is the predecessor of Mix I in the present study, at temperatures of 5 °C and 1 °C.

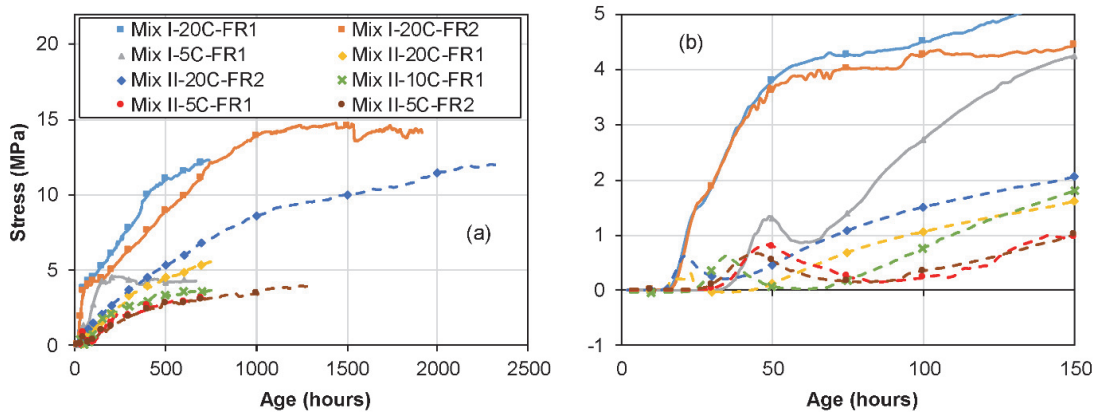


Figure 19: Development of eigenstresses under full restraint for Mix I and II under different quasi-isothermal temperatures in the age domain; (a) overall behavior and (b) early-age behavior.

The possible explanation of such a phenomenon may be the cancellation of the eigenstresses development due to the autogenous shrinkage by the higher relaxation potential of the mix at a lower temperature of 5 °C, which in turn leads to a stabilization of the stresses. However, low curing temperature has two contrasting effects on the viscous response of the material.

On the one hand, a lower temperature leads to a lower creep/relaxation response whereas on the other hand, a lower curing temperature would lead to a lower apparent age (maturity) of the material and consequently a higher viscous response. In the present scenario, it seems that the higher viscous response due to a lower maturity is more dominant than the lower viscous response due to the lower temperature. Another possible explanation, as noted by [29], is that the rate of hydration and consequently the rate of development of capillary stresses (or autogenous deformation) is much slower at lower temperatures in an “age or maturity” scale, thereby leading to more viscoelastic relaxation, when compared to a higher rate of capillary stress at 20 °C. The stress development at lower temperatures is therefore analogous to a test under lower strain rates, thereby leading to higher viscous relaxation. However, a similar stabilization or plateau was not seen in the case of Mix II even at 5 °C, although the viscous potential of Mix II is much higher than that of Mix I, as shown through tensile creep tests in creep rigs in Chapter 2 [21]. Nevertheless, it may be possible to see a stress stabilization in Mix II at a later age.

Even though the shrinkage strains acting on the mixes were almost similar at 20 °C, the rate of development of eigenstresses were much slower for Mix II. This can be attributed to the higher viscoelastic potential of Mix II, as mentioned earlier, which can lead to a greater relaxation of the developed eigenstresses. The slower development of eigenstresses in Mix II could also be attributed to the slower rate of development of elastic modulus as seen in figure 10. Figure 20 shows the comparison of average eigenstresses development at different temperatures in an age domain.

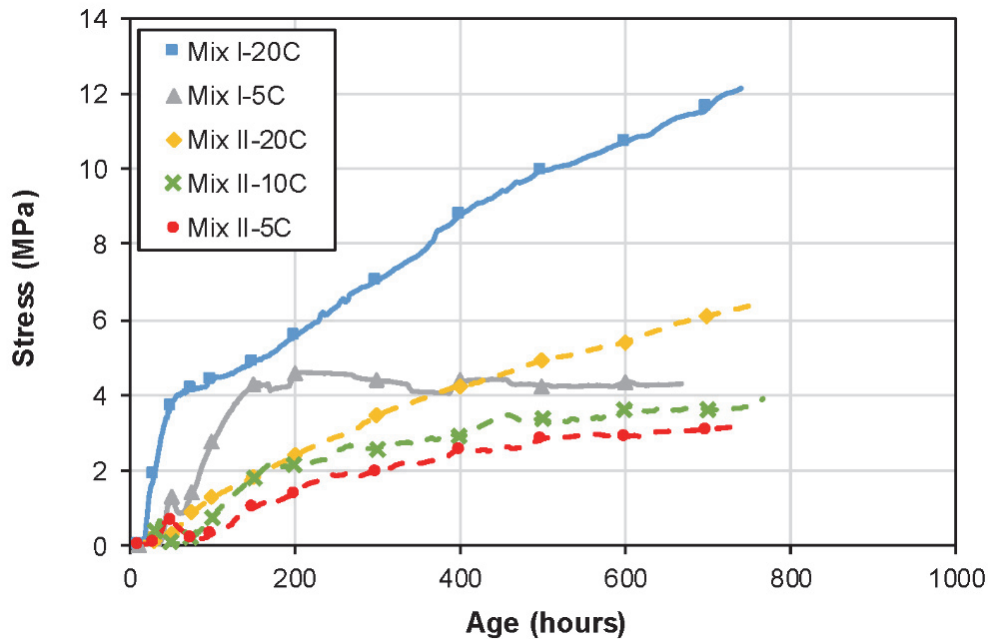


Figure 20: Comparison of the average eigenstresses development at different quasi-isothermal temperatures for Mix I and II in the age domain.

Figure 21 shows the developed eigenstresses under full restraint under various temperatures along with the resistance curves of the elastic limit (f_{Ute}) and tensile strength (f_{Utu}) at these temperatures. The resistance curves were obtained from monotonic tensile tests conducted until fracture for both mixes at different ages.

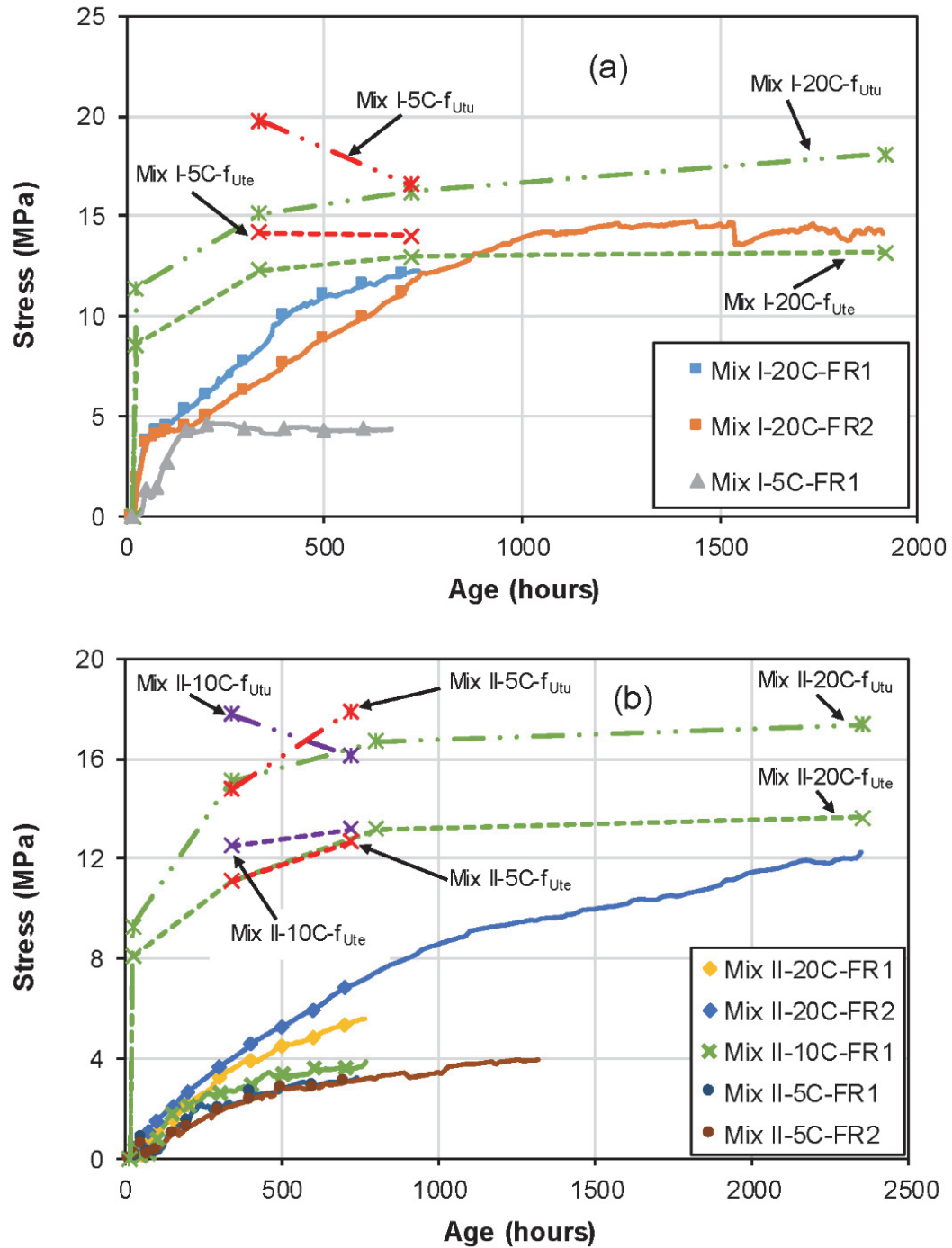


Figure 21: Comparison of the eigenstresses developed under full restraint with the resistance curves of elastic limit and tensile strength for (a) Mix I and (b) Mix II.

The tests at 1 day (24 hours) and after one month (>720 hours) were conducted on the specimens in the TSTM, whereas the tests at 14 days (336 hours) were conducted on dumbbell specimens of center cross section 50 mm x 30 mm in an electromechanical testing machine, KAPPA 250 DS from ZWICK/ROELL with a capacity of 250 kN. The tests at an age of 1 day were conducted only at a temperature of 20 °C for both mixes. More details regarding the uniaxial tests at 14 days could be found in Chapter 3 [11].

The cross sectional area of the dumbbell specimens in the uniaxial tests in the ZWICK (50mm x 30mm) are smaller than that of the TSTM specimens (100mm x 50mm). The orientation of the fibers will be more favorable for the tensile properties in the smaller cross section. This is the reason for a decrease in the resistance curve from 14 days to 30 days as can be seen in the case of Mix I-5C- f_{Ute} , Mix I-5C- f_{Utu} and Mix II-10C- f_{Utu} . Figure 21 shows that for Mix I-20C-FR2, the eigenstresses reached the strain-hardening domain after about 720 hours (one month), whereas for Mix II-20C-FR2, the eigenstresses were approaching the strain-hardening domain at about 2400 hours (just over 3 months). Even for the former, the stresses in the strain-hardening domain never reached the tensile strength of the mixes thereby ensuring the absence of a localized macrocrack. This ensures that, if there is no detrimental fiber orientation, both mixes can resist the developed eigenstresses even under fully restrained shrinkage conditions.

Figure 22 shows the development of the eigenstresses in the maturity domain whereas figure 23 shows the same in the DOR domain.

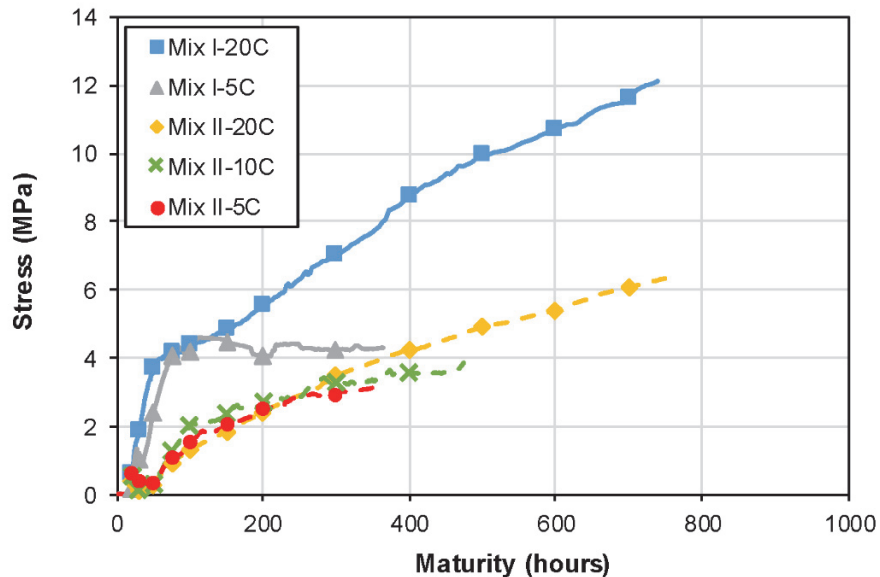


Figure 22: Comparison of the average eigenstresses development at different quasi-isothermal temperatures for Mix I and II in the maturity domain.

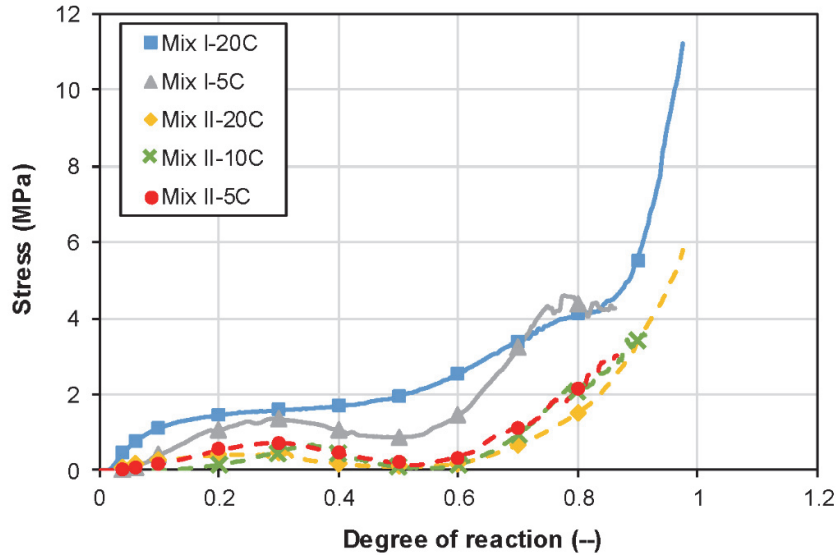


Figure 23: Comparison of the average eigenstresses development at different quasi-isothermal temperatures for Mix I and II in the DOR domain.

Unlike the autogenous shrinkage, the eigenstresses development is very similar for Mix II in the maturity domain, whereas for Mix I, the trend of stabilization of stresses at 5 °C is not seen in the test at 20 °C. The possible reason for the stabilization was discussed before. In the DOR domain, the eigenstresses development had even lesser scatter than those in the maturity domain. The stress development showed three clear zones; an increase in the beginning followed by a reduced rate of development (Mix I-20C) or a negative rate of development, which was further followed by an increase in the rate of development. Except for Mix I-20C, there was a slight decrease in the stresses from a DOR of about 0.3 to 0.6. This trend was similar to that in the case of the autogenous shrinkage, figure 18. Moreover, even in the DOR domain, Mix I showed much higher stresses at a particular value of DOR when compared to Mix II, which could be attributed to the higher relaxation potential of Mix II as discussed before in Chapter 2 [21].

4 Material level vs Structural level

4.1 Overview

In this section, the trends found in the structural level (autogenous shrinkage and eigenstresses development) will be discussed in view of the trends at a material level (degree of hydration, elastic modulus) in the age domain. For simplification, only the trends at 20 °C are discussed for both mixes. The age domain is divided into three main zones as can be seen in figure 24. However, it should be noted that, owing to the difference in the sizes of the specimens used in each test, and also to the type of arrangements for the curing and temperature control, there will be slight changes in the times at which a zone changes to the other. However, the difference is very small as can be seen from the discussions below.

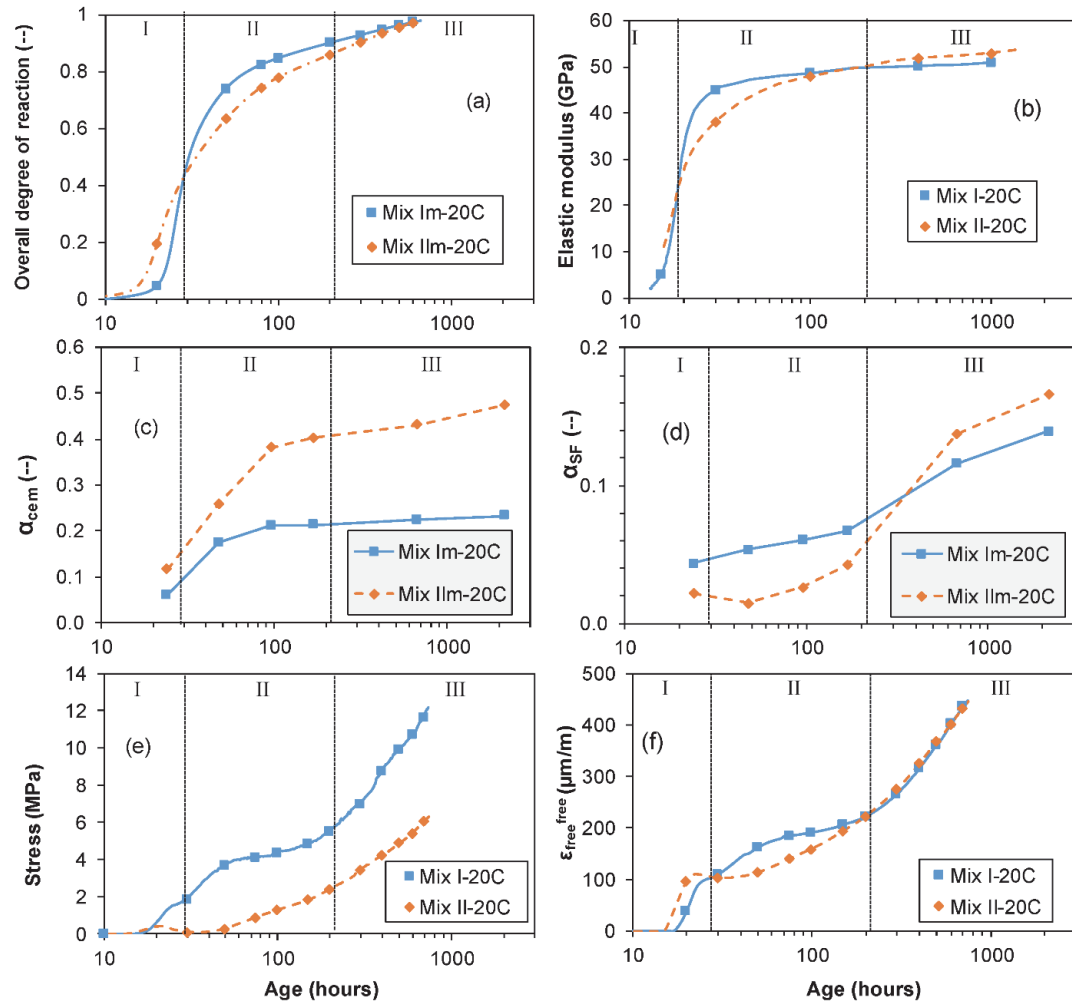


Figure 24: Comparison of the trends observed at the material level and the structural level. Material level: (a) development of degree of reaction from the isothermal calorimetry tests, (b) development of elastic modulus from VRF tests, (c) development of α_{cem} from ^{29}Si MAS NMR, and (d) development of α_{SF} from ^{29}Si MAS NMR. Structural level: (e) development of eigenstresses under full restraint in the TSTM and (f) development of autogenous deformations zeroed after swelling in the TSTM (All the tests were carried out at a curing temperature of 20 °C).

4.2 Zone I

Figure 24a shows the development of the overall degree of reaction of the mixes, calculated from the isothermal calorimetry tests. In figure 4, the development of overall degree of hydration for both mixes, calculated from the cumulative heat released was discussed. However, for comparison of the kinetics of both mixes, the degree of reaction gives a better understanding. In figure 24a, the overall degree of reaction of Mix II starts earlier than that of Mix I, due to the earlier setting of Mix II caused by the lower superplasticizer content.

However, it becomes similar for both mixes at around 25 - 30 hours, after which the zone II starts. Similar trends were seen in the case of development of elastic modulus, figure 24b, and that of autogenous shrinkage, figure 24f. It should be noted that in figure 24b, zone I is ending around 20 hours, slightly lesser than that in the other figures, which could be attributed to the difference in the specimen dimensions and curing conditions as indicated earlier. In equation (10), for similar temperatures and pore water, the variables that can be different between Mix I and II are the Kelvin radius r , which depends on the pore structure and the relative humidity, h . Since the elastic modulus is similar for both mixes at the end of zone I, it could be assumed that the microstructure and pore structure, and therefore the pore radius, will also be similar at that point [96]. This would then correspond to a similar capillary stress and therefore similar autogenous shrinkage, which is also experimentally observed in figure 24f. At the end of zone I, the α_{cem} is about 0.08 and 0.14 for Mix I and II, respectively, whereas the corresponding α_{SF} is about 0.05 and 0.02. Therefore, the contribution of silica fume in the pozzolanic reaction is much less in zone I and the main source of autogenous shrinkage arises from the degree of hydration of the cement particles. The main contribution of the silica fume in this zone is the filler effect, thereby refining the microstructure of the mixes and influencing the self-desiccation. The case is similar for the development of eigenstresses, wherein the influence of hydration of the cement is more than that of the silica fume. The reduced eigenstresses in the Mix II, when compared to Mix I, may originate from a higher relaxation potential of Mix II as discussed earlier. Moreover, a slight decrease in the autogenous deformation of Mix II also led to a decrease in the eigenstresses, as can be more clearly seen in figure 19b.

4.3 Zone II

In this zone, figure 24a shows a deviation in the rate of development of overall degree of reaction for the mixes. Initially, Mix I shows a higher rate of development until about 70 hours after which the trend is reversed until the end of Zone II. At the end of zone II (approximately 200 hours), the degree of reaction becomes almost similar for both mixes. The same trend is seen in the case of elastic modulus as well, which was attributed to the higher w/c ratio in Mix II as discussed in detail in section 3.3 and Appendix B. If it is assumed that a higher elastic modulus of Mix I in zone II is caused by more hydration products, then it implies that the pore structure of Mix I in zone II is finer than that of Mix II. A finer pore structure may lead to higher capillary stress and in turn, a higher autogenous shrinkage which is similar to what was observed experimentally in the TSTM as shown in figure 24f. It is also interesting to note that when the elastic modulus merges at the end of zone II, the autogenous shrinkage in both mixes also becomes similar, giving an indication that the pore structure may be identical at a similar elastic modulus. The development of eigenstresses in zone II for Mix I is somewhat stabilized whereas in the case of Mix II, it is slowly rising continuously. The trend is similar to the development of α_{cem} and the autogenous shrinkage for the respective mixes in this zone.

4.4 Zone III

In the zone III, the overall degree of hydration is still rising slowly. Even though, the relative contributions of α_{cem} in this zone are much less when compared to the previous zones, and there is a marked increase in the consumption of silica fume for the pozzolanic reaction, which is indicated by the higher rate of development of α_{SF} . This will lead to a further refinement of the microstructure. The autogenous shrinkage shows an increase in the rate of development from the beginning of zone III, which may be attributed to the finer pore structure because of the pozzolanic reaction. The eigenstresses also follow the same trend of the autogenous shrinkage, although with lesser change of rate in Mix II.

5 Conclusions

The influence of three curing temperatures, 20 °C, 10 °C and 5 °C, on the development of hydration and mechanical properties, and the development of autogenous deformations and eigenstresses under full restraint conditions were investigated for two types of SH-UHPFRC mixes with silica fume. Mix I with pure type I cement and Mix II with 50% replacement of cement with limestone filler, both having a similar steel fibrous mix. The following findings have been made in the present study.

- Using the master curve method on the cumulative heat of hydration curves at different temperatures obtained from the isothermal calorimetry tests, the activation energy E_a/R of Mix I and II were found to be 3300 K and 4000 K, respectively. It was found that, except for the autogenous shrinkage, a single activation energy could be used to include the effect of different curing temperatures on the overall degree of hydration and dynamic elastic modulus of both mixes in a maturity domain.
- Using a ‘Double Danish model’, the ultimate degrees of hydration of Mix I and Mix II were found to be 0.29 and 0.51, respectively.
- Using ^{29}Si MAS NMR, the degree of hydration of cement (alite and belite) and the percentage of silica fume consumed in the pozzolanic reactions were determined. The trends of α_{SF}/α_{cem} revealed that there might be two phases of pozzolanic reaction with different rates of consumptions of the silica fume. The trends also revealed that it was the heat produced from the second phase of the pozzolanic reaction that was represented by the second term of the Double Danish model.
- A systematic increase in the autogenous shrinkage was observed as the curing temperatures increased, which was attributed to greater thermal activation at higher temperature. The trend of development of autogenous shrinkage in the degree of reaction domain revealed three separate domains for both mixes; a positive rate of development until a DOR of about 0.2 - 0.3 followed by a zero or negative rate until a DOR of 0.6, which was further followed by a positive rate of development.

- The development of eigenstresses also followed the same trend as that of the autogenous shrinkage with higher stresses being developed at higher curing temperatures. The curves of the development of eigenstresses under different curing conditions almost merged in the degree of reaction domain. The eigenstresses developed were much lower in the case of Mix II, owing to its greater relaxation potential.
- It was shown that except for Mix I cured at 20 °C, the eigenstresses in none of the other tests reached the resistance envelope of the elastic limit or the tensile strength, even under full restraint conditions, during the duration of the tests. For Mix II cured at 20 °C, the eigenstresses were only approaching the strain-hardening domain even at the end of three months. This ensures that, unless in the case of a detrimental fiber orientation, eigenstresses developed due to restrained shrinkage may never lead to the formation of localized macrocracks even at very low temperatures.
- The influence of the development of degree of hydration of cement and the reaction of silica fume for pozzolanic reaction on the development of autogenous shrinkage and eigenstresses were discussed. It was shown that the delayed pozzolanic reaction of silica fume at a later age, might lead to further refinement of the pore structure of the materials, leading to a further increase in the rate of development of the autogenous shrinkage and eigenstresses.

Acknowledgements

The project was financially supported by the Swiss National Science Foundation (grant 200021_153394/1). The authors would like to gratefully acknowledge the help given by the technicians of GIC-ENAC-EPFL Mr. S. Despont, Mr. G. Guignet and Mr. S. Demierre and Mr. A. Hajiesmaeili in performing the experimental works in the GIS laboratory in EPFL. The authors would also like to acknowledge the help given by Ms. Y. Briki, Mr. L. Sofia and Mr. J. D. Rego in conducting the isothermal calorimetry tests at LMC/EPFL. Mix II was developed by Mr. A. Hajiesmaeili.

References

- [1] E. Denarié, E. Brühwiler, Cast-on Site UHPFRC for improvement of existing structures – achievements over the last 10 years in practice and research, in: High Perform. Fiber Reinf. Cem. Compos. 7(2015) 473–480.
- [2] K. Wille, S. El-Tawil, A.E. Naaman, Properties of strain hardening ultra high performance fiber reinforced concrete (UHP-FRC) under direct tensile loading, Cem. Concr. Compos. 48 (2014) 53–66. doi:<https://doi.org/10.1016/j.cemconcomp.2013.12.015>.

- [3] M. Bastien-Masse, E. Denarié, E. Brühwiler, Effect of fiber orientation on the in-plane tensile response of UHPFRC reinforcement layers, *Cem. Concr. Compos.* 67 (2016) 111–125. doi:10.1016/j.cemconcomp.2016.01.001.
- [4] K. Habel, Structural behavior of elements combining ultra-high performance fiber reinforced concretes (UHPFRC) and reinforced concrete, Doctoral thesis No: 3036, Ecole Polytechnique Fédérale de Lausanne, Switzerland (2004).
- [5] A. Kamen, E. Denarié, H. Sadouki, E. Brühwiler, Thermo-mechanical response of UHPFRC at early age - Experimental study and numerical simulation, *Cem. Concr. Res.* 38 (2008) 822–831. doi:10.1016/J.CEMCONRES.2008.01.009.
- [6] A. Kamen, E. Denarié, H. Sadouki, E. Brühwiler, UHPFRC tensile creep at early age, *Mater. Struct.* 42 (2008) 113–122. doi:10.1617/s11527-008-9371-0.
- [7] A. Kamen, E. Denarié, E. Brühwiler, Thermal effects on physico-mechanical properties of ultra-high-performance fiber-reinforced concrete, *ACI Mater. J.* 104 (2007) 415–423.
- [8] A. Kamen, E. Denarié, H. Sadouki, E. Brühwiler, Evaluation of UHPFRC activation energy using empirical models, *Mater. Struct.* 42 (2009) 527–537. doi:10.1617/s11527-008-9400-z.
- [9] A. Switek-Rey, E. Denarié, E. Brühwiler, Early age creep and relaxation of UHPFRC under low to high tensile stresses, *Cem. Concr. Res.* 83 (2016) 57–69.
- [10] AFNOR. 2016 NF P18-470 - Concrete - Ultra-high performance fiber reinforced concrete - Specifications, performance, production and conformity, Paris, France (2016).
- [11] M.A. Hafiz, E. Denarié, Tensile response of UHPFRC under very low strain rates and low temperatures, submitted to *Cement and Concrete Research*, April (2019).
- [12] E. Denarié, Deliverable D25b “Guidance for the use of UHPFRC for rehabilitation of concrete highway structures,” (2006).
- [13] E. Denarié, J. Silfwerbrand, H. Beushausen, Structural Behavior, in: *Bond. Cem. Mater. Overlays Repair, Lining or Strength. Slabs or Pavements*, Springer (2011): pp. 81–106.
- [14] M. Kazemi Kamyab, Autogenous Shrinkage and Hydration Kinetics of SH-UHPFRC under Moderate to Low Temperature Curing Conditions, Doctoral thesis No: 5681, Ecole Polytechnique Fédérale de Lausanne, Switzerland (2013).
- [15] A.M. Soliman, M.L. Nehdi, Effect of drying conditions on autogenous shrinkage in ultra-high performance concrete at early-age, *Mater. Struct.* 44 (2011) 879–899. doi:10.1617/s11527-010-9670-0.
- [16] P. Schiessl, K. Beckhaus, I. Schachinger, P. Rucker, New Results on Early-Age Cracking Risk of Special Concrete, *Cem. Concr. Aggregates.* 26 (2004) 1–9.

- [17] I. Schachinger, K. Schmidt, D. Heinz, P. Schießl, Early-age cracking risk and relaxation by restrained autogenous deformation of ultra high performance concrete, in: 6th Int. Symp. High Strength / High Perform. Concr., Leipzig, Germany (2002): pp. 1341–1354.
- [18] A. Kamen, Comportement au jeune âge et différé d'un BFUP écrouissant sous les effets thermomécaniques, Doctoral thesis No: 3827, Ecole Polytechnique Fédérale de Lausanne, Switzerland (2007).
- [19] D.Y. Yoo, J.-J. Park, S.-W. Kim, Y.-S. Yoon, Influence of ring size on the restrained shrinkage behavior of ultra high performance fiber reinforced concrete, *Mater. Struct.* 47 (2014) 1161–1174. doi:10.1617/s11527-013-0119-0.
- [20] D.-Y. Yoo, N. Banthia, Y.-S. Yoon, Geometrical and boundary condition effects on restrained shrinkage behavior of UHPFRC slabs, *KSCE J. Civ. Eng.* 22 (2018) 185–195. doi:10.1007/s12205-017-0587-9.
- [21] M.A. Hafiz, A. Hajiesmaeili, E. Denarié, Tensile response of low clinker UHPFRC subjected to fully restrained shrinkage, *Cem. Concr. Res.* 124 (2019). doi:https://doi.org/10.1016/j.cemconres.2019.105804.
- [22] L. Sorelli, R. Davila, F. Ulm, V. Perry, P. Seibert, Risk analysis of early-age cracking in UHPC structures, in: *Proc. 2nd Int. Symp. UHPC*, Kassel, Ger. (2008): pp. 331–338.
- [23] M.A. Hafiz, E. Denarié, Tensile viscous response of Strain Hardening UHPFRC under high restraint and isothermal conditions, in: *Euro C - 2018 Comput. Model. Concr. Struct.* (2018): pp. 903–912.
- [24] C. Hua, P. Acker, A. Ehrlacher, Analyses and models of the autogenous shrinkage of hardening cement paste: I. Modelling at macroscopic scale, *Cem. Concr. Res.* 25 (1995) 1457–1468.
- [25] O.M. Jensen, Autogenous Phenomena in Cement-Based Materials, Doctoral thesis, Technical University of Denmark (2005).
- [26] D.P. Bentz, O.M. Jensen, Mitigation strategies for autogenous shrinkage cracking, *Cem. Concr. Compos.* 26 (2004) 677–685. doi:https://doi.org/10.1016/S0958-9465(03)00045-3.
- [27] P. Acker, Swelling, shrinkage and creep: a mechanical approach to cement hydration, *Mater. Struct.* 37 (2004) 237–243. doi:10.1007/BF02480632.
- [28] G. Sant, P. Lura, J. Weiss, The influence of temperature on unrestrained volume changes in cementitious materials., in: *Concr. Durab. Serv. Life Plan. – Concr.* (2009): pp. 538–546.
- [29] G. Sant, The influence of temperature on autogenous volume changes in cementitious materials containing shrinkage reducing admixtures, *Cem. Concr. Compos.* 34 (2012) 855–865. doi:https://doi.org/10.1016/j.cemconcomp.2012.04.003.

- [30] A. Aili, M. Vandamme, J.-M. Torrenti, B. Masson, Is long-term autogenous shrinkage a creep phenomenon induced by capillary effects due to self-desiccation?, *Cem. Concr. Res.* 108 (2018) 186–200. doi:10.1016/J.CEMCONRES.2018.02.023.
- [31] O.M. Jensen, P.F. Hansen, Influence of temperature on autogenous deformation and relative humidity change in hardening cement paste, *Cem. Concr. Res.* 29 (1999) 567–575. doi:https://doi.org/10.1016/S0008-8846(99)00021-6.
- [32] P. Turcry, A. Loukili, L. Barcelo, J.M. Casabonne, Can the maturity concept be used to separate the autogenous shrinkage and thermal deformation of a cement paste at early age?, *Cem. Concr. Res.* 32 (2002) 1443–1450. doi:https://doi.org/10.1016/S0008-8846(02)00800-1.
- [33] G. Sant, B. Lothenbach, P. Juilland, G. Le Saout, J. Weiss, K. Scrivener, The origin of early age expansions induced in cementitious materials containing shrinkage reducing admixtures, *Cem. Concr. Res.* 41 (2011) 218–229.
- [34] C. Jiang, Y. Yang, Y. Wang, Y. Zhou, C. Ma, Autogenous shrinkage of high performance concrete containing mineral admixtures under different curing temperatures, *Constr. Build. Mater.* 61 (2014) 260–269. doi:https://doi.org/10.1016/j.conbuildmat.2014.03.023.
- [35] P. Lura, K. van Breugel, I. Maruyama, Effect of curing temperature and type of cement on early-age shrinkage of high-performance concrete, *Cem. Concr. Res.* 31 (2001) 1867–1872. doi:https://doi.org/10.1016/S0008-8846(01)00601-9.
- [36] Ç. Yalçinkaya, H. Yazıcı, Effects of ambient temperature and relative humidity on early-age shrinkage of UHPC with high-volume mineral admixtures, *Constr. Build. Mater.* 144 (2017) 252–259. doi:https://doi.org/10.1016/j.conbuildmat.2017.03.198.
- [37] E. Gallucci, X. Zhang, K.L. Scrivener, Effect of temperature on the microstructure of calcium silicate hydrate (C-S-H), *Cem. Concr. Res.* 53 (2013) 185–195. doi:https://doi.org/10.1016/j.cemconres.2013.06.008.
- [38] I. Pane, W. Hansen, Investigation of blended cement hydration by isothermal calorimetry and thermal analysis, *Cem. Concr. Res.* 35 (2005) 1155–1164. doi:https://doi.org/10.1016/j.cemconres.2004.10.027.
- [39] K.O. Kjellsen, R.J. Detwiler, O.E. Gjrv, Development of microstructures in plain cement pastes hydrated at different temperatures, *Cem. Concr. Res.* 21 (1991) 179–189. doi:https://doi.org/10.1016/0008-8846(91)90044-I.
- [40] J.I. Escalante-García, J.H. Sharp, Effect of temperature on the hydration of the main clinker phases in portland cements: part i, neat cements, *Cem. Concr. Res.* 28 (1998) 1245–1257. doi:https://doi.org/10.1016/S0008-8846(98)00115-X.
- [41] J.I. Escalante-García, J.H. Sharp, Effect of temperature on the hydration of the main clinker phases in portland cements: part ii, blended cements, *Cem. Concr. Res.* 28 (1998) 1259–1274. doi:https://doi.org/10.1016/S0008-8846(98)00107-0.

- [42] B. Lothenbach, F. Winnefeld, C. Alder, E. Wieland, P. Lunk, Effect of temperature on the pore solution, microstructure and hydration products of Portland cement pastes, *Cem. Concr. Res.* 37 (2007) 483–491. doi:https://doi.org/10.1016/j.cemconres.2006.11.016.
- [43] I. Elkhadiri, M. Palacios, F. Puertas, Effect of curing temperature on cement hydration, *Ceram. - Silikaty.* 53 (2009) 65–75.
- [44] K.O. Kjellsen, R.J. Detwiler, Reaction kinetics of portland cement mortars hydrated at different temperatures, *Cem. Concr. Res.* 22 (1992) 112–120. doi:https://doi.org/10.1016/0008-8846(92)90141-H.
- [45] P. Rossi, J.P. Charron, M. Bastien-Masse, J.L. Tailhan, F. Le Maou, S. Ramanich, Tensile basic creep versus compressive basic creep at early ages: comparison between normal strength concrete and a very high strength fiber reinforced concrete, *Mater. Struct.* 47 (2014) 1773–1785.
- [46] A. Loukili, P. Richard, J. Lamirault, A Study on Delayed Deformations of an Ultra High Strength Cementitious Material, *Spec. Publ.* 179 (1998) 929–950.
- [47] M. Cheyrezy, M. Behloul, Creep and shrinkage of ultra-high performance concrete, in: *Creep, Shrinkage Durab. Mech. Concr. Other Quasi-Brittle Mater. (Concreep 6)* (2001): pp. 527–538.
- [48] V.Y.Y. Garas, K.E.E. Kurtis, L.F.F. Kahn, Creep of UHPC in tension and compression: Effect of thermal treatment, *Cem. Concr. Compos.* 34 (2012) 493–502. doi:10.1016/J.CEMCONCOMP.2011.12.002.
- [49] Y. Xu, J.J. Liu, J.J. Liu, P. Zhang, Q. Zhang, L. Jiang, Experimental studies and modeling of creep of UHPC, *Constr. Build. Mater.* 175 (2018) 643–652. doi:10.1016/J.CONBUILDMAT.2018.04.157.
- [50] A.E. Switek, Time-Dependent Response of Ultra High Performance Fiber Reinforced Concrete (UHPFRC) under Low to High Tensile Stresses, Doctoral thesis No: 4899, Ecole Polytechnique Fédérale de Lausanne, Switzerland (2011).
- [51] V.Y. Garas, L.F. Kahn, K.E. Kurtis, Short-term tensile creep and shrinkage of ultra-high performance concrete, *Cem. Concr. Compos.* 31 (2009) 147–152. doi:10.1016/J.CEMCONCOMP.2009.01.002.
- [52] V.Y. Garas, A.R. Jayapalan, L.F. Kahn, K.E. Kurtis, Micro- and Nanoscale Characterization of Effect of Interfacial Transition Zone on Tensile Creep of Ultra-High-Performance Concrete, *Transp. Res. Rec.* 2141 (2010) 82–88. doi:10.3141/2141-14.
- [53] A. Switek-Rey, E. Denarié, E. Brühwiler, Tensile creep of UHPFRC under low and high stresses, in: *4th Int. Conf. Constr. Mater. – Performance, Innov. Struct. Implic., Nagoya, Japan* (2009): pp. 432–437.

- [54] K. Habel, J.P. Charron, E. Denarié, E. Brühwiler, Autogenous deformations and viscoelasticity of UHPFRC in structures. Part I: experimental results, *Mag. Concr. Res.* 58 (2006) 135–145.
- [55] A. Switek-Rey, E. Denarié, E. Brühwiler, Early age creep and relaxation of UHPFRC under low to high tensile stresses, *Cem. Concr. Res.* 83 (2016) 57–69. doi:10.1016/J.CEMCONRES.2016.01.005.
- [56] P. Acker, M. Behloul, Ductal Technology: A large spectrum of properties, a wide range of applications, in: *Proc. Int. Symp. Ultra High Perform. Concr.*, Kassel, Germany (2004): pp. 11–23.
- [57] S. Utsi, J.-E. Jonasson, Estimation of the risk for early thermal cracking for SCC containing fly ash, *Mater. Struct.* 45 (2012) 153–169. doi:10.1617/s11527-011-9757-2.
- [58] G. Ji, Cracking risk of concrete structures in the hardening phase: Experiments, material modeling and finite element analysis., *Doctoral Thesis*, Norwegian University of Science and Technology. (2008).
- [59] I. Mehdipour, K.H. Khayat, Elucidating the Role of Supplementary Cementitious Materials on Shrinkage and Restrained-Shrinkage Cracking of Flowable Eco-Concrete, *J. Mater. Civ. Eng. ASCE*. 30 (2018).
- [60] K. Kuder, D. Lehman, J. Berman, G. Hannesson, R. Shogren, Mechanical properties of self consolidating concrete blended with high volumes of fly ash and slag, *Constr. Build. Mater.* 34 (2012) 285–295. doi:https://doi.org/10.1016/j.conbuildmat.2012.02.034.
- [61] B.A. Gedam, N.M. Bhandari, A. Upadhyay, Influence of Supplementary Cementitious Materials on Shrinkage, Creep, and Durability of High-Performance Concrete, *J. Mater. Civ. Eng.* 28 (2016) 04015173 (1-11). doi:10.1061/(ASCE)MT.1943-5533.0001462.
- [62] W.S. Langley, G.G. Carette, V.M. Malhotra, Structural concrete incorporating high volumes of ASTM class fly ash, *Mater. J.* 86 (1989) 507–514.
- [63] V. Sivasundaram, G.G. Carette, V.M. Malhotra, Mechanical properties, creep, and resistance to diffusion of chloride ions of concretes incorporating high volumes of ASTM Class F fly ashes from seven different sources, *Mater. J.* 88 (1991) 407–416.
- [64] G.G. Carette, V.M. Malhotra, Characterization of Canadian fly ashes and their relative performance in concrete, *Can. J. Civ. Eng.* 14 (1987) 667–682.
- [65] P. Rossi, A. Arca, E. Parant, P. Fakhri, Bending and compressive behaviors of a new cement composite, *Cem. Concr. Res.* 35 (2005) 27–33. doi:10.1016/J.CEMCONRES.2004.05.043.

- [66] E. Denarié, K. Habel, J. Wuest, SAMARIS deliverable D13, Report on preliminary studies for the use of HPFRCC for the rehabilitation of road infrastructure components (2004). <http://samaris.zag.si>.
- [67] E. Denarié, Recommendations for the tailoring of UHPFRC recipes for rehabilitation, deliverable ARCHES D06 (2009). <http://arches.fehrl.org>.
- [68] SIA (2017), Cahier Technique 2052, Béton fibré ultra-performant (BFUP): Matériaux, dimensionnement et exécution, SIA, Zürich. (2017).
- [69] L. Wadsö, Operational issues in isothermal calorimetry, *Cem. Concr. Res.* 40 (2010) 1129–1137. doi:<https://doi.org/10.1016/j.cemconres.2010.03.017>.
- [70] K. Scrivener, R. Snellings, B. Lothenbach, A practical guide to microstructural analysis of cementitious materials, Crc Press (2018).
- [71] J. Skibsted, H.J. Jakobsen, C. Hall, Quantification of calcium silicate phases in Portland cements by ^{29}Si MAS NMR spectroscopy, *J. Chem. Soc. Faraday Trans.* 91 (1995) 4423–4430. doi:[10.1039/FT9959104423](https://doi.org/10.1039/FT9959104423).
- [72] S.L. Poulsen, V. Kocaba, G. Le Saoût, H.J. Jakobsen, K.L. Scrivener, J. Skibsted, Improved quantification of alite and belite in anhydrous Portland cements by ^{29}Si MAS NMR: Effects of paramagnetic ions, *Solid State Nucl. Magn. Reson.* 36 (2009) 32–44. doi:<https://doi.org/10.1016/j.ssnmr.2009.05.001>.
- [73] J. Skibsted, M.D. Andersen, The Effect of Alkali Ions on the Incorporation of Aluminum in the Calcium Silicate Hydrate (C–S–H) Phase Resulting from Portland Cement Hydration Studied by ^{29}Si MAS NMR, *J. Am. Ceram. Soc.* 96 (2013) 651–656. doi:[10.1111/jace.12024](https://doi.org/10.1111/jace.12024).
- [74] Z. Dai, T.T. Tran, J. Skibsted, Aluminum Incorporation in the C–S–H Phase of White Portland Cement–Metakaolin Blends Studied by ^{27}Al and ^{29}Si MAS NMR Spectroscopy, *J. Am. Ceram. Soc.* 97 (2014) 2662–2671. doi:[10.1111/jace.13006](https://doi.org/10.1111/jace.13006).
- [75] S. Kolluru, J. Popovics, S.P. Shah, Determining Elastic Properties of Concrete Using Vibrational Resonance Frequencies of Standard Test Cylinders, *Cem. Concr. Aggregates.* 22 (2000) 81.
- [76] SIA 262/1:2013- Construction en beton Specifications complementaires (2013).
- [77] O. Bjontegaard, Thermal dilatation and autogenous deformation as driving forces to self-induced stresses in high performance concrete, Doctoral thesis, The University of Trondheim, Norway (1999).
- [78] J.P. Charron, J. Marchand, M. Pigeon, B. Bissonnette, Test Device for Studying the Early-Age Stresses and Strains in Concrete, *Spec. Publ.* 220 (2004) 113–124. doi:[10.14359/13153](https://doi.org/10.14359/13153).
- [79] K. Kovler, Testing system for determining the mechanical behavior of early age concrete under restrained and free uniaxial shrinkage, *Mater. Struct.* 27 (1994) 324–330.

- [80] E. Berodier, K. Scrivener, Understanding the Filler Effect on the Nucleation and Growth of C-S-H, *J. Am. Ceram. Soc.* 97 (2014) 3764–3773. doi:10.1111/jace.13177.
- [81] Bazzoni. A, Study of early hydration mechanisms of cement by means of electron microscopy, Doctoral Thesis No: 6296, EPFL, Switzerland (2014).
- [82] J.I. Escalante-Garcia, J.H. Sharp, The effect of temperature on the early hydration of Portland cement and blended cements, *Adv Cem Res.* 12 (2000) 121–130.
- [83] M.T. Palou, E. Kuzielová, M. Žemlička, M. Boháč, R. Novotný, The effect of curing temperature on the hydration of binary Portland cement, *J. Therm. Anal. Calorim.* 125 (2016) 1301–1310. doi:10.1007/s10973-016-5395-9.
- [84] C. Angulski da Luz, H. R. D., Influence of curing temperature on the process of hydration of supersulfated cements at early age, *Cem. Concr. Res.* 77 (2015) 69–75. doi:https://doi.org/10.1016/j.cemconres.2015.07.002.
- [85] F. Han, Z. Zhang, D. Wang, P. Yan, Hydration kinetics of composite binder containing slag at different temperatures, *J. Therm. Anal. Calorim.* 121 (2015) 815–827. doi:10.1007/s10973-015-4631-z.
- [86] B. Klemczak, M. Batog, Heat of hydration of low-clinker cements, *J. Therm. Anal. Calorim.* 123 (2016) 1351–1360. doi:10.1007/s10973-015-4782-y.
- [87] P.F.G. Banfill, Superplasticizers for Ciment Fondu. Part 2: Effects of temperature on the hydration reactions, *Adv. Cem. Res.* 7 (1995) 151–157. doi:10.1680/adcr.1995.7.28.151.
- [88] L. D'Aloia, G. Chanvillard, Determining the “apparent” activation energy of concrete: Ea—numerical simulations of the heat of hydration of cement, *Cem. Concr. Res.* 32 (2002) 1277–1289. doi:https://doi.org/10.1016/S0008-8846(02)00791-3.
- [89] E. Wirquin, M. Broda, B. Duthoit, Determination of the apparent activation energy of one concrete by calorimetric and mechanical means: Influence of a superplasticizer, *Cem. Concr. Res.* 32 (2002) 1207–1213. doi:https://doi.org/10.1016/S0008-8846(02)00770-6.
- [90] F.P. Hansen, E.J. Pedersen, Maturity computer for controlled curing and hardening of concrete, *Nord. Betong* 1 (1977) 21–25.
- [91] E. Denarié, Internal Communication, MCS, EPFL, Switzerland (2012).
- [92] V. Waller, “Relations entre composition des bétons, exothermie en cours de prise et résistance à la compression”, thèse de doctorat, LCPC, Nantes, France (2001).
- [93] O.M. Jensen, P.F. Hansen, Water-entrained cement-based materials: I. Principles and theoretical background, *Cem. Concr. Res.* 31 (2001) 647–654. doi:https://doi.org/10.1016/S0008-8846(01)00463-X.

- [94] P. Lura, O.M. Jensen, K. van Breugel, Autogenous shrinkage in high-performance cement paste: an evaluation of basic mechanisms, *Cem. Concr. Res.* 33 (2003) 223–232.
- [95] W. J. Weiss, P. Lura, F. Rajabipour, G. Sant, Performance of Shrinkage-Reducing Admixtures at Different Humidities and at Early Ages, *Mater. J.* 105(5) (2008), 478-486. doi:10.14359/19977.
- [96] W. Huang, H. Kazemi-Kamyab, W. Sun, K. Scrivener, Effect of cement substitution by limestone on the hydration and microstructural development of ultra-high performance concrete (UHPC), *Cem. Concr. Compos.* 77 (2017) 86–101. doi:<https://doi.org/10.1016/j.cemconcomp.2016.12.009>.

Appendix A

The relative ^{29}Si NMR intensities (I) and degrees of hydration (H) for alite and belite and the percentage of silica fume reacted (α_{SF}) from the deconvolutions of the ^{29}Si MAS NMR spectra of Mix I_m and Mix II_m at different temperatures are shown in Tables A1 and A2, respectively.

Table A1: Data from the deconvolutions of the ^{29}Si MAS NMR spectra of Mix I_m at different ages of hydration and cured at different temperatures.

Temp	Age (days)	I(belite)	I(alite)	I (C-S-H)	I(SF)	H(belite)	H(alite)	α_{cem}	α_{SF}
	Anhydrous	3.40	37.0		59.6				
20 °C	1	3.28	34.7	5.1	57.0	3.5	6.2	6.0	4.4
	2	3.16	30.3	10.1	56.4	7.1	18.1	17.4	5.4
	4	3.09	28.9	12.1	56.0	9.1	21.9	21.1	6.0
	7	3.15	28.8	12.5	55.6	7.4	22.2	21.2	6.7
	28	3.20	28.3	15.8	52.7	5.9	23.5	22.4	11.6
	90	3.15	28.0	17.6	51.3	7.4	24.3	23.2	13.9
10 °C	1	3.40	36.7	1.4	58.5	0.0	0.8	0.8	1.9
	2	3.39	33.9	6.1	56.7	0.3	8.4	7.9	4.9
	7	3.32	32.0	9.1	55.6	2.4	13.5	12.8	6.7
	28	3.33	31.0	11.4	54.9	2.1	16.2	15.3	7.9
5 °C	1	3.33	36.6	0.8	59.3	2.1	1.1	1.1	0.5
	2	3.39	34.7	3.4	58.5	0.3	6.2	5.8	1.9
	4	3.36	32.8	6.2	57.7	1.2	11.4	10.7	3.2
	7	3.46	29.2	10.4	56.9	1.8	21.1	19.6	4.5
	28	3.33	28.9	13.0	54.7	2.1	21.9	20.6	8.2

Table A2: Data from the deconvolutions of the ^{29}Si MAS NMR spectra of Mix IIm at different ages of hydration and cured at different temperatures.

Temp	Age (days)	I(belite)	I(alite)	I(C-S-H)	I(SF)	H(belite)	H(alite)	α_{cem}	α_{SF}
	Anhydrous	2.81	28.7		68.5				
20 °C	1	2.57	25.3	5.1	67.0	8.5	11.8	11.6	2.2
	2	2.89	20.7	8.9	67.5	0.0	27.9	25.9	1.5
	4	2.55	17.2	13.5	66.7	9.3	40.1	38.1	2.6
	7	2.50	16.6	16.3	65.6	11.0	42.2	40.1	4.2
	28	2.51	15.7	22.7	59.1	10.7	45.3	43.0	13.7
	90	2.06	14.7	27.1	57.1	26.7	48.8	47.3	16.6
10 °C	1	2.68	27.6	2.1	67.7	4.6	3.8	3.9	1.2
	2	2.55	23.5	6.7	67.2	9.3	18.1	17.5	1.9
	28	2.57	17.7	15.3	64.5	8.5	38.3	36.4	5.8
5 °C	1	2.75	28.5	0	68.3	2.1	0.7	0.8	0.3
	2	2.58	25.4	4.9	67.1	8.2	11.5	11.3	2.0
	4	2.59	22.9	7.6	67.0	7.8	20.2	19.4	2.2
	7	2.57	20.4	10.5	66.5	8.5	28.9	27.6	2.9
	28	2.46	18.8	13.9	64.8	12.5	34.5	33.1	5.4

Appendix B

This section discusses the trend of the elastic modulus as seen in figure 10. At any particular temperature, the dynamic elastic moduli of Mix I and II are comparable in the beginning, whereas at around an elastic modulus of 20 GPa, the rate of development becomes much slower in Mix II, for all the curing temperatures. Moreover, the trend inverts at around an elastic modulus of 40 GPa, and the values for both mixes start converging again. At a later age, the values of elastic moduli start to become more or less similar for both mixes. The time required to reach similar values depends on the curing temperature, with the 20 °C specimens reaching similar values of elastic moduli at around 180 hours and the 5 °C specimens at around 3000 hours. The 10 °C specimens should have had similar values between an age of 180 hours and 3000 hours, which was not observed in the present study, may be because of slight errors in the experimental measurements and also due to a scatter in the fiber orientation between individual test specimens.

Nevertheless, the trend of lower rate of development for Mix II at around 20 GPa and the same for Mix I at around 40 GPa could be explained by the difference in two main parameters; the silica fume/cement (SF/C) ratio and the water/cement (w/c) ratio, as discussed in Chapter 2 [21]. Mix I has a SF/C ratio of 0.26 and Mix II has the same at 0.4, whereas the w/c ratio of Mix I is 0.163 and that of Mix II is 0.310. Jensen [25] has shown that an increase in the SF/C ratio leads to an increase in the rate of drop of relative humidity in cement paste specimens, and therefore an increase in the rate of overall hydration in the specimens. However, as shown by [14,92], only 20% mass of silica fume contributes to the pozzolanic reaction in cement based specimens. As such the difference in the effect of SF/C ratio on the trend of hydration, will be minimal in the current mixes I and II, as both of them have an SF/C ratio higher than 20%.

On the other hand, Jensen [25] has also shown a similar trend of increase in the drop of relative humidity with a decrease in the w/c ratio in the cement paste samples. Even though the drop in relative humidity is much faster in the beginning as the w/c ratio decreases, the ultimate value of the relative humidity becomes more or less similar for paste specimens with w/c less than 0.3. This trend in the drop in relative humidity is analogous to the development of elastic moduli in the present case with Mix I with lower w/c ratio showing a much faster development in the beginning, but ultimately having similar values as that of Mix II with a w/c ratio of 0.310. More details regarding the discussion could be found in Chapter 2 [21].

Chapter – 6

Conclusions and Outlook

1 Overview

This chapter summarizes the important findings of the four main chapters of the thesis and provides insights and scopes for future extensions. The findings described below might be considered as answers to the main objectives of the thesis as described in the section 3 of Chapter 1. The contributions of the thesis are summarized under four main headings;

1. Influence of very low strain rates on the tensile response of SH-UHPFRC
2. Influence of moderate to low curing temperatures on the kinetics of hydration and tensile response of SH-UHPFRC
3. Development of a viscoelastic-viscohardenening model to predict the tensile response of SH-UHPFRC in the elastic and hardening domain
4. Influence of partial replacement of cement clinker with limestone filler

In the upcoming sections, the main findings under each of these four categories will be described briefly.

2 Synthesis of main findings

2.1 Influence of very low strain rates on the tensile response of SH-UHPFRC

2.1.1 Tensile response under monotonic strain rates

- i. Acoustic emission measurements on uniaxial tensile tests confirmed the validity of the inverse analysis procedure used for the determination of the elastic limit in tension. The elastic limit was found to decrease considerably with the decrease in the strain rate. At very low loading rates, the elastic limit showed a drop of 19%-28% when compared to that at a quasi-static strain rate. The results are even more interesting for softening UHPFRC or less robust SH-UHPFRC.
- ii. The elastic modulus under tension was found to be insensitive to the range of strain rates tested. It was suggested that the range of strain rates tested (1×10^{-5} 1/s – 5×10^{-9} 1/s) were not low enough to show a change in the elastic modulus in the tensile response, which was confirmed by the developed viscoelastic-viscohardenening model.
- iii. The strain at tensile strength increased as the strain rate decreased. It was attributed to the fact that even at lower strain rates, when the elastic limit is lower, the fibrous mix remains the same and therefore becomes more efficient in achieving strain-hardening.

- iv. Both the tensile strength and the hardening modulus were found to be insensitive to the range of strain rates investigated. It was concluded that the strain rate insensitivity could either be because of the strain rate insensitivity of the fiber pullout at these loading rates, or because the factors like fiber grouping and fiber orientation, offset the intrinsic rate sensitivity. It was also postulated that the strain rate insensitivity could be explained by possible differences in the imposed strain rate on the overall specimen and the strain rate acting for the progressive pullout of the fibers along the multiple crack planes, in the hardening domain.

2.1.2 Tensile response under restrained shrinkage deformations

- i. Tests on UHPFRC under full restraint conditions were done for the first time using a newly developed close loop deformation control method. A value of 0.2 MPa was chosen as the trigger value to activate the closed loop of deformation control, to be low enough to minimize history of loading effects on the viscous response before its activation, while being high enough to demonstrate a sufficient stiffness of the specimen to respond to a closed loop deformation control without yielding out of control.
- ii. The test results showed that the rate of development of eigenstresses was much slower for Mix II. This was attributed to the higher relaxation potential of this mix as was confirmed through tensile creep tests at 20 °C at an age of 14 days.
- iii. Most importantly, the test results revealed that except for Mix I cured at 20 °C, even under full restraint conditions, the developed eigenstresses did not reach even the elastic limit of the material, during the duration of the tests. The eigenstresses in Mix I cured at 20 °C reached the strain-hardening domain after about one month, whereas the same in Mix II cured at 20 °C were only approaching the strain-hardening domain even after three months. However, it clearly indicates that it is necessary to have UHPFRC with robust strain-hardening able to accommodate unfavorable fiber orientations to avoid the possibility of the localized macro crack, as far as possible, in structural applications.

2.2 Influence of moderate to low curing temperatures on the kinetics of hydration and tensile response of SH-UHPFRC

The influence of moderate to low temperatures on the response of the studied SH-UHPFRC mixes will be discussed under two sections: kinetics of hydration at a material level and the tensile response at a structural level.

2.2.1 Kinetics of hydration

- i. Using a Double Danish model on the cumulative heat of hydration curves from the isothermal calorimetry at different temperatures, the ultimate degrees of hydration of Mix I and II were calculated to be 0.29 and 0.51 respectively. According to the Waller model [1], the degree of hydration of cement for Mix I and II were 0.30 and 0.52 respectively, whereas the Jensen model [2] predicts respectively 0.30 and 0.50 for the same.
- ii. A single activation energy was able to incorporate the effect of different curing temperatures on the development of cumulative heat of hydration and elastic modulus for each of the mixes. Using the master curve method, the E_a/R values of Mix I and II were calculated to be 3300 K and 4000 K respectively.
- iii. Even though the degree of hydration of cement (α_{cem}) and percentage of silica fume reacted for pozzolanic reaction (α_{SF}) showed higher rates of development at higher curing temperatures in an age domain, the ratio of α_{SF}/α_{cem} in a maturity domain showed a unique trend under all curing temperatures. The ratio indicated the possibility of two phases of pozzolanic reaction with different rates of consumption of the silica fume. It was speculated that the second stage of pozzolanic reaction might have led to further refinement of the pore structure, leading to changes in the rate of development of autogenous shrinkage and eigenstresses. The trends also indicated that it could be the heat produced from the second phase of the pozzolanic reaction that was represented by the second term of the Double Danish model.

2.2.2 Tensile response

- i. The elastic limit and tensile strength were both found to increase with a decrease in curing temperature, which was attributed to the formation of a denser microstructure with lesser quantities and sizes of capillary pores, and a better fiber matrix bond at lower temperatures. The elastic modulus and strain at tensile strength were found to be insensitive to the curing temperature.
- ii. A systematic increase in the autogenous shrinkage was observed in the age domain as the curing temperatures increased, which was attributed to higher rate of hydration at higher temperature. The trend of development of autogenous shrinkage in the degree of reaction domain revealed three separate domains for both mixes; a positive rate of development until a DOR of about 0.2-0.3 followed by a zero or negative rate of development until a DOR of 0.6, which was further followed by a positive rate of development. However, the autogenous shrinkage in both mixes showed higher values at 20 °C, which was attributed to the scatter in the measurements. In any case, a more intrinsic domain that includes the state of microstructure and pore structure, would be an even better domain to define the influence of curing temperature on the autogenous shrinkage.

- iii. The eigenstresses development under full restraint indicated similar trends in the degree of reaction domain for both mixes, with Mix II showing slightly lower values at any particular DOR, owing to its higher relaxation potential. More importantly, except for Mix I cured at 20 °C, even after one month, the eigenstresses in none of the other tests reached the resistance envelope of the elastic limit or the tensile strength during the duration of the tests, even under full restraint conditions. The eigenstresses in Mix I cured at 20 °C reached the strain-hardening domain after about one month, whereas the same in Mix II cured at 20 °C were only approaching the strain-hardening domain even after three months. For Mix I cured at 20 °C, even though the eigenstresses reached the strain-hardening domain, it never reached the tensile strength of the material. This ensures that, unless in the case of a detrimental fiber orientation, eigenstresses developed due to restrained shrinkage may never lead to the formation of localized macrocracks in practical applications even under very low temperatures, for these specific mixes and fibrous composition.

2.3 Development of a viscoelastic-viscohardenig model to predict the tensile response of SH-UHPFRC in the elastic and hardening domain.

- i. A viscoelastic-viscohardenig model was developed which was able to predict the tensile responses of the mixes under different loading conditions. The model was used to discuss the interaction of ageing, hydration, early age volume changes, viscoelastic phenomena and damage and their influence on the overall tensile behavior of UHPFRC.
- ii. The model takes into consideration the rate dependency of the elastic limit as well as the progressive damage in the strain-hardening domain.
- iii. Confirming the measurements, the model predicted a “fast hydration rate induced non-linearity” when loaded under strain rates in the range of 1×10^{-7} 1/s- 1×10^{-8} 1/s at an age 1 hour after setting, which was attributed to the non-linearity in the development of elastic modulus at the same age. This effect became negligible as the strain rates were reduced further below 1×10^{-9} 1/s. The effect was also not seen when the loading age was greater than 2 days.
- iv. At a strain rate of 1×10^{-11} 1/s, the model predicted an apparent strain softening response, attributed to the combined effect of hardening and a more dominant non-linear viscous relaxation. However, it was also suggested that it might be possible to have a higher hardening modulus at lower strain rates because of possible differences in the strain rates being applied on the overall specimen and on the crack planes where fibers are pulled out.

2.4 Influence of partial replacement of cement clinker with limestone filler.

- i. It was demonstrated for the first time that equivalent strain-hardening tensile response as that of conventional UHPFRC mixes (with 100% cement clinker) could be achieved for UHPFRC mixes with 50% replacement of cement clinker with two types of limestone fillers (Mix II).
- ii. Through monotonic uniaxial tensile tests, it was shown that the elastic limit and the tensile strength of Mix II at an age of 14 days, were almost similar (or even more in some cases) than that of Mix I, ensuring its applicability for traffic even after 14 days.
- iii. The rate of development of eigenstresses was much slower for Mix II when compared to Mix I, which could be attributed to the observed higher viscous potential of Mix II.
- iv. Moreover, the workability in the fresh state as well the capillary absorption in the hardened state were found to be almost similar to that of Mix I.
- v. The studies indicate that the degree of hydration is still low, even in Mix II ($\text{DOH}=0.51$), indicating a possibility of further replacement of cement with limestone filler. However, [3] has shown that even though a 54% replacement of cement clinker with limestone filler led to an increase in the compressive strength of UHPC matrix compared to that of UHPC matrix with no replacement, a 74% replacement led to a decrease in the compressive strength. As such, there is a limit for the replacement of the cement clinker, which could be further investigated.

2.5 Overall conclusion

The main finding of the thesis is that even under a low temperature of 5 °C, the main resistance parameters like elastic limit and tensile strength develop faster than the restrained shrinkage eigenstresses, even under full restraint. Furthermore, even if the eigenstresses reach the strain-hardening domain, as in the case of Mix I at 20 °C, the rate of shrinkage at this stage is so negligible that the viscoelastic (linear/non-linear) potential of the material will prevent the eigenstresses from crossing the tensile strength of the material. Therefore, except in the case of detrimental fiber orientation, the eigenstresses due to restrained shrinkage will never lead to the formation of a localized macro cracks for curing temperatures below 20 °C, for these specific mixes and fibrous composition. However, the influence of additional loads (dead load, live load, traffic load etc) may add to the already developed eigenstresses, which may lead to the formation of new macrocracks at a later age.

A more complex test procedure, to study the development of eigenstresses under the influence of fully restraint shrinkage along with sustained or fatigue loads is therefore needed to completely predict the tensile response of the material. Moreover, it should also be noted that in reality, the drying shrinkage in certain situations would also lead to the development of eigenstresses in addition to the influence of the autogenous shrinkage and thermal deformations.

Furthermore, it should be remembered that the tests were done only for two types of mixes with a specific fibrous mix under quasi-isothermal and sealed conditions. The fact that the eigenstresses didn't cross the elastic limit (except for Mix I at 20 °C) under these specific conditions for the tested mixes does not fully guarantee that a combination of low temperatures and restrained shrinkage may never lead to the formation of macrocracks for other types of UHPFRC mixes and other environmental conditions. In reality, the temperature evolution is not quasi-isothermal as in the case of the TSTM [4,5], and the high increase in the temperature when the heat flow increase during hydration, may lead to a systematic increase in the autogenous shrinkage as well the developed eigenstresses during this period [6]. Even though, [6] had shown that the developed eigenstresses and autogenous deformations under these conditions become similar to those under quasi-isothermal conditions at a later age, whether the sudden increase in the eigenstresses during the increased heat flow will lead to the formation of microcracks is still an open question. The significant difference of the measured elastic limit and eigenstresses at a very early age (1 day age) might indicate that the increase in the eigenstresses due to this "realistic" temperature may not lead to the formation of microcracks, at least for the mixes studied in the present thesis.

However, the situation may be different for other UHPFRC mixes, especially with higher dosages of calcined clay, as discussed in [7], where the resistance parameters develop slower, due to the competition to consume water between the cement hydration and the pozzolanic reaction of kaolinite. The situation will also be different in mixes with lower fibrous volume or fibrous mix with only one type of macrofibers, due to the reduction in the elastic limit, as discussed in section 2.3 of Chapter 1.

Moreover, since even the degree of hydration of Mix II was only 0.51, it might be possible to produce even more environmental friendly low clinker SH-UHPFRC mixes, with further replacement of cement clinker with limestone filler (more than 50%) as shown by [3]. However, [3] has only studied the influence of replacement more than 50% on the compressive strength of the UHPC mixes. More studies are required to understand the tensile response and protective properties of such UHPC/UHPFRC mixes with more than 50% replacement of cement clinker with limestone filler.

3 Perspectives and future works

The possible extensions of the present work will be discussed under four main headers;

- i. Mix development
- ii. Material level investigation
- iii. Structural level investigation
- iv. Modeling

3.1 Mix development

- i. As indicated, in the overall conclusion, it might be possible to produce even more environmental friendly low clinker SH-UHPFRC mixes, with more than 50% replacement of the cement with inert fillers like limestone powder as shown by [3]. However, it was also shown that a replacement level of 74% led to a decrease in the compressive strength of the studied UHPC mixes [3]. Therefore, the limit of replacement should be further investigated in order to have the most eco-friendly SH-UHPFRC mixes. Moreover, [3] has not studied the tensile and protective properties of these mixes with more than 50% replacement of cement clinker with limestone filler, and therefore needs to be investigated, even though those for mixes with 50% replacement were studied in the present thesis.

- ii. Because of the very low reactivity of silica fume, especially under moderate to low temperatures, it might be possible to replace the same using similar but less costly inert ultrafines, having a similar particle size distribution. [8,9] have studied the use of nano-silica either to fully replace or to be used in combination with silica fume in UHPC mixes. However, the cost of nano-silica is much more and is much less available than silica fume, thereby eliminating the possibility of its use over silica fume [7].

Furthermore, many studies have been carried out to investigate the possibility of replacing silica fume in UHPFRC mixes with metakaolin (calcined clay with minimum of 85% kaolinite [10]). [11,12] showed that metakaolin reacts more than silica fume resulting in a comparable or equivalent mechanical properties, but their mixing times were increased. [13] developed a mix with complete replacement of silica fume with metakaolin, without significant loss in the mechanical properties. It was shown that the replacement of silica fume with metakaolin led to a decrease in the autogenous shrinkage [14] and the drying shrinkage [15]. The durability properties for mixes with metakaolin studied by [16] showed excellent penetration resistance to aggressive agents, and the protective properties were similar to that of a reference UHPFRC with silica fume. However, the price of metakaolin is also similar to that of silica fume, therefore not bringing substantial advantage over silica fume.

More recently, calcined clays with relatively modest amount of kaolin, was used to replace the silica fume in UHPC matrix with limestone filler [7], which exhibited similar compressive strengths when compared to a UHPC mix with silica fume. However, the tensile mechanical properties, and durability properties were not studied for these mixes. Even though the mixes have similar compressive strengths, the tensile mechanical properties need not be as efficient as the reference mixes, because of the reduced bond strength in the absence of silica fume. As such, more investigation should be carried out to study the tensile response of such mixes.

3.2 Material level investigation

- i. Assumptions were made in the present study that when the elastic moduli in Mix I and II become similar, the pore structure and consequently the autogenous shrinkage also become similar in them. A detailed study on the microstructure using SEM (Scanning Electron Microscope) imaging and MIP (Mercury Intrusion Porosimetry) will be able to confirm these assumptions. It might also indicate the possible differences in the microstructure (less dense/ more dense CSH) due to the proposed possible second stage of the pozzolanic reaction and silica fume consumption.
- ii. It was proposed in the thesis that the strain rate insensitivity of the tensile strength of SH-UHPFRC might be because of the possible differences in the imposed strain rate on the overall specimen and the strain rate acting for the pullout of the fibers, which bridge the multiple cracking planes that develop in the hardening domain. As such, it is necessary to determine the actual strain rate acting along the crack planes during fiber pullout using techniques like Digital Image Correlation (DIC) or using latest deformation measurement techniques like video extensometers.
- iii. Once a correlation is established between the overall strain rate and the strain rate at which the fibers are pulled out, single fiber pullout tests should be carried out, to study the influence of low strain rates and low curing temperatures on the pullout behavior of the fibers. This will aid in the explanation of the strain rate insensitivity of the tensile strength and hardening modulus, observed in the present study.

3.3 Structural level investigation

- i. The lack of more experimental relaxation tests at different strain levels and ages in the hardening domain for both mixes were highlighted in the thesis. As such, an extensive experimental campaign to study the same is highly recommended. Moreover, full restraint tests should be conducted in the hardening domain right after setting. Monotonic tests at 20 °C at an age of 24 hours (after addition of water) indicated that the elastic limit was already higher than 8 MPa for both Mix I and II.

As such, it is possible to monotonically load the specimen until a stress level of 8 MPa at an age of 24 hours, followed by a full restraint test using the procedure developed in the thesis. This will also help in obtaining the parameters of the viscohardening part of the proposed model from very early age.

- ii. Tensile fracture tests need to be conducted at an age of 1 day (or few hours after setting) for specimens cured at lower temperatures of 10 °C and 5 °C, similar to the tests conducted at 24 hours under a curing temperature of 20 °C in the present study. If it can be ensured that the elastic limit at these ages is significantly higher than the developed eigenstresses, the possibility of microcracking at a very early age could be eliminated.
- iii. Recent advances in Digital Image Correlation technique has revealed the possibility of its application on fresh cement mortar to quantify the settlement and autogenous shrinkage [17]. This technique could be used in the TSTM tests under full restraint not only to study the deformations occurring in the restraint specimen, but also to detect the presence of microcracks at very early age, if any. However, there might be challenges of temperature and moisture control in the upper face of the TSTM specimen where the DIC is applied. The temperature control could at least be done through the other three faces in contact with the mold, and it can be assumed that it will be conducted even to the upper face of the specimen. However, this is not the case with the moisture control, as the drying shrinkage will occur through the upper face of the specimen. However, this can be eliminated by keeping a moist atmosphere around the specimen or by spraying water on the upper face at regular intervals. Optical strain gages can also be used embedded in the specimen to have information about microcracks occurring in the material under full restraint.
- iv. A more comprehensive experimental campaign should be carried out using Acoustic emission detection to study the development of microcracks for different rates of loading and curing temperatures. The procedure for determining the elastic limit in the current thesis was based on the proportionality of the stress-strain response in the elastic domain and the deviation from it. The tests in the present thesis have indicated the presence of few AE events even before the calculated elastic limit (based on the deviation from linearity). As such, it might be possible to postulate another definition for the elastic limit, based on the extent of microcracks/ AE events developed, which can be achieved through a detailed study using Acoustic emission technique for different strain rates and curing temperatures. Moreover, a combination of acoustic emission and DIC techniques might explain the trend of increase of the non-linear relaxation in the hardening domain.

3.4 Modeling

- i. A viscoelastic-viscohardenening model was developed in the present study to predict the tensile response of both mixes at low and high stress levels. However, the model was only applied on tests at 20 °C. The influence of temperature on the viscous response of the material was not included in the model. As shown in chapter 5, a degree of hydration domain was able to include the effect of curing temperatures on the mechanical properties of SH-UHPFRC. As such, the viscoelastic-viscohardenening model could be extended into the degree of hydration domain, using the general Arrhenius equation as shown below, equations 1 and 2. However, the influence of temperature on the parameters of the Maxwell chains should also be checked. On the one hand, a higher temperature leads to a higher creep response; whereas on the other hand, a higher curing temperature would lead to a higher apparent age (maturity/degree of hydration) of the material and consequently a lower creep response [18]. This would therefore mean that, even under the same degree of hydration, the mixes might show different viscous response under different curing temperatures. A sub-model should therefore be incorporated in the previous model to include this dependency of the viscous parameters on the curing temperature.

$$\frac{d\alpha}{dT} = A(\alpha).F(T) \quad (1)$$

$$F(T) = e^{-\frac{E_a}{R} \left(\frac{1}{273+T} \right)} \quad (2)$$

where, $d\alpha/dT$ is the rate of hydration, $A(\alpha)$ is the chemical affinity and $F(T)$ is the temperature function defined by the Arrhenius equation.

- ii. Moreover, as discussed in section 3.3, full restraint tests need to be conducted in the hardening domain a few hours after setting, to obtain the parameters of the viscohardenening part of the model in this age frame too.
- iii. A meso-level model that can predict the influence of low strain rates on the fiber pullout behavior, should be developed and incorporated within the VE-VH model, so that the possibility of differences in the overall strain rates and the fiber pullout strain rate, as discussed in section 3.2 could be included. This will also confirm whether the proposed hypothesis of a “strain softening behavior” under very low strain rates is valid or not.
- iv. A model incorporating a more intrinsic domain that includes the state of microstructure and pore structure, should be developed to define the influence of curing temperature on the autogenous shrinkage.

References

- [1] V. Waller, “Relations entre composition des bétons, exothermie en cours de prise et résistance à la compression”, thèse de doctorat, LCPC, Nantes, France, (2001).
- [2] O.M. Jensen, Autogenous Phenomena in Cement-Based Materials, Doctoral thesis, Technical University of Denmark, (2005).
- [3] W. Huang, H. Kazemi-Kamyab, W. Sun, K. Scrivener, Effect of cement substitution by limestone on the hydration and microstructural development of ultra-high performance concrete (UHPC), *Cem. Concr. Compos.* 77 (2017) 86–101.
- [4] A. Kamen, Comportement au jeune âge et différé d’un BFUP écrouissant sous les effets thermomécaniques, Doctoral thesis No: 3827, Ecole Polytechnique Fédérale de Lausanne, Switzerland, (2007).
- [5] K. Habel, Structural behavior of elements combining ultra-high performance fiber reinforced concretes (UHPFRC) and reinforced concrete, Doctoral thesis No: 3036, Ecole Polytechnique Fédérale de Lausanne, Switzerland, (2004).
- [6] A. Kamen, E. Denarié, H. Sadouki, E. Brühwiler, Thermo-mechanical response of UHPFRC at early age - Experimental study and numerical simulation, *Cem. Concr. Res.* 38 (2008) 822–831. doi:10.1016/J.CEMCONRES.2008.01.009.
- [7] W. Huang, H. Kazemi-Kamyab, W. Sun, K. Scrivener, Effect of replacement of silica fume with calcined clay on the hydration and microstructural development of eco-UHPFRC, *Mater. Des.* 121 (2017) 36–46.
- [8] T. Oertel, F. Hutter, R. Tänzler, U. Helbig, G. Sestl, Primary particle size and agglomerate size effects of amorphous silica in ultra-high performance concrete, *Cem. Concr. Compos.* 37 (2013) 61–67. doi:https://doi.org/10.1016/j.cemconcomp.2012.12.005.
- [9] R. Yu, P. Spiesz, H.J.H. Brouwers, Effect of nano-silica on the hydration and microstructure development of Ultra-High Performance Concrete (UHPC) with a low binder amount, *Constr. Build. Mater.* 65 (2014) 140–150. doi:https://doi.org/10.1016/j.conbuildmat.2014.04.063.
- [10] Additions pour béton hydraulique - Métakaolin - Spécifications et critères de conformité. French Standard (NF P 18-513), (2012).
- [11] A. Taфраoui, G. Escadeillas, S. Lebailli, T. Vidal, Metakaolin in the formulation of UHPC, *Constr. Build. Mater.* 23 (2009) 669–674. doi:10.1016/J.CONBUILDMAT.2008.02.018.
- [12] B. Rabehi, Y. Ghernouti, K. Boumchedda, Strength and compressive behavior of ultra high-performance fiber-reinforced concrete (UHPFRC) incorporating Algerian calcined clays as pozzolanic materials and silica fume, *Eur. J. Environ. Civ. Eng.* 17 (2013) 599–615.

- [13] E. Nguyen Amanjean, T. Vidal, Low cost ultra-high performance fiber reinforced concrete (UHPRFC) with flash metakaolin, in: *Key Eng. Mater.*, Trans Tech Publ, (2015): pp. 55–63.
- [14] S. Staquet, B. Espion, Early age autogenous shrinkage of UHPC incorporating very fine fly ash or metakaolin in replacement of silica fume, in: *Int. Symp. Ultra High Perform. Concr. Kassel Ger.*, (2004): pp. 587–599.
- [15] Z. Li, Drying shrinkage prediction of paste containing meta-kaolin and ultrafine fly ash for developing ultra-high performance concrete, *Mater. Today Commun.* 6 (2016) 74–80. doi:<https://doi.org/10.1016/j.mtcomm.2016.01.001>.
- [16] A. Tafroui, G. Escadeillas, T. Vidal, Durability of the Ultra High Performances Concrete containing metakaolin, *Constr. Build. Mater.* 112 (2016) 980–987. doi:<https://doi.org/10.1016/j.conbuildmat.2016.02.169>.
- [17] E.D. Dzaye, E. Tsangouri, K. Spiessens, G. De Schutter, D.G. Aggelis, Digital image correlation (DIC) on fresh cement mortar to quantify settlement and shrinkage, *Arch. Civ. Mech. Eng.* 19 (2019) 205–214. doi:<https://doi.org/10.1016/j.acme.2018.10.003>.
- [18] M. Kazemi Kamyab, Autogenous Shrinkage and Hydration Kinetics of SH-UHPRFC under Moderate to Low Temperature Curing Conditions, Doctoral thesis No: 5681, Ecole Polytechnique Fédérale de Lausanne, Switzerland, (2013).


Curriculum Vitae

MOHAMED ABDUL HAFIZ

<https://www.linkedin.com/in/mohamed-abdul-hafiz-5517a8123/>

Route du Pont Bleu 21, 

1023-Crissier

+41 779 83 83 88 

mohamed.hafiz@epfl.ch 

mahafiz8@gmail.com



SUMMARY

Enthusiastic structural engineer with a demonstrated history of working in higher education institutions. Skilled in structural engineering and concrete technology, especially in the field of development of Ultra High Performance Fiber Reinforced Cementitious Composites (UHPFRC) for rehabilitation works. Experienced in the field of experimental testing and numerical modelling required in the field of structural engineering. Eager to channel all my efforts in the domain of civil engineering research along with its practice in the field.



EDUCATION

Ph.D. in Structural Engineering | *École Polytechnique Fédérale de Lausanne (EPFL), Switzerland*

August 2015 – July 2019

- Working experience in well equipped structural engineering and material science laboratories in EPFL, which is one among the top 15 technological universities in the world since 2012.
- Ph.D. thesis on the tensile behaviour of Ultra High Performance Fibre Reinforced Cementitious Composites under low strain rates and low temperatures.
- Ph.D. supervisor: Dr. Emmanuel Denarie, Structural Maintenance and Safety Laboratory (MCS), Department of Civil Engineering, EPFL.

Master of Technology, M.E (Engineering) in Structural Engineering | *Indian Institute of Science, Bangalore, India*

August 2013 – July 2015

- 1st rank holder in Structural Engineering in the Civil Engineering Department in the Indian Institute of Science for the 2013-2015 academic batch.
- Master thesis on the fatigue and fracture behavior of graphite.
- Thesis supervisor: Prof. J. M. Chandra Kishen, Department of Civil Engineering, IISc Bangalore.

Bachelor of Technology, B.Tech in Civil Engineering | Government Engineering College, Trichur, India

August 2008 – June 2012

- 1st rank holder in Civil engineering in the University of Calicut for the 2008-2012 academic batch.
- Bachelor thesis on "Proposal for design of a triangular railway station in Shoranur, Kerala".



PROFESSIONAL EXPERIENCE

Doctoral assistant | École Polytechnique Fédérale de Lausanne (EPFL), Switzerland

August 2015 – July 2019

- Teaching assistant during Ph.D.
- Supervised multiple projects and practical lab sessions for master level civil engineering students.

Guest lecturer | Conquer Group, Malappuram, Kerala

February 2013 – May 2013

- Taught undergraduate courses in Civil engineering

Summer Intern | CIDBI, Trichur, Kerala

April 2011



RELEVANT SKILLS AND EXPERTISE

- Engineering software packages – STAAD Pro, AutoCAD, ABAQUS, DIANA.
- Miscellaneous – MS Office, MATLAB.
- Teamwork, multidisciplinary thinking, public speaking.
- Good professional communication skills.
- Self-motivated and goal oriented.



LANGUAGES KNOWN

- English (highly proficient), Malayalam (native), Hindi, Arabic, French (A1 level)



WORKSHOPS ATTENDED

- International summer school on "Concrete with Supplementary Cementitious Materials", Lyngby, Denmark, August 2016.

- Workshop on “Teaching toolkit I,” EPFL, Lausanne, Switzerland, March 2016.



ORAL AND POSTER PRESENTATIONS

- Oral presentation on the topic “*Tensile viscous response of Strain-Hardening UHPFRC under high restraint and isothermal conditions*”, Euro C conference on Computational modelling of Concrete and Concrete Structures, Bad Hofgastein, Austria, Feb 26 – Mar 1, 2018.
- Oral presentation on the topic “*Experimental study of tensile response of Strain-Hardening UHPFRC at early age*,” 4th International Conference on Strain-Hardening Cement-Based Composites (SHCC 4), Dresden, Germany, September 18-20, 2017.
- Poster presentation on the topic “*Experimental study of tensile response of Strain-Hardening UHPFRC at early age*,” 4th International Conference on Strain-Hardening Cement-Based Composites (SHCC 4), Dresden, Germany, September 18-20, 2017.



PUBLICATIONS

- **M.A. Hafiz**, A. Hajiesmaeili, E. Denarié, “*Tensile response of low clinker UHPFRC subjected to fully restrained shrinkage*”, Cement and Concrete Research, Vol 124, October (2019). doi:<https://doi.org/10.1016/j.cemconres.2019.105804>.
- **M.A. Hafiz**, E. Denarié, “*Experimental Study of Tensile Response of Strain-Hardening UHPFRC at Early Age*” in Strain-Hardening Cementitious Composites, Springer, Dresden, Germany, 2018: pp. 308–315.
- **M.A. Hafiz**, E. Denarié, “*Tensile viscous response of Strain-Hardening UHPFRC under high restraint and isothermal conditions*”, in Euro C - 2018 Computational modelling of Concrete Structures, March 2018: pp. 903–912.
- **M.A. Hafiz**, A. Hajiesmaeili, E. Denarié, “*Tensile response of UHPFRC under very low strain rates and low temperatures*”, submitted to Cement and Concrete Research, April 2019.
- **M.A. Hafiz**, E. Denarié, “*Modelling of the tensile behavior of SH-UHPFRC at low and high stress levels, under very low loading rates*”, submitted to Journal of Engineering Mechanics, July 2019.
- **M.A. Hafiz**, Jørgen Skibsted, E. Denarié, “*Influence of low curing temperatures on the tensile response of low clinker Strain-Hardening UHPFRC under full restraint*”, submitted to Cement and Concrete Research, June 2019.



AWARDS AND HONORS

- 1st rank holder in Civil Engineering in the year 2012 from the University of Calicut, Kerala.

- 1st rank holder in Structural Engineering in the year 2015 from Indian Institute of Science, Bangalore.
- School topper in the AISSCE 12th standard examination conducted by CBSE in the year 2008.
- School topper in the AISSE 10th standard examination conducted by CBSE in the year 2006.
- Recipient of the CBSE Central Sector Scholarship for outstanding performance in AISSCE exam of 12th grade.
- Achieved an All India Rank of 50 among 68000 candidates in the Graduate Aptitude Test in Engineering (GATE) exam in the year 2013.
- Secured 3rd prize in state level Paper Presentation competition during the technical fest "EXTRICO" conducted by the Indian Society for Technical Education (ISTE) in the year 2009.
- Member of the IISc Bangalore College Football Team during the year 2014.
- Member of the GEC, Trichur College Football Team during the years 2010, 2011.
- Member of the GEC, Trichur College Badminton Team during the year 2011.



PERSONAL PROFILE

Name	Mohamed Abdul Hafiz
Sex	Male
Nationality	Indian
Date of birth	03-07-1990
Father's name	Abdul Nazer
Mother's name	Amina Kutty
Residential address (Switzerland)	Route du Pont Bleu 21, 1023- Crissier



REFERENCES

1. **Dr. Emmanuel Denarié**
Senior Scientist, Lecturer
Structural Maintenance and Safety Laboratory (MCS)
Institute of Civil Engineering (IIC)
School of Architecture, Civil and Environmental Engineering (ENAC), EPFL
CH-1015 Lausanne, Switzerland
Phone: +41 (0) 21 693 28 93
Email: emmanuel.denarie@epfl.ch
2. **Prof. Eugen Brühwiler**
Full professor
Structural Maintenance and Safety Laboratory (MCS)
Institute of Civil Engineering (IIC)

School of Architecture, Civil and Environmental Engineering (ENAC), EPFL,
CH-1015 Lausanne, Switzerland
Phone: +41 (0) 21 693 28 82
Email: eugen.bruehwiler@epfl.ch

3. Prof. P. P. Sivan

Associate Professor
Department of Civil Engineering
Government Engineering College, Thrissur, India
Phone: +91 (0) 9809 631 256
Email: ppsivan@yahoo.com



DECLARATION

I hereby declare that the details given above are correct and I bear the responsibility for the correctness of the particulars.

Date: 18-07-2019

Place: Lausanne, Switzerland

[Mohamed Abdul Hafiz]

